THÈSE

Pour obtenir le grade de

DOCTEUR DE L'UNIVERSITÉ GRENOBLE ALPES

École doctorale : PHYS - Physique
Spécialité : Physique pour les Sciences du Vivant
Unité de recherche : Laboratoire Interdisciplinaire de Physique

Analyse Optique de la Fonction du Canal Nav1.2 Neuronal : Rôles Physiologiques et Implications dans Les Canalopathies à Perte de Fonction de SCN2A

Optical Analysis of Nav1.2 Function in Neurons: Physiological Roles and Pathological Implications in SCN2A Loss-of-Function Channelopathies

Présentée par :

Fatima ABBAS

Direction de thèse :

Marco CANEPARI CHARGE DE RECHERCHE HDR, INSERM DELEGATION AUVERGNE RHONE-ALPES	Directeur de thèse

Rapporteurs :

PAOLA PEDARZANI
FULL PROFESSOR, UNIVERSITY COLLEGE LONDON
FLORIAN LESAGE
DIRECTEUR DE RECHERCHE, INSERM PACA - CORSE

Thèse soutenue publiquement le **24 novembre 2025**, devant le jury composé de :

HERVE DUBOUCHAUD, PROFESSEUR DES UNIVERSITES, UNIVERSITE GRENOBLE ALPES	Président
PAOLA PEDARZANI, FULL PROFESSOR, UNIVERSITY COLLEGE LONDON	Rapporteure
FLORIAN LESAGE, DIRECTEUR DE RECHERCHE, INSERM PACA - CORSE	Rapporteur
CELINE AUGER, CHARGEE DE RECHERCHE, CNRS ILE-DE- FRANCE VILLEJUIF	Examinatrice
CECILE DELACOUR, CHARGEE DE RECHERCHE HDR, CNRS DELEGATION ALPES	Examinatrice

Acknowledgements

This work is, first and foremost, solemnly dedicated to people suffering from neurological disorders, and to their families and support systems helping them throughout the hardships. Especially the children inflicted with SCN2A-related conditions, whose faces and struggles remain carved in my memory, and were the strength that kept me going whenever the weight of this project felt overwhelming. My greatest hope would be that my contribution, though modest in the grand scheme of Science, could add a piece to the collective effort in building foundations for future therapies.

My most heartfelt thanks go to my supervisor, Dr. Marco Canepari. Five years ago, I arrived from Lebanon as an intern, with little experience and many uncertainties. You saw the potential in me, trusted me, and welcomed me into your team. Thank you for guiding me with patience and conviction, for sharing your knowledge generously, and for offering me the space I needed to flourish. These years together have shaped not only my scientific path but also my personal growth journey. I remain deeply grateful for everything I have learned under your guidance.

I would also like to express my deepest gratitude to the members of my jury, Prof. Paola Pedarzani, Dr. Florian Lesage, Dr. Céline Auger, Dr Cécile Delacour, And Prof. Hervé Doubouchaud. Not only will my thesis be read and evaluated with the highest rigor and thoroughness, but I feel privileged that my work will be presented to members of the scientific field with a stature as high and eloquent as yours.

Next, I thank all the collaborators on this project. Many thanks to Dr. Michel De Waard and his team for developing highly selective toxins; to Prof. Michele Migliore and Elisabetta Giacalone for their ongoing work on the NEURON model; and to LBFA Animal Facility team, especially Cindy Tellier, for their dedicated efforts in maintaining the mouse line. I am also thankful to the members of l'Institut de pharmacologie moléculaire et cellulaire, in particular Dr. Massimo Mantegazza, Sandrine Cestèle, and Martina Simonti for carrying forward this project from a different perspective and for many fruitful discussions.

I would also like to extend my thanks to LIPHY members, and in particular, OPTIMA team, for being a stimulating and supportive environment. Dr. Thomas Boudou and Prof. Philippe Peyla, thank you for following my work as members of my CSI and for enriching my experience through our valuable discussions each year. From within our team, my sincere appreciation goes to Dr. Luiza Filipis for taking my hands and introducing me into this world, you gave me the courage to step forward. To Dr. Laila Blömer, thank you for your contribution to this project and for being an example of the strong woman in Science. To Dr. Ömer İpek, though you were only there for a short period, thank you for writing programs to analyze the enormous amount of Data I threw in your direction. To Sherine and Thibault, thank you for brightening up the workdays with humor and fun.

Joudi and Hanadi, who would've thought that it would be in France that I make such great friends from my homeland? Thank you for always making me less homesick and more loved and supported. Reem, I can only thank you for your presence, company and support.

To my family, my greatest source of strength, I owe everything to you. There has been no accomplishment I achieved or milestone I set out for, except that they were driven by a profound urge to make you proud. To my father, my first supporter who foresaw things in me no one else did: your unwavering belief has been a guiding force all my life. To my sunshine of a mother, who herself has endured severe migraine and neurological illness for as long as I can remember, I dedicate the culmination of my efforts to you. I'm merely reaping the benefits of the love and support you sowed in me. My beloved brothers, Hussein and Bilal, having you in my life will forever feel like I have a shoulder to lean onto. To my sisters, Mona and Farah, you are the joy of my life, the ones who bring laughter and warmth no matter the distance. Reem, blue days were only numbered because I had you there. And to my new extended family, especially Sara, you are a gem, thank you for showering me with love ever since I stepped in.

And finally, to my husband, Fawaz. My companion, my anchor, my love. You came to France at the time I needed you most, and your presence changed everything. You have been beside me in silence when I needed calm, and you have lifted me with your words when I needed strength. Your love, care, and endless support have been my haven throughout the stormiest days, and the greatest gift of my life. I only wish it's enough for you to know, that I carried you with me in every step of the way and that you are in every line of this thesis, like it is enough for me to know that I wouldn't have done this without you.

Lastly, Alhamdulillah, from the path to the destination, and for every step in between.

This thesis was funded by L'Agence Nationale de la Recherche (ANR) and the LabEx Ion Channel Science and Therapeutics, completed at Laboratoire Interdiplinaire de Physique (LIPhy) and Université Grenoble Alpes.

Abstract

The *SCN2A* gene encodes the voltage-gated sodium channel (VGNC) $Na_v1.2$, predominantly expressed in the axon initial segment (AIS) of excitatory neurons in the cortex, vital for the generation and back-propagation of action potentials (APs). Pathogenic variants of *SCN2A* are associated with a wide spectrum of neurodevelopmental disorders, including autism and intellectual disability, commonly linked to $Na_v1.2$ loss-of-function (LoF). Despite its physiological importance, little is known about the mechanisms by which $Na_v1.2$ dysfunction alters neuronal excitability and how these perturbations evolve during postnatal development.

In this thesis, we investigated the pathophysiology underlying *SCN2A* LoF channelopathies in two *SCN2A* LoF mouse models with features of autistic-like behavior: a heterozygote knock-out (*Scn2a*$^{+/-}$), and a knock-in (*Scn2a*$^{+/L1314P}$) carrying a patient-derived missense variant, and we compared them to wild-type (*Scn2a*$^{+/+}$) mice. We combined whole-cell patch clamp recordings with ultrafast optical imaging of sodium (Na^+), calcium (Ca^{2+}), and membrane potential (V_m) in cortical slices to resolve the submillisecond dynamics (50-100 µs scale) of AP generation in layer 5 pyramidal neurons (L5PNs) during a defined postnatal period (P21-40).

At the AIS, sodium and calcium imaging revealed reduced proximal Na^+ influx and impaired distal Ca^{2+} signals in *Scn2a*$^{+/-}$ neurons, whereas *Scn2a*$^{+/L1314P}$ showed preserved Na^+ signaling but selective disruption in the refinement of $Na_v1.2$-mediated Ca^{2+} kinetics. Somatic whole-cell recordings further distinguished AP parameters in the two models at early juvenile stages (P21-24), *Scn2a*$^{+/-}$ cells showed wider APs, while *Scn2a*$^{+/L1314P}$ neurons exhibited reduced AP amplitude. AIS voltage imaging was consistent with sharper waveforms in the distal AIS in the knock-in (KI) despite preserved Na^+ amplitude. Together, these results indicate distinct mechanisms by which LoF alters AP initiation and somatic waveform, with evidence pointing to altered K^+ channel recruitment. To further probe which conductance shapes these differences, we applied local pharmacology targeting K_v1, K_v7, and BK channels. We observed the strongest widening of distal AIS APs by blocking K_v1, particularly in *Scn2a*$^{+/L1314P}$ neurons, whereas BK and K_v7 blockers produced smaller effects. We next

extended the analysis to the somatodendritic domain using brief three-AP bursts and we evaluated the integrative nonlinear Ca^{2+} responses in apical dendrites. These exploratory experiments provide the first description of dendritic Ca^{2+} electrogenesis in *SCN2A* LoF models and suggest that this regenerative process is reshaped rather than abolished despite perturbations at the AIS level. In parallel, we also assessed the effect of a VGNC activator, the scorpion toxin AaH-II. While not isoform selective, subcellular delivery of AaH-II near the AIS demonstrated a spatially structured sensitivity to $Na_v1.2$ inactivation, producing local changes in Na^+ and Ca^{2+} signals, highlighting thus the importance of high-resolution pharmacological approaches to assess candidate modulators at their sites of physiological enrichment.

In summary, our results shed light on the divergent functional consequences of *SCN2A* LoF mutations. In juvenile mice, haploinsufficiency primarily reduces $Na_v1.2$ activity, whereas the L1314P variant produces a distinct excitability impairment with a strong susceptibility to K_v1 modulation. This challenges the widely accepted concept of gain-of-function (GoF) and loss-of-function (LoF) which is applied to classify channelopathies. By combining our cutting-edge techniques with age-specific analyses and targeted pharmacological interventions, we establish a novel approach for physiological phenotyping and drug assessment at the subcellular level, offering valuable insights into complex genotype-phenotype correlations and advancing the path toward therapeutic strategies targeted to specific patterns of $Na_v1.2$ dysfunctions in *SCN2A*-related disorders.

Keywords: *SCN2A*, $Na_v1.2$, Channelopathies, Axon Initial Segment, Patch-Clamp, Ultrafast Optical Imaging, Neuronal Excitability

Résumé

Le gène *SCN2A* code pour le canal sodique potentiel-dépendant (VGNC) $Na_v1.2$, principalement exprimé dans le segment initial de l'axone (AIS) des neurones excitateurs corticaux, et essentiel à la génération et à la rétropropagation des potentiels d'action (PA). Les mutations de *SCN2A* sont associées à un large spectre de troubles neurodéveloppementaux, comme l'autisme et la déficience intellectuelle, fréquemment liés à une perte de fonction (LoF) de $Na_v1.2$. Malgré son importance physiologique, les mécanismes par lesquels sa dysfonction altère l'excitabilité neuronale et leur évolution au cours du développement demeurent mal caractérisés.

Dans cette thèse, nous avons étudié la physiopathologie des canalopathies *SCN2A* LoF dans deux modèles murins présentant des traits autistiques : un hétérozygote knock-out (*Scn2a*$^{+/-}$) et un knock-in (*Scn2a*$^{+/L1314P}$) porteur d'un variant missense dérivé d'un patient, comparés à des souris sauvages (*Scn2a*$^{+/+}$). Nous avons combiné des enregistrements patch-clamp avec de l'imagerie optique ultrarapide du sodium (Na^+), du calcium (Ca^{2+}) et du potentiel de membrane (V_m) dans des tranches corticales pour résoudre à l'échelle de 50 à 100 µs la génération du PA dans les neurones pyramidaux de la couche 5, pendant une période postnatale définie (P21-40).

Au niveau de l'AIS, l'imagerie des courants calciques et sodiques a montré une diminution de l'influx sodique proximal et des signaux calciques distaux altérés dans les neurones *Scn2a*$^{+/-}$. En revanche, les neurones *Scn2a*$^{+/L1314P}$ présentaient une signalisation sodique préservée mais un raffinement calcique perturbé. Les enregistrements somatiques en whole-cell ont distingué les paramètres de PA aux stades juvéniles précoces (P21-24) : les cellules *Scn2a*$^{+/-}$ montraient des PA élargis, alors que les neurones *Scn2a*$^{+/L1314P}$ présentaient des amplitudes réduites. L'imagerie de tension à l'AIS était cohérente avec des PA plus aigus dans la portion distale malgré une amplitude Na^+ quasi normale. Ces observations indiquent des mécanismes distincts par lesquels la LoF modifie l'initiation du PA et sa forme somatique, impliquant une modification du recrutement des canaux potassiques. Pour tester cette hypothèse, nous avons appliqué des agents pharmacologiques ciblant localement les canaux K_v1, K_v7 et BK. Le blocage de K_v1 a induit l'élargissement le plus marqué des PA distaux,

surtout dans les neurones *Scn2a*$^{+/L1314P}$. Nous avons ensuite étendu l'analyse au domaine somato-dendritique et évalué les réponses calciques non linéaires dans les dendrites apicales lors des bursts de trois PA. Ces expériences constituent la première description de l'électrogénèse calcique dans des modèles *SCN2A* LoF et indiquent que ce processus régénératif est remodelé plutôt qu'aboli, malgré les perturbations observées à l'AIS. En parallèle, nous avons évalué l'effet d'un activateur de VGNC, la toxine scorpionique AaH-II. Bien que non sélective, son administration près de l'AIS a montré une sensibilité spatiale à l'inactivation de $Na_v1.2$, produisant des modifications locales des signaux Na^+ et Ca^{2+}, soulignant l'intérêt d'approches pharmacologiques à haute résolution pour évaluer les modulateurs sur leurs sites physiologiques.

En résumé, nos résultats révèlent des conséquences fonctionnelles divergentes des mutations *SCN2A*. Chez les juvéniles, l'haplo-insuffisance réduit surtout l'activité de $Na_v1.2$, tandis que le variant L1314P altère différemment l'excitabilité avec une susceptibilité à la modulation de K_v1. Cela remet en question le cadre GoF/LoF couramment utilisé pour classer les canalopathies. En intégrant des techniques de pointe, des analyses développementales précises et de la pharmacologie ciblée, nous proposons une approche nouvelle de phénotypage physiologique et d'évaluation pharmacologique à l'échelle subcellulaire, éclairant ainsi les corrélations génotype-phénotype complexes et ouvrant la voie à des thérapies adaptées à des profils précis de dysfonction de $Na_v1.2$.

Mots clés : *SCN2A*, $Na_v1.2$, Canalopathies, Segment initial de l'axone, Patch-Clamp, Imagerie optique ultrarapide, Excitabilité neuronale

Table of Contents

LIST OF FIGURES ..... **XI**

LIST OF TABLES ..... **XIII**

LIST OF ABBREVIATIONS ..... **XIV**

CHAPTER 1: INTRODUCTION **1**

1.1 A HISTORICAL PERSPECTIVE **2**
1.2 NEURAL SIGNALING BASICS: EXCITABILITY MECHANICS AND INFORMATION PROCESSING **6**
1.2.1 Polarized Membrane and Resting Potential *7*
1.2.2 From Rest to Response: The Onset of Signaling *9*
1.2.3 Transmitting The Pulse: Synaptic Signal Relay *11*
1.3 VOLTAGE-GATED ION CHANNELS **13**
1.3.1 Potassium Channels *15*
1.3.2 Voltage-Gated Calcium Channels *19*
1.3.3 Voltage-Gated Sodium Channels *20*
1.4 VOLTAGE-GATED SODIUM CHANNEL TYPE-II **27**
1.4.1 Structural and Molecular Profile *27*
1.4.2 Selectivity for Sodium And Emerging Calcium Conductance *29*
1.4.3 Gating Kinetics and Modulation *30*
1.4.4 Pharmacology and Drug Sensitivity *32*
1.4.5 Mapping of $Na_v1.2$ In The Brain *34*
1.5 SYNERGISTIC ION CHANNEL FUNCTION AT THE AXON INITIAL SEGMENT **40**
1.5.1 $Na_v1.2$ Versus $Na_v1.6$ *40*
1.5.2 Potassium Channels and Calcium Channels *42*
1.6 CHANNELOPATHIES IN THE NERVOUS SYSTEM **44**
1.6.1 Overview: Classifications and Clinical Spectrums *44*
1.6.2 Genetic Channelopathies of The CNS *45*
1.6.3 SCN2A-Related Disorders *47*
1.6.4 SCN2A Loss-of-Function Mutations in Autism *51*
1.7 OPEN RESEARCH QUESTION ADDRESSED IN THIS THESIS **54**

CHAPTER 2: METHODOLOGY **57**

2.1 EXPERIMENTAL ANIMAL MODELS AND ETHICAL APPROVAL **58**
2.2 CORTICAL SLICE PREPARATION **60**
2.3 ESTABLISHING WHOLE-CELL PATCH IN CORTICAL NEURONS **61**
2.3.1 Selection of Optimal Brain Slices and Healthy Pyramidal Neurons *61*
2.3.2 Whole-Cell Patch Clamp Configuration *62*
2.4 OPTICAL IMAGING **63**
2.4.1 The Imaging System *63*
2.4.2 Fluorescent Indicators *66*
2.5 PHARMACOLOGICAL MODULATORS FOR ION CHANNELS **68**
2.6 EXPERIMENTAL PROTOCOLS **69**
2.6.1 Electrophysiology Coupled to Ultrafast Imaging in the AIS *69*
2.6.2 Electrophysiology Coupled to Calcium Imaging at the Apical Tuft *72*
2.6.3 Electrophysiology Without Imaging *74*
2.6.4 Drug Delivery in Brain Slices *75*
2.7 OPTICAL DATA ANALYSIS **76**
2.7.1 Sodium Imaging *76*
2.7.2 Voltage Imaging *77*

2.7.3 Calcium Imaging ... *78*
2.8 Statistical Data Analysis ... **79**
2.8.1 Overview of Statistical Tests ... *79*
2.8.2 The Kolmogorov-Smirnov Test ... *80*

CHAPTER 3: CHARACTERIZATION OF ACTION POTENTIAL INITIATION AT THE AXON INITIAL SEGMENT IN *SCN2A* LOSS-OF-FUNCTION MODELS ... **82**

3.1 Selective Reduction in $Na_V1.2$-Mediated Sodium Influx in *Scn2a*$^{+/-}$ Mice ... **83**
3.1.1 Sodium Influx Is Reduced in the Proximal AIS in Scn2a$^{+/-}$ Cells ... *87*
3.1.2 Na^+ Influx in Scn2a$^{+/L1314P}$ Neurons Does Not Appear Different from That in Scn2a$^{+/+}$ ... *87*
3.2 Calcium Currents Highlight Functional $Na_V1.2$ Deficits in *Scn2a*$^{+/-}$ Mice ... **88**
3.2.1 Developmental Refinement of $Na_V1.2$-Mediated Ca^{2+} Influx Is Different in The Three Strains ... *90*
3.2.2 Reduced Ca^{2+} Delays in Scn2a$^{+/-}$ L5PNs ... *92*
3.3 Somatic APs in *Scn2a*$^{+/-}$ and *Scn2a*$^{+/L1314P}$ and *Scn2a*$^{+/+}$ Mice ... **93**
3.3.1 Somatic AP Amplitude in The Three Strains ... *97*
3.3.2 Somatic AP Width in The Three Strains ... *97*
3.4 Exceptionally Sharp Action Potentials Are Generated at The Distal AIS of *Scn2a*$^{+/L1314P}$ Cells ... **98**
3.5 The Effects of Blocking K_V1, K_V7, and BK Channels in The AIS ... **101**
3.5.1 K_V1 Channel Block Preferentially Widens Distal Aps with The Strongest Effect in Scn2a$^{+/L1314P}$ Cells *103*
3.5.2 Distal Aps in Scn2a$^{+/L1314P}$ Cells Are Poorly Affected by K_V7 Channel Block ... *104*
3.5.3 BK Channel Block Produces the Weakest Modulation of AP Shape ... *104*
3.6 Summary and Insights ... **105**

CHAPTER 4: INSIGHTS INTO SOMATIC AND DENDRITIC EXCITABILITY IN *SCN2A*$^{+/-}$ AND *SCN2A*$^{+/L1314P}$ MOUSE MODELS ... **107**

4.1 Somatic Action Potential Amplitude During Short-Interval Bursts ... **109**
4.2 Descriptive Characterization of Regenerative Dendritic Calcium Responses in *SCN2A* LoF Models ... **113**
4.2.1 Dendritic Calcium Electrogenesis Increases with Age in Scn2a$^{+/-}$ but Declines in Scn2a$^{+/L1314P}$ ... *115*
4.2.2 Dendritic Ca^{2+} Electrogenesis Occurs at Comparable Frequencies Across Experimental Groups ... *117*
4.2.3 Dendritic Ca^{2+} Electrogenesis Amplitude Ratios in the Three Strains ... *120*
4.3 Summary and Insights ... **122**

CHAPTER 5: ANALYSIS OF THE EFFECT OF THE SCORPION TOXIN AAH-II ON ACTION POTENTIAL GENERATION IN THE AXON INITIAL SEGMENT ... **123**

5.1 AaH-II Prolongs Inactivation of $Na_V1.2$ and $Na_V1.6$ with Limited Isoform Selectivity ... **126**
5.1.1 Automated Patch-Clamp in HEK293 Cells Expressing Either $Na_V1.2$ or $Na_V1.6$ ... *126*
5.1.2 Assessment of AaH-II Selectivity Between $Na_V1.2$ and $Na_V1.6$ ... *127*
5.2 Local AaH-II Delivery in L5 Pyramidal Neurons Alters Somatic AP Shape in a Concentration-Dependent Manner ... **129**
5.3 AaH-II alters the Action Potential Preferentially in the AIS ... **131**
5.4 AaH-II Enhances Sodium and Calcium Influx in the AIS ... **132**
5.5 AaH-II Selectively Enhances NaV1.2-Mediated Ca^{2+} Influx in the Distal AIS ... **134**
5.6 Summary and Insights ... **136**

CHAPTER 6: DISCUSSION ... **138**

6.1 Key Strengths of the Present Work ... **139**
6.1.1 Leveraging Sample Size Magnitude for Juvenile Characterization ... *139*

6.1.2 Strengthening Reliability with Rigorous Statistics 140
6.1.3 A Dual-Model Approach to SCN2A LoF 140
6.1.4 Synergistic Multi-Compartment Analysis to Understand $Na_v1.2$ Channelopathies Pathophysiology 141
6.2 AIS IONIC MECHANISMS IN *SCN2A* LOF MODELS 142
6.2.1 Canonical AIS Ionic Refinement in WT L5PNs 142
6.2.2 Disrupted Ionic Refinement in SCN2A Mutant Models 144
6.2.3 Methodological Constraints 146
6.3 ACTION POTENTIAL WAVEFORM ALONG THE SOMA-AIS AXIS 147
6.3.1 Baseline Waveform Refinement in WT Somatosensory L5PNs 147
6.3.2 Transient Perturbations in SCN2A Lof Models 150
6.4 REMODELING OF POTASSIUM CURRENTS IN *SCN2A* PATHOPHYSIOLOGY 152
6.4.1 Distal AIS Kv1-Dominated Phenotype in L1314P Mutants 153
6.4.2 Somatic-Proximal Potassium Current Deficits in Haploinsufficient Neurons 154
6.4.3 How Local Is A "Local" Potassium Block When Interpreted with AP Waveform? 155
6.5 AIS PLASTICITY AND MECHANISTIC COMPLEXITY IN *SCN2A* LOF PHENOTYPES 156
6.5.1 From Channel Dysfunction to Structural-Functional Remodeling at The AIS 157
6.5.2 Plasticity, Channel Remodeling, And Alternative Mechanisms in SCN2A LoF Models 159
6.6 SOMATODENDRITIC EXCITABILITY IN *SCN2A* LOF 161
6.7 AAH-II CHARACTERIZATION AND $NA_V1.2$ MODULATION FOR *SCN2A* LOF RESCUE 164
6.8 CHALLENGES OF MODELING DISEASE WITH HAPLOINSUFFICIENT ANIMALS 166
6.9 TOWARD A BETTER UNDERSTANDING OF *SCN2A*-RELATED DISORDERS BEYOND GAIN AND LOSS-OF-FUNCTION 168

List of Figures

Figure 1.1 Key milestones in the history of modern electrophysiology 5
Figure 1.2 Early intracellular recording of an AP in the squid giant axon 11
Figure 1.3 Phylogenetic relationships among the voltage-gated channel superfamily members based on the similarity of their pore region sequences 14
Figure 1.4 Structural and subcellular classifications of neuronal potassium channels 18
Figure 1.5 Phylogenetic Organization and Distribution of Voltage-Gated Sodium Channel α-Subunits 21
Figure 1.6 Cryo-EM structure of the eukaryotic sodium channel Na_VPaS resolved at 3.8 Å 24
Figure 1.7 Structural and organizational features of the human voltage-gated sodium channel $Na_V1.2$ 28
Figure 1.8 AIS molecular structure 37
Figure 1.9 Differential compartmentalization of $Na_v1.2$ and $Na_v1.6$ along the axon initial segment of cortical neurons 42
Figure 1.10 Mechanisms by which ion channel mutations disrupt function and contribute to disease Inherited mutations in ion channel genes can impair function through several mechanisms ... 45
Figure 1.11 Brain MRI abnormalities in patients with SCN2A variants *47*
Figure 1.12 Spectrum of SCN2A/$Na_V1.2$ mutations and their clinical association 49
Figure 1.13 SCN2A highlighted among autism-associated genes 52
Figure 1.14 $Na_V1.2$ at the AIS: from channel physiology to *SCN2A* channelopathies 56
Figure 2.1 Breeding, genotyping, and experimental timeline for SCN2A mouse models 59
Figure 2.2 Overview of slice preparation and patch-clamp recordings from Layer 5 pyramidal neurons 63
Figure 2.3 Schematic of the imaging setup. 65
Figure 2.4 Visualization and protocol synchronization for AIS recordings. 70
Figure 2.5 Experimental configuration of electrophysiology-coupled ultrafast optical imaging in the AIS and apical tuft of Layer 5 pyramidal neurons 73
Figure 2.6 Visualization of dual pipette positioning for local drug application 76
Figure 2.7 ING-2 calibration 77
Figure 2.8 Example of Calcium imaging and I_{Ca} estimation at the AIS 78
Figure 3.1 Na^+ influx in the AIS of *Scn2a*$^{+/+}$, *Scn2a*$^{+/-}$ and *Scn2a*$^{+/L1314P}$ L5 pyramidal neurons. 85
Figure 3.2 Scatter plot of $R_{p/d}$ against age in AIS Na^+ influx measurements 86
Figure 3.3 Ca^{2+} influx in the AIS of *Scn2a*$^{+/+}$, *Scn2a*$^{+/-}$ and *Scn2a*$^{+/L1314P}$ L5 pyramidal neurons. 89
Figure 3.4. Histograms of delays between peaks of the Ca^{2+} current in proximal sites with respect to distal sites. 91
Figure 3.5 Mean ± SD of delay for the three strains and the three age groups. 92
Figure 3.6 Scatter plots of analyzed somatic action potential parameters against age 95
Figure 3.7 Somatic AP of *Scn2a*$^{+/+}$, *Scn2a*$^{+/-}$ and *Scn2a*$^{+/L1314P}$ L5 pyramidal neurons. 96

Figure 3.8 Analysis of the action potential shape in the AIS of *Scn2a*$^{+/+}$, *Scn2a*$^{+/-}$ and *Scn2a*$^{+/L1314P}$ L5 pyramidal neurons. 99
Figure 3.9 Effects of local K_v1, K_v7, and BK channel blockers on AP waveform in the AIS of *Scn2a*$^{+/+}$, *Scn2a*$^{+/-}$, and *Scn2a*$^{+/L1314P}$ L5 pyramidal neurons. 102
Figure 4.1 Somatic AP amplitude ratios from three consecutive APs in *Scn2a*$^{+/+}$, *Scn2a*$^{+/-}$ and *Scn2a*$^{+/L1314P}$ L5 pyramidal neurons. 112
Figure 4.2 Representative examples illustrating the classification criteria for dendritic Ca^{2+} electrogenesis 114
Figure 4.3 Percentage of dendritic Ca^{2+} electrogenesis positive cells in Scn2a$^{+/+}$ (WT), Scn2a$^{+/-}$ (KO), and Scn2a$^{+/L1314P}$ (KI) mice across the two extremes age groups: young (P21-24) and old (P30-36). 116
Figure 4.4 Example of the determination of the interpulse interval threshold for dendritic Ca^{2+} electrogenesiss 118
Figure 4.5 Supralinear Ca^{2+} response evoked at intermediate IPI. 119
Figure 4.6 Scatter plot showing individual IPI thresholds (ms) for supralinear calcium responses as a function of age for each genotype *Scn2a*$^{+/+}$ (black), *Scn2a*$^{+/-}$ (red), and *Scn2a*$^{+/L1314P}$ (blue)... 120
Figure 5.1 Concentration-response analysis of the effect of AaH-II on $Na_v1.2$ and $Na_v1.6$ currents in HEK293 cells 128
Figure 5.2 Concentration -dependent effect of AaH-II on the somatic action potential (AP) of layer 5 pyramidal neurons in brain slices 130
Figure 5.3 Effect of local delivery of 7 nM AaH-II on the action potential (AP) waveform at the soma and axon initial segment (AIS) of layer 5 pyramidal neurons 131
Figure 5.4 Effect of local delivery of 7 nM AaH-II on the Na^+ and Ca^{2+} influx during the AP generation in the AIS of L5 pyramidal neurons. 133
Figure 5.5 AaH-II delivery increase Ca^{2+} influx associated with the AP only in the distal AIS 135

List of Tables

Table 3.1 Summary of number of cells at different postnatal days analyzed for somatic AP in 15 *Scn2a*$^{+/+}$ mice, 12 *Scn2a*$^{+/-}$ mice and 14 *Scn2a*$^{+/L1314P}$ mice. 93
Table 3.2 Mean ± SD of AP_{thr}, $AP_{amp,}$ and AP_{wid} in cells from 15 *Scn2a*$^{+/+}$ female mice, 12 *Scn2a*$^{+/-}$ female mice and 14 *Scn2a*$^{+/L1314P}$ female mice at three time windows (P21-37, P21-24 and P30-37). 94
Table 3.3 Mean ± SD of AP_{wid} at proximal, medial, and distal AIS sites in cells from 26 *Scn2a*$^{+/+}$ female mice, 23 *Scn2a*$^{+/-}$ female mice and 29 *Sc*n2a$^{+/L1314P}$ female mice at three time windows (P21-37, P21-24 and P30-37)..... 100
Table 4.1 Mean ± SD of R_1 (AP_2/AP_1), R_2 (AP_3/AP_2), and R_3 (AP_3/AP_1) in cells from 14 *Scn2a*$^{+/+}$ female mice, 13 *Scn2a*$^{+/-}$ female mice, and 12 *Scn2a*$^{+/L1314P}$ female mice at three age windows (P21-24, P30-36, and P21-36)..... 110
Table 4.2 Summary of dendritic Ca^{2+} electrogenesis prevalence across genotypes..... 115
Table 4.3 Prevalence of dendritic Ca^{2+} electrogenesis across genotypes and three age groups. 116
Table 4.4. Mean ± SD of IPI_{thr} in cells with nonlinear apical Ca^{2+} response from 10 *Scn2a*$^{+/+}$ female mice, 15 Scn2a$^{+/-}$ female mice and 13 *Scn2a*$^{+/L1314P}$ female mice at three time windows (P21-24, P30-36, and P21-36)..... 119
Table 4.5 Mean ± SD of S_3/S_2 ratio in amplitude-based Ca^{2+} electrogenesis cells from 9 *Scn2a*$^{+}/^{+}$ female mice, 14 *Scn2a*$^{+/-}$ female mice, and 13 *Scn2a*$^{+/L1314P}$ female mice at three time windows (P21-24, P30-36, and P21-36)..... 121
Table 5.1 Mean ± SEM of the percentage change in current amplitude induced by AaH-II in HEK293 cells expressing either $Na_v1.2$ or $Na_v1.6$ channels 128

List of Abbreviations

ACSF	Artificial cerebrospinal fluid
AD	Alzheimer's Disease
AIS	Axon initial segment
ALS	Amyotrophic lateral sclerosis
AnkG	Ankyrin-G
AP	Action potential
AP_{amp}	Action potential amplitude
AP_{thr}	Action potential threshold
AP_{wid}	Action potential width
ASD	Autism spectrum disorder
bAP	Back-propagating action potential
BK	Big or Large conductance calcium-activated potassium channel
CaM	Calmodulin
CaMBD	Calmodulin-binding domain
CAM	Cell adhesion molecule
Ca_v	Voltage-gated calcium channel
CNS	Central nervous system
d	Distal
DTX	Dendrotoxin
DRG	Dorsal root ganglia
ET	Extratelencephalic
GoF	Gain-of-function
HH	Hodgkin and Huxley
HVA	High-voltage activated
Hwtx	Huwentoxin
IbTx	Iberiotoxin
I_{Ca}	Calcium current
ID	Intellectual Disability
ING-2	Ion Natrium Green
I_{Na}	Sodium current

I_{NaP}	Persistent sodium current
I_{NaT}	Transient sodium current
IPI	Inter-pulse interval
IPI_{thr}	Inter-pulse interval threshold
iPSC	Induced pluripotent stem cell
IT	Intratelencephalic
JPW1114	Voltage-sensitive dye
KI	Knock-in
K_{2P}	Two-pore domain potassium channel
K_{Ca}	Calcium-activated potassium channel
KO	Knock-out
KS	Kolmogorov–Smirnov test
K_v	Voltage-gated potassium channel
L2	Layer 2
L5	Layer 5
L5PN	Layer 5 pyramidal neuron
LoF	Loss-of-function
LTP	Long-term potentiation
LVA	Low-voltage activated
m	Medial
Na_v	Voltage-gated sodium channel
$Na_v1.2$	Voltage-gated sodium channel subtype 1.2
Na_vAb	Bacterial voltage-gated sodium channel
OGB	Oregon Green BAPTA
PD	Pore domain
p	Proximal
RMP	Resting membrane potential
SCN2A	Voltage-gated sodium channel α subunit 2 Gene
SES	Standardized effect size
SF	Selectivity filter
SK	Small conductance calcium-activated potassium channel
SP	Statistical power
TTX	Tetrodotoxin

TTL5	Thick-tufted Layer 5 pyramidal neuron
$V_{1/2}$	Half-maximal activation voltage
VGIC	Voltage-gated ion channel
VGKC	Voltage-gated potassium channel
VGNC	Voltage-gated sodium channel
V_m	Membrane potential
VSD	Voltage sensor domain
WMW	Wilcoxon–Mann–Whitney test
WT	Wild type

1

INTRODUCTION

1.1 A HISTORICAL PERSPECTIVE 2
1.2 NEURAL SIGNALING BASICS: EXCITABILITY MECHANICS AND INFORMATION PROCESSING 6
1.2.1 Polarized membrane and resting potential 7
1.2.2 From rest to response: the onset of signaling 9
1.2.3 Transmitting the pulse: Synaptic signal relay 11
1.3 VOLTAGE-GATED ION CHANNELS 13
1.3.1 Potassium channels 15
1.3.1.1 Voltage-gated potassium channels 15
1.3.1.2 Calcium-activated potassium channels 16
1.3.2 Voltage-gated calcium channels 19
1.3.3 Voltage-gated sodium channels 20
1.3.3.1 Structure 20
1.3.3.2 Molecular architecture of the alpha subunit 22
1.3.3.3 Pore Domain 22
1.3.3.4 Selectivity filter 22
1.3.3.5 Activation and inactivation gates 23
1.3.3.6 Voltage sensing domain 23
1.3.3.7 Structural and Functional Dynamics of Na_V Channels: From Voltage Sensing to Inactivation 24
1.3.3.8 Beta subunit 25
1.3.3.9 Tissue expression and subcellular localizations 26
1.4 VOLTAGE-GATED SODIUM CHANNEL TYPE-II 27
1.4.1 Structural and Molecular Profile 27
1.4.2 Selectivity for Sodium and Emerging Calcium Conductance 29
1.4.3 Gating Kinetics and Modulation 30
1.4.3.1 Kinetics and biophysical properties 30
1.4.3.2 Multilevel regulation of $Na_V1.2$ 31
1.4.4 Pharmacology and Drug Sensitivity 32
1.4.5 Mapping of $Na_V1.2$ in the Brain 34
1.4.5.1 Tissue Distribution: A Focus on Cortical Layer V 34
1.4.5.2 The Axon Initial Segment: A Key Site for $Na_V1.2$ Compartmentalization and Activity 36
1.5 SYNERGISTIC ION CHANNEL FUNCTION AT THE AXON INITIAL SEGMENT 40
1.5.1 $Na_V1.2$ versus $Na_V1.6$ 40
1.5.2 Potassium Channels and Calcium Channels 42
1.6 CHANNELOPATHIES IN THE NERVOUS SYSTEM 44
1.6.1 Overview: Classifications and Clinical Spectrums 44
1.6.2 Genetic Channelopathies of the CNS 45
1.6.3 SCN2A-Related Disorders 47
1.6.3.1 Functional Spectrum Classification 48
1.6.3.2 Limitations of the GoF/LoF Model 50
1.6.4 SCN2A Loss-of-Function Mutations in Autism 51
1.6.4.1 Phenotypes and Experimental Models of $Na_V1.2$-LoF 52
1.7 OPEN RESEARCH QUESTIONS ADDRESSED IN THIS THESIS 54

"The brain is wider than the sky," wrote Emily Dickinson (1862). With merely a few words, Dickinson, with her poet's feather, portrayed the immense and complex nature of our cognitive realm. Her interpretation mirrors, not only in artistic expression but also in a scientific manner, the boundless potential of scientific research echoed in Isaac Newton's legendary observation: "To myself, I seem to have been only like a boy playing on the seashore, while the great ocean of truth lay all undiscovered before me".

The journey of Neuroscience, in many ways, is summarized by these words. The deeper we dive into the profound mysteries of the brain, the more we seek to probe its elusive secrets, the more it resists, standing as an extraordinarily intricate system that baffles our comprehension every day, while remaining far from being fully understood. Santiago Ramón y Cajal, acknowledged as the father of modern Neuroscience for shaping our understanding of the nervous system's architecture, elegantly put it: "As long as our brain is a mystery, the universe, the reflection of the structure of the brain, will also be a mystery."

Insatiable curiosity, devoted dedication, and the thirst for knowledge have long driven the exploration of this vast scientific field. As such, the quest to decrypt the enigma of neuronal excitability has grown among the fundamental cornerstones of Neuroscience, aiming to unravel the entangled mechanisms that govern neural function and behavior. But how far have we really come? The past century has witnessed a series of major breakthroughs that have gradually illuminated the molecular and biophysical principles of neuronal signaling. From early theoretical models of ionic movement, to in-depth investigations of ion channels and their associated disorders, the "channelopathies", our understanding has drastically evolved.

1.1 A Historical Perspective

At the dawn of modern Neuroscience in the late 19th century Santiago Ramón y Cajal revolutionized our thinking about the structural and functional organization of the human brain. At a time when the reticular theory, which held that the nervous system was a continuous "net" of uninterrupted nerves, was proponent; Cajal argued this viewpoint and was the first to demonstrate, using Golgi staining methods, that the brain is composed of discrete, fundamental units called neurons (Bock, 2013; López-Muñoz et al., 2006; Ramón y

Cajal, 1888; Rozo et al., 2024). Yet, the question regarding the communication between these individual cells remained unresolved. In 1897, Charles Sherrington bridged this gap by adopting and refining the "synapse" concept as a critical site for signal integration, a specialized junction where neurons emit and receive signals (Pearce, 2004; Sotelo, 2020). Sherrington's pioneering research into synaptic transmission, combined with Cajal's innovative insights, established a new framework for the neuronal communication paradigm, and laid a strong foundation toward examining the electrical properties of neurons.

Building upon their work, the German physiologist Julius Bernstein developed the "Membrane Theory of Electrical Potentials" in biological cells and tissues. He suggested that the movement of ions across the cellular membranes shapes the neuronal electrical activity, hence providing the first plausible fundamental concept of bioelectric events, an idea that continues to hold true to this day (Bernstein, 1902; Seyfarth, 2005).

Into this torrent of progress stepped the English zoologist John Zachary Young who, in the 1930s, introduced and characterized the structure of the squid giant axon. This axon was of ample size to allow the intracellular insertion of a microelectrode, providing a practical method to investigate neuronal excitability and setting the stage for a new era of electrophysiology research (Jones, 2022).

Alan Hodgkin and Andrew Huxley, prominent figures in biophysics, used this model to perform their groundbreaking experiments. In 1939, they carried out the first direct measurement of the entire action potential of squid gigantic axons. The goal of further research was to figure out the biochemical processes that underlie the generation of this pulse (Hodgkin & Huxley, 1939). A huge technical progress was introduced by the voltage clamp technology that shifted the experimental labor to measuring ion currents by injecting voltage. Using this approach in 1952, Hodgkin and Huxley elucidated the ionic processes underlying the onset and propagation of action potential. They reported that exceeding the threshold resulted in a sudden increase in sodium permeability which they rationalized by anticipating the existence of a hypothetical family of unknown entities which they called voltage-gated sodium channels; whereas the molecular identity of this family was

established only in the 1960s. The core of their ionic theory was the identification of two main, separate ionic components that carry out the action potential: A sodium inward current, followed by a slow potassium outward current to restore charge balance across the plasma membrane. With a set of first-order differential equations, Hodgkin and Huxley translated these currents in mathematical terms and presented the HH model that described and simulated action potentials with incredible accuracy (Hodgkin & Huxley, 1952).

After the ionic basis of the action potential was finally revealed, the focus of Neuroscience began to shift towards the synaptic transmission. In this emerging landscape, Bernard Katz shed light on the mechanisms of neurotransmitter release in the middle of the 20th century. His research, built upon prior discoveries, offered a mechanistic explanation of the chemical communication within the nervous system, thereby refining and enhancing our comprehension of the synaptic functions (Augustine & Kasai, 2006; Del Castillo & Katz, 1954; Fatt & Katz, 1952).

As the disparity between electrical excitability and chemical interaction among neurons was reconciled, the language of nerve cells has been progressively decoded. Earlier predictions of Hodgkin and Huxley have been later confirmed by the identification of voltage-gated sodium channels as primary contributors in action potential generation, sparking a major interest in understanding how specific ion channels mediate neuronal excitability. However, a thorough study of an individual ion channel has only been made possible by the innovation of the patch clamp technique by Neher and Sakmann in 1976. With unprecedented precision, this method allowed for recording of ionic currents from single ion channels, thus providing, as Neher and Sakmann described, “a unique tool for investigating the functional properties of ion channels in a direct and detailed way” (Hamill et al., 1981; Neher & Sakmann, 1976). For their effort, they were honored the Nobel Prize in Physiology or Medicine in 1991, further legitimizing the place of patch-clamp technique among the greatest inventions in electrophysiology.

In the pursuit of research into ion channels, a critical realization came out: the same molecules that maintain the integrity of healthy neural function are subject to disruptions that can lead to severe neurological disorders. The term “channelopathy” was first used in

the context of cystic fibrosis in 1989, a condition associated with mutations in the cystic fibrosis transmembrane conductance regulator (CFTR) channel (Gargus, 2003; Riordan et al., 1989). This family of diseases has since broadened to confine a range of disorders caused by impairments of ion channels, and has marked a new frontier in medical research, probing how slight changes can alter the functionality of ion channels, disrupting vital processes, and leading to profound neurological and developmental consequences, now known as channelpathies.

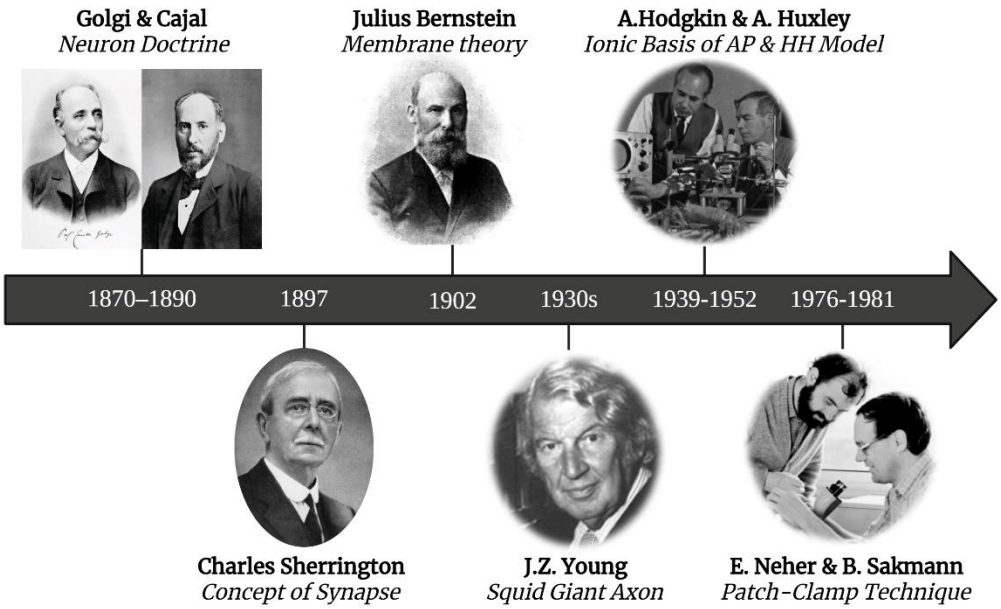

Figure 1.1 **Key milestones in the history of modern electrophysiology,** from the anatomical insights of Cajal to the Hodgkin-Huxley model and the introduction of the patch-clamp technique by Neher and Sakmann. *Created with BioRender.com*

Building on the legacy of these great minds, who unlocked the hidden dynamics of neuronal excitability and opened the door for investigating the molecular basis of channel-related diseases, this thesis delves in the present-day challenge of understanding the pathophysiological underpinnings of one particular category of channelopathies caused by loss-of-function mutations in the $Na_V1.2$ voltage-gated sodium channel. In the sections ahead, I will summarize the state of art on voltage-gated ion channels knowledge,

highlighting their role in orchestrating the electrical behavior of neurons, and how their mutations can disrupt brain function. Thereafter, I will particularly focus on $Na_V1.2$ voltage gated sodium channels, exploring their fundamental role in action potential's generation and their implication in neurological disorders. Lastly, I will state the key research questions addressed in this thesis.

1.2 Neural Signaling Basics: Excitability Mechanics and Information Processing

Neural communication is the core of all brain function; defined as the process by which neurons carry out the exchange of information through electrical and chemical signals, enabling the nervous system to regulate and integrate a broad range of physiological as well as cognitive functions (Hille, 2001). This communication hinges on precise and dynamic trafficking of signals among information processing units through intricate networks, orchestrating everything, from thought processes to motor control, and from simple reflexive actions to sophisticated intellectual tasks (Kandel et al., 2013). Thanks to the adaptive nature of these networks, repeated activity helps neurons to strengthen their connections and enhance the efficiency of their communication. This concept is referred to as synaptic plasticity and has been introduced in Donald Hebb's theory, whose principles inspired the famous rule, "Neurons that fire together, wire together." Hebb's principle emphasizes the fact that synchronized firing patterns sculpt neural networks, reinforcing communication pathways that are essential for learning, memory, and behavior (Bi & Poo, 2001; Hebb, 1949).

At the heart of neural signaling is the astounding capability of the brain to interpret and transmit information quickly and accurately. This efficiency is primarily driven by neuronal excitability: the ability of neurons to generate and propagate electrical impulses in response to various stimuli (Bean, 2007). Central to this process is the polarized state of the neuronal membrane, which serves as the basis of excitability. The following sections will provide an overview of the fundamental mechanisms, establishment of the resting membrane potential, the onset and propagation of action potentials, and, finally, the basics of synaptic transmission upon which the complex interconnectivity of the brain's networks is built.

1.2.1 Polarized Membrane and Resting Potential

Almost all cell types exhibit some form of polarity, a phenomenon that is a central tenet of physiology and subserves essential cellular functions including the cell cycle, proliferation, nutrient transport, waste removal, and the maintenance of homeostasis (Kadir et al., 2018). The fact that cells carry a transmembrane potential has been around for over a century, with earlier experiments by Höber in 1905 and further confirmation by Curtis and Cole in 1942 (Curtis & Cole, 1942; Höber, 1905). This polarized state arises from the differential distribution of ions between the intracellular and extracellular apparatus, creating a delicate yet powerful electrical gradient across the cell membrane. This membrane, in nerve cells, is composed of a phospholipid bilayer ~8-10 nm thick interspersed with proteins, and acts as a leaky capacitor that stores charge. Due to the hydrophobic nature of the bilayer, the free movement of ions is prevented. However, specific pathways for their movement across this barrier are provided by the embedded proteins including ion channels and pumps (Gentet et al., 2000; Jack et al., 1976).

Non-excitable cells, even though they do not have a firing phenotype, still maintain a dynamic membrane potential that is relatively stable, typically ranging from -10 to -70 mV millivolts (mV), as observed in fibroblasts and epithelial cells, where it supports vital cellular activities (Kadir et al., 2018). In contrast, neurons represent a specialized class of excitable cells, where the polarization of their membrane serves a purpose beyond the scope of maintaining cellular homeostasis, it is the key to defining their unique aptitude to fire and propagate electrical signals throughout the nervous system (Grider et al., 2023).

Under resting electrical conditions, we can think of the transmembrane electrical potential difference of a neuron, known as resting membrane potential (RMP), to be approximately -70mV. This potential represents the electrical voltage difference between the inside and the outside of the neuron. Few key ions contribute to the resting membrane potential with potassium (K^+) and sodium (Na^+) providing a dominant influence. The intracellular fluid has a high concentration of potassium (K^+) and negatively charged proteins, whereas extracellular fluid is rich in sodium (Na^+) and chloride (Cl^-) (Bean, 2009). Therefore, in a bid to tackle how this negative potential difference is generated, one has to understand how equilibrium potentials, membrane selective permeability, and ion pumps all function in

tangent. The quantitative measure of the equilibrium potential of a single ion can be determined from the Nernst equation which is given by:

$$E_{ion} = \frac{RT}{zF} \ln\left(\frac{[ion]_{outside}}{[ion]_{inside}}\right)$$

Where E_{ion} is the equilibrium potential for the ion, R is the gas constant, T is the temperature in Kelvin, z the charge of the ion, F is Faraday's constant, and $[ion]_{outside}$ and $[ion]_{inside}$ are the concentrations of the ion outside and inside the cell, respectively. The equilibrium potential reflects the membrane potential at which the ion's electrical and chemical forces, collectively referred to as the electrochemical gradient, are in a perfect balance, resulting in a no net movement of the ion across the membrane (Veech et al., 1995; Wright, 2004).

There comes the role of ion pumps, namely the Na^+/K^+ ATPase pump, which actively transports three Na^+ ions out of the cell and two K^+ ions in, thereby continuously maintaining a higher concentration of K^+ within and Na^+ outside against passive leak currents. Similar stable concentration gradients exist for other major ions, including Ca^{2+} and Cl^-, and are preserved throughout neuronal life by ongoing active transport mechanisms (Hammond, 2024). With these gradients in place, and owing to the membrane's semi-permeability, ionic fluxes occur according to their electrochemical gradients. The abundance of open potassium channels, specifically passive or "leak" channels, makes the membrane at rest highly accessible to potassium, allowing its diffusion down its concentration gradient. These channels correspond to the two-pore domain (K_{2P}) family, with TASK and TREK subtypes as their main neuronal representatives, and they generate the background conductance that stabilizes the resting membrane potential and sets input resistance (Feliciangeli et al., 2015; Lesage, 2003). As K^+ flows out, it leaves behind a negative internal charge relative to the outer compartment. The membrane also exhibits minor permeability to sodium; however, the number of open sodium channels is far lower, yielding to a permeability that is merely 5% of that of potassium (Chrysafides et al., 2023).

The RMP is in fact a weighted average of the equilibrium potentials for all those ions permeable through the membrane; hence, it is not calculated by the Nernst equation for a

single ion, but rather by the Goldman-Hodgkin-Katz (GHK) equation, which incorporates the permeability ratios of all ions:

$$V_m = \frac{RT}{F} \ln\left(\frac{P_K[\mathrm{K^+}]_{\text{outside}} + P_{Na}[\mathrm{Na^+}]_{\text{outside}} + P_{Cl}[\mathrm{Cl^-}]_{\text{inside}}}{P_K[\mathrm{K^+}]_{\text{inside}} + P_{Na}[\mathrm{Na^+}]_{\text{inside}} + P_{Cl}[\mathrm{Cl^-}]_{\text{outside}}}\right)$$

Here, V_m is the membrane potential, and P_{ion} represents the permeability of the membrane to a particular ion. Consequently, the RMP tends to be close to the potassium's equilibrium potential of -90 mV as it is the major determinant of that state. Nevertheless, due to the leakage of sodium and other ions from the cell at rest, the RMP will not align exactly with the potassium equilibrium potential (E_K) but will be slightly depolarized from it (Alvarez & Latorre, 2017; Enderle, 2005).

To sum up, resting membrane potential is not a static state but rather a dynamic equilibrium that arises from a finely tuned balance of electrochemical gradients (Chrysafides et al., 2023). This potential lays the necessary electrical groundwork that primes neurons for signaling and sets the stage for action potential generation, and thus develops their ability to react to inputs quickly and efficiently. Such delicate balance of ion displacement is what makes the execution of life's most complex functions, from conception to locomotion, possible.

1.2.2 From Rest to Response: The Onset of Signaling

The membrane's resting potential maintains the neuron in a charged and ready to go state. As electrically excitable cells, neurons can change their relative permeability to ionic species on a millisecond timescale, which consequently modifies their membrane potential (Chrysafides et al., 2023). When a depolarizing stimulus arrives, it throws off the delicate ion balance, and the membrane potential gradually shifts toward a critical value known by "threshold" (of -55mV to -50mV in many neurons). If the stimulation amplitude is below this threshold, the membrane will slightly depolarize and then revert to resting potential, which is referred to as a subthreshold fluctuation. But once the threshold value is crossed, the depolarization becomes self-sustaining because of the positive feedback loop initiated by sodium influx of ions, triggering the onset of an AP. Thus, the threshold serves as a decision

point, distinguishing between subthreshold stimuli and true spike generation (Drukarch & Wilhelmus, 2023; Fletcher, 2011; Grider et al., 2023).

One of the main characteristics of action potentials is that they happen in an all-or-nothing manner, implying that a stimulus elicits either a full-sized impulse or none at all (Grider et al., 2023). The first understanding of these voltage waveforms was provided by the pioneering intracellular recordings made from the squid giant axon by Hodgkin and Huxley (**Figure 1.2**), whose work revealed the distinct phases of the action potential. Depolarization occurs rapidly as voltage-gated sodium channels open to mediate the inward flow of Na^+ ions along their electrochemical gradient, bringing the membrane to a positive voltage approaching the sodium's reversal potential. Once generated, the action potential does not decay, rather, it relentlessly carries the information along meters of axon without changes in magnitude (Love & Webb, 1992).

Following the spike impulse, Na_v channels inactivate within milliseconds while the potassium conductance increases. A slower potassium efflux serves to restore the internal negativity by repolarizing the membrane potential (V_m)to the resting potential. The gradual closure of potassium channels produces a brief hyperpolarization of the membrane below the resting potential towards the Nernst equilibrium for K^+ (Kole et al., 2008; Shu et al., 2007).

During the passage of an action potential across a nerve cell membrane, the membrane ceases its capability of responding to further stimulus. This period of irresponsiveness is called refractory period, it allows neuronal recovery and ensures a unidirectional flow of the signal, and it comprises two phases (Barnett & Larkman, 2007). The absolute refractory period that immediately begins after an AP is elicited, where sodium channels enter their inactivated state, and the membrane becomes inexcitable. As these channels emerge out of inactivation, the relative refractory period occurs, during which the cell can be stimulated by strong stimuli greater than those required to usually initiate an AP (Hille, 2001).

Referred to as the language of neurons, this electrical pulse travels swiftly along the neural networks, serving as their major form of intercellular communication (Hille, 2001). In the words of neuroscientist Carl Cotman “Action potentials are so named because they are full of action. They are an electrical disturbance, an ionic storm, traveling along the axon with speeds up to 100 meters per second” (Cotman & McGaugh, 1980).

The action potential encompasses not merely a voltage spike, but the essence of neural signaling and all aspects of nervous system activity, with its ion channel-specific contributions and interplay detailed in later sections of this introduction.

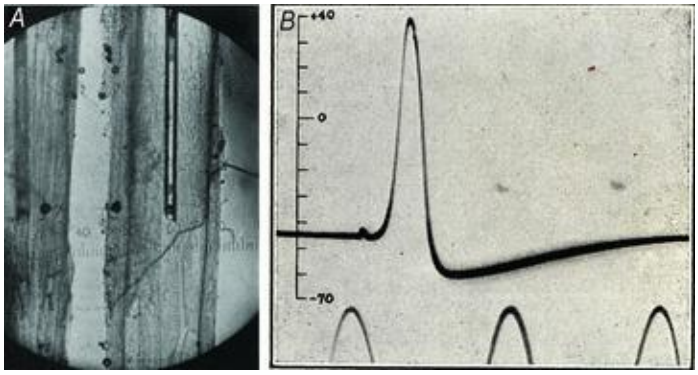

Figure 1.2 **Early intracellular recording of an AP in the squid giant axon. (A)** Image of a microelectrode inserted into the squid giant axon (~500 μm diameter), viewed simultaneously from two angles using a mirror system developed by Huxley to reduce membrane damage during insertion. **(B)** First intracellular voltage trace of an AP, recorded using this setup. Figure adapted from Schwiening (2012), who reproduced original material from Hodgkin & Huxley (1939, 1945)

1.2.3 Transmitting The Pulse: Synaptic Signal Relay

With the acceptance of the Neuron Doctrine, scientists acknowledged that neurons are discrete cells, not connected by a continuous reticular network; instead, a particular structure, the synapse, facilitates information relay and forms the site of communication between adjacent neurons. Located at the axonal terminus of the presynaptic cell, synapses form a link with the postsynaptic cell. The first electron micrographs of synapses were published in 1955, revealing with great resolution, their distinct organization: a presynaptic and a postsynaptic element, separated by a space termed the synaptic cleft (Meriney & Fanselow, 2019b). Though chemical transmission is the major mean of neuronal communication, direct electrical synapses, or gap junctions, also exist but are less common, prevailing in specific areas of the nervous system, such as the thalamus (Vaughn & Haas, 2022).

Upon reaching the axonal end, the action potential triggers a cascade of molecular events, to set the synaptic transmission in motion. Chemical communication across the synaptic cleft is mainly mediated by neurotransmitters, which are stored in presynaptic vesicles and unfolds through a chain of precise steps (Raz & Perouansky, 2018). First, the neurotransmitters are synthesized in the presynaptic nerve terminal and sequestered into secretory vesicles. The arriving action potential prompts then the release of these neurotransmitters in the synaptic cleft. From there, the neurotransmitters diffuse across the cleft, binding to appropriate receptors on the postsynaptic membrane, therefore triggering a signaling cascade. Finally, reuptake into the presynaptic element or enzymatic degradation processes take place to terminate the neurotransmitter's action, ensuring that the signal is precisely transmitted (Holz & Fisher, 2012). It is worth mentioning here the vital role of calcium in synaptic transmission. Unequivocally shown in their experiments, Katz and Miledi demonstrated that the neurotransmitter release is contingent upon the presence of calcium in the extracellular fluid (Katz & Miledi, 1967). Moreover, the pre and postsynaptic events are tightly regulated and subject to activity-dependent modulations, rendering synaptic transmission an important process for neural communication as well as a key element in plasticity and learning (Holz & Fisher, 2012).

In closing, the nervous system operates as a network of interconnected units at all hierarchical levels, starting from single neurons up to the whole brain. With roughly 100 billion neurons and quadrillion synapses in the human brain, each neuron forms an average of a thousand synaptic connections, modulating the membrane's electrical potential (Chen & Lui, 2023). This dynamic network is maintained by the resting potential that constitutes the neuron's energy reservoir, preparing it to generate electrical impulses in response to synaptic inputs. These inputs can either be depolarizing, increasing the voltage across the membrane, or hyperpolarizing; a factor that influences the likelihood of generating an action potential. In the case when a depolarizing stimulus can trigger a spike, the action potential propagates through the length of the axon, and ultimately, at the synaptic level, results in a chemical exchange of information (Bean, 2007).

Understanding the previously described principles of neuronal signaling is, with no doubt, essential for moving forward to the main actors in regulating membrane potential and

facilitating action potential propagation: voltage-gated ion channels. The structure of these ion channels, how they work together in making neurons ‘‘excitable’’, and the broader context of neurological function and dysfunction will be discussed in the following part.

1.3 Voltage-Gated Ion Channels

Ion channels are the gatekeepers of cellular communication. After decades of research and gene cloning, the Human Genome Project now lists more than 400 genes for ion channels, accounting for roughly 2% of the human genome. Not only between species, but even within an individual organism, ion channels vary significantly across tissues and developmental stages. (Bell et al., 2023; Hille, 2001; Imbrici et al., 2016).

An ion channel is a membrane-spanning protein, or an assembly of several proteins, that anchor within the membrane lipid bilayer, providing a selective passageway through which charged ions, specifically sodium, calcium, potassium, and chloride, can cross the membranes of cells and cellular organelles down their electrochemical gradient (Madden & Rusch, 2001). Ion channels are macromolecular protein complexes whose size varies considerably depending on channel type and organism. While some channels are formed of several thousand amino acids resulting in a combined molecular weight that might exceed 300 KDa (Sokolova et al., 2001), others are substantially smaller.

The gating of a channel refers to the conformational change between closed and open states, which is induced by an external or internal stimuli. Based on their gating mechanisms, the diverse family of ion channels can be classified in two broad categories (Imbrici et al., 2016). Ligand-gated ion channels, which are relatively voltage insensitive, open in response to the binding of a ligand molecule on the membrane's surface, typically glutamate in the case of AMPA receptors, or due to an intracellular mediator as in the case of cyclic nucleotide-gated (CNG) channels. Although functionally ligand-gated and playing a key role in sensory transduction by responding to intracellular cyclic AMP or cyclic GMP, CNG channels structurally and evolutionarily belong to the voltage-gated ion channel (VGIC) superfamily (Kaupp & Seifert, 2002; Mondal et al., 2025). On the other hand, the voltage-gated ion channels are gated by changes in membrane potential that govern their switch-like behavior between open and closed (Alexander et al., 2011). The family of VGICs shares a conserved

architecture, consisting of a pore-forming alpha subunit comprising a central membrane-spanning shaft to conduct ions, in addition to smaller auxiliary subunits (α2, β, Δ, γ) modulating the functioning of the channel (Barker et al., 2016).

The presence of a selectivity filter within the pore allows for the precise discrimination between different ions, leading to the classification of voltage-gated channels into three major categories: potassium, calcium, and sodium channels (see **Figure 1.3**) (Hendriks et al., 2021). In this section I will include a description of each of the above-mentioned channel types starting with the potassium channels followed by the voltage-gated calcium channels and lastly the most critical for this research, the voltage-gated sodium channels.

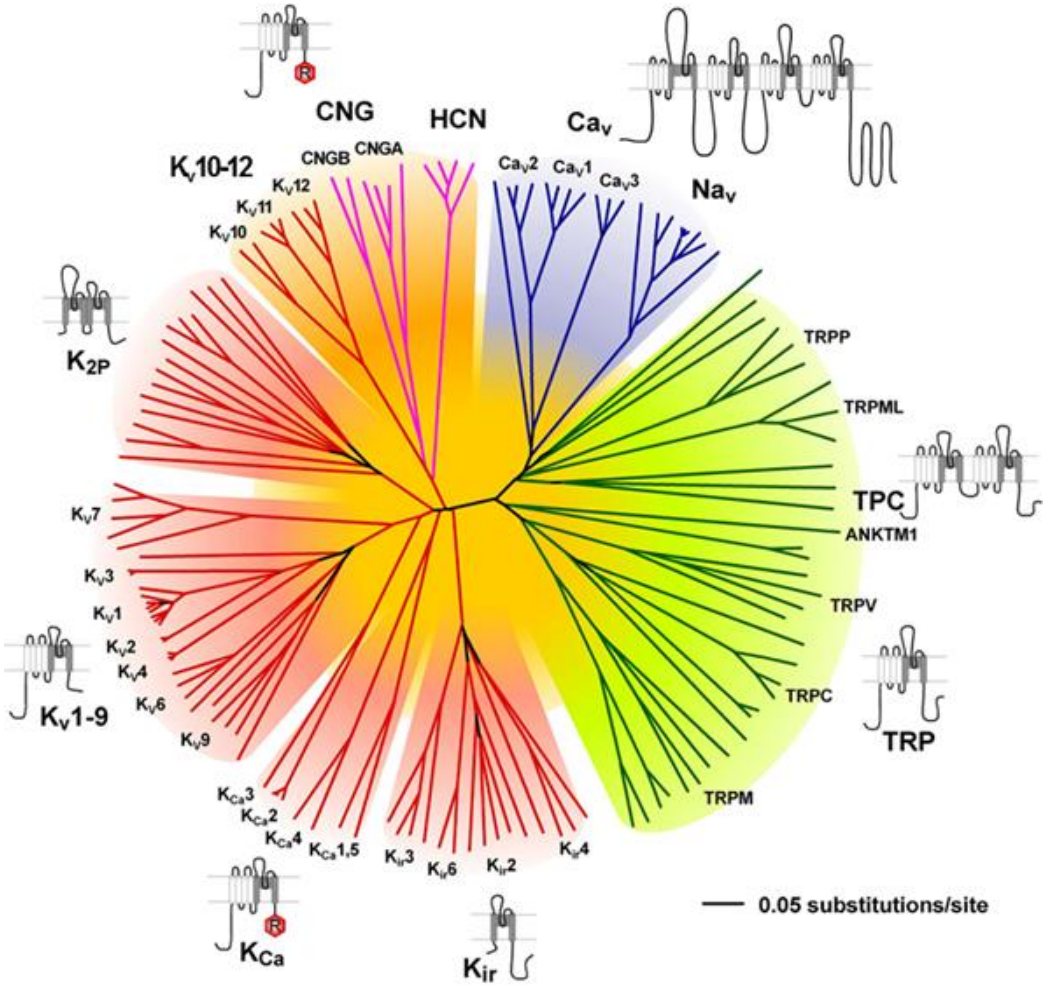

Figure 1.3 **Phylogenetic relationships among the voltage-gated channel superfamily members based on the similarity of their pore region sequences.** The global view represents 143 ion channel genes, clustered by sequence alignment of their minimal pore-forming regions. The major families are indicated in colors: blue for four-domain channels (Na_V and Ca_V), red for K^+ channels, magenta for cyclic nucleotide–gated (CNG and HCN) channels, and green for transient receptor

potential (TRP) and related channels. Background shadings indicate broader structural groups: light blue (Na_V and Ca_V), light red (K^+ channels), light green (TRP channels), and light orange (cyclic nucleotide–modulated channels with K_V10–12). Branch lengths reflect amino acid substitutions per site, and topologies were generated using minimum evolution analysis with bootstrapping. *Adapted from Yu & Catterall (2004)*

1.3.1 Potassium Channels

The potassium channel family reigns as the largest and most diverse class of ion channels in mammals. With over 80 genes encoding the major pore-forming alpha subunits in humans, these channels come in a huge array of structural combinations, each adapted to carry out specific functions across a variety of tissue localizations. In the nervous system, potassium channels act, alongside other channels, to modulate the electrical properties and firing of neurons, their starring role being to mediate the repolarization and to restore the resting state of the membrane (Qiu et al., 2025; Trimmer, 2015; Villa & Combi, 2016).

According to their structure, physiology, biophysical characteristics, and pharmacological sensitivities, this superfamily is subdivided into four types: voltage-gated potassium channels (K_V or VGKCs), calcium-activated potassium channels (K_{Ca}), inwardly rectifying potassium channels (K_{ir}), and two-pore domain potassium channels (K_{2P}) (**Figure 1.4**). This diversity lies behind their involvement in a wide range of physiological processes, from stabilizing the RMP and background excitability (K_{ir} and K_{2P}) to shaping phases of repolarization and hyperpolarization of the AP (K_V and K_{Ca}) (O'Connell et al., 2002; Tian et al., 2013). Two families of peculiar significance to this project by standing as main determinants of AP dynamics are described in the next sections: K_V (VGKCs) and K_{Ca}.

1.3.1.1 Voltage-Gated Potassium Channels

In the human genome, 40 different genes encoding the extensive voltage-gated potassium channel family were reported, giving rise to 12 distinct subfamilies, K_V1 to K_V12 (Gutman et al., 2005). The first evidence for these channels dates back to the famous experiments of Hodgkin and Huxley in the 1950s, where they anticipated the existence of voltage-dependent ion-selective channels responsible for mediating sodium and potassium ion fluxes (Hodgkin & Huxley, 1952). A few decades later, the first potassium channel gene to be cloned was the *Shaker* locus, brought to light through the analysis of Drosophila mutants (Papazian et al.,

1987). This discovery confirmed the earlier predictions and marked the first VGKC, allowing that period to witness the identification of multiple genes encoding K_V family members.

Mammalian K_V channels share a tetrameric organization and may exist as either homotetramers or heterotetramers. This structure has each monomer, akin to all voltage-gated ion channels, consisting of a principal alpha subunit with six α-helical transmembrane domains (S1, S2, S3, S4, S5, S6). The S5 and S6 segments, with the P loop interposed, delineate the ion conduction pore, where the p-loop contains the selectivity filter that orients the channel's permeability towards potassium (Bernèche & Roux, 2005; Kim & Nimigean, 2016). Conversely, the S1–S4 sequences are critical for channel voltage-gating, particularly the S4 segment, which directly senses the membrane voltage due to its positively charged residues (Gutman et al., 2005). Further, these four α-subunits can bind to regulatory β subunits and other K_V channel-interacting proteins that impact their activity, trafficking and location (Kuang et al., 2015; Villa & Combi, 2016).

K_V channels are widely expressed in both the central and peripheral nervous systems. They are categorized as high-voltage activation channels (e.g., as K_V2 and K_V3), and low-voltage activation channels (e.g., K_V1, K_V4, and K_V7) based on their biophysical dynamics. The general functions of VGKC sub-families in the nervous-system have been broadly characterized and relatively well-established; they shape neuronal excitability by contributing to the cell's repolarization and influencing various phases of the action potential (Shah & Aizenman, 2013). In addition to their engagement in the immediate regulation of excitability, as articulated by L. Chow in the title of his review, they exhibit "actions beyond action potential". This includes their roles in neuronal exocytosis and neurite formation, glial cell and glioma proliferation, as well as their contribution to cell death and cell survival signaling pathways (Chow & Leung, 2020).

1.3.1.2 Calcium-Activated Potassium Channels

Calcium activated potassium channels (K_{Ca} channels) constitute a heterogeneous and specialized family of ion channels, distinguished from other potassium channels, by their unique ability to translate intracellular Ca^{2+} signals to changes in membrane potential. Based on their single channel conductance, K_{Ca} channels are divided into three subtypes: small conductance (SK_{Ca}), intermediate conductance (IK_{Ca}), and large conductance (BK_{Ca})

channels. All K_{Ca} channel subtypes are tetramers of α subunits, embedded in the plasma membrane, where they serve key roles in neuronal excitability (Kshatri et al., 2018; N'Gouemo, 2011).

From a biophysical standpoint, K_{Ca} channels fall into two main phylogenetic groups based on their voltage dependence and calcium sensitivity (Wei et al., 2005). SK and IK belong to the first group, where activation is membrane voltage-independent and solely gated by intracellular calcium fluctuations. Structurally, their α subunits feature six transmembrane helices (S1–S6), with the S5 and S6 helices forming the K^+-selective pore region (Kshatri et al., 2018). Remarkably sensitive to low intracellular Ca^{2+} levels, these channels rely on a calmodulin (CaM) binding domain (CaMBD) within the channel protein, where CaM can bind and induce conformational changes that trigger channel opening (Adelman, 2016; Fanger et al., 1999; Schumacher et al., 2001). Seminal work by Pedarzani and colleagues further demonstrated that SK channel gating can be modulated by small molecules (1-EBIO, CyPPA, NS309), and that this pharmacological enhancement selectively shapes neuronal excitability and afterhyperpolarizations (Hougaard et al., 2007; Pedarzani et al., 2001; Pedarzani et al., 2005; Pedarzani & Stocker, 2008). While IKs are predominantly found in cells of the blood, SKs exhibit a wide expression throughout the central nervous system (CNS) (Kshatri et al., 2018).

Three members of the SK channels family were reported since their cloning in 1996 by Adelman and colleagues, SK1 ($K_{Ca}2.1$), SK2 ($K_{Ca}2.2$) and SK3 ($K_{Ca}2.3$) encoded by the *KCNN1*, *KCNN2*, and *KCNN3* genes, respectively (Köhler et al., 1996). These subtypes exhibit a non-homogeneous, often overlapping, distribution patterns in the CNS, with SK1 and SK2 channels showing a higher expression in neocortex, hippocampus, and cerebellum compared to SK3 (Sailer et al., 2002). Their major role is to mediate rapid K^+ outward, driving membrane repolarization and hyperpolarization, and thereby impacting mechanisms of synaptic transmission, plasticity, neuronal firing, and learning processes (Sun et al., 2020).

In parallel, the second group includes the big-conductance BK channels ($K_{Ca}1.1$), product of the *KCNMA1* gene. Unlike SK and IK channels, BK channels are activated by both intracellular calcium and membrane voltage, giving them dual gating properties (Horrigan and Aldrich, 2002; Tian et al., 2013). In terms of topology, BK channels differ from the first group by the

presence of an additional S0 membrane spanning helix in their α subunits, resulting in a seven-helix configuration instead of six. As in VGICs, the S0-S4 segments confer voltage sensitivity, while the S5-S6 segments form the pore and selectivity filter. Another difference from the SK/IK channels is their mechanism of calcium sensing that does not involve any CaM interaction, rather, calcium ions directly bind at specific sites within the channel protein (Tian et al., 2013; Yusifov et al., 2008).

The profile of BK channel expression covers several brain areas, including the cortex and hippocampus, where they fulfil a multitude of functions, which highly depend on their subcellular location and interactions with other channel isoforms (Kshatri et al., 2018). In dendrites and nerve terminals, a tight coupling between BK and VGCCs has been established, supporting their role in regulating the duration and amplitude of the dendritic spikes and neurotransmitter release (Wanner et al., 1999; Blömer et al., 2024). Further, a coupling with the sodium channel subtype $Na_v1.2$, a central focus of this project, has been recently identified in the axonal compartment (Filipis et al., 2023). This interaction modulates the shape and repolarization of generating APs, revealing the complex interplay between ion channels in regulating neuronal excitability, a mechanism that will be brought to the spotlight in a later section of this dissertation.

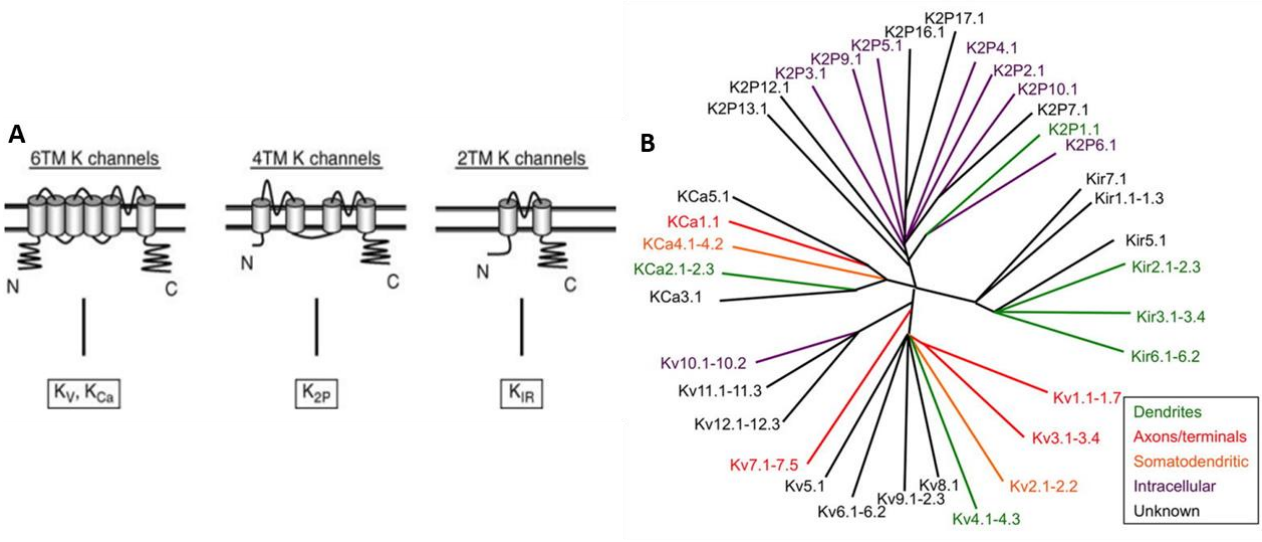

Figure 1.4 **Structural and subcellular classifications of neuronal potassium channels.** ***(A)*** The topology architectures of K^+ channel α-subunits based on transmembrane domain structures (6TM, 4TM, 2TM) are schematically presented. ***(B)*** Simplified dendrogram of potassium channel subtypes illustrating their primary subcellular localization within neurons. *Panel A adapted from Mathie and Veale (2008); panel B adapted from Trimmer (2015)*

1.3.2 Voltage-Gated Calcium Channels

Voltage-gated calcium channels (VGCCs or Ca_V) are transmembrane proteins that, in electrically excitable cells, form the main route for calcium entry into the cell after depolarization of the membrane, thereby converting electrical signals into a range of physiological responses. Ten distinct Ca_V α-subunits have been described, which are divided into three sub-families (Ca_V1, Ca_V2 and Ca_V3), producing five distinct types of calcium currents in both neuronal and non-neuronal tissues: L-type ($Ca_V1.1$-1.4), P/Q-type ($Ca_V2.1$), N-type ($Ca_V2.2$), R-type ($Ca_V2.3$) and T-type ($Ca_V3.1$-3.3) (Catterall, Perez-Reyes, et al., 2005). Structure wise, Ca_V channels reside in the membranes as heteromultimeric complexes with their alpha subunits bordering the calcium-selective central pore, and interacting with various auxiliary subunit types (α2δ1-4, β1-4 and γ1-8), which conveys the diversity of this channel family and its numerous activities (Schampel & Kuerten, 2017).

According to their electrophysiological characteristics, VGCCs are classified into low-voltage activated (LVA) consisting of the Ca_V3 channels which open at relatively low membrane voltage levels, and high-voltage-activated (HVA) channels, including Ca_V1 and Ca_V2 channels, whose probability of opening increases at more depolarized membrane potentials (Huang et al., 2024).

Within the nervous system, Ca_V channels are detectable in multiple areas to mediate excitability besides regulating a number of intracellular mechanisms depending on their specialized localizations. To begin with the Ca_V1 family ($Ca_V1.1$ and $Ca_V1.3$), mostly found in postsynaptic regions, they generate the L-type current which stands for "long-lasting" and are integral to postsynaptic signaling complex facilitating processes like long term potentiation (LTP), a key mechanism for learning and memory, as well as gene transcription, and long-term post-synaptic plasticity (Nanou & Catterall, 2018). Ca_V2 channels include $Ca_V2.1$ conducting the P/Q-type current (first described in Purkinje cells), $Ca_V2.2$ conducting the N-type, and $Ca_V2.3$ conducting the R-type current. P/Q and N-type channels are predominantly expressed in presynaptic terminals, promoting calcium-dependent neurotransmitter release and modulating short-term synaptic plasticity. Nonetheless, these channels are also broadly expressed across neuronal compartments (Schampel & Kuerten, 2017). Finishing with the Ca_V3 family, responsible of producing the T-shaped current, or

"transient", they notably drive the rhythmic neuronal firing in regions such as the thalamus governing the sleep rhythm, this role was described in early work on thalamic neurons (McCormick & Bal, 1997), and further expanded in later studies (Cueni et al., 2008; El Ghaleb et al., 2021; Schampel & Kuerten, 2017).

1.3.3 Voltage-Gated Sodium Channels

1.3.3.1 Structure

In their pioneering 1949 paper, Hodgkin and Huxley identified sodium as the major depolarizing ion and they subsequently predicted that its flow was guided by voltage-sensitive "gates" in the membrane lipid bilayer (Hodgkin & Katz, 1949; Hodgkin & Huxley, 1952a). For nearly three decades, the molecular identity of sodium channels remained elusive. In 1980, William Catterall and Daniel Beneski achieved a partial purification of sodium channel from neural membranes, using photoactivatable covalent labeling of channels with modified ^{125}I-labled scorpion toxin (Beneski & Catterall, 1980). Their work was able to identify three major polypeptides: a large α subunit weighing 260 kDa, and two small β subunits (mass 30-40 kDa) non-covalently associated: a β1 and a disulfide-linked β2 (Hartshorne et al., 1982; Hartshorne & Catterall, 1981-1984).

This biochemical characterization eventually facilitated the first successful cloning of a voltage-gated sodium channel (VGNC) α-subunit in 1984. The full nucleotide sequence of 7230 nucleotides disclosed some interesting features that anticipated the overall architecture of the sodium channel. Strikingly, it showed four repeating units, each including a region of quasi-evenly spaced positive residues, presumably serving as the voltage-sensor (Noda et al., 1984,1986a). By the dawn of the new millennium, ten genes encoding the sodium channel alpha subunit had been identified in mammals (Goldin, 2001).

The last three decades of research have shaped our understanding of the voltage-gated sodium channels, and reached a structural milestone with the landmark determination of the high-resolution crystal structure of the bacterial Na_V channel, Na_VAb (Payandeh et al., 2011). Homology models were built upon integrating human Na_V channel sequences with bacterial crystallographic data, and complemented by molecular dynamics simulations (MDS) providing insights into how these channels function at the molecular level (De Lera

Ruiz & Kraus, 2015). What makes prokaryotic sodium channels ideal models for structural studies is their simple architecture. As homotetramers, they consist of four-fold symmetric polypeptide chains exhibiting high sequence homology in contrast to the complex pseudotetrameric organization of their mammalian counterparts. Eukaryotic Nav channels are composed of a large pore-forming α subunit, which can be coupled to one or two smaller regulatory β subunits (Bagnéris et al., 2014; Catterall, 2012; Payandeh et al., 2011).

In humans, nine similar alpha subunits have been identified Nav1.1, Nav1.2, Nav1.3, Nav1.4, Nav1.5, Nav1.6, Nav1.7, Nav1.8, and Nav1.9, respectively encoded by the genes *SCN1A*, *SCN2A*, *SCN3A*, *SCN4A*, *SCN5A*, *SCN8A*, *SCN9A*, *SCN10A*, and *SCN11A* (**Figure 1.5**). Nav channel isoforms share a great sequence homology, exceeding 50%, and are classified within a single superfamily (De Lera Ruiz & Kraus, 2015). The International Union of Pharmacology adopted the naming convention Nav1.x for this family which indicates the primary permeating ion "Na^+", followed by the main regulator of channel activity "voltage", and then the family and isoform designation (Goldin et al., 2001).

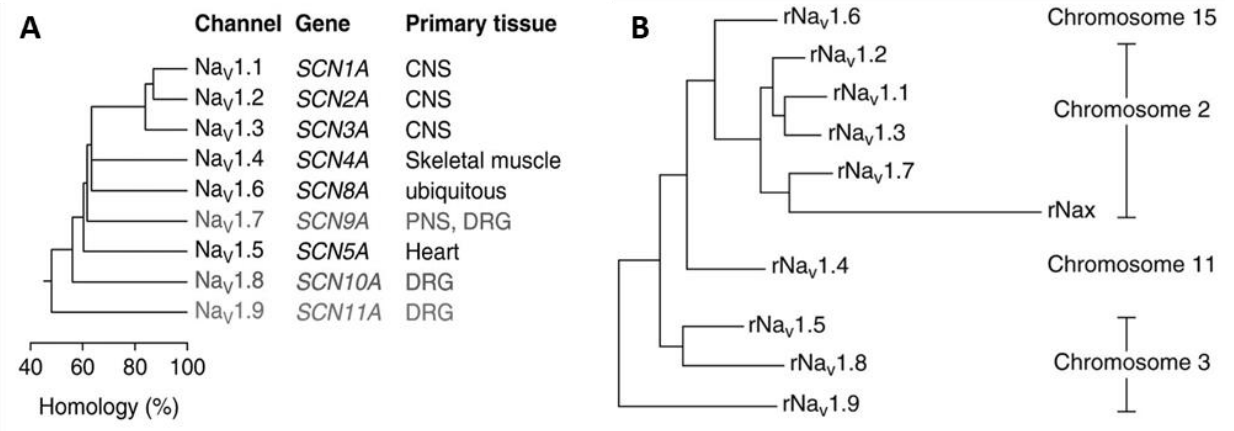

Figure 1.5 **Phylogenetic Organization and Distribution of Voltage-Gated Sodium Channel α-Subunits.** ***(A)*** Phylogenetic tree of human Nav channel α-subunits (*SCN1A*–*SCN11A*), by sequence homology and their primary tissue expression site. ***(B)*** Phylogenetic tree of rat Navchannel α-subunits including the chromosomal arrangement of the corresponding human orthologues, labelled on the right. *Panel A adapted from Nau and Leipold (2017); panel B extracted from Yu and Catterall (2003)*

1.3.3.2 Molecular Architecture of the Alpha Subunit

The α-subunit, which confers sodium conductance identity, is a large single polypeptide with a molecular size of 220–260 kD, consisting of roughly 2000 amino acids. It is composed of four homologous domains (I-IV), each containing six membrane spanning segments (S1-S6). The transmembrane S5 and S6 segments together with the extracellular P-loops form the pore domain (PD) and the ion selectivity filter (SF), with S6 lining the intracellular portion of a water-filled cavity. Whereas S1-S4 segments comprise the voltage sensor domain (VSD), home to channel's gating (**Figure 1.6**) (Catterall et al., 2020; Numa & Noda, 1986).

1.3.3.3 Pore Domain

The pore domain (PD) is formed by S5 and S6 segments, and is gated, at its cytoplasmic terminus, by an activation gate created by the intracellular ends of four S6 segments, and contains a central water-filled cavity (Catterall et al., 2020). This cavity houses residues that interact with most Na_V-blocking drugs, highlighting the PD relevance in drug binding and therapeutic targeting (Shen et al., 2017). In parallel, from a structural perspective, a study by Daniel L. Minor and coworkers interestingly demonstrated that bacterial Na_V pore-only constructs, lacking the VSD, can form functional and biochemically accessible ion channels, rendering the PDs of Na_V channels excellent structural models for studying selectivity and permeability governing factors (Shaya et al., 2011).

1.3.3.4 Selectivity Filter

The PD contains the selectivity filter (SF), which is the geometrically narrowest region of the pore, permitting the passage of sodium ions preferentially over their key rivals. PD is constituted by the reentrant P-loop from the extracellular ends of the S5-S6 of each domain, consistently composed of the key amino acids DEKA that play a major role on determining the Na^+ selectivity by specifically interacting with the permeating ion: D for aspartate in DI, E for glutamate in DII, K for lysine in DIII, and A for alanine in DIV. The passage of Na^+ molecules through the SF occurs in their hydrated form, surrounded by a square array of water molecules, whereas K^+ ions traverse K_V channel pores in a practically fully dehydrated form (Payandeh et al., 2011-2012). Researchers have shown that DEKA can be easily mutated to shift the channel's permeability towards K^+ and Ca^{2+}, where a single point

mutation by replacing lysine (or K) at position 1237 by glutamate (or E) can abolish the Na^+ selectivity of this filter (Heinemann et al., 1992; Li et al., 2016; Li et al., 2023). It is also reported that the pore size is regulated by a salt bridge situated between lysine and aspartate or glutamate, allowing for better accommodation of Na^+ compared to K^+ (Tikhonov & Zhorov, 2004). Moreover, differences in the free energy profiles of these ions may further influence ion selectivity (Boda et al., 2015).

1.3.3.5 Activation and Inactivation Gates

A voltage-dependent activating gate and a time-sensitive inactivating gate are characteristic of VGNCs. The activation gate comprises four hydrophobic amino acid residues, one from each intracellular terminus of the S6 helices, creating a tiny intracellular cavity and responsible for controlling access to the extracellular pore of Na_v channels. Whereas the inactivation gate consists of an intracellular loop that links the repeating domains DIII and DIV, often referred to the "IFM" motif (isoleucine, phenylalanine, methionine). In the classical model, when the channel enters fast inactivation, it operates as a hinged lid, folding into the intracellular aperture of the pore. More recent studies by the Bezanilla group, however, propose alternative mechanisms for fast inactivation, suggesting that the inactivation particle can remain bound while the channel enters its inactivated state (Liu et al., 2023; Liu & Bezanilla, 2025).

These two gates function synergistically to ensure a controlled depolarization: the activation gate opens for a few milliseconds, permitting sodium influx necessary for depolarization, after which the inactivation gate's closure halts this flow irrespective of the activation gate's condition or persistent stimulation (Catterall, 2000-2013).

1.3.3.6 Voltage Sensing Domain

Another critical structural component of VGNCs is the voltage-sensing domain (VSD), located within the S1-S4 segments of each domain in the Na_V α-subunit. Acting as the channel's sensor, the VSD's flexibility is mediated by the presence of positively charged amino acids (mainly arginine) in the S4 helix. At rest, these positive residues are stabilized by interactions with negative charges. Upon depolarization, as the intracellular medium becomes more positively charged, it repels the voltage sensor, prompting the S4 segments to rotate and shift

toward the extracellular surface. This movement induces a conformational change that results in the opening of the channel's pore, allowing the sodium ions influx into the cell (Catterall, 2010; Payandeh et al., 2011).

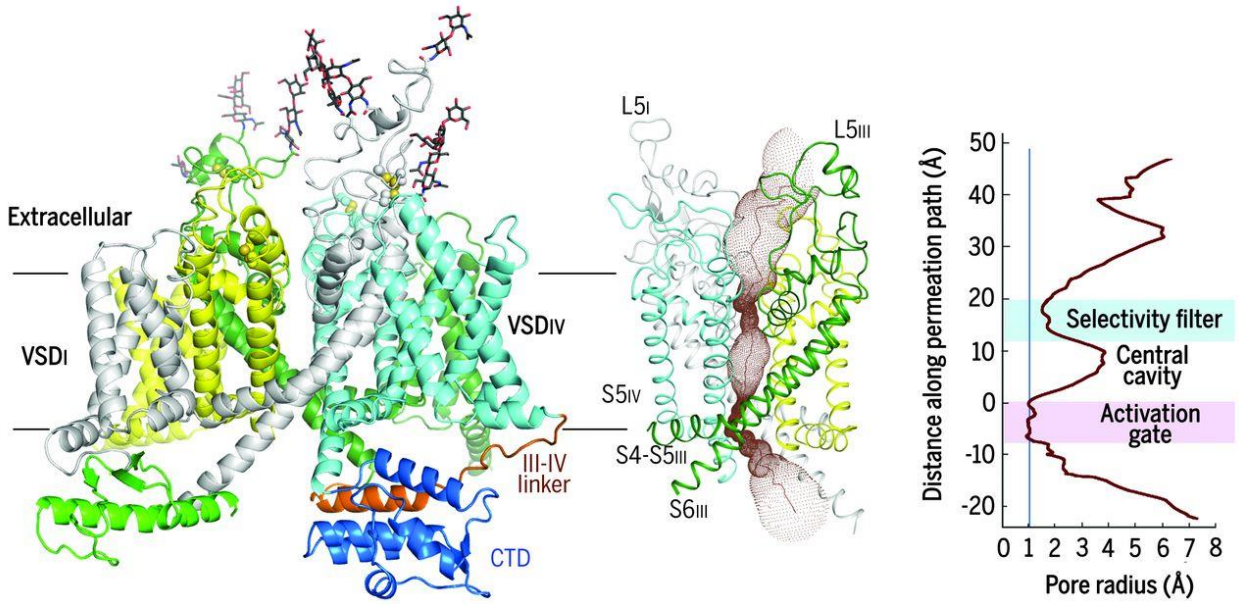

Figure 1.6 **Cryo-EM structure of the eukaryotic sodium channel Na_VPaS resolved at 3.8 Å.** ***Left:*** The overall architecture of Na_VPaS (PaFPC1), a eukaryotic sodium channel identified in the American cockroach (Periplaneta americana). The four domains (DI–DIV) are are indicated in different colors. The structure includes characteristic eukaryotic elements, including the intracellular III–IV linker (orange), which is involved in fast inactivation, and the C-terminal domain (blue). ***Middle:*** Side view of the pore domain of Na_VPaS with the permeation path illustrated by brown dots. ***Right:*** Quantified pore radius along the axial conduction pathway, revealing three functional regions: the selectivity filter, central cavity, and intracellular activation gate. The narrowing near the cytoplasmic end reflects a non-conducting, closed state of the channel. *Reproduced from Shen et al., (2017)*

1.3.3.7 Structural and Functional Dynamics of Na_v Channels: From Voltage Sensing to Inactivation

In previous sections, we have examined the different constituent parts of the VGNC α-subunit. It is now important to explore how these components orchestrate their actions and actively respond to changes in membrane potential transitioning from a resting state, to activation, ion permeation, and inactivation.

In this respect, when the membrane is maintained at its resting potential, the cell's inside is negatively charged relative to the outside, and the VSD holds the channel locked in its closed conformation.

Upon the arrival of a stimulus that depolarizes the membrane, the S4 segment of the channel moves outwards by electrostatic forces and elicits a series of structural changes that propagate to the S6 segment. This movement triggers the opening of the activation gate and avails the pore to the Na^+ ions entry inside the cell. The selectivity filter is responsible for Na^+ preference over other cations, it contains negatively charged amino acids that allow hydrated Na^+ ions to pass through while rejecting larger or smaller ones.

Shortly after the channel opens, the inactivation occurs and effectively shuts out the flow of Na^+ ions regardless of a depolarized membrane. This process of inactivation has traditionally been described as a "plug" that temporarily seals the channel, whereas recent studies suggest that the inactivation particle may remain associated with the channel during inactivation (Liu et al., 2023; Liu & Bezanilla, 2025).

Once the membrane potential has returned to the resting baseline (repolarization phase), the VSD shifts back to its initial position and the activation gate closes, ceasing the entry of Na^+ ions. At this stage, the inactivation is relieved and the inactivation gate is detached. Now the channel has reached the state where it can undergo the next cycle of activation.

This type of interdependent mechanism ensures the coordination of the Na_V channel's fast opening and closing, which in turn supports the propagation of action potentials in neurons and other excitable cells (Ahern et al., 2015; De Lera Ruiz & Kraus, 2015; Catterall et al., 2017).

1.3.3.8 Beta Subunit

Eukaryotic Na_v α-subunits are generally coupled to one or two auxiliary β-subunits. The β-subunits belong to the immunoglobulin (Ig) domain family that participates in a number of cell adhesion-related activities. In mammals, four genes (*SCN1B–SCN4B*) encode the β subunits proteins designated as β1, β2, β3, and β4 (Namadurai et al., 2015). The alternative splicing of the *SCN1B* gene produces a fifth variant known as β1B. All isoforms of β-subunits are expressed as transmembrane proteins, except β1B, which lacks the transmembrane domain and is thus soluble (Qin et al., 2003).

Although the α subunit can independently construct a fully functional Nav channel, the β subunits are important for optimizing channel kinetics and modulating their surface expression (Kraner et al., 1985). These subunits shape Nav channel behavior in many ways and are important regulators of neuron excitability. They can increase the peak current density by increasing the channels' presence on plasma membranes. They can also shift the voltage range of activation and inactivation, hence affecting the conformational changes that the Nav channels go through during APs (Brackenbury & Isom, 2011; Chen & Cannon, 1995; Nevin et al., 2020; Yu et al., 2005). The gating effects of the β -subunits, though not apparent, are of profound importance. Several genetic mutations in these subunits have been reported to cause different hereditary human diseases including epilepsy, neuropathies, cardiac rhythm dysfunction, and some cancers (Chahine, 2011; Namadurai et al., 2015).

1.3.3.9 Tissue Expression and Subcellular Localizations

The distribution of different Na_v channels is tightly regulated to match their functional roles. Of the nine isoforms, the central nervous system exhibits a predominant expression of $Na_v1.1$, $Na_v1.2$, $Na_v1.3$, and $Na_v1.6$, whereas $Na_v1.7$, $Na_v1.8$, and $Na_v1.9$ are mainly distributed across the peripheral nervous system. $Na_v1.4$ is mostly restricted to the skeletal muscles, and $Na_v1.5$ is mostly found in the cardiac tissue (**Figure 1.5A**) (Goldin, 2001).

A systematic investigation of the four brain Nav isoforms localizations has been performed by Whitaker et al. (2001) using immunohistochemical methods. This study revealed that Nav1.1, Nav1.2, Nav1.3, and Nav1.6 channels were found in the cerebral cortex, deep brain nuclei, hippocampal structures, insular cortex, and cerebellum, with varying levels of expression. Nav1.1 is predominant in inhibitory GABAergic interneurons (Rubinstein et al., 2015; F. H. Yu et al., 2006), while Nav1.2 and Nav1.6 prevail in excitatory and glutamatergic neurons (Sanders et al., 2018; Syrbe et al., 2016). Nav1.3 is primarily expressed during embryonic and neonatal stages, but its levels decrease as development progresses, and other sodium channel isoforms, particularly Nav1.1 and Nav1.2, gradually take over its role in mature neurons (Whitaker et al., 2001).

Besides the unique tissue expression, CNS Nav channels display a differential distribution along neuronal compartments. Nav1.1 is primarily localized in the cell body, proximal processes, proximal axon initial segment (AIS). Nav1.2 is specifically concentrated in the

proximal AIS and unmyelinated axons of mature neurons, whilst $Na_V1.3$ is particularly abundant in somatodendritic compartments. In contrast, $Na_V1.6$ shows a broader distribution, this protein is present in the soma, proximal processes, distal AIS, and nodes of Ranvier (Aman et al., 2009; Candenas et al., 2006; Fukuoka & Noguchi, 2011; Kerr et al., 2007; Raymond et al., 2004; Vacher et al., 2008).
In the PNS, $Na_V1.7$, $Na_V1.8$, and $Na_V1.9$ are found in the cell bodies and axons of sensory neurons, particularly in the dorsal root ganglia (DRG) of the spinal nerves, where they play key roles in the modulation of nociceptive pathways (Goldin, 1999; J. Wang et al., 2017).

The vital contribution of sodium channels to the optimal functioning of the nervous systems of higher organisms cannot be overstated. Despite the great similarities among VGNC family members, our focus narrows to a particular isoform: $Na_V1.2$. With its pivotal role in brain's excitability, this sodium channel stands as a crossroad of fundamental neurophysiology and the pathophysiology of neurological disorders. This dissertation centers on the in-depth analysis of $Na_V1.2$'s biophysical properties in the context of loss-of-functions channelopathies, investigating how its dysfunction reshapes neuronal excitability and drives diseases such as autism spectrum disorder (ASD).

1.4 Voltage-Gated Sodium Channel Type-II

1.4.1 Structural and Molecular Profile

$Na_V1.2$ stands as a central figure in the brain's excitability as an architect that sets the framework for APs. Originally isolated from the rat CNS, it was commonly referred to as rat type II sodium channel (Noda et al., 1986).
$Na_V1.2$ channel has a structure akin to its VGNC counterparts: a pore-forming alpha subunit associated with one or two regulatory beta subunits (**Figure 1.7A,C**). The alpha-subunit, primary protein constituting the voltage-gated sodium channel type II, is encoded by the *SCN2A* gene. In humans, *SCN2A* is made up of 31 exons and is situated on the long arm of chromosome 2 (2q24.3), within the same gene cluster as other VGNC isoforms $Na_V1.1$ (*SCN1A*) and $Na_V1.3$ (*SCN3A*) (Catterall et al., 2005; Litt, 1989). $Na_V1.2$ protein is relatively large, made up of 2005 amino acids with a molecular weight of approximately 228 kDa

(Channelpedia). It spans the membrane as a single chain polypeptide, folding into four homologous domains (I-IV), with each comprising six transmembrane segments (S1-S6), therefore creating a 24-helix bundle. The different specialized elements of this architecture, their locations, and described roles in the previous section, are significantly conserved in this isoform: a pore-domain with an accompanying selectivity filter, a voltage-sensor, and fast activating and inactivating gates (Pan et al., 2019).

A

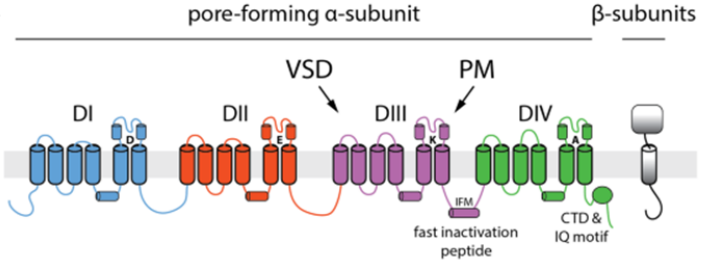

B

Domain	Segment	Codon	Domain	Segment	Codon
Domain 1	N-terminal Domain	1 – 124	Domain 3	D3/S1	1204 – 1227
	D1/S1	125 – 148		Extracellular Loop	1228 – 1240
	Extracellular Loop	149 – 156		D3/S2	1241 – 1266
	D1/S2	157 – 176		Intracellular Loop	1267 – 1272
	Intracellular Loop	177 – 189		D3/S3	1273 – 1294
	D1/S3	190 – 208		Extracellular Loop	1295 – 1298
	Extracellular Loop	209 – 214		D3/S4	1299 – 1320
	D1/S4	215 – 234		Intracellular Loop	1321 – 1339
	Intracellular Loop	235 – 250		D3/S5	1340 – 1367
	D1/S5	251 – 274		Pore Loop	1368 – 1446
	Pore Loop	275 – 401		D3/S6	1447 – 1473
	D1/S6	402 – 427		D3–D4 Linker	1474 – 1526
	D1–D2 Linker	428 – 753			
Domain 2	D2/S1	754 – 778	Domain 4	D4/S1	1527 – 1550
	Extracellular Loop	779 – 789		Extracellular Loop	1551 – 1561
	D2/S2	790 – 813		D4/S2	1562 – 1585
	Intracellular Loop	814 – 821		Intracellular Loop	1586 – 1591
	D2/S3	822 – 841		D4/S3	1592 – 1615
	Extracellular Loop	842 – 847		Extracellular Loop	1616 – 1625
	D2/S4	848 – 867		D4/S4	1626 – 1647
	Intracellular Loop	868 – 883		Intracellular Loop	1648 – 1662
	D2/S5	884 – 904		D4/S5	1663 – 1685
	Pore Loop	905 – 957		Pore Loop	1686 – 1751
	D2/S6	958 – 983		D4/S6	1752 – 1776
	D2–D3 Linker	984 – 1203		C-terminal Domain	1777 – 2005

C

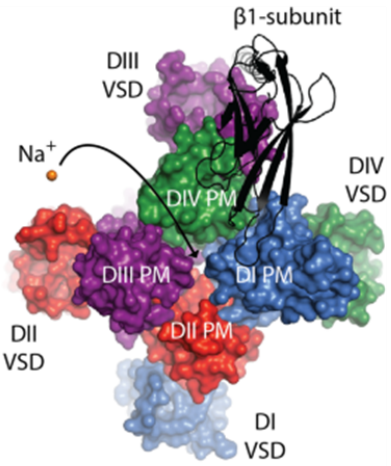

Figure 1.7 **Structural and organizational features of the human voltage-gated sodium channel $Na_V1.2$.** ***(A)*** Schematic topology of the $Na_V1.2$ α-subunit showing the four homologous domains (DI–DIV), with six transmembrane segments in each. Voltage-sensing domains (VSDs) and pore modules (PMs) are indicated, as well as main structural motifs such as the fast inactivation peptide (IFM motif) and the C-terminal IQ motif as site for calmodulin binding. ***(B)*** Codon-level annotation of individual transmembrane segments, extracellular and intracellular loops, and domain linkers in human $Na_V1.2$. ***(C)*** Top view of the $Na_V1.2$ channel showing the spatial arrangement of the four domains around the central permeation pathway and the domain-swapped configuration between pore modules and

voltage-sensing domains, which underlies allosteric coupling in gating. *Panels A and C extracted from Kruth et al. (2020); panel B modified from Abbott et al. (2024), color scheme adjusted to match the domain color code in panels A and C*

1.4.2 Selectivity for Sodium and Emerging Calcium Conductance

With the various strategies implemented by their selectivity filter, Na_V channels are adapted to conduct their native ion, Na^+, with tenfold greater efficiency compared to its cation contenders, K^+ or Ca^{2+} (Hille, 1971). The hypothesis attributing some Ca^{2+} permeability to Na_V channels arose from studies integrating electrophysiological recordings with Ca^{2+} imaging over squid giant axons, which demonstrated that an initial phase of Ca^{2+} influx induced by depolarization is sensitive to the well-known VGNC blocker "tetrodotoxin" (TTX) (Baker et al., 1971; Meves and Vogel, 1973). Further, this permeability has been reported in rat hippocampus CA1 nerve cells and myocytes (Akaike & Takahashi, 1992; Santana et al., 1998).

In the past few years, there has been a surge in the examination of TTX-sensitive calcium routes across the cortex. Maarten Kole's group identified, through calcium imaging in rat brain slices, a component of Ca^{2+} current that was sensitive to TTX ($I_{Ca(TTX)}$). By combining both sodium and calcium imaging, they observed that this $I_{Ca(TTX)}$ in the axons, reflected the kinetics of the voltage-activated Na^+ currents (I_{Na}) mediated by VGNCs. Further experiments in HEK-293 cells transfected with the human $Na_v1.2$ showed a TTX-sensitive internal Ca^{2+} rise upon stimulation. In light of these findings, they assumed that the identity of this calcium permeation refers to the sodium channel $Na_v1.2$, and estimated its Ca^{2+} conductance to be approximately 0.4% (Hanemaaijer et al., 2020).

This study marked a significant step forward in associating Ca^{2+} permeation to Na_V channels within the mammalian nervous system. Nonetheless, there still had been an apparent lack of consensus on the direct identification of $Na_v1.2$ to be the specific channel responsible for Ca^{2+} conductance owing to the non-specific effects of tetrodotoxin (TTX), which blocks a broad range of voltage-gated sodium channel (VGNC) subtypes (Tsukamoto et al., 2017). Recognizing this limitation, our group sought to overcome the pharmacological constraint using a new drug with enhanced sensitivity and specificity towards $Na_v1.2$, named G1G4-

huwentoxin-IV (hwtx). Leveraging this selective agent, Luiza Filipis and colleagues were able to more accurately dissect and characterize the Ca^{2+} permeation mediated by $Na_v1.2$, providing compelling evidence that reinforces its role in Ca^{2+} conductance while excluding contributions from other VGNC subtypes. By performing ultrafast imaging on mice brain slices, they found that the selective block of $Na_v1.2$ rather than the traditional calcium gateways, VGCCs, drove effects on the shape of axonal action potential similar to those observed when blocking BK channel; which led to conclusion that $Na_v1.2$ serves as a source of calcium necessary for the activation of BK channels (Filipis et al., 2023). The downstream targets of the $Na_v1.2$ dual permeability to Na^+ and Ca^{2+}, along with its interactions with other channels and implications in AP generation, will be further elaborated in later sections.

1.4.3 Gating Kinetics and Modulation

1.4.3.1 Kinetics and Biophysical Properties

With its fast gating properties coupled with a clear voltage dependence for opening and closing, $Na_v1.2$ mediates the transient sodium current (I_{NaT}) that facilitates the rapid depolarizing phase of APs in excitatory neurons. $Na_v1.2$ activates at membrane potentials close to -50 mV, with a half-maximal activation ($V_{1/2}$) near -24 mV. The activation mechanism is fast and occurs on a submillisecond timescale ($\tau_{act} \sim 0.4$ ms). Shortly after, the inactivation takes place, which is a property common to all Na_V channels subtypes, with a time constant of roughly 1-2 ms and steady-state inactivation occurring at more hyperpolarized membrane potentials ($V_{1/2}$ about -60 mV). Within 2 to 10 ms, $Na_v1.2$ is able to recover from inactivation, thus allowing it it to support high-frequency firing (Clare et al., 2000; Qu et al., 2001; Rush et al., 2005).

Besides the transient sodium current, $Na_V1.2$ can also contribute to persistent sodium currents (I_{NaP}), particularly in the proximal axon (Astman et al, 2006). And under certain conditions, such as β-subunit modulation or disease-causing gain-of-function mutations, $Na_V1.2$ channels have been shown to give rise to resurgent currents (Mason et al., 2019).

1.4.3.2 Multilevel Regulation of $Na_V1.2$

The kinetics of $Na_V1.2$ channels can be modulated by a variety of intrinsic and extrinsic factors that fine-tune the gating properties of $Na_V1.2$ channels. Endogenous factors include their associated auxiliary subunits beta, particularly β1 and β2 subunits, which have significant influence on $Na_V1.2$ voltage dependence and gating speed, or intracellular proteins such as fibroblast growth factors (FGF12) (Patino & Isom, 2010; Seiffert et al., 2022). Additionally, physical conditions like temperature also affect $Na_V1.2$ properties; for instance, febrile-range temperatures (40–41 °C) were reported to increase current amplitude, activation speed, and to enhance inactivation recovery (Ye et al., 2018).

Beyond these, multiple levels of molecular regulation further modulate $Na_V1.2$ function. At the transcriptional level, *SCN2A* expression is tightly restricted to neurons via the REST/NRSF complex (neural restrictive silencer element/repressor element 1). This repressor interacts with the NRSE/RE-1 element in the 5'-UTR region of the *SCN2A* gene, and recruits chromatin-modifying corepressors such as Sin3A and CoREST, preventing transcription in non-neuronal cells, and guaranteeing the cell-type specificity of $Na_V1.2$ expression (Battaglioli et al., 2002; Belyaev et al., 2004; Chong et al., 1995; Schade & Brown, 2000).

At the level of alternative splicing, *SCN2A* undergoes developmentally regulated exon selection of its isoforms 5N (neonatal) and 5A (adult), first demonstrated by Sarao et al. (1991). 5N is strongly expressed in the brain during early development, particularly in the cortex, and it gradually shifts to 5A during the postnatal period. This transition exceeds the molecular level and modulates excitability, seizure susceptibility, and behavior. It has been reported that mice expressing exclusively the adult isoform (5A) showed elevated AP firing and increased sensitivity to seizures in early postnatal life compared to wild-type (WT) counterparts, with alterations in synaptic properties and behavior persisting into adulthood (Gazina et al., 2010; 2015; Liang et al., 2021).

Lastly, post-translational modulations of $Na_V1.2$ are numerous and include phosphorylation, ubiquitination, methylation, SUMOylation (Y. Chen et al., 2006; Kotler et al., 2022) and proteolysis. Phosphorylation by kinases such as PKA, PKC, CK2, GSK3, and Fyn modifies channel gating, current amplitude, and membrane localization (Ahn et al., 2007; Beacham et

al., 2007; Li et al., 1992; Onwuli & Beltran-Alvarez, 2016). On the other hand, the E3 ligase Nedd4-2 ubiquitinates $Na_V1.2$, causing the channel to internalize and undergo degradation (Fotia et al., 2004). As for methylation of arginine residues by PRMTs, it drives an increased $Na_V1.2$ membrane expression and accelerated recovery from inactivation (Baek et al., 2014; Guo et al., 2015). Also, $Na_V1.2$ channels are subject to proteolytic cleavage by calpain within their intracellular loops, although the fragments remain associated to the membrane, and the functional implications are only partially understood (Von Reyn et al., 2009).

1.4.4 Pharmacology and Drug Sensitivity

$Na_V1.2$, similar to the majority of VGNCs, is sensitive the guanidine-based neurotoxin tetrodotoxin (TTX), a toxin isolated from the puffer fish, which at nanomolar concentrations completely blocks the channel activity (De Lera Ruiz & Kraus, 2015). Multiple pharmacological agents including small molecules, peptide toxins, or gating modulators, can also interact with $Na_V1.2$ and alter its biophysical properties.

Some act as activators, in form of partial or full agonists, including β-scorpion toxin Css IV (pKd = 9.7), batrachotoxin (pKd = 9.1), aconitine (pKd = 5.9), and veratridine (pKd = 5.2) (Cestèle et al., 1998; De Lera Ruiz & Kraus, 2015; Linford et al., 1998). Others act as inhibitors of inactivation, such as the α-scorpion AaH-II, which, although not fully selective for $Na_V1.2$, offers a promising pharmacological tool and will be further addressed in the experimental part of this thesis (Abbas et al., 2024).

In contrast, a wide variety of inhibitors and antagonists target different functional states of the channel. Gating inhibitors include ATX-II (pEC_{50} = 8.1), δ-Hexatoxin-Mg1a (pEC_{50} = 4.5), which slow or prevent fast activation (Oliveira et al., 2004; Yamaji et al., 2009). Here, pEC_{50} is the negative base-10 logarithm of the concentration (in Molar) producing half-maximal effect on channel gating. Others like Huwentoxin-IV (pKd = 7.8; $IC_{50} \simeq 150$ nM), Phrixotoxin-3 (IC_{50} = 0.6 nM), and Protoxin II, produce a gating shift of the activation to more depolarized potentials, thus inhibiting the channel opening by a voltage dependent fashion (De Lera Ruiz & Kraus, 2015; Minassian et al., 2013; Schmalhofer et al., 2008). $Na_V1.2$ can also be affected by pore-blocking agents, which are in essence, ligands that block ion movement through the pore of the channel. This family comprises the potent TTX (potently pIC_{50} = 8.0), μ-Conotoxin

SmIIIA (pKd = 8.9), Saxitoxin (pIC_{50} = 8.8) Etidocaine (pIC_{50} = 6.0), Lidocaine (pIC_{50} = 5.0), Phenytoin (pIC_{50} = 4.7–4.9), Lacosamide (pIC_{50} = 4.5), and others (Abdelsayed et al., 2013; Bricelj et al., 2005; Ragsdale et al., 1994; Wilson et al., 2011). Here, pIC_{50} is the negative base-10 logarithm of the IC_{50}, the concentration required to inhibit 50% of channel activity. Further, several small molecules with significant therapeutic activity have also expanded this repertoire, including GNE-131 (pIC_{50} = 8.1) and GNE-616 (pKd = 7.9), in addition to XPC-5462 (IC_{50} = 10.3 nM) and XPC-6444 (IC_{50} = 125 nM) (Focken et al., 2018; Goodchild et al., 2024).

Characterizing drug sensitivity and exploring the pharmacological modulators for $Na_V1.2$ offers, without a doubt, valuable insights into the channel's function and regulation and paves the way toward proper targeting in therapy. However, most of the drugs mentioned tend to act on multiple Na_V subtypes due to the high sequence homology in the pore-forming domains and voltage-sensing regions across the Na_V1 family, resulting in overlapping affinity profiles of many drugs for multiple isoforms (England & De Groot, 2009).

Only a small number of compounds have shown preferential effects on $Na_V1.2$. As an example from a recent study by our group, the recombinant G1G4-huwentoxin IV variant demonstrated enhanced selectivity as a $Na_V1.2$ blocker over co-expressed Na_V1 channels (Filipis et al., 2023). The major challenge, however, is still to design truly selective and isoform-specific modulators and enhancers. Such pharmacological specificity is required not only to elucidate the physiological role of $Na_V1.2$, but also to avoid non desired off-target effects on closely related isoforms like $Na_V1.6$ within a hub such as the AIS, particularly in the presence of subtle mutations. Achieving a high degree of precision is also a necessary step toward the ultimate aim of developing viable guided selective therapeutic strategies for $Na_V1.2$ related dysfunctions.

1.4.5 Mapping of $Na_v1.2$ In The Brain

1.4.5.1 Tissue Distribution: A Focus On Cortical Layer V

1.4.5.1.1 Regional and Cellular Expression of $Na_v1.2$

$Na_V1.2$ channel, alongside $Na_V1.1$, 1.3, and 1.6, are the main expressed isoforms in the central nervous system (Goldin et al., 2000). Molecular cloning and mRNA analysis by Noda et al. (1986) demonstrated the prominence of brain II sodium channel, later named $Na_V1.2$, as one of the most abundantly expressed sodium channel transcripts in the brain of adult rats. Shortly after, immunocytochemical localization of these channels by Westenbroek et al. (1989, 1992) identified a heterogeneous pattern of $Na_V1.2$ distribution throughout the rat brain, with a particularly dense expression in the forebrain, specifically within the cerebral neocortex. $Na_V1.2$ immunoreactivity was also detected in the substantia nigra, unmyelinated mossy fibers of granule cells, dendrites and axons of CA1 and CA3 pyramidal cells including the stratum radiatum of the hippocampus, as well as in the molecular layer of the cerebellum (Vacher et al., 2008). Recent studies expanded this distribution to the globus pallidus and unmyelinated axons of projection fibers within the striatum (Nadella et al., 2022; Yamano et al., 2022; Yamagata et al., 2017). In the thalamus, $Na_V1.2$ is highly expressed in the ventral posterolateral nucleus (Zhao et al., 2006), and in the hypothalamus, expression is in the zona incerta, subthalamic nucleus and lateral hypothalamic area (Jarnot & Corbett, 2006).

This tissue-specific distribution is further refined by cellular and layer specific profile of expression. $Na_V1.2$ channels exhibit higher densities in excitatory pyramidal neurons in both cortical and hippocampal regions (Ogiwara et al., 2018). In the neocortex, they are predominantly present in pyramidal neurons of layers I/II and IV–VI, but also they can be found in some interneuron subtypes, such as reelin positive (RLN+) and VIP+ interneurons derived from the caudal ganglionic eminence (Yamagata et al., 2017). Notably, $Na_V1.2$ is expressed in SST+ but not PV+ interneurons in mouse prefrontal cortex (Li et al., 2014).

1.4.5.1.2 Layer-V Pyramidal Neurons and Relevance as A Model System

The mammalian cortex is organized into six stacked layers, or laminae, each contributing uniquely to the neocortical architecture and connectivity. These laminae are arranged parallel to the brain's surface and house specific types of neurons that underlie their role and classification (Ramaswamy & Markram, 2015). Dendritic and axonal projections of cells located in deeper layers are found in Layer 1, the molecular layer at the outermost end of the cortex. Underneath are layers 2 and 3, home to small pyramidal-shaped cells, that are crucial for both local processing and inter-hemispheric communication. Further down is Layer 4, which is known as internal granular layer and consists of small spherical neurons, this layer constitutes the major recipient of thalamic sensory inputs. Following is the Layer 5 or pyramidal layer, rich in large pyramidal cells, and stands out as the primary output pathway of the cerebral cortex. Lastly, Layer 6, which hosts a variety of neuron types, and for that is known as the polymorphic layer (Miyashita, 2022).

Zooming into the pyramidal neurons of the fifth layer, morphologically characterized by their pyramid-shape, triangular soma, with two distinct dendritic domains: basal dendrites extending from the base, and apical dendrites ascending from the apex and crossing upper cortical layers, and a single axon that emerges from the soma and projects towards the white matter, branching into multiple collaterals that spread throughout the neocortex (Jiang et al., 2020). Layer 5 pyramidal neurons (L5PNs) are broadly classified into two subclasses based on their axonal projection targets: intratelencephalic (IT), and extratelecephalic (ET) neurons (Moberg & Takahashi, 2022; Reiner et al., 2003). IT neurons, mostly located in the upper half of Layer V (L5a), project to cortical areas and striatum. Often referred to as "slender untufted", they are characterized by less pronounced apical trunks without obvious terminal tufts (Baker et al., 2018). The other population, ET, or "thick-tufted pyramidal neurons" (TTL5), are predominantly found in the deeper part of layer V (L5b), and distinguished by their larger cell body and thick apical dendrite with many distal branches that arborize extensively into a tuft within the layer I. TTL5 neurons innervate subcortical areas such as the thalamus, midbrain, brainstem, in addition to the spinal cord (Kita & Kita, 2012; Ramaswamy & Markram 2015; Rojas-Piloni et al., 2017).

In L5PNs, basal, apical, and oblique dendrites serve as synaptic relays for excitatory inputs, whereas inhibitory inputs are mostly received by the soma, axon initial segment, and terminal tufts (Ramaswamy & Markram 2015; Sempere-Ferràndez et al., 2019). Dendrites act as coincidence detectors, integrating incoming signals from distinct branches. Based on the intensity of these signals, forward propagating potentials may reach the soma, exceed the generation threshold, and initiate an AP (Spruston, 2008).

In this project, we have particularly chosen L5PNs as our primary model to investigate the function of $Na_V1.2$. Pyramidal cells represent 70–85% of cortical neurons, and within this population, L5PNs serve as the main computational units and excitatory integrators of the cortex, being the only neocortical cell type with dendrites spanning across all six layers of cortex. In addition, their biophysical properties and ion channel expression patterns have been extensively studied in the rodent somatosensory cortex (Elston, 2003; Marek & Schoepp, 2021; Ramaswamy & Markram, 2015; Romand et al., 2011; Shai et al., 2015). Furthermore, their clear anatomical compartmentalization marked by an extensive dendritic arborization and a well-defined axon makes them an ideal model for examining ion channel properties at the subcellular level. In particular, they allow for selectively targeting the AIS, where $Na_V1.2$ exert high expressions and crucial functions (Hu et al, 2009).

1.4.5.2 The Axon Initial Segment: A Key Site for $Na_v1.2$ Compartmentalization and Activity

1.4.5.2.1 Molecular Architecture

The heterogeneous distribution of $Na_V1.2$ in the cortex might arise from the differential expression and localization of these channel subtypes within individual neurons. It has been widely accepted that $Na_V1.2$ channels are more densely localized in premyelinated axons, particularly in the axon initial segment (AIS), compared to cell bodies and dendrites (Wollner and Catterall, 1986).

Located at the boundary between the cell body and the axon, the AIS is defined as a unique subcellular compartment that begins at the axon hillock and extends up to ~40 microns from the soma (Inda et al., 2006). The AIS was first described more than half a century ago (Palay

et al., 1968), and has come to be understood as a layered molecular scaffold spanning from bundles of microtubules to the membrane associated complexes (Leterrier, 2016). This highly complex molecular architecture depends largely on anchoring proteins such as the Ankyrin-G (AnkG), which serves as the central component of this scaffold. With a membrane-binding domain of 24 ankyrin repeats (Bennett and Lorenzo, 2013), AnkG binds and anchors AIS-specific membrane proteins, including voltage gated sodium (Na_V), potassium (K_V) channels, in addition to other cell adhesion molecules (CAMs) (Davis et al., 1996; Garrido et al., 2003; Wang et al., 2014).

The hallmark of the AIS might be its strikingly high density of VGNCs, potentially leading to a conductance up to ~4,000 pS/μm^2, which is approximately 30-50 times greater than in the soma or the dendrites (Kole et al., 2008; Lorincz and Nusser, 2010). To achieve this dense clustering, AnkG interacts with a conserved motif located in the II–III intracellular loop of Na_V channels (Garrido et al., 2003; Gasser et al., 2012; Srinivasan et al., 1988). The complex molecular structure of the AIS is further detailed in **Figure 1.8.**

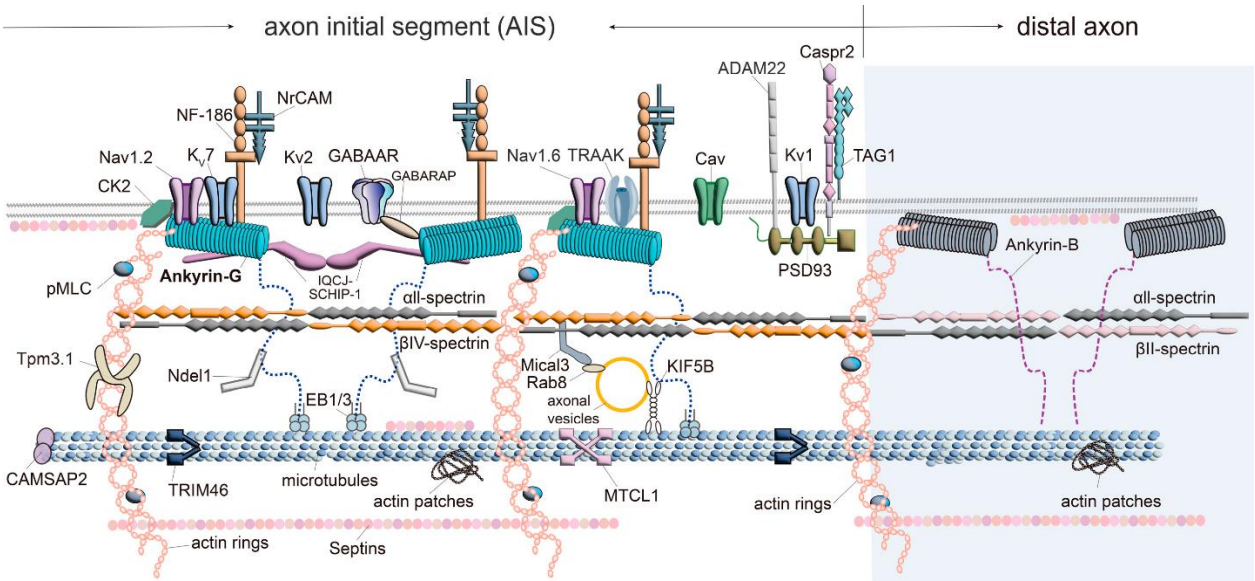

Figure 1.8 **AIS molecular structure.** Membrane proteins, such as voltage-gated ion channels and adhesion molecules, are anchored by the N-terminal domain of Ankyrin-G (sky blue). The C-terminal of AnkG is inserted into spectrin tetramers composed of βIV-spectrin (orange) and αII-spectrin (gray), which are linked to periodic actin rings (pink). In the distal axon, βIV-spectrin is replaced by βII-spectrin (pink), showing a shift in cytoskeletal composition beyond the AIS. $Na_V1.2$ and K_V7 channels predominantly localize proximally, while $Na_V1.6$, K_V1, and TRAAK channels are concentrated in the distal regions of the A IS. Cell adhesion molecules such as NF-186 and NrCAM

define AIS boundaries. AnkG binds to microtubules via EB1/EB3 proteins and Ndel1. Microtubule bundles are crosslinked by TRIM46 and MTCL1. Additional proteins including CK2, Mical3, Tpm3.1, and septins contribute to the structural organization and regulation of the AIS. *Adapted from Zhu et al. (2025)*

1.4.5.2.2 Developmental Profile of Na_v Channels in The AIS

During early postnatal development, $Na_V1.2$ is expressed throughout the AIS and axonal compartment, and for a brief time in development, is the dominant isoform of sodium channel for action potential initiation (Boiko et al., 2001; Gazina et al., 2015). This early phase also involves an expression of $Na_v1.3$, which is abundant during embryonic and very early postnatal stages (Beckh et al., 1989). However, as a developmental outcome these expressions are transient. When observed in mice after the first postnatal week, corresponding to late gestation through the first year of life in humans (Workman et al., 2013), $Na_V1.6$ gradually replaced $Na_V1.2$ to occupy the distal AIS compartment, with $Na_V1.2$ remaining within the proximal compartment (Hu et al., 2009). This spatial expression change is not simply morphological; the functional change is also evident, given that $Na_V1.6$ is known for its activation at more hyperpolarized potentials, contributing to the broader shift in excitability and firing thresholds observed during early circuit maturation (Bender and Trussell, 2012). A similar refinement takes place at the Ranvier nodes of the CNS and PNS, $Na_V1.2$ channels are primarily detected in the mammalian immature Ranvier nodes, but are then gradually replaced by $Na_V1.6$ during development (Freeman et al., 2015; Schafer et al., 2006).

1.4.5.2.3 Mechanisms of AIS Assembly and Maintenance

Unlike nodes of Ranvier that rely on help from myelinating glia to form, the AIS relies on intrinsic properties to develop (Dzhashiashvili et al., 2007). Numerous studies have delineated the mechanisms supporting the assembly and maintenance of AIS and the non-redundant role of AnkG has been demonstrated both in-vitro and in-vivo. Indeed, AnkG-deficient mice in cerebellar Purkinje cells were unable to cluster any other AIS components, and AIS assembly was hindered when cortical neurons were electroporated with shRNA against AnkG (Leterrier et al., 2010). In cultured hippocampal neurons, in contrast, knockdowns of CAMs and Na_V channels barely affected the AIS development, whereas AnkG

knockdown completely prevented its formation. While CAMs and Na_V channels are not required for the AIS assembly (Dzhashiashvili et al., 2007; Hedstrom et al., 2007; Xu and Shrager, 2005), and their clustering at the AIS level depends on AnkG not the other way around, their depletion compromises the integrity and impairs the stability of the built-up AIS, and does not rule out their involvement in its maintenance (Zonta et al., 2011).
Intriguingly, beyond its fundamental role in AIS assembly, AnkG has also been genetically linked to a variety of neurodevelopmental and psychiatric disorders, such as schizophrenia, bipolar disorder, ID, and attention deficit hyperactivity disorder (ADHD). Although rare de novo variants of AnkG have been also observed in several autism cases, a definitive causative relationship has yet to be made (Kloth et al., 2017; Yoon et al., 2022). Nevertheless, these findings suggest that mutations impacting the AIS scaffolding may increase susceptibility to a range of brain disorders.

The self-assembly of the AIS allows it to autonomously establish a distinct molecular identity, which has been the subject of much interest because it confers to this compartment the role of a physiological and a physical barrier between somatodendritic and axonal domains (Rasband, 2010a). After channels are anchored at the AIS, they exhibit remarkably low lateral mobility, and their diffusion and turnover become limited (Angelides et al., 1988; Brachet et al., 2010). This allows the AIS to maintain a stable high-density channel population, in addition to an enhanced excitability relative to adjacent compartments, which is paramount to its primary role as site of action potential initiation (Clark et al., 2009; Bender and Trussell, 2012).

1.4.5.2.4 AIS Plasticity

Despite its stability and maintained complex structure, the AIS shape is meticulously regulated and capable of adapting to physiological changes or pathological alterations (Jamann et al., 2018; Yamada and Kuba, 2016; Yoshimura and Rasband, 2014;). A significant factor that might facilitate its plasticity is the interdependence of the components. This includes transient changes, lasting from seconds to minutes, brought on by channel modulation, in addition to prolonged changes (hours to days) indicating changes in morphology (Petersen et al., 2016).

Over the past decade, AIS plasticity has been established as an important homeostatic process and modulator of neuronal excitability across diverse experimental models. In vivo, sensory deprivation drove an increase in the AIS length and excitability in the auditory and somatosensory cortex even in adult animals (Kuba et al., 2010). In hippocampal neuronal cultures, on the other hand, chronic depolarization, optogenetic stimulation, or suppression of M-type potassium currents led to a distal shift of the AIS, along with changes in AP threshold (Grubb & Burrone, 2010; Lezmy et al., 2017). On an even faster scale, Amélie Fréal recently showed a rapid endocytosis of voltage-gated sodium channels at the distal aspect of the AIS in response to NMDA receptor activation, a process that occurs within minutes and consequently raises the action potential threshold (Fréal et al., 2023).

If one conclusion can be drawn from these findings, it would be the significance of AIS plasticity across multiple cellular contexts for the refinement of neuronal activity in a flexible and input-dependent manner. This concept also applies to the context of neurological disorders, where disruptions in AIS structure and dynamics may arise in response to intrinsic alterations in its constituent ion channels, and have been also implicated in neurodegenerative diseases such as Alzheimer's (Li et al., 2024), an idea that informs the rationale of the questions addressed in this study.

1.5 Synergistic Ion Channel Function at The Axon Initial Segment

1.5.1 $Na_V1.2$ Versus $Na_V1.6$

The AIS, as described earlier, is densely populated with all the key players associated with AP, such as Na_V, K_V, Na^+/K^+ pumps and leak channels (Leterrier et al., 2015). In cortical pyramidal neurons, it is home to two voltage-gated sodium channel subtypes, $Na_V1.2$ and $Na_V1.6$. One can picture them as a dynamic explosive duet that supports the Na^+ inward during the rising phase and onset of APs. Yet, these channels are distinguished by their spatial distribution and their biophysical properties, both contributing to the unique excitability of the AIS (**Figure 1.9**).

Hu et al. (2009), using immunostaining, demonstrated that $Na_V1.2$ is enriched in the proximal AIS while $Na_V1.6$ is the predominant isoform between 30 and 50 μm from the soma,

a region that corresponds to what Stuart et al. (1997a) previously identified in vivo as the site of AP initiation. In line with this spatial expression, Colbert and Pan (2002) reported that sodium channels that are located more distally from the soma activate at more hyperpolarized potentials, by approximately 10 mV than somatic ones, resulting in the capacity of more distal channels to generate APs.

To accurately characterize the distinct properties of each isoform, Rush et al. (2005) co-expressed TTX-resistant forms of $Na_V1.2$ and $Na_V1.6$ in dorsal root ganglion neurons. $Na_V1.6$ demonstrated a significantly more hyperpolarized voltage of activation and a larger persistent current relative to $Na_V1.2$. This persistent current, found greatest in the AIS (Astman et al., 2006), provides a steady subthreshold depolarization that influences the threshold for spike initiation (Kole and Stuart, 2007). Physiologically, these advantages render $Na_V1.6$ more adapted for AP initiation and repetitive firing (Spratt et al., 2021). Despite this, in an interesting in vivo study where $Na_V1.6$ was genetically deleted from excitatory forebrain neurons, Katz et al. (2018) reported that $Na_V1.2$ underwent redistribution along the entire AIS and maintained the initiation of APs. Notably, the hyperpolarized activation threshold, which is a defining characteristic of $Na_V1.6$, was preserved. This finding highlighted that the molecular environment of the AIS confers key functional properties to any subtype of sodium channel expressed there. The authors concluded that, possibly, an additional advantage is mediated by the precise spatial localization of $Na_V1.2$ and $Na_V1.6$ in the AIS. This is noteworthy as it complements the studies by Colbert and Pan (2002) and Kole et al. (2008), which showed that lower AP threshold recorded at the AIS, reflects not only the high density of sodium channels and their intrinsic gating properties, but also the AIS-specific regulatory environment.

As for $Na_V1.2$ channels, depletion caused, in developing excitatory neurons, but not in adult ones, an impaired AP initiation (Spratt et al. 2021). Furthermore, the absence of $Na_V1.2$ led to reduced AP backpropagation into dendrites, confirming the localization-based hypothesis proposed by Hu et al. (2009): that $Na_V1.2$, being predominant at the proximal AIS, is better adapted to facilitate the AP backpropagation toward the soma and dendrites.

Beyond that, another major role of $Na_V1.2$, in regulating the AP shape through its exclusive permeability to calcium ions in the AIS, was recently brought to light (previously elaborated in 1.4.2). It has been demonstrated using targeted pharmacological manipulation combined

with computational NEURON modeling that $Na_V1.2$ channels are functionally coupled to BK channels at the AIS. Indeed, $Na_V1.2$ mediates an early Ca^{2+} current that mimicks the kinetics of Na^+ current, which further triggers the activation BK CAKCs channels. This interplay between $Na_V1.2$ mediating the AP rise and BK with their role in regulating the peak and repolarizing phase of AP, is considered a key determinant of the shape of the AP waveform at its generating site (Filipis et al., 2023).

Collectively, these findings convey a model whereby $Na_V1.2$ and $Na_V1.6$ work in tandem, with unique biophysical properties and spatially segregated expression patterns, to define the peculiar excitability of the AIS.

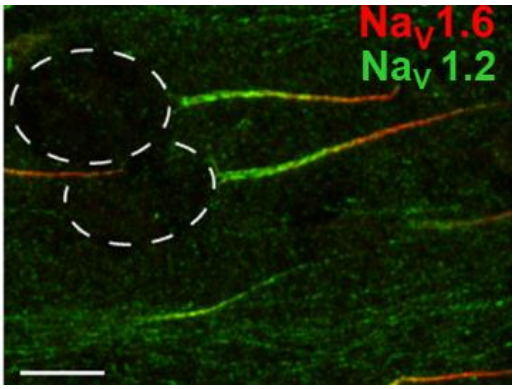

Figure 1.9 **Differential compartmentalization of $Na_v1.2$ and $Na_v1.6$ along the axon initial segment of cortical neurons**. Maximum intensity projection of a 5-µm-thick confocal z-stack showing immunohistochemical staining of voltage-gated sodium channel isoforms in the neocortex. $Na_v1.2$ (green) is enriched in the proximal AIS, while $Na_v1.6$ (red) are more abundant in the distal AIS. Dashed lines indicate the neuronal cell bodies. Scale bar: 10 µm. *Adapted from Grubb et al. (2011)*

1.5.2 Potassium Channels and Calcium Channels

Multiple voltage-gated potassium channels are anchored at the AIS. They play a critical role in repolarizing the AP and determining the duration and the shape of the spikes, as well as in regulating the resting membrane potential and setting the firing threshold (Garrido, 2023; Kole et al. 2007). AnkG and sodium channels are the first to be identified during the AIS development, while potassium channels emerge subsequently during AIS maturation (Debanne & Garrido, 2018; Jenkins & Bennett, 2001; Sanchez-Ponce et al., 2012).

The primary VGKC in the AIS of most neuronal types is the low-threshold K_V1 subtype referred to the delayed rectifier potassium channels (IK). Immunocytochemical

investigations revealed a higher presence of $K_V1.1$ and $K_V1.2$ channels in the AIS (Dodson et al., 2002; Goldberg et al., 2008; Lorincz and Nusser, 2008). In accordance, direct patch-clamp recordings from AIS of cortical pyramidal neurons have shown a high density of dendrotoxin (DTX)-sensitive, rapidly activating, but slowly inactivating K_V1-type currents at the AIS of cortical pyramidal neurons (Shu et al., 2007). Further, Kole et al. (2007) reported that K_V1 channels are expressed, with a 10-fold increase in channel density over the first 50 μm of the AIS. Another member of the delayed rectifier VGKCs, $K_V2.1$, was identified in low densities over the whole AIS (King et al. 2014).

In addition to IK K^+ channels, antibody labeling also revealed that the AIS distal region in pyramidal neurons exhibits elevated concentrations of K_V7 channels, particularly $K_V7.2$ and $K_V7.3$ channels (Pan et al., 2006). These channels are more compartmentalized distally, and generate the slow activating and non-inactivating M-type current (Battefeld et al. 2014; Brown and Passmore, 2009).

Moreover, A-type K^+ channels, mainly $K_v4.2/K_v4.3$, with contributions from $K_v1.4$ and $K_v3.3/K_v3.4$, were rarely seen in axonal compartments, while they were more abundant in somatodendritic regions. These channels generate a current marked by rapid inactivation rates, which contributes to controlling repetitive firing frequencies and AP backpropagation (Colbert & Pan, 2002; Guan et al., 2011; Gutman et al., 2005).

BK channels, on the other hand, are expressed in the AIS of cortical pyramidal neurons at lower densities than other channels, such as K_v1 (Trimmer, 2015). They critically modulate the AP repolarization and are of great importance, being the downstream target for $Na_V1.2$-mediated Ca^{2+} current; however, the molecular basis for the interaction between $Na_V1.2$ and BK channels remains ambiguous (Echevarria-Cooper et al., 2022; Filipis et al., 2023).

Besides $Na_V1.2$, routes for Ca^{2+} influx in the AIS are also provided by the classical mediators: the VGCCs. Yet, information regarding their distribution and localization in the AIS is limited. In L5 cortical neurons, $Ca_V2.1$ (P/Q-type) and $Ca_V2.2$ (N-type) channels, both high-voltage activated subtypes, have been identified in this compartment, where they influence spike and burst timing and modulate the AP threshold (Garrido, 2023; Yu et al., 2010).

To sum up, the unique AIS function as an AP initiation zone relies on the interplay of the above-mentioned VGIC families rather than the role of individual conductances; a synergy

that coordinates the phases of AP, and carries the integrity of neuronal firing. Within this complex and tightly regulated microenvironment, $Na_V1.2$ serves as a central player in generating APs, as it modulates their rising phase and the subsequent neuronal output. Therefore, it is not surprising that mutations affecting $Na_V1.2$ are disrupt this delicate ionic balance, and drive repercussions that permeate the entire electrophysiological framework of the neuron. In the last section of this introduction, I will explore how such perturbations lead to channelopathies, charting the path from molecular dysfunction to distorted neuronal activity and neurological disorders.

1.6 Channelopathies in The Nervous System

1.6.1 Overview: Classifications and Clinical Spectrums

A wide range of neurological disorder affecting both the central and peripheral nervous system stems from disruptions in ion channels, and are referred to "channelopathies". Considering the fundamental functions driven by ion channels, deeply examined in previous sections, in maintaining the excitable identity of our nervous system, it is evident that their dysfunction leads to erroneous electrical signaling and a broad spectrum of diseases with pathogenic mechanisms, way far from straightforward, involving alterations of ion channels gating, assembly, trafficking, abundance, interaction with other proteins, or even, ion selectivity (Kullmann, 2010; Männikkö & Kullmann, 2024; Spillane et al., 2015).

Etiologically, neurological channelopathies can be widely classified as acquired or genetic (inherited). Acquired channelopathies might arise from exposure to toxins or alterations in ion channel transcription, trafficking or assembly; but their primary cause is autoimmune disease of the central or peripheral nervous system, in which autoantibodies target specific ion channels and block their activities. These acquired forms often manifest in later life stages (Männikkö & Kullmann, 2024; Rajakulendran & Kullmann, 2013).

Genetic channelopathies, in contrast, represent a broad branch of disorders that tend to arise early in life as a result of genetic or de-novo mutations in ion channel subunits (**Figure 1.10**). Some occur exclusively during a limited developmental period, such as self-limiting neonatal seizures. While others may remain unresolved or evolve over time. In certain cases, discrete

(episodic) attacks lead to a stable or progressive impairment, as observed in episodic ataxia and familiar migraine syndromes (Kullmann, 2010; Spillane et al., 2015).

Since the channelopathy term was introduced, roughly three decades ago, the inherited CNS channelopathy field has been rapidly expanding, considering the large number of genes encoding ion channel subunits, their highly specific and variable expression profile across neuronal populations, in addition to the highly possible alternative splicing these channels undergo (Lipscombe et al., 2013).

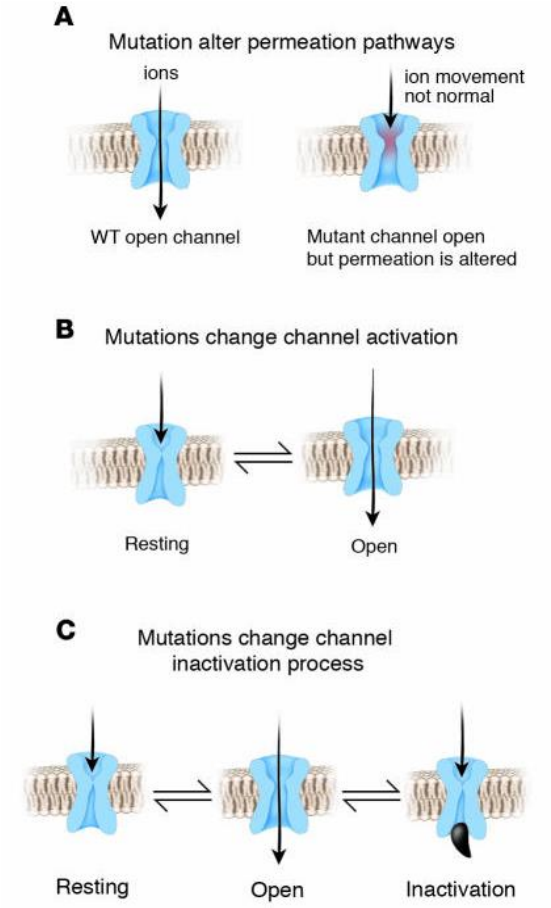

Figure 1.10 **Mechanisms by which ion channel mutations disrupt function and contribute to disease** Inherited mutations in ion channel genes can impair function through several mechanisms. ***(A)*** Mutations may alter the permeation pathway, reducing or aberrantly modifying ion flux despite channel opening. ***(B)*** Mutations may affect activation gating, impairing the transition from the resting to the open state. ***(C)*** Mutations may alter inactivation, destabilizing the non-conducting state and increasing persistent current. *Adapted from Kass (2005)*

1.6.2 Genetic Channelopathies of The CNS

Though individually rare and underdiagnosed, mutations associated with genetic channelopathies are often monogenic, with an estimated prevalence of 35 per 100,000 in neurology (Jurkat-Rott et al., 2010), and capable of disrupting the channel kinetics by touching any of the stages of ion channel biogenesis from transcription, to mRNA processing,

splicing, translation, folding and trafficking, as well as subunit assembly; with a diverse spectrum of clinical outcomes (Spillane et al., 2015; Van Loo & Becker, 2020).

The classification of genetic channelopathies is based either on the type of channel affected, or the particular region of nervous system implicated. It has been shown that different clinical phenotypes may emerge from mutations in the same channel (Verriello et al., 2025). Ongoing extensive research, aided by advances in electrophysiology, genetic tools and high-throughput genomic studies, has greatly enriched our knowledge about the different channelopathies and their clinical features (Harraz & Delpire, 2023). In what follows, I will briefly summarize the different genetic channelopathies in the CNS to illustrate the diversity of phenotypes associated to mutations of specific ion channel genes.

Sodium channel mutations in $Na_V1.1$ (*SCN1A*) and $Na_V1.6$ (*SCN8A*) alpha-subunit genes were tightly linked to syndromes that range from benign familial neonatal-infantile seizures to generalized epilepsy with febrile seizures plus (GEFS+), or more severely, Dravet syndrome and developmental epileptic encephalopathies. Besides, the β1 subunit gene SCN1B implications in GEFS+ phenotypes were also reported (Kullmann, 2002). Potassium channelopathies, on the other hand, involve *KCNQ2*, *KCNQ3*, and *KCNB1* genes, whose pathogenic variants drive the bulk of neonatal seizures, early-onset epileptic encephalopathies, and intellectual deficits (De Kovel et al., 2017; Miceli et al., 2015; Millichap et al., 2016). Other potassium channel mutations, affecting KCNMA1, KCNC3, KCND3, KCNJ11, are linked to cerebellar ataxias and early absence epileptic conditions (Spillane et al., 2016; Verriello et al., 2025). Last, mutations in calcium channels in CACNA1A are responsible of overlapping conditions such as familial hemiplegic migraine, episodic ataxia type 2, spinocerebellar ataxia type 6, and possibly absence epilepsy (Kullmann & Waxman, 2010).

The next section tackles the *SCN2A*, a gene whose dysfunction underlies a range of neurodevelopmental phenotypes, and deemed a central focus of this thesis.

1.6.3 *SCN2A*-Related Disorders

Upon its initial association with disease in 2002, The Sodium Channel Voltage-Gated Type II Alpha (*SCN2A*) gene has evolved to gain a major clinical relevance in neurodevelopmental disorders (Heron et al., 2002). Residing on the long (q) arm of chromosome 2 at position 24.3, the human *SCN2A* gene spans over 150 kilobases between the sodium channel gene *SCN3A* and the nuclear protein gene *CSRNP3*; it includes 27 exons, and encodes the 2005 amino-acid $Na_V1.2$ alpha subunit (Abbott et al., 2024; Sanders et al., 2018). Although its fundamental role in neuronal excitability has long been explored, it is the increasingly complex clinical landscape of *SCN2A* disorders that has brought this gene to the forefront of neurogenetics. In their 2018 review, Sanders et al. reported more than 250 heterozygous pathogenic variants associated with neurodevelopmental conditions. However, recent databases list more than 1,250 *SCN2A* variants, and estimate the birth of over 400 affected individuals each year in the United States alone (Sanders et al., 2018; Simple ClinVar Broad Institute). In addition, large-scale sequencing studies have consistently ranked *SCN2A* among the top de novo risk genes for neurodevelopmental disorders (Gillentine et al., 2022).

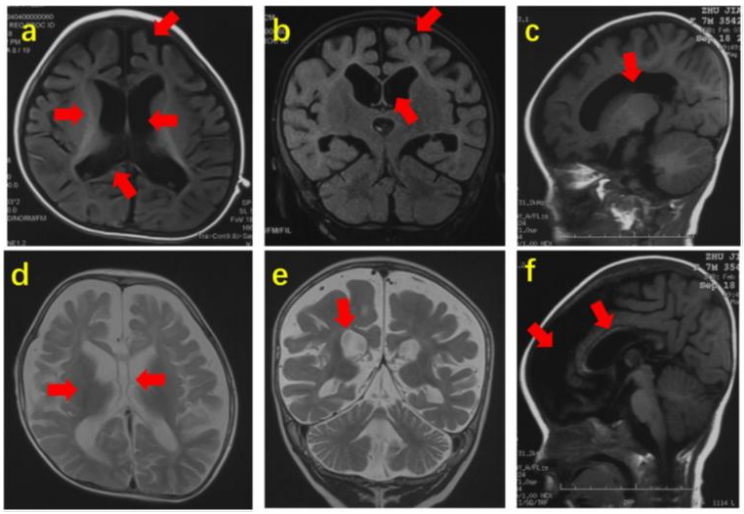

Figure 1.11 **Brain MRI abnormalities in patients with SCN2A variants**. ***(a, b)*** Axial and coronal T1-weighted images of a patient (22 months) show agenesis of the corpus callosum, delayed white matter myelination, dysplasia of the frontotemporal lobes, and ventricular enlargement. ***(c, f)*** Sagittal T1-weighted images of another patient (7 months) reveal similar features, including corpus callosum agenesis, frontotemporal dysplasia, and enlarged lateral ventricles. ***(d, e)*** Axial and coronal T2-weighted images of a third patient (12 months) confirm callosal agenesis, white matter

hypomyelination, and ventricular enlargement. Red arrows indicate the structural abnormalities. *Adapted from Zeng et al. (2022)*

1.6.3.1 Functional Spectrum Classification

The growing spectrum of defined *SCN2A* variants has led to the need to a functional classification, in particular to distinguish between gain-of-function (GoF) and loss-of-function (LoF) mutations. This binary framework, extensively adopted by the literature, was supported by growing electrophysiological evidence associating the effects of *SCN2A* variants to two main categories of clinical phenotypes (Abbott et al., 2024; Echevarria-Cooper et al., 2022). Studies such as those by Ben-Shalom et al. (2017) and Sanders et al., (2018) have contributed to delineating this classification by demonstrating that alterations in variants linked to early-onset epilepsy tend to increase $Na_V1.2$ activity, whereas those linked to intellectual disability (ID) or autism spectrum disorder (ASD) tend to decrease it.

One way to address this dichotomy is via the effect of the mutation on the voltage-dependence of $Na_V1.2$ and its kinetics. Mutations that shift the activation to more hyperpolarized potentials, or accelerate the recovery from inactivation could lead to increased $Na_V1.2$ activity and thus greater neuronal excitability. These features are commonly associated to GoF mutations. By contrast, mutations that bring activation to more depolarized potentials or destabilize the open state generally result in decreased neuronal excitability, consistent with a LoF profile (Abbott et al., 2024).

Therefore, the clinical phenotypes emerging from *SCN2A* mutations are best understood as illustrated along a bidirectional scheme, ranging from complete LoF to strong GoF (**Figure 1.12A**). At the extreme LOF end, homozygous *Scn2a*$^{-/-}$ knockout mice die perinatally (Planells-Cases et al., 2000; Shin et al., 2019). Partial LoFs, including protein-truncating or missense mutations, often result in haploinsufficiency, and are typically correlated with ASD and ID, with mild or no epilepsy at all (Echevarria-Cooper et al., 2022). As the severity of LoF diminishes, phenotypes may preferentially change to a later-onset of epilepsy or milder ND traits (Ben-Shalom et al., 2017; Berecki et al., 2022; Wolff et al., 2017).

At the opposite side of the spectrum, mild GOF mutations are linked to benign familial neonatal-infantile seizures (BFNIS). More pronounced GoF are further associated to early-onset developmental and epileptic encephalopathies (DEE) such as Ohtahara syndrome.

The wild-type functional level sits between these two extremes, where both hyper and hypoactivity imply an abnormal function of $Na_V1.2$, leading to pathological conditions (Léna & Mantegazza, 2019).

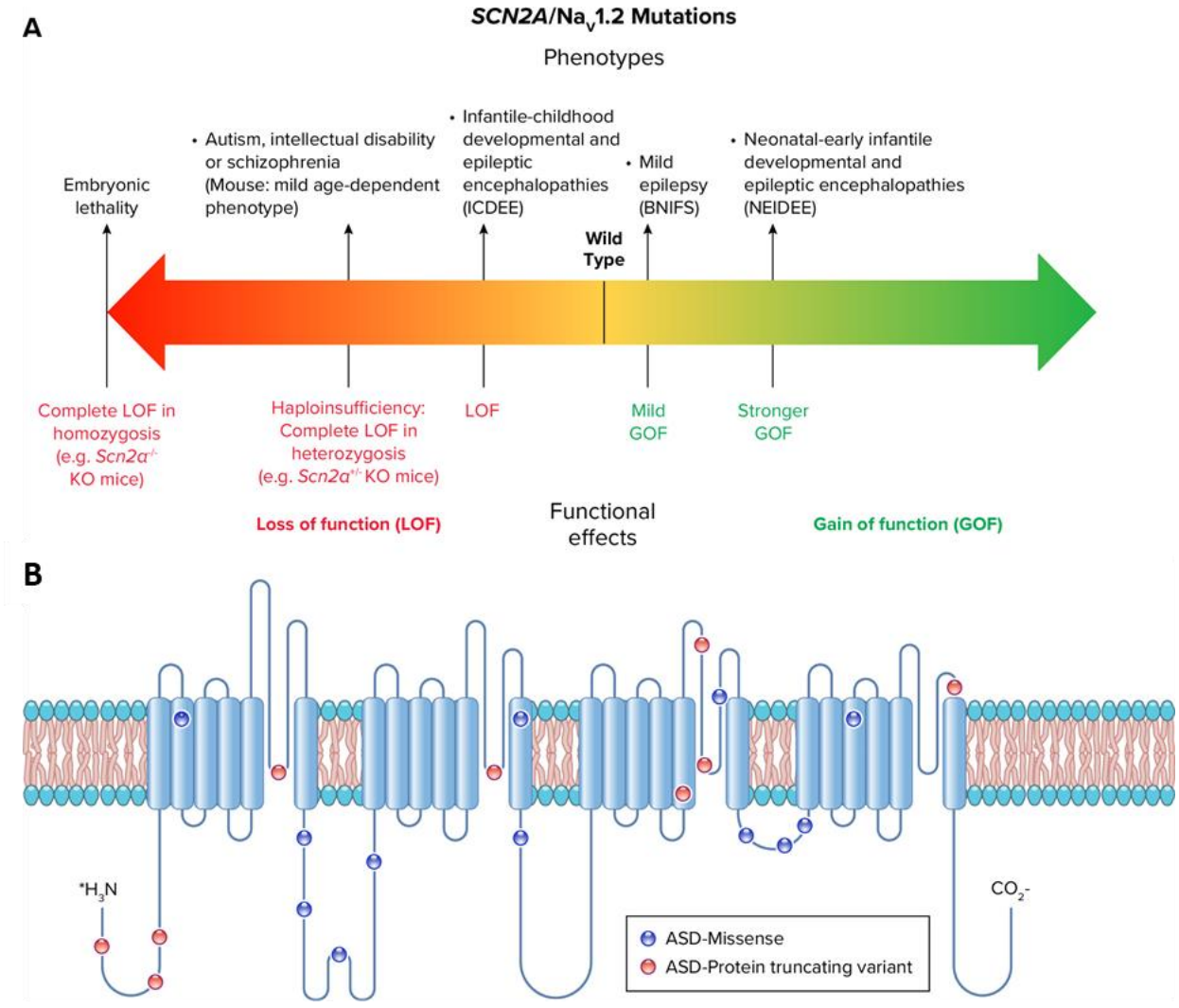

Figure 1.12 **Spectrum of *SCN2A*/$Na_V1.2$ mutations and their clinical association.** ***(A)*** *SCN2A* mutations span a spectrum from complete loss-of-function (LoF) to strong gain-of-function (GoF), with corresponding phenotypic manifestations. Severe GOF mutations result in neonatal–early infantile developmental and epileptic encephalopathies (NEIDEE), while milder GOF mutations generally lead to benign neonatal-infantile familial seizures (BNIFS). LOF mutations cause infantile–childhood developmental and epileptic encephalopathies (ICDEE). Haploinsufficiency, or heterozygous complete LOF, is associated with autism spectrum disorder (ASD), intellectual disability (ID), and schizophrenia, typically without seizures. Homozygous LOF is lethal in mice at embryonic stages. ***(B)*** Schematic representation of the topology of $Na_V1.2$ channel showing the map of *SCN2A* variants identified in ASD cases. 12 Missense mutations (red) and 9 protein-truncating

variants (blue) are found in both transmembrane and cytoplasmic domains. *Adapted from Mantegazza et al. (2021)*

1.6.3.2 Limitations of The GoF/LoF Model

Although the GoF/LoF paradigm has been very useful for shaping therapeutic approaches and mapping general genotype–phenotype associations, it cannot fully capture the phenotypic heterogeneity present in *SCN2A*-related disorders.

Remarkably, between 20-30% of patients diagnosed with loss of function (LoF) mutations suffer from seizures despite an overall decrease in $Na_V1.2$ activity (Zhang et al., 2021). Recent studies suggest that compensatory mechanisms can take place and paradoxically increase neuronal excitability within the context of $Na_V1.2$ deficiency. For instance, Spratt et al (2021) reported high frequency burst firing in $Na_V1.2$ knockout neurons due to a defective repolarization, even though the sodium conductance was reduced. By the same token, Zhang et al (2021) demonstrated that severe $Na_V1.2$ loss in adult mice results in an intrinsic hyperexcitability, and they attributed this effect to a downregulation of potassium channels, specifically a reduced $K_V1.1$ channel activity. Further, assuming that all LoF mutations recapitulate a simple haploinsufficiency remains debatable. The *Scn2a*$^{+/K1422E}$ mouse model, associated with developmental delay and ASD, offers a clear example of this complexity and presents a nonclassical biophysical profile of LOF, including a larger Ca^{2+} permeability, decreased sensitivity to tetrodotoxin, and an impaired AP initiation in the AIS (Echevarria-Cooper et al., 2022).

Together, these observations challenge the rigidity of this GoF/LoF binary categorization and emphasize the significant contribution of other factors, including the developmental stage, the co-expression and regulation of ion channels, in modulating the phenotypic outcomes seen in $Na_V1.2$ channelopathies.

1.6.4 *SCN2A* Loss-of-Function Mutations in Autism

Autism spectrum disorder is a complex neurodevelopmental condition characterized, as per the diagnostic criteria of the most recent edition of the Diagnostic and Statistical Manual of Mental Disorders (DSM-5-TR), by enduring deficits in communication and social interaction, coupled with restricted and repetitive patterns of behaviors and interests, which manifest during early developmental period and result in substantial functional impairments. The clinical profile of ASD exhibits a significant heterogeneity in severity and often co-occurs with intellectual disabilities or language impairments (DiStefano et al., 2025).

Over the past two decades, ASD has been increasingly diagnosed; recent estimates indicate that 1 in 31 children in the United States and 1 out of 100 children globally are affected. A part of the growth in prevalence is attributed to greater awareness, extended diagnostic criteria, and improved access to evaluations (Shaw et al., 2025; Zeidan et al., 2022). The etiology of ASD is multifactorial, defined by a tangled interplay between environmental and genetic factors.

SCN2A was first correlated with ASD through an exome-sequencing study in 2012 (Sanders et al., 2012); and of all candidate genes, *SCN2A* is one of the most consistently validated risk genes for ASD. It is currently classified as a category one ASD gene in the SFARI Gene database and, in terms of gene-level evidence, is one of the best supported with an EAGLE score of 109.3 (a metric expressing the probability of a causal role in ASD) (DiStefano et al., 2025; SFARI Gene). However, despite this strong genetic correlation, *SCN2A*, a gene encoding a voltage-gated sodium channel, was regarded atypical in ASD pathophysiology at a time when research largely prioritized synaptic proteins or regulatory genes in the neuronal nuclei (Abbott et al., 2024; Fu et al., 2022).

This perspective has been challenged by large-scale exome meta-analyses such as that by Satterstrom et al. (2020), which analyzed nearly 12,000 ASD cases and identified 102 genes with powerful genetic evidence. *SCN2A* was among the highest ranked genes, based on its burden of both protein-truncating and missense variants (**Figure 1.13**) (Satterstrom et al., 2020). Further supporting its clinical relevance, a recent study in May 2025 pooled data from 11 cohorts with a total of 695 ASD individuals, and reported that mutation in *SCN2A* were identified in 10.8% of cases, with de-novo missense mutations representing the majority

(77%). These variants and consequent phenotypes are typically grouped as *SCN2A* LoF mutations that dampen the activity of $Na_v1.2$ channels and impair the neuronal excitability in different means (DiStefano et al., 2025).

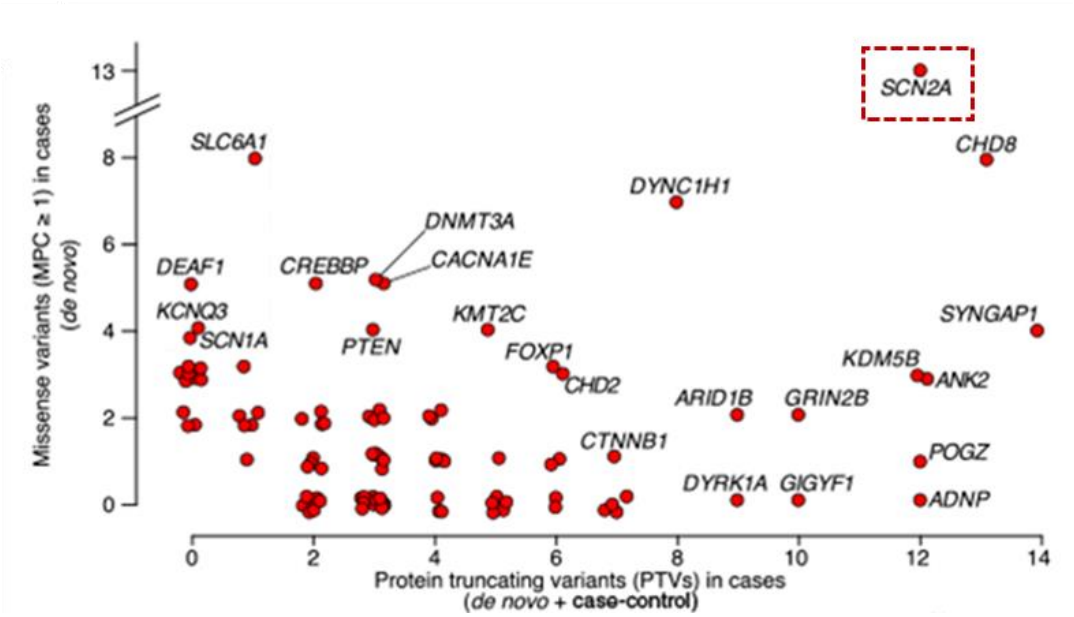

***Figure 1.13 SCN2A* highlighted among autism-associated genes.** Scatterplot showing the number of truncating variants (x-axis) and missense variants (y-axis) identified in ASD individuals across a large cohort of nearly 12,000 ASD cases. Red dots indicate individual genes associated with ASD; selected genes are labeled. *SCN2A* is highlighted (dashed box) to denote its significant position based on the combined burden of the two types of variants together. *Adapted and modified from Satterstrom et al. (2020)*

1.6.4.1 Phenotypes and Experimental Models of $Na_v1.2$-LoF

Although there is no specific syndrome for *SCN2A*-associated ASD/ID, it does appear that some behavioral patterns are shared. Sanders et al. (2018) reported that affected children tend to be placid, exhibiting a delayed social development with low eye contact and rarely initiate social interaction. Some repetitive behaviors, such as chewing objects or hand movements, are also common. They also found that motor abnormalities might be present but less pronounced than social difficulties, as well as additional comorbidities, including sleep disturbances, gastrointestinal problems, cortical visual impairment, and altered pain perception, creating a broad characteristic behavioral profile.

Mouse models were generated as an effective tool to understand $Na_V1.2$ deficiency-related pathophysiology. Mouse genetics allow to study not only *SCN2A* haploinsufficiency, which

mimicks the condition resulting from heterozygous LoF variants, but also genetic conditions found in humans. Although constitutive knockout is a lethal model, the heterozygous KO (*Scn2a*$^{+/-}$) and gene-trap models allowed partial Na$_V$1.2 deficiency to be investigated. Gene-trap mice, with approximately 75% transcript loss, served to reveal more pronounced phenotypes that were not easily apparent in heterozygous *Scn2a*$^{+/-}$ mice including elevated anxiety, disrupted nesting, and fractured sleep, implicating a broader network dysfunction (Planells-Cases et al., 2000; Spratt et al., 2021; Zhang et al., 2021). In contrast, *Scn2a*$^{+/-}$ mice exhibited a more selective behavioral phenotype that varies with age. Massimo Mantegazza group has reported that juvenile *Scn2a*$^{+/-}$ mice display more features reflecting aspects of *SCN2A*-related ASD, such as reduced ultrasonic vocalizations, stereotyped and repetitive behaviors, altered emotional responses, as well as memory deficits. These age-specific traits, which coincide with those reported in some young autistic patients carrying *SCN2A* mutations, offered a valid framework for using the heterozygous *SCN2A* KO models to examine the potential pathophysiological deficits linked to Na$_V$1.2 LoF during adolescent and juvenile developmental stages (Léna & Mantegazza, 2019).

Recently, a new knock-in mouse model carrying the human L1314P missense mutation in SCN2A was generated to reproduce a clinically identified variant associated with severe non-syndromic autism spectrum disorder (Simonti, 2025a). In vitro assays, this mutation has been characterized as negative-dominant, suggesting that its pathogenic mechanism may extend beyond a simple reduction in Nav1.2 function. Moreover, behavioral analyses of *Scn2a*$^{L1314P/+}$ mice, detailed in the doctoral thesis of Martina Simonti (Simonti, 2025b), revealed repetitive behaviors, hyporeactivity to aversive stimuli, and altered decision-making, indicating persistent ASD-relevant phenotypes into adulthood. At the neuronal level, impaired excitability was reported in immature prefrontal pyramidal neurons, together with reduced membrane expression of Na$_V$1.2 despite unchanged mRNA levels, suggesting altered protein processing or trafficking. This knock-in model complements heterozygous knockout approaches by allowing the functional consequences of a clinically identified SCN2A variant to be examined directly.

1.7 Open Research Questions Addressed in This Thesis

Despite the well-established clinical relevance and the advances made through genetic and behavioral studies, LoF mutations in the *SCN2A* gene, strongly tied to autism and intellectual disability, continue to raise fundamental questions about the subcellular level mechanisms of these neurodevelopmental disorders. This thesis is motivated by the gaps in current knowledge and aims to explore the functional impact of *SCN2A* LoF mutations using a combination of advanced electrophysiological and imaging approaches in genetically modified mouse models. In this section I outline the open research questions that guided the subsequent chapters.

First, the compartment-specific consequences of $Na_v1.2$ loss are not fully mapped. Within the AIS, proximal and distal domains exhibit distinct functional properties, yet how *SCN2A*-related disorders differentially alter excitability in these subregions remains unresolved. Likewise, the relative effects of $Na_v1.2$ dysfunctions at the soma versus dendrites has not been systematically characterized, despite evidence of paradoxical outcomes. In Chapter 3 we explore this question by combining whole-cell patch-clamp recordings with high-speed Na^+, Ca^{2+}, and V_m imaging at the AIS to dissect ionic mechanisms underlying AP initiation and waveform shape at proximal and distal sites, and by assessing single AP generation at the soma. Chapter 4 extends this analysis to the apical dendrite, where short trains of APs were paired with Ca^{2+} imaging in the tuft to test directly whether $Na_v1.2$ deficiency alters dendritic calcium electrogenesis. Together, these experiments allow a multi-compartmental view of how $Na_v1.2$ perturbations reshape excitability.

Second, phenotypes associated with *SCN2A* mutations are highly age-dependent and the developmental course of these outcomes is poorly delineated. *Scn2a*$^{+/-}$ mice display hypoexcitability in early postnatal stages (Spratt et al., 2019), yet adult models can develop absence seizures (Ogiwara et al., 2018). This implies that associated deficits may be transient or evolving. Crucially, the juvenile window (P21-P40), a critical period for cortical refinement, may harbor intermediate or compensatory states not captured at P4 or P60. Across AIS, somatic, and dendritic recordings, we tracked excitability throughout this

juvenile period, in order to identify transient, stable, or progressive traits that define the developmental trajectory of $Na_v1.2$ loss of function.

In addition, as emphasized in earlier sections, neurons adapt to chronic channel loss through homeostatic mechanisms involving both structural and molecular adjustments. However, the extent of such responses in *SCN2A* mutants is poorly defined. AIS plasticity and ion channel remodeling are anticipated, and could mask or even reshape the primary consequences of $Na_v1.2$ loss. Distinguishing direct channel effects from regulatory feedbacks is therefore an open challenge. Chapter 3 approaches this issue by integrating targeted pharmacology of K^+ channels with V_m imaging to test the contribution of altered repolarization to the observed phenotypes, while Chapter 4 examines whether the changes in somatodendritic excitability reflect AIS-level alterations or suggest the engagement of additional adaptive pathways.

Furthermore, a persistent obstacle in studying $Na_v1.2$ is the lack of isoform and compartment specific pharmacological tools. Chapter 5 presents a proof-of-principle study in wild-type (WT) mice, where local application of the VGNC activator AaH-II allowed probing subcellular $Na_v1.2$ contributions at its site of physiological enrichment, the AIS. This approach demonstrates the methodological potential of compartment-specific pharmacology for dissecting $Na_v1.2$ function.

Finally, the conventional GoF versus LoF dichotomy is too coarse to capture the heterogeneous spectrum of *SCN2A* phenotypes. Several variants do not conform to simple categorization, even LoF classified mutations can sometimes produce gain-like outcomes at the network level (Spratt et al., 2021). By comparing *Scn2a*$^{+/-}$ (KO) and *Scn2a*$^{+/L1314P}$ (KI) models of autism, this thesis tackles whether different molecular deficits lead to overlapping alterations in excitability or instead produce unique physiological profiles. This comparative strategy helps separate mutation-specific features from general principles of $Na_v1.2$ dysfunction.

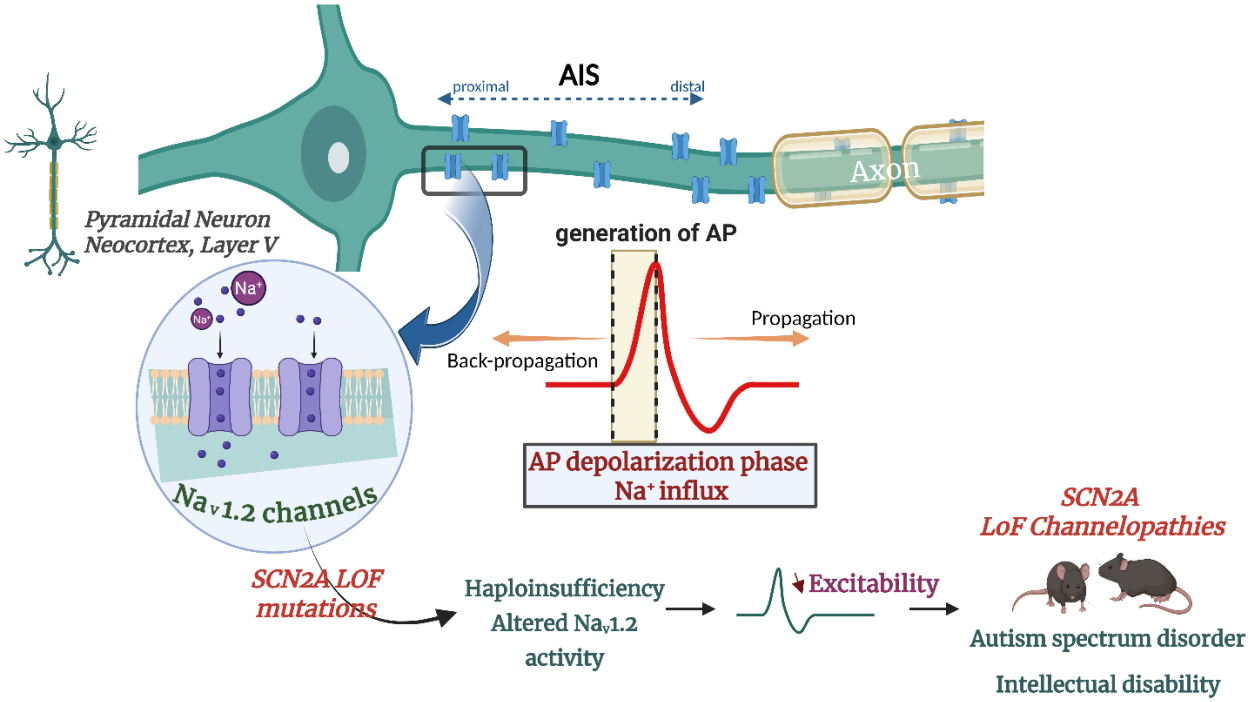

Figure 1.14 **$Na_V1.2$ at the AIS: from channel physiology to *SCN2A* channelopathies.** Schematic illustrating how $Na_V1.2$ channels, enriched in the proximal axon initial segment (AIS) of Layer 5 pyramidal neurons, contribute to action potential initiation and back-propagation. *SCN2A* loss-of-function mutations can lead to haploinsufficiency, reduced excitability, and are associated with neurodevelopmental disorders such as autism and intellectual disability. This figure recapitulates the physiological and pathological framework explored in this thesis. *Created with BioRender.com*

2

METHODOLOGY

2.1 EXPERIMENTAL ANIMAL MODELS AND ETHICAL APPROVAL 57
2.2 CORTICAL SLICE PREPARATION 60
2.3 ESTABLISHING WHOLE-CELL PATCH IN CORTICAL NEURONS 61
2.3.1 Selection of Optimal Brain Slices and Healthy Pyramidal Neurons 61
2.3.2 Whole-Cell Patch Clamp Configuration 62
2.4 OPTICAL IMAGING 63
2.4.1 The Imaging System 63
2.4.2 Fluorescent Indicators 66
2.4.2.1 Sodium indicator 66
2.4.2.2 Voltage-Sensitive Dye 66
2.4.2.3 Calcium indicator 67
2.5 PHARMACOLOGICAL MODULATORS FOR ION CHANNELS 68
2.6 EXPERIMENTAL PROTOCOLS 69
2.6.1 Electrophysiology Coupled to Ultrafast Imaging in the AIS 69
2.6.1.1 Electrophysiological Protocol 69
2.6.1.2 Imaging Protocol 70
2.6.2 Electrophysiology Coupled to Calcium Imaging at the Apical Tuft 72
2.6.3 Electrophysiology Without Imaging 74
2.6.3.1 Single Somatic Action Potential 74
2.6.3.2 Burst of Three Action Potentials 75
2.6.4 Drug Delivery in Brain Slices 75
2.7 OPTICAL DATA ANALYSIS 76
2.7.1 Sodium Imaging 76
2.7.2 Voltage Imaging 77
2.7.3 Calcium Imaging 78
2.8 STATISTICAL DATA ANALYSIS 79
2.8.1 Overview of statistical tests 79
2.8.2 The Kolmogorov-Smirnov test 80

2.1 Experimental Animal Models and Ethical Approval

All experiments were conducted on cortical brain slices obtained from female C57BL/6 mice aged between postnatal day 21 and 40, spanning from early to late juvenile period. We exclusively used female mice in this study to reduce the variability due to sex differences in brain excitability. Three genotypes were included in this project: wild-type (WT; *Scn2a*$^{+/+}$), heterozygous knockout (KO; *Scn2a*$^{+/-}$), and heterozygous knock-in (KI; *Scn2a*$^{+/L1314P}$). All animals used in the experiments were generated from crosses between heterozygous *Scn2a*$^{+/-}$ males or heterozygous *Scn2a* $^{+/L1314P}$ males and wild-type *Scn2a*$^{+/+}$ females (**Figure 2.1**).

The *Scn2a*$^{+/-}$ and *Scn2a*$^{+/L1314P}$ mouse lines were provided by the laboratory of Massimo Mantegazza (Institut de Pharmacologie Moléculaire et Cellulaire, Université Côte d'Azur, Nice France), who engineered and behaviorally characterized these models to study $Na_v1.2$ loss-of-function mutations. *Scn2a*$^{+/-}$model recapitulates $Na_v1.2$ haploinsufficiency, and has been shown to display an age-dependent autistic phenotype with intellectual disability, including reduced ultrasonic vocalizations, repetitive behaviors, altered emotional responses, and memory impairments (Léna and Mantegazza, 2019). The *Scn2a*$^{+/L1314P}$ KI line carries a missense mutation, replacing a highly conserved leucine at position 1314 with proline, identified in a patient with autism spectrum disorder (ASD) and intellectual disability (ID), without epilepsy; consistent with a loss-of-function mechanism (Simonti, 2025b). Only wild-type C57BL/6 females used for breeding were either bred in-house or purchased directly from Charles River Laboratories.

All animals were housed in the accredited animal facility in the Biology Department of the Université Grenoble-Alpes (LBFA, Saint-Martin-d'Hères, France) under standard environmental conditions. After weaning on postnatal day 21 (P21), mice were group-housed in same-sex cages (4 to 6 animals per cage). Ear or phalangeal samples were collected from all animals and sent for genotyping at postnatal day 7 (P7). Genotyping analysis was carried out at the Genotyping Platform of the Neurocentre Magendie (Bordeaux Neurocampus, Bordeaux, France) following standard PCR-based protocols.

All animal procedures were reviewed and approved by the institutional ethics committee (D3842110001) and were carried out in accordance with the European Directive 2010/63/EU on the care, welfare, and treatment of animals used for scientific purposes, following the three R's principles (refinement, reduction, and replacement of animals wherever possible).

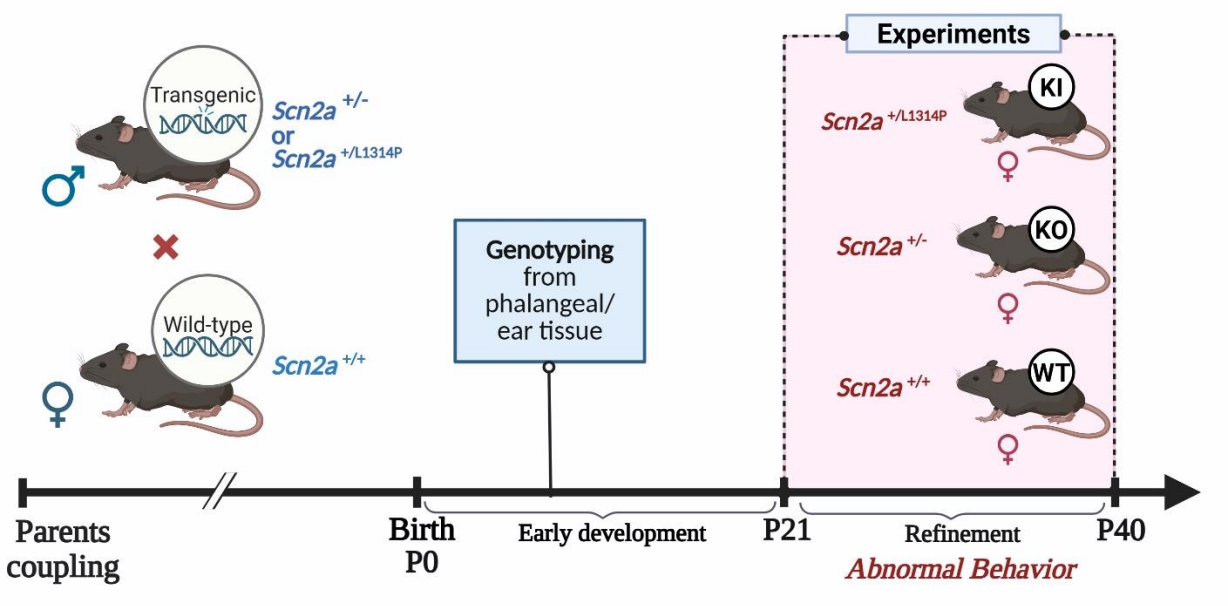

Figure 2.1 **Breeding, genotyping, and experimental timeline for *SCN2A* mouse models.** Heterozygous transgenic males (*Scn2a*$^{+/-}$ or *Scn2a*$^{+/L1314P}$) were crossed with wild-type females (*Scn2a*$^{+/+}$) to produce offspring of three genotypes: wild-type (WT), heterozygous knockout (KO), and heterozygous knock-in (KI). Genotyping was performed at postnatal day 7 (P7) on samples collected from ear or phalangeal tissue. All electrophysiology and imaging experiments were conducted between P21 and P40. This window corresponds to the period of refinement from early to late juvenile, during which abnormal behavioral phenotypes were described in both KO and KI mice. *Created with BioRender.com*

2.2 Cortical Slice Preparation

In all experiments, cortical slices were prepared using according to the protocol detailed in Blömer et al. (2021). Mice were anesthetized with isoflurane inhalation and rapidly decapitated using surgical scissors. To ensure cooling while maintaining neuronal viability, the brain was quickly extracted and immersed for three minutes in ice-cold carbogenated slicing solution (bubbled with 95% O_2 and 5% CO_2). The solution contained (in mM): 125 NaCl, 26 $NaHCO_3$, 2.5 $MgSO_4$, 3 KCl, 1 NaH_2PO_4, 0.5 $CaCl_2$, and 20 glucose.

The brain was then blotted dry on filter paper to drain off any excess fluid, and the cerebellum and olfactory bulbs were discarded. Hemispheres were separated by a midsagittal cut along the brain midline, and mounted onto a custom-made slicing platform with a 15° slope. This inclination is necessary to preserve the integrity of the entire L5PN trajectory, especially the axon initial segment (AIS), by ensuring their alignment parallel to the slicing plane (**Figure 2.2A**).

The hemispheres were glued, and the mounted stage was placed directly in the vibratome chamber (Leica VT1200, Wetzlar, Germany) filled with ice-cold slicing solution. Sagittal slices were cut at 350 µm thickness. A bent syringe needle was used to gently free the slice, and each slice was carefully transferred using a Pasteur pipette into a pre-warmed solution of oxygenated artificial cerebrospinal fluid (ACSF) at 37°C. The ACSF composition was (in mM): 125 NaCl, 26 $NaHCO_3$, 1 $MgSO_4$, 3 KCl, 1 NaH_2PO_4, 2 $CaCl_2$, and 20 glucose. Slices showing uninterrupted blood vessels traversing the cortex were particularly noted throughout the slicing, as an indication of a well-preserved neuronal morphology. Generally, two to three sagittal slices per hemisphere provided appropriate neurons for targeted recordings. After all slices were collected, they were incubated in the ACSF bath at 37°C for 30 minutes, then allowed to acclimate to room temperature for at least an hour prior to experiments.

2.3 Establishing Whole-Cell Patch in Cortical Neurons

2.3.1 Selection of Optimal Brain Slices and Healthy Pyramidal Neurons

Electrophysiology and imaging experiments were restricted to slices within six hours from their preparation. After incubation and recovery, slices were individually transferred to the recording chamber, gently secured with a harp grid (ALA Scientific), and continuously perfused with oxygenated extracellular solution (ACSF, 95% O_2 / 5% CO_2) at a stable flow rate of approximately 2 mL/min at 32-34°C.

A 10× objective was used to visualize the structural landmarks for an optimal slice. First, the slice was screened for intact blood vessels, running parallel to the slice surface, from cortical surface (dorsal end) toward the hippocampal side (ventral end), to verify appropriate slicing orientation and preserved cellular architecture. The somatosensory cortex was identified at this stage as the widest part of the cortex. Different cortical layers were identified and neuronal viability was assessed using IR-DIC visualization with a 60× water-immersion objective. By inspecting dead layer 5 pyramidal neurons (L5PNs), which appear darker and shrunken, and by using the trajectory of their apical dendrites as a guide, we checked the overall orientation of neurons within the layer 5 and made sure that the slice plane matched the orientation of the cortical column. Healthy L5PNs neurons were selected about 500–900 μm from the dorsal end of the cortex and 20–35 μm below the slice surface. This depth range was carefully chosen to preserve the morphological integrity of neuronal processes, which are more likely to be damaged in more superficial neurons, against poor optical clarity and higher light scattering encountered in deeper tissues.

A neuron was considered to be healthy if it had a large triangular soma, smooth membrane contours, and a nucleus that was barely visible with minimal contrast against the surrounding. Cells with a swollen soma or a clearly visible round nucleus were grouped as unhealthy and were therefore excluded due to signs of poor viability (**Figure 2.2B**).

2.3.2 Whole-Cell Patch Clamp Configuration

A DMZ puller (Martinsried, Germany) or a Sutter P-1000 Micropipette Puller (Sutter Instrument, USA) was used to pull patch pipettes from borosilicate glass capillaries (OD, 1.5 mm; ID, 1.17 mm; Harvard Apparatus) to a resistance of 4-5 MΩ when filled with intracellular solution. Pipettes were front-filled with dye-free intracellular solution containing (in mM): 125 $KMeSO_4$, 5 KCl, 8 $MgSO_4$, 5 Na_2-ATP, 0.3 Tris-GTP, 12 Tris-phosphocreatine, and 20 HEPES, pH adjusted to 7.3-7.35 with KOH. This internal solution was prepared in 50 mL batches, aliquoted into 1 mL vials, and stored at -20 °C to prevent ATP and GTP degradation. For imaging experiments, pipettes were backfilled with the same intracellular solution but containing additional fluorescent indicators (**Figure 2.2A**). Full information about indicator types and concentrations are listed in the corresponding optical imaging sections (2.4.2).

Prior to immersion in ACSF, a small positive pressure (~15 mbar) was applied in order to prevent dye leakage, to maintain tip integrity, and to limit exchange between the intra and extracellular fluids. Whole-cell patching was achieved using a 60× Olympus water immersion objective (NA 1.0, WD 2 mm), a Scientifica micromanipulator, and a motorized stage, that allowed the highly accurate visual positioning of the pipette under IR-DIC optics. Upon reaching the slice surface, a high positive pressure (~100 mbar) was applied and held as the pipette advances toward the soma, blowing away any tissue between the pipette tip and the targeted neuron. Pressure was released upon contact to establish a Giga-Ohm seal in voltage-clamp mode, with a holding potential of -60 mV and a junction potential compensated to 0 mV. Pipette resistance was monitored by injecting brief test pulses (-5 mV, 0.5 ms) throughout the approach. The position of the pipette was adjusted at this point, so the tip does not push the cell, and whole-cell configuration was achieved by applying a brief, strong suction (**Figure 2.2A**). Only cells with series resistance about 10 MΩ or lower, and whose value remained stable throughout the experiment were accepted for recordings. If there was a leak of the dye at the soma or in the extracellular space around it, the cells were rejected (**Figure 2.2C**).

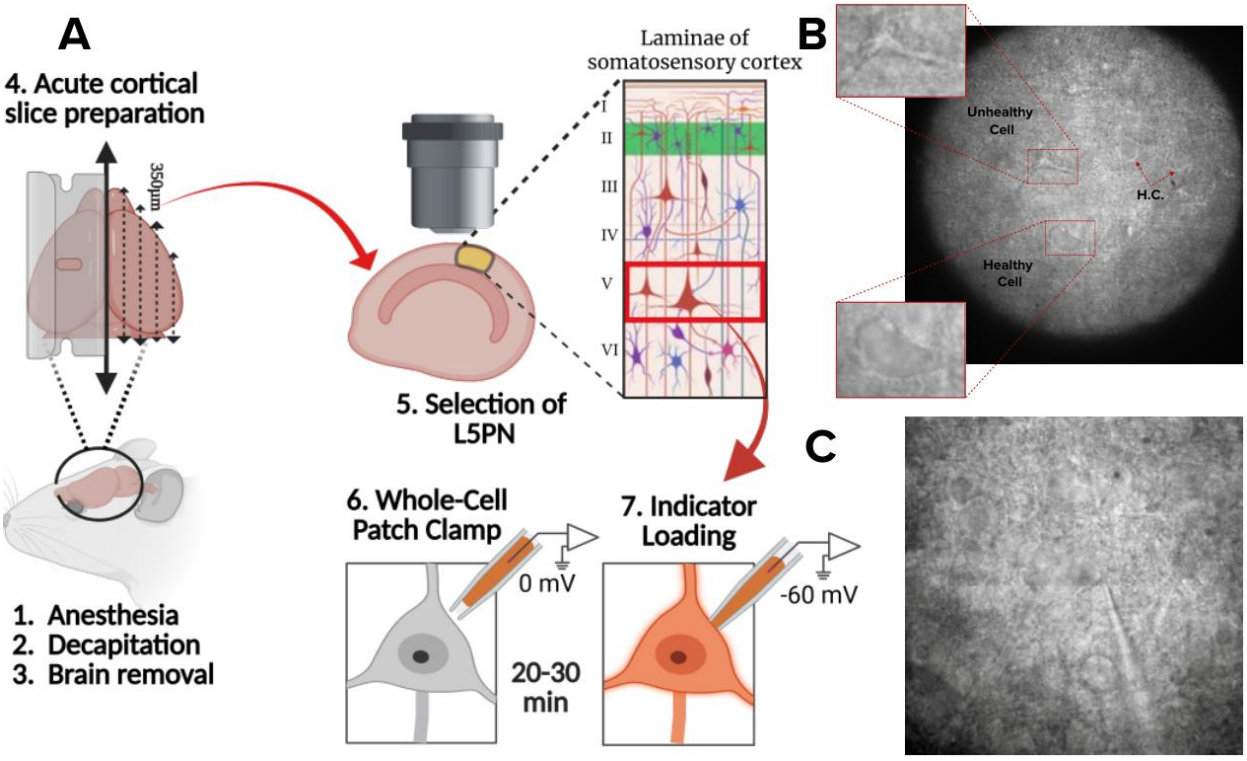

Figure 2.2 **Overview of slice preparation and patch-clamp recordings from Layer 5 pyramidal neurons.** ***(A)*** (1-4) Simplified schematic of the preparation process from anesthesia to brain slicing, (5) followed by visual selection of Layer 5 pyramidal neurons (L5PNs) in the somatosensory cortex, (6) whole-cell patch clamp recording, and (7) intracellular indicator loading. ***(B)*** IR-DIC image acquired with a 60× objective showing a healthy Layer 5 pyramidal neuron (H.C.) selected for patching. Insets reveal differences in morphology between a healthy and unhealthy cell that is typically asymmetric with a stronger contrast. ***(C)*** IR-DIC image (60×) of a patch pipette approaching a healthy neuron in a cortical slice. *Created with BioRender.com*

2.4 Optical Imaging

2.4.1 The Imaging System

The optical setup used for electrophysiology and imaging experiments is schematized in **Figure 2.3** All optical recordings were conducted using an upright SliceScope Pro System (Scientifica, Uckfield, UK) mounted on a TMC anti-vibration table. The microscope was equipped with a motorized XY translation stage, a motorized Z-drive to estimate, with micron precision, the depth of the recording plane from the slice surface, PatchStar micromanipulators (Scientifica), and an IR-DIC (Scientifica) system to facilitate targeted

patching of healthy neurons. Optical elements included a standard 10× air objective (Olympus) for initial general visualization, and a 60× water immersion objective (Olympus; NA = 1.0, WD = 2 mm) for patching and high-resolution imaging. A perfusion system (Scientifica) maintained the bath at a constant temperature of 32-34°C throughout the recordings; and the pipette pressure was monitored using a manometer (World Precision Instruments).

Fluorescence signals were collected using a DaVinci-2K CMOS camera (SciMeasure, Decatur, GA), with a low-noise 2k × 2k pixel sensor with 15 µm × 15 µm pixels and a quantum efficiency of 65%. The camera operated in correlated double sampling (CDS) mode and was controlled using Turbo-SM acquisition software (RedShirtImaging). A variable 1×/0.5× demagnification system (Cairn Research) was used, with the 1× configuration used for patching and navigation, and the 0.5× used during fluorescence imaging. At 0.5×, each camera pixel corresponds to ~500 nm of the sample.

The illumination was provided by a Tri-Line LaserBank (Cairn Research). Depending on the experiment, either a 520 nm (0.5 W) or a 465 nm (1.2 W) multimode diode laser head (Ushio) was used. A custom telescope (Cairn Research) built at the fiber output allowed for alternative spatial configurations: when both lenses were inserted, it generated a homogeneous wide-field illumination at the sample; when one lens was used, the system produced a concentrated and homogeneous illumination of ~30 µm circular spot at the sample. Emission and excitation filters, as well as dichroic mirrors (Semrock Rochester, NY), were chosen according to the fluorescent indicator and are detailed in later sections (2.4.2). The timing of illumination, the start of the camera acquisition, and the timing of somatic current injection, were precisely controlled by a Master-9 pulse stimulator (A.M.P.I.), enabling sub-millisecond synchronization across all components.

In addition to this system, part of the voltage dataset was acquired out using another system built on an Olympus BX51 microscope (Tokyo, Japan), with a 60×/1.0 NA objective (Tokyo, Japan), equipped with NeuroCCD-SMQ camera (RedShirtImaging, Decateur, CA) (see methods in Blömer et al., 2024) and, more recently, a Kinetix sCMOS camera (Teledyne Photometrics) (see methods in Abbas et al., 2025).

Laser wavelength, illumination mode (focused spot or wide-field), and acquisition frame rate (1 kHz, 10 kHz, or 20 kHz) were protocol-specific and are described in the imaging protocol sections below.

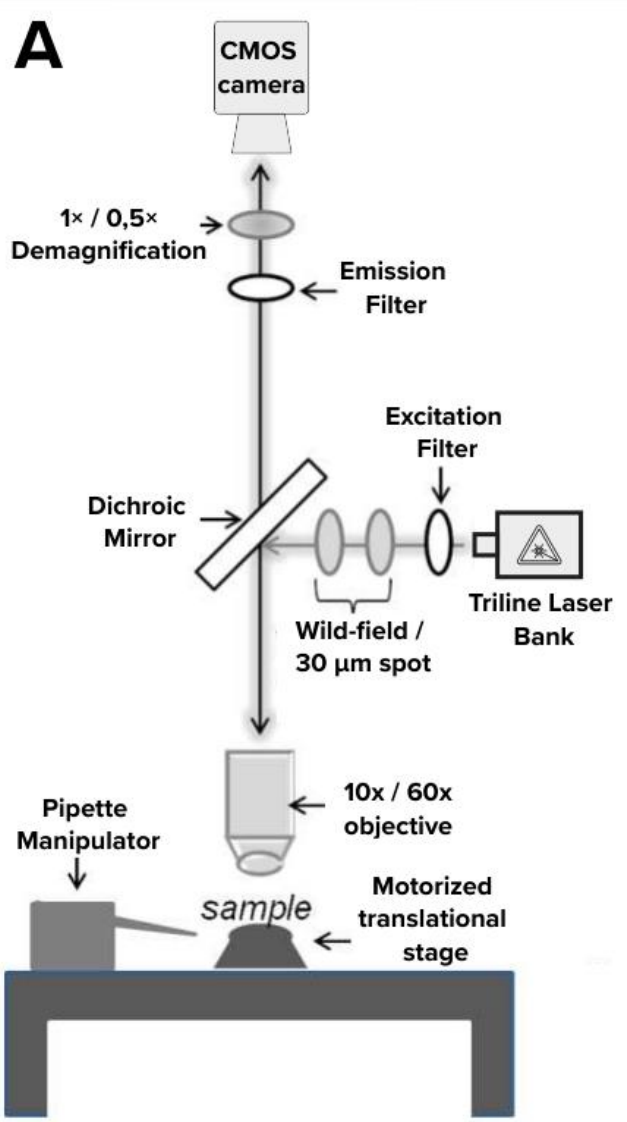

Figure 2.3 **Schematic of the imaging setup**.

2.4.2 Fluorescent Indicators

2.4.2.1 Sodium Indicator

To record the Na^+ influx associated with APs along the AIS at single-neuron resolution in brain slices, the Na^+-sensitive fluorescent dye ION Natrium Green - 2 (ING-2; Ion Indicators; KD=20 mM) was used. Compared to earlier dyes such as Na^+-binding benzofuran isophthalate (SBFI) (Minta & Tsien, 1989), ING-2 provides a substantially improved signal-to-noise ratio and allows higher acquisition rates, enabling the reconstruction of sodium current (I_{Na}) kinetics in subcellular compartments like the AIS during in the time course of the physiological AP.

The loading protocol I followed was adapted from Blömer et al., (2021). Briefly, ING-2 was freshly diluted before the experiment in intracellular solution to a final concentration of 0.5 mM. This was reported to be the maximal tolerated concentration for stable recordings in brain slices, though it imposes some constraints on the rate and number of trials. One practice that helped minimizing the toxicity of the dye was removing particulate impurities. The dye-solution was vortexed, centrifuged, and only the clear supernatant was utilized for cell-loading; with the purification step repeated until no pellet was visible. This relatively simple, yet efficient step helped to eliminate the aggregates and impurities of the dye that might compromise the cell viability. The final dye-solution was stored on ice and protected from light to maintain its stability. This approach was used consistently for all dye preparations, which were kept with the intracellular solution in a chilled box during the course of experiments to minimize degradation.

After establishing the whole-cell configuration, the dye was allowed to diffuse and equilibrate within the neuron, and to reach the AIS within approximately 20–25 minutes. Acquisition timing and illumination details are provided in the experimental protocol section (2.6.2.1).

2.4.2.2 Voltage-Sensitive Dye

For high temporal resolution monitoring of rapid membrane potential changes, we used the voltage-sensitive dye D-2-ANEPEQ (JPW1114, Thermo Fisher Scientific). This dye binds to

the membrane, and responds linearly to voltage fluctuations in physiological ranges of roughly -100 to +100 mV, rapidly shifting its fluorescence spectrum because of an intramolecular charge redistribution upon excitation. Although it is lipophilic, D-2-ANEPEQ retains sufficient water solubility to allow reliable microinjection into neurons. Following cytoplasmic delivery, the dye quickly integrates into the internal side of the lipid bilayer and gradually spreads throughout the neuronal membrane surface. Subcellular imaging of compartments like the AIS required a minimum equilibration period of 20-25 minutes to provide homogeneous membrane labeling.

To limit the risk of cytotoxicity, we used dye concentrations between 0.2 and 0.5 mg/mL. Intracellular application of JPW1114 and other styryl dyes has been shown to induce photodynamic membrane damage, which is thought to occur by reactive oxygen species generation within the lipid bilayer upon repeated illumination (Antic and Zecevic, 1999; Milojkovic et al., 2007). These effects may compromise membrane integrity and disrupt ion channel function, resulting in an impairment of neuronal excitability. Nonetheless, when used at controlled concentrations and with limited optical trials, such dyes can produce stable recordings without significant changes to AP properties (Canepari et al., 2007). So to avoid these complications, we adopted a double-patching approach. After the cells were loaded, we carefully retracted the patch pipette, forming an outside-out patch, which allowed the membrane to reseal and the neuron to recover. This cell was then re-patched with dye-free solution filled pipette to reduce undesired pharmacological effects of intracellular overload with JPW1114. I will provide further details on optical imaging parameters, excitation source, acquisition rate, and adequate filters, in section 2.6.2.2.

2.4.2.3 Calcium Indicator

Calcium imaging targeting the AIS and the apical tuft was performed using the low-affinity calcium indicator Oregon Green BAPTA-5N (OGB-5N; Thermo Fisher Scientific). Stock solutions of 20 mM were prepared, aliquoted, and stored at –20 °C. On the day of experiment, a vial was diluted in the intracellular solution to a final concentration of 2 mM. OGB-5N, with a dissociation constant KD of approximately 35μM, is an excellent indicator for recording large and fast calcium transients with minimal endogenous calcium signal buffering (Delvendahl et al., 2015). A further benefit of OGB-5N is its relatively high baseline

fluorescence, which facilitated the visualization of the soma and the fine neuronal processes during the dye loading phase.

After accessing the cell, the dye was allowed to diffuse in the cytosol to reach the compartments of interest. 20-25 minutes of loading time was sufficient to image from the AIS, while 30-40 minutes or longer was required to image from the apical tuft, depending on the neuron morphology and the dendritic branching extent. At the concentration used, OGB-5N provided robust fluorescence signals with a good signal-to-noise ratio, without altering the intrinsic firing properties of the neuron. Protocol and acquisition details for calcium imaging are presented in section 2.6.2.3.

2.5 Pharmacological Modulators for Ion Channels

All chemical drugs and toxins were purchased from either Tocris (Bristol, UK), Sigma-Aldrich (St. Louis, MO), or Smartox Biotechnology (Saint Egrève, France). They were appropriately dissolved, aliquoted, and stored at -20° C. Before application, an aliquot was freshly diluted in the ACSF (extracellular solution) to the desired final concentration.

Only potassium channels exhibiting a relatively large expression in the AIS were targeted. We used Dendrotoxin (DTX), a peptide isolated from *Dendroaspis polylepis* (black mamba snake) venom, at 500 nM to inhibit $K_v1.1$ channels. XE991, known as 10,10-bis(4-pyridinylmethyl)-9(10H)-anthracenone, was used to block KCNQ2/3 ($K_v7.2/K_v7.3$) potassium channels with high affinity at 10 µM. Lastly, Iberiotoxin (IbTx), a scorpion-derived peptide from *Buthus Tamulus* venom, was applied at 1 µM, as a selective inhibitor of large-conductance Ca^{2+}-activated potassium channels BK.

AaH-IIR62K, a mutated form of AaH-II was used to characterize its low-concentration effects on sodium channel modulation in the AIS, site of AP initiation. AaH-II is originally purified from scorpion toxin of Androctonus *australis hector* venom, and is known for its high-affinity binding to mammalian VGNCs and its effect on prolonging channel inactivation (Benoit & Dubois, 1987). The peptide was also produced by Smartox Biotechnology. The characterization of this toxin presents an integral part of this thesis; and all procedures, including effective dosing and assessment of drug-channel selectivity, were established in our previous work (Abbas et al., 2024) and will be further explored in Chapter 5. Prior to its

administration in brain slices, the selectivity of AaH-II for AIS sodium isoforms was evaluated in HEK293 cells expressing either the human $Na_v1.2$ or $Na_v1.6$. These experiments were performed by the group of Dr. Michel De Waard (Nantes Université, l'institut du thorax, France) using the SyncroPatch 384PE platform. The experimental protocol and corresponding findings, which constitute an external collaborative effort, are also presented in Chapter 5.

2.6 Experimental Protocols

2.6.1 Electrophysiology Coupled to Ultrafast Imaging in the AIS

2.6.1.1 Electrophysiological Protocol

As previously described, following the whole-cell configuration, the fluorescent indicator was allowed to diffuse for 20-25 minutes until the AIS was appropriately labeled. Throughout the loading phase, series resistance was continuously monitored, and the cell was held at -60 mV in voltage clamp to stabilize the cell's resting potential and to limit spontaneous firing.

Electrophysiological recordings were then performed in current-clamp mode using a Multiclamp 700A amplifier (Molecular Devices, CA). Electrophysiology data were acquired at 20 kHz via a USB-6221 acquisition board (National Instruments, TX). The resting potential was adjusted between –60 and –80 mV by applying steady holding current.

For these experiments, optical recordings were acquired over a fixed window of 8 ms, during which a single somatic AP was evoked and accompanying changes in sodium, calcium, or membrane potential in the AIS were simultaneously captured with to high-speed imaging. The synchronization of this protocol was done with the Master-9 which was triggered with a TTL output of the electrophysiology A/D acquisition board. Upon receiving this trigger, the Master-9 delivers precisely timed TTL outputs as follows: (1) it triggers with no delay the laser illumination for a duration of ~10 ms; (2) starts the camera acquisition 0.5 ms after laser onset to prevent acquisition of images while the laser is turning on; (3) and triggers

somatic current injections from the patch clamp amplifier delayed by ~2 ms from the camera acquisition to ensure the firing of an AP during the imaging window (**Figure 2.4B**).

Single APs were evoked by brief somatic current injections of 3-5 ms duration and 3-5 nA amplitude square pulses. The recorded somatic AP was corrected for a liquid junction potential of -11 mV, calculated based on the composition of our intracellular solution (Canepari et al., 2010). We also measured and adjusted the bridge potential for each recording to compensate for artifacts introduced by the large magnitude of stimulation.

2.6.1.2 Imaging Protocol

The 0.5× demagnification was used for imaging as it increases the photon collection per pixel by a factor of four, thereby improving image quality and resolution. Initial fluorescence of the cell was checked under low-intensity light from the diode (laser off), and the AIS was centered within the field that will be illuminated by the 30 µm spot, provided by the telescope. Data were acquired using the DaVinci 2K CMOS camera with 500 nm per pixel spatial resolution (**Figure 2.5A**). Due to the morphological variability of the AIS, we standardized our analyses to extract fluorescence signals from defined subregions: proximal (prox ~5-10 µm from the soma) and distal (dist ~35-40 µm) sites, and in some cases the medial domain (med ~20-25 µm), or averaged across the entire length of the AIS depending on the specific experimental goals.

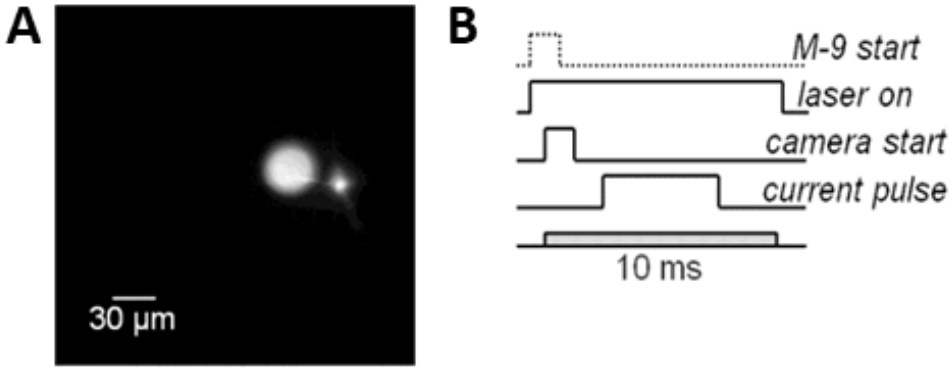

Figure 2.4 **Visualization and protocol synchronization for AIS recordings.** ***(A)*** L5PN loaded with the sodium-sensitive dye ING-2 shown under 512 × 512 pixel acquisition and 0.5× demagnification. A focused laser spot of ~30 µm illuminates the AIS. ***(B)*** Time diagram used for ultrafast imaging protocol: The Master-9 device triggers laser illumination, camera acquisition, and somatic current

injection with precise delays, to elicit a single AP within the 8 ms imaging window. *Adapted from Blömer et al. (2021).*

2.6.1.2.1 Sodium Imaging Parameters

ING-2 was excited with the 520 nm laser line of the Tri-Line LaserBank, band-pass filtered at 517 ± 10 nm, and directed to the preparation using a 538 nm long-pass dichroic mirror; and before detection, emission was band-pass filtered at 559 ± 17 nm. The camera configuration was set at 128 × 30 pixels, allowing an acquisition frame rate of 10 kHz with 0.1 ms exposure time and 80 frame sequences (**Figure 2.5A**).

2.6.1.2.2 Voltage Imaging Parameters

After establishing the second patch with a dye-free intracellular solution, the previously loaded and equilibrated voltage-sensitive dye, JPW114, was excited using the 520 nm laser line, band-pass filtered at 517 ± 10 nm and directed to the preparation using a 538 nm long-pass dichroic mirror, similar to ING-2. As for the emission, fluorescent signals were band-pass filtered at >610 nm prior to detection. To probe the changes of membrane potential in the AIS with the ability of resolving the different AP phases, recordings were performed two times faster with an acquisition rate of 20 kHz. Voltage imaging recordings were acquired either with the DaVinci-2K CMOS camera configured at 128 × 14-pixel stripe, the NeuroCCD-SMQ camera configured at 26X4 pixels (Blömer et al, 2024), or the Kinetix sCMOS camera configured at 200X140 pixel (Abbas et al., 2025), all sampled at 20 KHz.

2.6.1.2.3 Calcium Imaging Parameters

OGB-5N was excited using the 465 nm laser line, band-pass filtered at 469 ± 17 nm and directed to the preparation using a 495 nm long-pass dichroic mirror. Emitted OGB-5N fluorescence was filtered at 525 ± 25 nm before detection. The same acquisition protocol as sodium was employed, with a frame rate of 10 kHz.

Indicator	Laser Ex *nm*	Ex Filter *nm*	Em Filter *nm*	Frame Rate *kHz*
ING-2	520	517 ± 10	559 ± 17	10
JPW1114	517 ± 10	520–560	>610	20
OGB-5N	465	469 ± 17	525 ± 25	10

Table 2.1 Optical indicators and acquisition parameters used for AIS imaging experiments. Summary of fluorescent indicators used to monitor AIS signals. ING-2 sodium-sensitive dye; OGB-5N (Oregon Green BAPTA-5N) calcium indicator; JPW1114 voltage-sensitive dye. All indicators were delivered by the patch pipette and imaged using focused laser spot illumination of 30 µm.

2.6.2 Electrophysiology Coupled to Calcium Imaging at the Apical Tuft

To explore the Calcium Electrogenesis phenomenon in the tuft of the apical dendrite, simultaneous whole-cell current-clamp recordings coupled to Ca^{2+} imaging were performed. The timing of optical imaging and stimulation was coordinated as outlined in earlier methods (Section 2.6.1.1). Following the whole-cell patch, the calcium indicator OGB-5N was allowed to diffuse into the neuron for approximately 30-40 minutes, or even longer, until the apical tuft could be visualized under low-intensity illumination.

Anatomically speaking, the apical dendrites of the L5PN project vertically through cortical layers and arborize extensively between layers 1 and 2, often over distances exceeding 500 µm away from the soma in mice cortices (Karimi et al., 2020). Due to their geometry, successful imaging of the tuft is challenging. It depends primarily on the successful preparation of brain slices, as it requires that a large portion of the apical dendrite lies in the focal plane (ideally parallel), which is very sensitive to the angle chosen for slicing. In some preparations, the apical dendrite extended too deep, or grew beyond the slice, and was therefore cut, making it difficult or impossible to capture the distal arbor. Experiments were thus conducted only in slices with an unambiguously preserved and focused apical tuft.

Excitation was provided by the 465 nm laser line from the Tri-Line LaserBank, using the same optical path described in Section 2.6.1.2.2 for Ca^{2+} imaging at the AIS (469 ± 17 nm excitation filter, 495 nm long-pass dichroic, 525 ± 25 nm emission filter).

The recording protocol consisted of trains of three somatic APs that were triggered by 3-4 nA, 3-4 ms square pulse each, delivered at inter-pulse intervals of 6, 8, 10, 12, and 14 ms to gradually evaluate temporal threshold for dendritic calcium electrogenesis. Ca^{2+} fluorescence was recorded using the DaVinci 2K CMOS camera at a spatial resolution of 0.5 µm per pixel. A 512 × 100 pixel region of interest comprising the tuft was selected, and images were acquired at 1 kHz with an exposure time of 1 ms per frame, over a total recording duration of 50 ms, repeated two times (2 trials) for each cell. This protocol permitted the monitoring of calcium dynamics in large regions of the apical tuft with temporal resolution fast enough to capture regenerative dendritic events (**Figure 2.5C**).

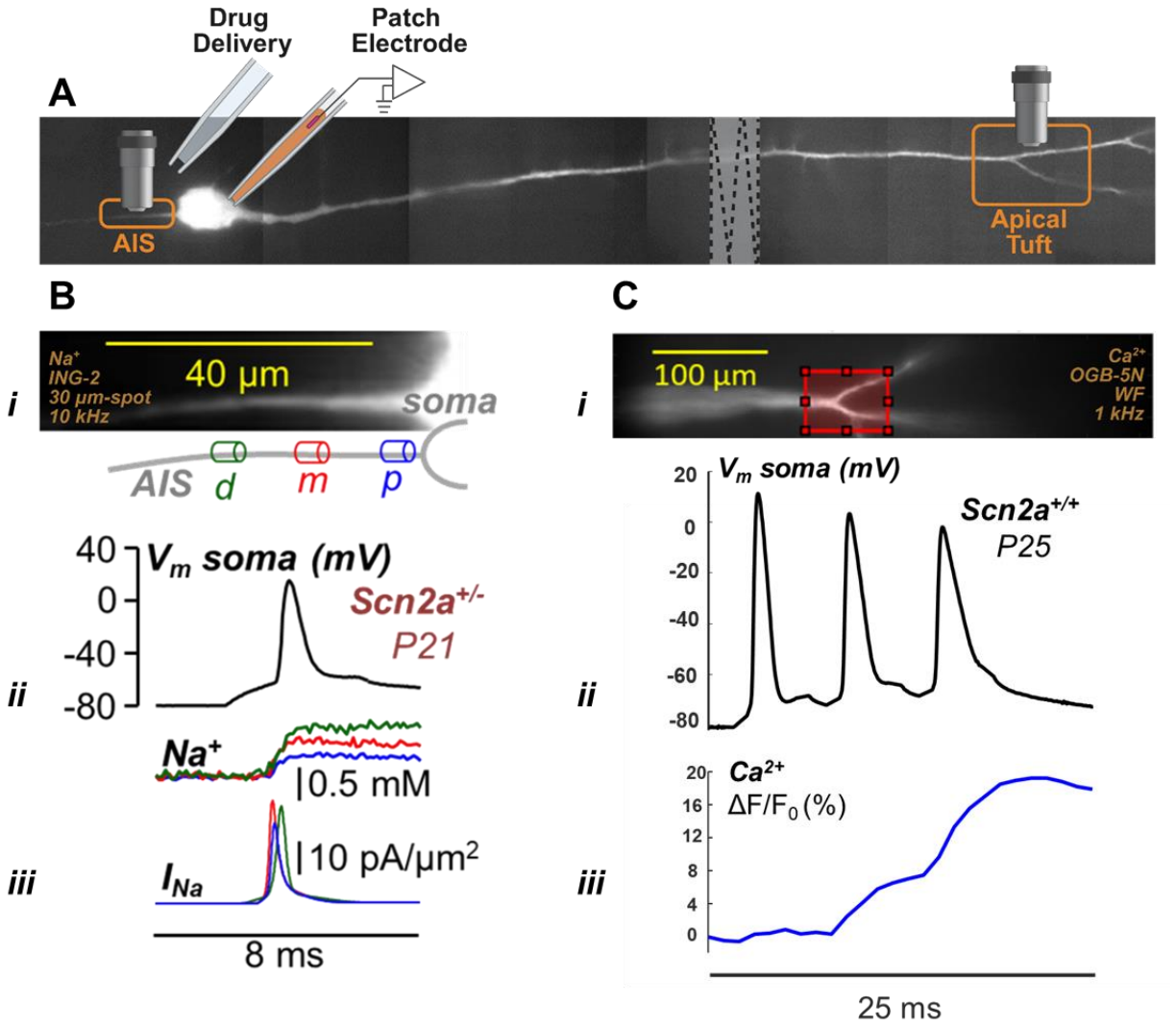

Figure 2.5 **Experimental configuration of electrophysiology-coupled ultrafast optical imaging in the AIS and apical tuft of Layer 5 pyramidal neurons.** ***(A)*** Overview L5PN filled with OGB-5N

illustrating the spatial configuration of the patch pipette, drug delivery pipette, optical recording regions: the axon initial segment (AIS, left) and the apical tuft (right), both visualized using a 60× water immersion objective. Pharmacological agents were locally applied close to the AIS. ***(B)*** Example of sodium imaging at the AIS. (i) Fluorescent image of the AIS (128 × 30 pixels) and corresponding reconstruction indicating defined subregions: proximal (p∼5-10 µm), medial (m∼20-25 µm), and distal (d∼35-40 µm), recorded at 10 kHz with 30 µm laser spot illumination and the sodium indicator ING-2 delivered with patch pipette. (ii) Somatic AP evoked by a brief current injection in a *Scn2a*$^{+/-}$ mouse at P21. (iii) Corresponding Na^+ fluorescence signals (top), and calculated sodium currents (I_{Na}) (bottom) across AIS domains. ***(C)*** Calcium imaging in the apical tuft. (i) Fluorescence image of the apical dendrite loaded with OGB-5N and imaged at 1 kHz under wide-field laser illumination with the region of interest (red square) selected for Ca^{2+} measurements. (ii) Somatic voltage trace during a three AP train recorded in a *Scn2a*$^{+/+}$ neuron at P25. (iii) Corresponding calcium signal ($\Delta F/F_0$) from the tuft region shown in the red box.

2.6.3 Electrophysiology Without Imaging

2.6.3.1 Single Somatic Action Potential

This protocol was developed to characterize the AP properties in L5PN across different animal models under minimally perturbed conditions, in the absence of optical indicators, laser illumination, or intense electrical stimulation. In contrast to the imaging experiments that required large-amplitude, brief current pulses to time the AP firing with imaging acquisition windows, these recordings involved lower intensity stimulation, in the range of 50–300 pA, to evoke responses more representative of the physiological case.

After achieving the whole-cell configuration, neurons were initially held at -60 mV in voltage-clamp mode for ∼3-5 minutes to stabilize the cell membrane and monitor series resistance. For current-clamp recordings, the V_m was left at its natural resting level, and no steady holding current was applied. Single APs were elicited by somatic injection of small amplitude square pulses of current (50-300 pA, 150 ms duration), sufficient to slowly depolarize the membrane and to gradually bring it to the threshold without disrupting baseline excitability. In these recordings, the bridge potential remained minimal and was not corrected. With the simplicity of this approach, I was able to record from a large pool of neurons, including a total of 416 cells across the three genotypes.

2.6.3.2 Burst of Three Action Potentials

A three-AP burst, without optical imaging, was used to assess intrinsic excitability and fundamental electrophysiological properties during short trains of activity in L5PN across the three genotypes.

After whole-cell configuration and stabilization in voltage-clamp mode at -60 mV, the amplifier was then switched to current-clamp mode, and the membrane potential was adjusted and set at -70 mV. Three somatic APs were elicited by delivering three square current pulses (3-4 nA amplitude, 4 ms duration each), with a fixed inter-pulse interval of 6 ms. This protocol was adapted from the stimulation used in Calcium Electrogenesis experiments (Section 2.6.2), but without imaging related technical limitations. It also offered a controlled evaluation of repetitive firing, spike fidelity, and the overall somatic excitability across a greater number of cells and preparations.

2.6.4 Drug Delivery in Brain Slices

Drugs were dissolved as described in Section 2.5. Pharmacological interventions were only conducted in a subset of experiments where the drug or blocker was locally applied by a second pipette (2-4 μm tip diameter) at nearly 20 μm from the optical recording site, the AIS. Gentle pressure was used to deliver the solution for 1-2 minutes, ensuring localized and stable exposure before recording (**Figure 2.6**).

Drug pipettes were pulled from the same type of glass capillaries (OD, 1.5 mm; ID, 1.17 mm; Harvard Apparatus) as patch pipettes, using different heating parameters to obtain a larger tip diameter suitable for local pressure application.

After applying the drug, the same protocol used under control conditions was repeated to examine the induced alterations. In order to minimize possible cross-contamination and cumulative effects, no further cells were patched within the same subregion of the slice after drug delivery. In most cases, the slice was replaced after one or two applications.

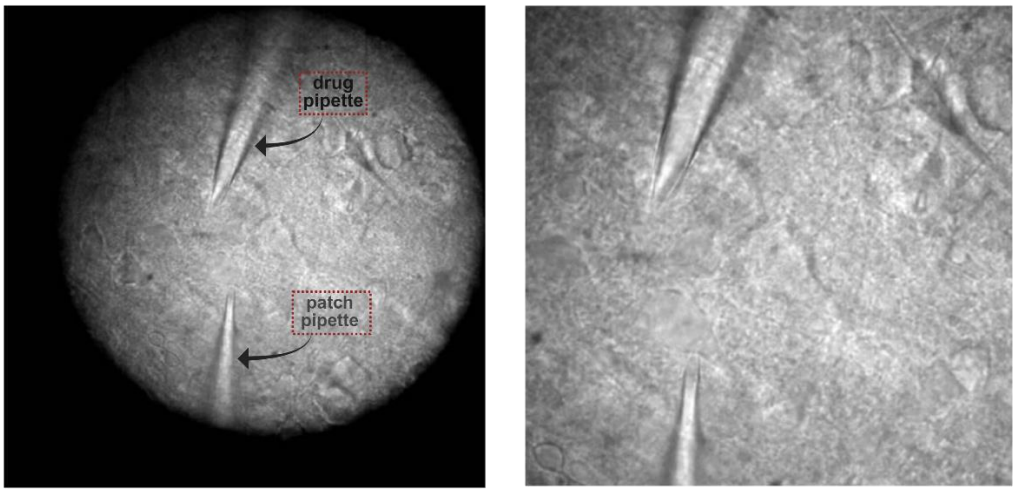

***Figure 2.6* Visualization of dual pipette positioning for local drug application.** Transmitted light images of a Layer 5 region in a cortical slice, acquired with a 60× objective, showing the patch pipette and a nearby drug pipette positioned ~20 µm from the AIS (left), and a zoomed-in view of the same area (right) illustrating the precise protocol for local pharmacological interventions.

2.7 Optical Data Analysis

Na^+, Ca^{2+}, and membrane potential (V_m) optical recordings were analyzed using a custom-written MATLAB code. The raw fluorescence signals (F) were first corrected for background autofluorescence and expressed as fractional fluorescence changes ($\Delta F/F_0$), where F_0 was determined as the average baseline fluorescence before the stimulation. To correct for photo-bleaching, fluorescent transients of the no stimulation recordings were fitted with a multi-exponential function, and the fit was subtracted from the experimental traces. Detailed processing protocols for each imaging type are described in what follows.

2.7.1 Sodium Imaging

In Na^+ imaging recordings, the sodium current (I_{Na}) was estimated as previously detailed (Filipis & Canepari, 2021). Four trials with identical somatic responses were typically recorded per cell, with 1-minute pause between trials to allow equilibration of the bleached indicator. Trials were aligned temporally by overlaying the somatic action potentials from each trial, and spatially by adjusting for small x-y displacements across image sequences. Fluorescence signal was extracted from standardized 5 µm regions of interest located at proximal (5-15 µm from the soma), medial (med ~20-25 µm), and distal (30-40 µm)

segments of the AIS. Each trial was individually corrected for photo-bleaching using tri-exponential fits of fluorescence transients in single trials with no stimulation.

Following the correction and alignment, the trials were averaged to improve the signal-to-noise ratio (SNR). The resulting $\Delta F/F_0$ traces were converted into a Na^+ transient as previously described: ING-2 fluorescence was determined at known NaCl concentrations between 0 and 25 mM using the same optical system with internal solution free of Na_2ATP. Fluorescence intensity was fitted against sodium concentration, establishing that a 1% change in $\Delta F/F_0$ corresponded to 0.175 mM $\Delta[Na^+]$ at a baseline of 10 mM (**Figure 2.7**). The $\Delta[Na^+]$ was corrected for longitudinal diffusion, and the axonal diameter was estimated from the fluorescence profiles and modeled as a series of truncated cones to calculate local volume and surface area. $\Delta[Na^+]$ signals were converted into a Na^+ superficial density. This signal was then fitted with a two-component model function: a subthreshold sigmoid function, and a suprathreshold component defined by the product of three sigmoids. The sodium current was finally obtained by the time derivative of the fitted surface charge signal. For full methodological details and model validation, see Filipis & Canepari (2021).

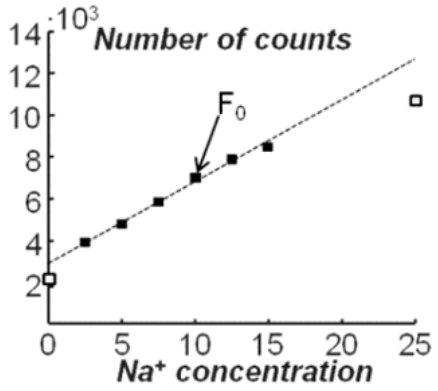

Figure 2.7 **ING-2 calibration.** (C) Calibration curve illustrating the fluorescence signal (counts) as a function of known intracellular sodium concentrations using solutions containing 80 µM ING-2. The dashed line represents the linear fit across the physiological range (2.5-15 mM), with F_0 indicating the baseline fluorescence at rest. *From Blömer et al. (2021).*

2.7.2 Voltage Imaging

For voltage imaging, data was also corrected for bleaching, and averaged from 4-6 trials per cell. Fluorescent signals were extracted from defined 5 µm subregions: proximal, distal, and

in some cases medial sites, or averaged across the entire AIS. V_m transients were not calibrated to an absolute voltage scale, but considering that the size of the AP in the AIS is comparable to the somatic AP, $\Delta F/F_0$ waveforms were normalized to the somatic AP peak to allow consistent measurement of axonal AP width across cells.

2.7.3 Calcium Imaging

In experiments addressing the AP initiation in the AIS, calcium signals were corrected for photo-bleaching and analyzed from 6-7 averaged trials per cell (**Figure 2.8)**. Fluorescence traces ($\Delta F/F_0$) were extracted from the abovementioned proximal and distal sites of the AIS. The calcium transients were normalized to their asymptotic levels and fitted with a four-sigmoid model function. The calcium current (I_{Ca}) was estimated by time-deriving the fitted $\Delta F/F_0$ signal. All methodological details and model validation are delineated in Jaafari & Canepari (2015).

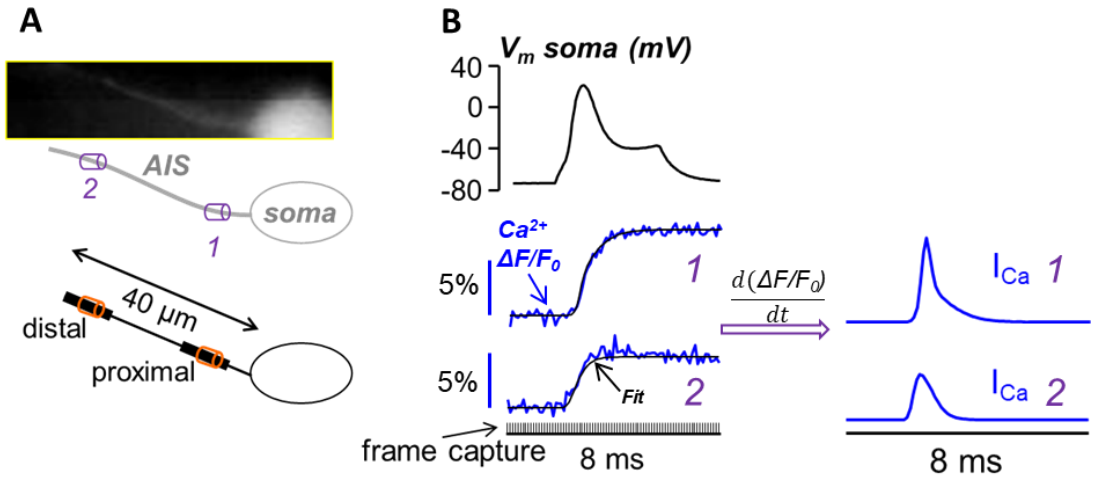

Figure 2.8 **Example of Calcium imaging and I_{Ca} estimation at the AIS.** ***(A)*** Fluorescence image of a L5PN filled with OGB-5N (128 × 30 pixels), showing the AIS and two selected regions proximal and distal, illuminated with 30 µm laser spot. ***(B)*** Top: Somatic membrane potential (V_m) recorded with the patch electrode. Middle: Corresponding Ca^{2+} transients (blue traces) represented as fractional change of fluorescence ($\Delta F/F_0$) recorded at 10 kHz in the two subregions of the AIS, corrected for photobleaching, normalized to their asymptotic value, and fitted with a 4-sigmoid function (black traces). Bottom: Calcium currents (I_{Ca}) estimated from the time derivative of the fitted Ca^{2+}-$\Delta F/F_0$ signals.

2.8 Statistical Data Analysis

2.8.1 Overview of Statistical Tests

All analyses were performed on whole-cell patch clamp recordings and high-speed optical imaging data obtained in cortical slices from *Scn2a*$^{+/+}$, *Scn2a*$^{+/-}$, and *Scn2a*$^{+/L1314P}$ female mice across postnatal days P21-40. Given the multidimensional nature of the characterization in this project, a conservative statistical model was applied to limit the likelihood of Type I errors (false positives), while maintaining sensitivity to effects that have a physiological significance. In all tests, we considered $p < 0.01$ as the threshold for significance.

In pharmacological analyses, in order to test the effect of a drug on the AP shape, or Na^+ and Ca^{2+} currents within the same group of experiments, parametric paired t-tests were applied on paired measurements recorded in control conditions and in the presence of a channel's pharmacological modulator.

For unpaired and independent comparisons, datasets were grouped according to genotype and age windows. Two types of comparisons were carried out: between genotypes within the same age window (WT vs. KO, WT vs. KI, KO vs. KI at P21-24, P30-40, P21-40), and within the same genotype but different age ranges (P21-24 vs. P30-40). To examine differences in the measured variables among groups, we favored non-parametric tests, which are sensitive to distribution, over mean-based approaches, since many of the variables such as sodium influx and AP parameters displayed skewness and, in some cases, multimodal distributions, which were most pronounced in *Scn2a*$^{+/L1314P}$ cells.

To analyze of Ca^{2+} signal kinetics at the AIS, specifically the delays between proximal and distal Ca^{2+} currents, and the inter-pulse interval threshold for dendritic Ca^{2+} electrogenesis, which were reported by discrete values, we used the two-sample Wilcoxon-Mann-Whitney (WMW) test. As this test does not directly offer an indication about effect magnitude, we complemented it with a standardized effect size (SES) that estimates of the strength of the observed effects and that was calculated as: $SES = {Z}/{\sqrt{N}}$, where Z is the standardized test statistic and N is the total number of observations (Fritz et al., 2011). Significant comparisons were those that met both $p < 0.01$ and $SES > 0.5$ criteria. The SES threshold was

interpreted based on Cohen's guidelines (1988), for which SES > 0.5 represents a large effect size, so that reported findings reflect robust differences rather than trivial deviations (Calin-Jageman, 2018). For all other comparisons, we employed the Kolmogorov-Smirnov (KS) test detailed below.

2.8.2 The Kolmogorov-Smirnov Test

The two-sample KS test was the primary test used for unpaired comparisons between genotypes and/or age groups, and was applied to different datasets in Chapter 3 and 4, including the AIS imaging experiments, specifically to compare proximal-to-distal maxima of Na^+ currents in the AIS ($R_{p/d}$) and the fractional changes in V_m transient width (AP_{wid}), also to compare somatic AP parameters (AP_{wid}, AP_{thr}, AP_{amp}), and amplitude of dendritic Ca^{2+} electrogenesis responses (S_3/S_2).

In contrast to mean-based alternatives, KS is non-parametric and has the property to detect any distributional difference, including shifts in central tendency, variance, skewness, or the presence of subpopulations (Kolmogorov, 1933; Smirnov, 1948). This is of particular importance for electrophysiological and optical variables in disease models, where genotype and age specific changes frequently result in subpopulation effects rather than global mean differences, and where significant heterogeneity can be found between cells within the same group. The KS statistic (D) represents the maximum absolute difference between the empirical cumulated distribution functions (ECDFs) of the two samples. Given the null hypothesis of identical distributions, the sampling distribution of D is known, which enables p-values to be computed (Massey, 1951). This makes KS test particularly suitable for this work in order to detect statistical differences, both in central tendency and in overall distributional shape.

One of KS test limitations is its higher sensitivity near the center of the distribution than at the tails, and its reduced statistical power for detecting small effect sizes, in particular when sample sizes are modest. Therefore, to strengthen reliability, we implemented a dual criterion for statistical significance: results were considered significant only if $p < 0.01$, minimizing false positives and ensuring that reported effects represent robust differences unlikely to arise from sampling noise, in addition to a statistical power ≥ 0.8. This threshold

level is widely accepted as an appropriate cutoff for balancing between sensitivity and specificity (Krzywinski & Altman, 2013; Nahm, 2016). This approach addresses both types of errors: a stringent α-level reduces Type I error (false positives), and a power of at least 0.8 minimizes the likelihood of Type II error (false negatives). In practice, this means that non-significant findings may be interpreted more confidently as a lack of large effects rather than failure to detect them because of insufficient sensitivity (Button et al., 2013; Cohen, 1988).

Finally, sample sizes in all experiments were limited by experimental feasibility constraints, including the availability of three different genotype animals within a defined age window, balancing among developmental stages, and varying experimental success. This was partially compensated by ensuring a balanced distribution of cells among genotypes and age groups for each set of experiment, as well as post hoc verification of power, that detected effects reached sufficient statistical power (SP > 0.8) before being considered significant. When power was less than 0.8, no significance was reported, even if the p-values were below 0.01.

3

Characterization of Action Potential Initiation at The Axon Initial Segment in *SCN2A* Loss-of-Function Models

3.1 SELECTIVE REDUCTION IN $Na_V1.2$-MEDIATED SODIUM INFLUX IN *SCN2A*$^{+/-}$ MICE 83
3.1.1 Sodium influx is reduced in the proximal AIS in Scn2a$^{+/-}$ cells 87
3.1.2 Na^+ influx in Scn2a$^{+/L1314P}$ neurons does not appear different from that in Scn2a$^{+/+}$ 87
3.2 CALCIUM CURRENTS HIGHLIGHT FUNCTIONAL $Na_V1.2$ DEFICITS IN *SCN2A*$^{+/-}$ MICE 88
3.2.1 Developmental refinement of $Na_V1.2$-mediated Ca^{2+} influx is different in the three strains 90
3.2.2 Reduced Ca^{2+} delays in Scn2a$^{+/-}$ L5PNs 92
3.3 SOMATIC APS IN *SCN2A*$^{+/-}$ AND *SCN2A*$^{+/L1314P}$ AND *SCN2A*$^{+/+}$ MICE 93
3.3.1 Somatic AP amplitude in the three strains 97
3.3.2 Somatic AP width in the three strains 97
3.4 EXCEPTIONALLY SHARP ACTION POTENTIALS ARE GENERATED AT THE DISTAL AIS OF *SCN2A*$^{+/L1314P}$ CELLS 98
3.5 THE EFFECTS OF BLOCKING K_V1, K_V7, AND BK CHANNELS IN THE AIS 101
3.5.1 K_V1 channel block preferentially widens distal APs with the strongest effect in Scn2a$^{+/L1314P}$ cells. 103
3.5.2 Distal APs in Scn2a$^{+/L1314P}$ cells are poorly affected affected by K_V7 channel block 104
3.5.3 BK channel block produces the weakest modulation of AP shape 104
3.6 SUMMARY AND INSIGHTS 105

This chapter addresses whether *SCN2A* loss-of-function perturbs the action potential initiation at the AIS, the compartment where $Na_V1.2$ are preferentially expressed, and where associated alterations, if present, are most likely to emerge.

Here, we integrated somatic electrophysiology, high-speed imaging at the AIS, and targeted pharmacological analyses to examine the AP generation and its associated mechanisms in two heterozygous *SCN2A* LoF mouse models: a knock-out (KO; *Scn2a*$^{+/-}$) and a knock-in (KI;

Scn2a$^{+/L1314P}$). We compared the findings with a control wild-type group (*Scn2a*$^{+/+}$), and we followed the changes across the juvenile period (P21-40).

First, at the AIS, we optically measured the sodium and calcium currents associated with APs elicited by somatic current injections. We then examined the spike properties in somatic APs, and assessed the waveform of the AP at its site of generation from ultrafast V_m transients. Finally, we combined AIS voltage imaging with targeted local pharmacology, and we focused on changes produced by blocking K_v1, K_v7, and BK channels in order to evaluate their roles and contributions to shaping AP alterations in *Scn2a*$^{+/-}$ and *Scn2a*$^{+/L1314P}$, and to explore their interactions with Nav1.2 deficits.

3.1 Selective Reduction in $Na_v1.2$-Mediated Sodium Influx in *Scn2a*$^{+/-}$ Mice

In a channelopathy involving $Na_v1.2$ channel, an essential first step toward understanding the associated pathophysiological mechanisms is to characterize the sodium influx during action potential initiation. We therefore began our analysis in *Scn2a*$^{+/-}$ and *Scn2a*$^{+/L1314P}$ mice by measuring Na^+ influx associated with the generation of an AP in the AIS of L5 pyramidal neurons of the somatosensory cortex, using a quantitative method described in Chapter 2 and previously reported in details (Filipis and Canepari, 2021).

To provide a larger pool of control cells, we performed new experiments in *Scn2a*$^{+/+}$ female mice, considering the exact age of each animal in a range of P21-P40. The two representative examples are shown in **Figure 3.1A** to illustrate the spatial profile of Na^+ influx along the AIS at different postnatal ages. In both cases, an AP was evoked at the soma, and the associated Na^+ concentration changes were extracted from three sites of the AIS: distal (*d*, 30-40 μm from the soma; green traces), medial (*m*, 15-25 μm; red traces), and proximal (*p*, 0-10 μm; blue traces), each site corresponding to 5μm-long AIS portion. In the P21 cell (left), Na^+ transients were comparable in size at the distal and medial sites, while the proximal signal was smaller. In contrast, the P30 cell showed similar magnitudes of Na^+ transients at *d* and *p* sites, with a larger medial signal.

To quantify the size of the signal, we fitted the raw fluorescence traces with a model function (and see Methods in Filipis and Canepari, 2021), estimated the AIS surface at each site, and calculated the time derivative to extrapolate the Na^+ current (I_{Na}). In these two examples, the smallest I_{Na} was observed at *p* in the P21 cell, and at *d* in the P30 cell. However, the quantification of the I_{Na} is limited by the temporal under-sampling of measurements. Thus, we focused our analysis on the amplitude of the transient fits, which are not subject to these specific sources of error, and we restricted our analysis on the *d* and *p* AIS sites.

In a previous study (Filipis et al., 2023), we showed that the partially selective $Na_v1.2$ blocker, G1G4-huwentoxin-IV, produced a reduced Na^+ influx in the proximal AIS, consistently with the known enrichment of $Na_v1.2$ in this region, in contrast to the predominant expressions of $Na_v1.6$ at the distal AIS (Hu et al., 2009). Since the absolute amplitude of the Na^+ concentration change was highly variable from cell-to-cell, we considered the ratio of proximal to distal Na^+ signals ($R_{p/d}$) to compare the relative $Na_v1.2$-mediated influx with respect to $Na_v1.6$.

In the two control examples shown in **Figure 3.1A**, the $R_{p/d}$ values were 0.63 at P21 and 1.02 at P30. In total, Na^+ influx was measured across 29 cells from 13 *Scn2a*$^{+/+}$ females and the values of $R_{p/d}$ plotted against the age are reported in **Figure 3.2** We observed that $R_{p/d}$ tended to increase with age, remaining consistently <1 in the 13 cells from the youngest group (P21-24), while values in the oldest group (P30-40) were distributed closer to 1, in accordance with our previous report (Filipis and Canepari, 2021). This developmental trend suggests a refinement of $Na_v1.2$ expression in the AIS during the examined juvenile period. We therefore, in this study, also analyzed our data with respect to two distinct time windows, in order to capture the potential changes in the critical period of juvenile maturation. Specifically, we examined data both across the full age range (P21-40), and separately in two age groups: a young group (P21-24) and an old group (≥P30).

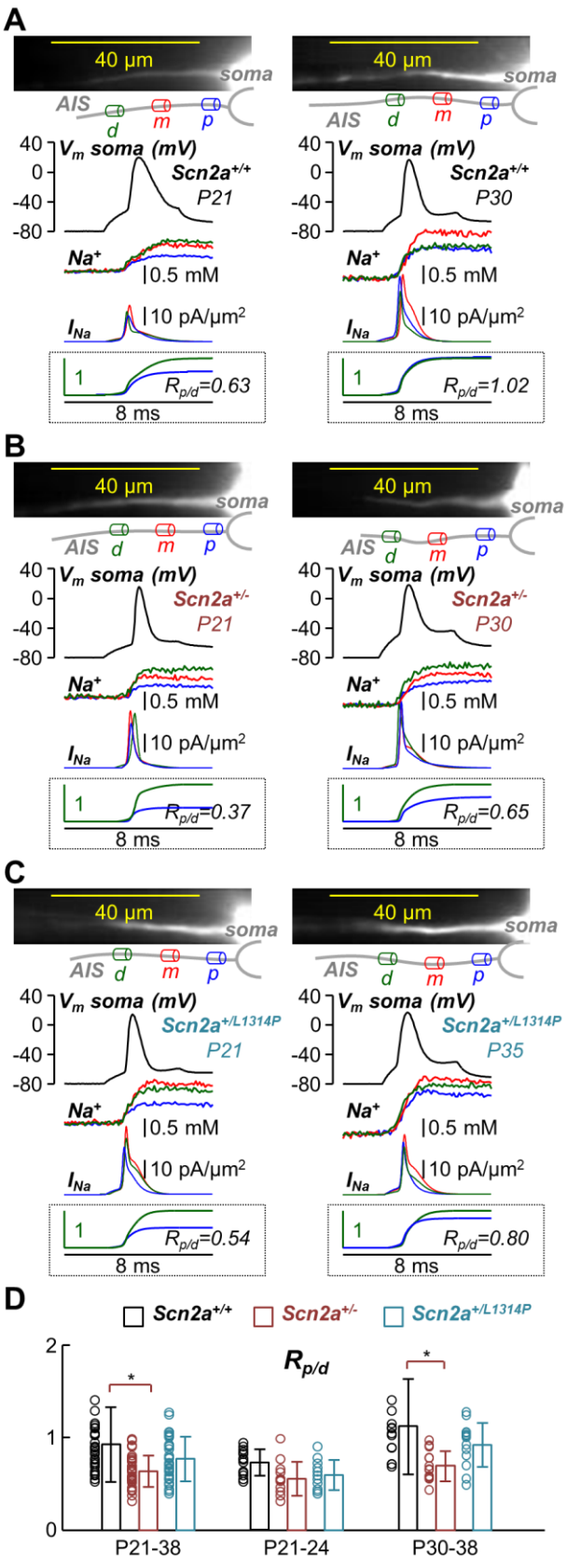

Figure 3.1 **Na⁺ influx in the AIS of *Scn2a*$^{+/+}$, *Scn2a*$^{+/-}$ and *Scn2a*$^{+/L1314P}$ L5 pyramidal neurons.**

(A) On the top-left, AIS of a *Scn2a*$^{+/+}$ L5 pyramidal neuron at P21 in the recording position, filled with ING-2 (ION Natrium Green - 2), with reconstruction indicating a distal (*d*, green cylinder), medial (*m*, red cylinder) and a proximal (*p*, blue cylinder) site. On the middle-left, an AP with associated Na⁺ transients from the three sites illustrated with the same color of the corresponding cylinders above. Below, Na⁺ currents (I_{Na}) derived from the fits of the Na⁺ transients. Inside the dotted inset, fits of the Na⁺ transients in the *d* and *p* sites normalized to the maximum of the *d* fit; the value of the ratio between the *p* and the *d* maxima ($R_{p/d}$) is reported. On the right, same measurements and analysis for another *Scn2a*$^{+/+}$ cell at P30. Notice the difference between the $R_{p/d}$ values in the two neurons.

(B) Same measurements and analysis for two *Scn2a*$^{+/-}$ L5 pyramidal neurons, one at P21 (left) and the other at P30 (right). Notice that $R_{p/d}$ is <1 in both cells.

(C) Same measurements and analysis for two *Scn2a*$^{+/L1314P}$ L5 pyramidal neurons, one at P21 (left) and the other at P35 (right).

(D) Scatter plots and mean ± SD of $R_{p/d}$ values for the three strains and the three age groups. In *Scn2a*$^{+/+}$ cells, $R_{p/d}$ was 0.92±0.40 at P21-40 (N=29), 0.73±0.14 at P21-24 (N=13) and 1.12±0.51 at P30-40 (N=13). In *Scn2a*$^{+/-}$ cells, $R_{p/d}$ was 0.64±0.17 at P21-40 (N=31), 0.56±0.18 at P21-24 (N=12) and 0.69±0.16 at P30-40 (N=13). In *Scn2a*$^{+/L1314P}$ cells, $R_{p/d}$ was 0.77±0.24 at P21-40 (N=31), 0.73±0.14 at P21-24 (N=11) and 0.92±0.24 at P30-40 (N=13). "*" indicates that the result of the two-sample KS-test between two groups gave SP>0.8 and p<0.01.

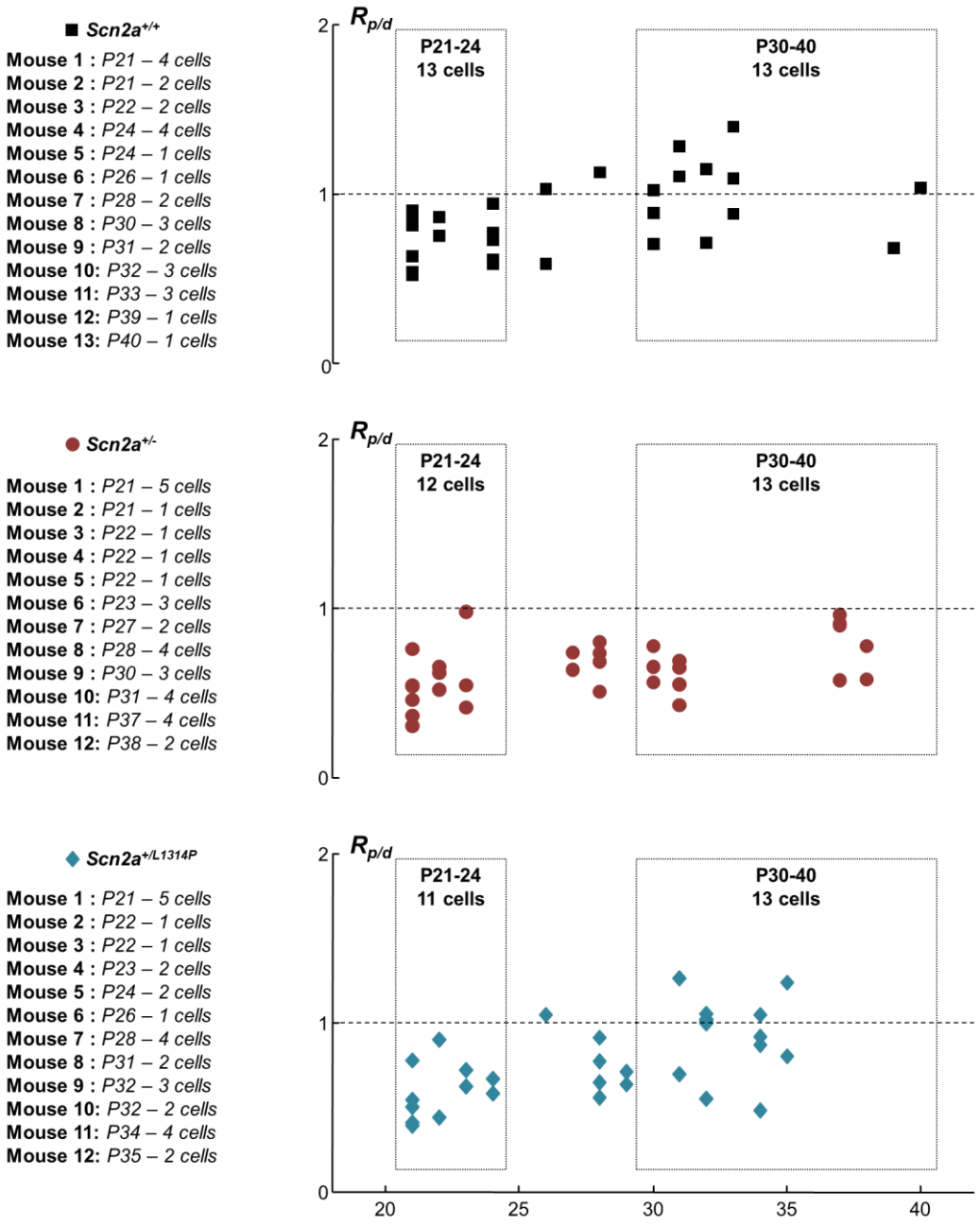

***Figure 3.2* Scatter plot of $R_{p/d}$ against age in AIS Na^+ influx measurements.** Top, scatter plot of $R_{p/d}$ against age of 29 *Scn2a*$^{+/+}$ cells from 13 female mice. The groups "young" (P21-24) and "old" (P30-40) are outlined by dotted rectangles. $R_{p/d}$ has tendency of increasing with age (SP=0.757 and p=0.0076, KS-test between P21-24 and P30-40 groups). Middle, scatter plot of $R_{p/d}$ against age of 31 *Scn2a*$^{+/-}$ cells from 12 female mice with no significant increase with age (SP=0.499 and p=0.0145, KS-test between P21-24 and P30-40 groups). Bottom, scatter plot of $R_{p/d}$ against age of 31 *Scn2a*$^{+/L1314P}$ cells from 13 female mice, with significant increase with age (SP=0.970 and p=0.0039, KS-test between P21-24 and P30-40 groups).

To assess potential differences among the different groups, we applied the two-sample Kolmogorov-Smirnov (KS) test, and we established that two groups are different when both the Statistical Power (SP) exceeded 0.8 and the p-value was <0.01 (see Methods). **Figure 3.1**D shows scatter plots of $R_{p/d}$ values for the three strains and the three age groups, together with the mean ± SD.

In *Scn2a*$^{+/+}$ cells, $R_{p/d}$ was 0.92 ± 0.40 in the full age range (P21-40, N = 29), 0.73 ± 0.14 in the youngest group (P21-24, N = 13), and 1.12 ± 0.51 in the oldest group (P30-40, N = 13). Statistical testing revealed a tendency toward increased Rp/d with age (P21-24 vs P30-40: SP = 0.757, p = 0.0076), which did not meet the criteria for significance.

3.1.1 Sodium Influx Is Reduced in The Proximal AIS in *Scn2a*$^{+/-}$ Cells

Figure 3.1B shows two examples of the same experiment performed in a cell at P21 (left) and in another cell at P30 (right), obtained from two *Scn2a*$^{+/-}$ female mice. In both cells, Na^+ signals were smaller in *p* with respect to *d* and the values of $R_{p/d}$ were 0.37 and 0.65 at P21 and P30 respectively. Across 31 cells from 12 *Scn2a*$^{+/-}$ females, $R_{p/d}$ values remained consistently <1 at all ages (**Figure 3.2**).

The corresponding averages were 0.64 ± 0.17 (P21-40, N = 31), 0.56 ± 0.18 (P21-24, N = 12), and 0.69 ± 0.16 (P30-40, N = 13). Statistical testing confirmed that $R_{p/d}$ values in *Scn2a*$^{+/-}$ cells were significantly smaller than in *Scn2a*$^{+/+}$ cells both when considering the full age range P21-40 (SP=0.952 and p=0.0023), and in the oldest group P30-40 (SP=0.821 and p=0.0076). However, no significant change with age was found within Scn2a$^{+/-}$ neurons (SP= 0.499, p=0.0145), and values remained consistently <1 in both the youngest and oldest age groups.

3.1.2 Na^+ Influx in *Scn2a*$^{+/L1314P}$ Neurons Does Not Appear Different from That in *Scn2a*$^{+/+}$

Similarly, two examples from *Scn2a*$^{+/L1314P}$ are shown in **Figure 3.1**C, at P21 (left) $R_{p/d}$ =0.54, and P35 (right) $R_{p/d}$=0.80. In this group, comprising 31 cells from 12 *Scn2a*$^{+/L1314P}$ females, values of $R_{p/d}$, also reported in **Figure 3.2**, were qualitatively similar to the *Scn2a*$^{+/+}$ cells, with values >1 measured in 6 cases in the older group.

In *Scn2a*$^{+/L1314P}$ cells, intermediate values were observed, with 0.77 ± 0.24 (P21-40, N=31), 0.73 ± 0.14 (P21-24, N=11), and 0.92 ± 0.24 (P30-40, N=13). In this genotype, $R_{p/d}$ increased significantly with age (SP=0.970, p=0.0039), indicating a Na^+ influx developmental trajectory more comparable to *Scn2a*$^{+/+}$ than to *Scn2a*$^{+/-}$. However, $R_{p/d}$ values did not differ significantly from WT at examined age groups. Only a trend toward lower values was observed in the oldest group (SP= 0.814, p= 0.028).

Given that $R_{p/d}$ translates to the relative contribution of $Na_v1.2$-mediated influx in the proximal AIS, these differences suggest that $Na_v1.2$ activity is differentially affected in the two models. Although *Scn2a*$^{+/-}$ cells consistently exhibited lower $R_{p/d}$ ratios, *Scn2a*$^{+/L1314P}$ neurons showed a developmental increase in $R_{p/d}$, no significant difference was nonetheless detected when comparing the oldest group to the WT. Taken together, these results indicate that the proximal Na^+ influx, predominantly attributed to $Na_v1.2$ channels, is selectively reduced in *Scn2a*$^{+/-}$ cells, but not in *Scn2a*$^{+/L1314P}$ cells.

3.2 Calcium Currents Highlight Functional $Na_v1.2$ Deficits in *Scn2a*$^{+/-}$ Mice

Besides acting as a voltage-gated Na^+ channel, $Na_v1.2$ also conducts Ca^{2+} ions (Hanemaaijer et al., 2020), a property we recently characterized in cortical pyramidal neurons (Filipis et al., 2023). This dual permeability offers an additional mean to examine the activity of $Na_v1.2$ channels by addressing their Ca^{2+}-mediated influx. Importantly, Ca^{2+} entry through $Na_v1.2$ exhibits different kinetics compared to that mediated by voltage-gated calcium channels (VGCCs), which allows the two routes to be separated temporally. In the two representative examples shown in **Figure 3.3**A, the fractional Ca^{2+} fluorescence changes ($\Delta F/F_0$), associated with an AP evoked in the soma, are reported from the *d* and *p* sites of the AIS for two *Scn2a*$^{+/+}$ cells at P22 (left) and at P31 (right). The kinetics of the $\Delta F/F_0$ signal integrate two components of Ca^{2+} influx, one mediated by $Na_v1.2$ and the other mediated by VGCCs, and whose relative contributions depend on subcellular location. As previously shown, the Ca^{2+} component that is mediated by VGCCs is predominant at the proximal AIS, while the component driven by $Na_v1.2$ is more prominent at the distal site (Filipis et al., 2023).

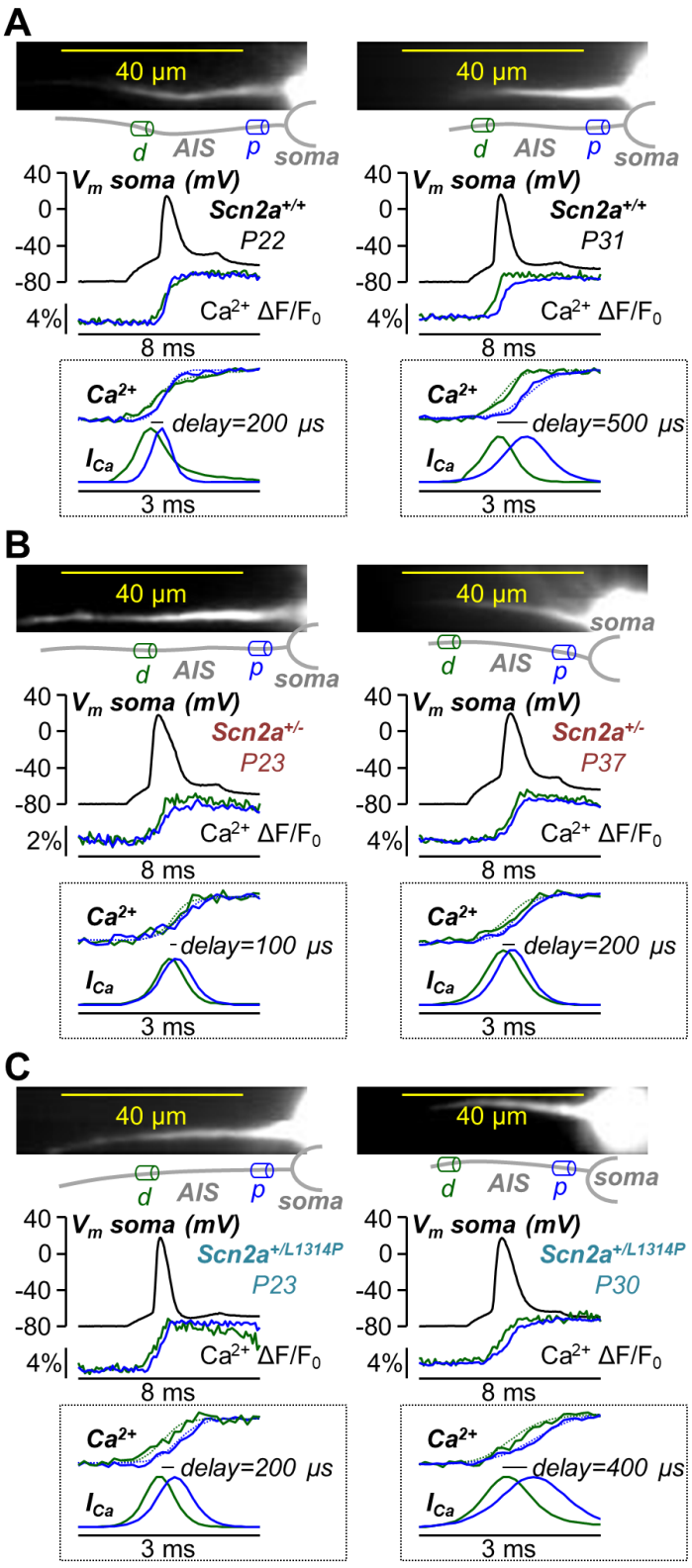

Figure 3.3 **Ca^{2+} influx in the AIS of *Scn2a*$^{+/+}$, *Scn2a*$^{+/-}$ and *Scn2a*$^{+/L1314P}$ L5 pyramidal neurons.**

(A) On the top-left, AIS of a *Scn2a*$^{+/+}$ L5 pyramidal neuron at P22 filled with OGB-5N in the recording position with reconstruction indicating a distal (*d*, green cylinder) and a proximal (*p*, blue cylinder) site. On the middle-left, an AP with corresponding Ca^{2+} transients from the two sites illustrated with the same color of the corresponding cylinders above. Inside the dotted inset, the same Ca^{2+} transients over 3 ms with fits (dotted lines) and, below, corresponding derived Ca^{2+} currents (I_{Ca}); *delay* between I_{Ca} peak at *d* and at *p* (200 µs) is indicated. On the right, same measurements and analysis for another *Scn2a*$^{+/+}$ cell at P31. In this case *delay* was 500 µs.

(B) Same measurements and analysis for two *Scn2a*$^{+/-}$ L5 pyramidal neurons, one at P23 (left) and the other at P37 (right). The values of *delay* were 100 µs and 200 µs in the younger and older cells respectively.

(C) Same measurements and analysis for two *Scn2a*$^{+/L1314P}$ L5 pyramidal neurons, one at P23 (left) and the other at P30 (right). The values of *delay* were 200 µs and 400 µs in the younger and older cells respectively.

Thus, by deriving the kinetics of the total Ca^{2+} current (I_{Ca}), using a previously described approach (Jaafari and Canepari, 2016), we were able to distinguish the two components based on their temporal profiles. The peak of the I_{Ca} signal consistently occurred earlier at the distal AIS, reflecting the faster kinetics of $Na_v1.2$ channels, and was delayed at proximal sites, supporting a stronger VGCC contribution near the soma (Filipis et al., 2023). This delay provides a quantitative measure of $Na_v1.2$-Ca^{2+} influx with respect to VGCC signal, and can be therefore used to evaluate, indirectly, the disruptions in $Na_v1.2$ function among genotypes.

3.2.1 Developmental Refinement of $Na_v1.2$-Mediated Ca^{2+} Influx Is Different in The Three Strains

In the two WT examples, shown in **Figure 3.3A**, the delay between the distal and proximal I_{Ca} was 200 μs (2 frames) at P22 and 500 μs (5 frames) at P31. Across 38 cells from 16 *Scn2a*$^{+/+}$ females, we quantified and plotted the *delays* for the full age range (P21-38) and for the two subgroups (P21-24 and P30-38) in **Figure 3.4**. Since *delays* were measured as discrete values, we applied to two independent groups the more appropriate two-sample Wilcoxon-Mann-Whitney (WMW) test for statistical comparisons, and considered that two groups are different when both the Standardized Effect Size (SES) exceeded 0.5 and the p-value was <0.01. In *Scn2a*$^{+/+}$ cells, delays significantly increased with age: the oldest group showed a significantly larger delay than the youngest (SES=0.66 and p=0.0012), and the mean of the delay at P30-38 (383 ± 111 μs) was consistent with our earlier findings (Filipis et al., 2023). This increase suggests an enhanced $Na_v1.2$-Ca^{2+} influx in WT cells at older ages.

Next, to determine whether a similar developmental pattern occurred in *SCN2A* LoF models, we examined the Ca^{2+} recordings in *Scn2a*$^{+/-}$ neurons. Two representative examples are shown in **Figure 3.3B**, from a cell at P23 (left) and another at P37 (right). We calculated the *delay* values in 39 cells obtained from 15 *Scn2a*$^{+/-}$ females for the three age groups, which are summarized in **Figure 3.4**. In contrast to controls, no significant age-dependent difference in I_{Ca} was detected in these mice (SES=0.23 and p=0.1709).

A similar analysis was performed in *Scn2a*$^{+/L1314P}$ animals. Two examples illustrated in **Figure 3.3C** report the results of Ca^{2+} recordings performed in two cells at P23 (left) and P30

(right). In this group, delays were measured across 37 cells from 10 females and reported in a histograms of delays (**Figure 3.4**). Similar to the case of *Scn2a*$^{+/-}$ mice, the *delays* did not differ between the youngest group and the oldest group (SES=0.29 and p=0.1268), indicating a lack of the Ca^{2+} kinetics refinement in both transgenic animal models.

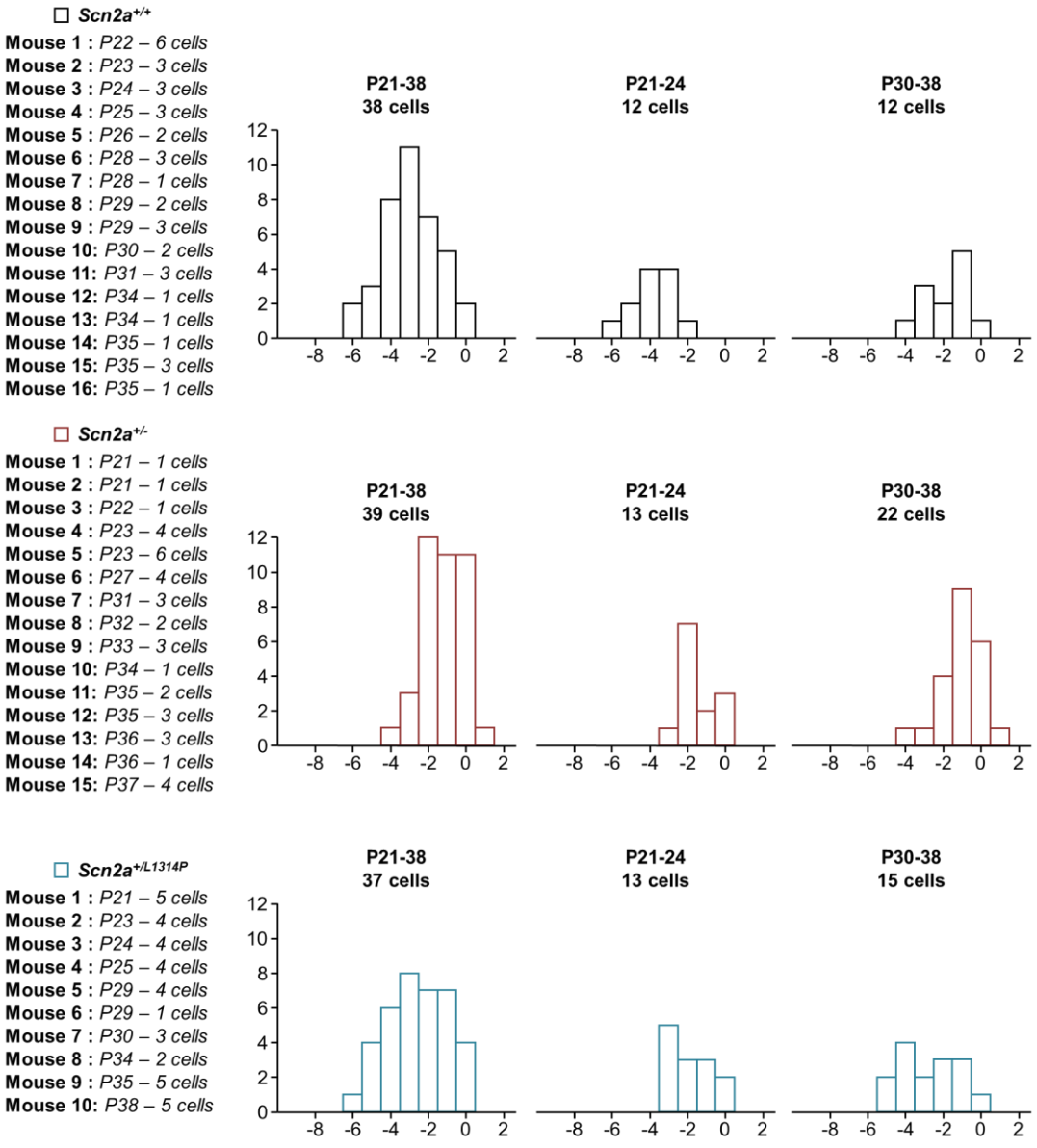

***Figure 3.4*. Histograms of delays between peaks of the Ca^{2+} current in proximal sites with respect to distal sites.** Top, values from 38 *Scn2a*$^{+/+}$ cells from 16 female mice at P21-38, P21-24 (12 cells) and P30-38 (12 cells). Middle, values from 39 *Scn2a*$^{+/-}$ cells from 15 female mice at P21-38, P21-24 (13 cells) and P30-38 (22 cells). Bottom, values from 37 *Scn2a*$^{+/L1314P}$ cells from 10 female mice at

P21-38, P21-24 (13 cells) and P30-38 (15 cells). In each histogram, the x-axis is expressed in number of frames where each unit corresponds to 100 µs.

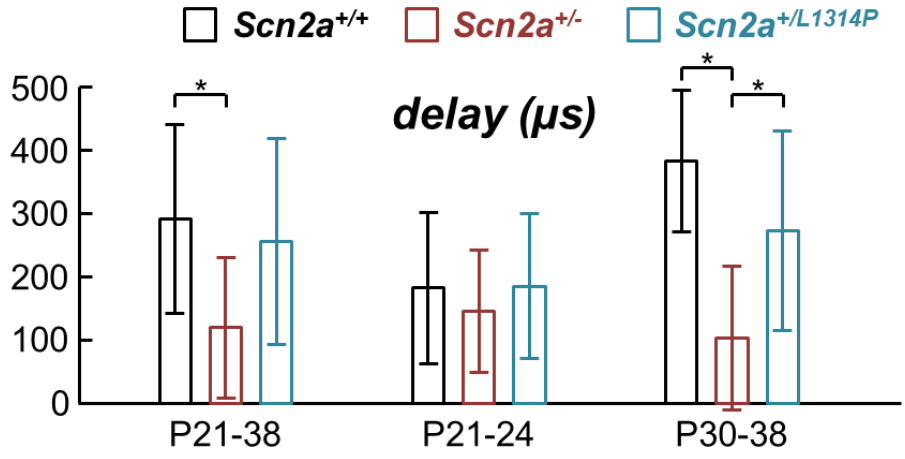

***Figure 3.5* Mean ± SD of delay for the three strains and the three age groups.** In *Scn2a*$^{+/+}$ cells, delay was 292±150 µs at P21-40 (N=38), 183±119 µs at P21-24 (N=12) and 383±111 µs at P30-40 (N=12). In *Scn2a*$^{+/-}$ cells, delay was 121±110 µs at P21-40 (N=39), 146±97 µs at P21-24 (N=13) and 105±113 µs at P30-40 (N=22). In *Scn2a*$^{+/L1314P}$ cells, delay was 257±163 µs at P21-40 (N=37), 185±114 µs at P21-24 (N=13) and 273±160 µs at P30-40 (N=15). "*" indicates that the result of the two-sample WMW-test between two groups gave SES>0.5 and p<0.01.

3.2.2 Reduced Ca^{2+} *Delays* in *Scn2a*$^{+/-}$ L5PNs

Next, we determined whether the alterations observed in the previous analysis of Na^+ signals could be reproduced in the kinetics of I_{Ca}. To test this hypothesis, we conducted a final comparative analysis between genotypes, all mean ± SD values of the delays for the three strains and the three age groups are reported in **Figure 3.5**. Across both the full age range P21-40 (SES=0.55 and $p=1.25\cdot10^{-5}$) and the oldest group P30-38 (SES=0.75 and $p=1.09\cdot10^{-5}$), *delays* in *Scn2a*$^{+/-}$ cells were significantly smaller than those in *Scn2a*$^{+/+}$ cells, and smaller than *Scn2a*$^{+/L1314P}$ cells only in the oldest group (SES=0.51 and p=0.0018).

To sum up, both *SCN2A* LoF models failed to show the AIS refinement of Ca^{2+} influx kinetics observed in *Scn2a*$^{+/+}$ cells. In *Scn2a*$^{+/-}$, Ca^{2+} *delay* values were consistently shorter, closely aligning with the Na^+ influx analysis, both indicating a significant decrease of functional $Na_V1.2$ channels in the KO model. Results from *Scn2a*$^{+/L1314P}$, by contrast, were more variable

and did not show a consistent pattern in the two measurements of Na^+ and Ca^{2+} ionic mechanisms.

3.3 Somatic APs in *Scn2a*$^{+/-}$ and *Scn2a*$^{+/L1314P}$ and *Scn2a*$^{+/+}$ mice

Following the analysis of Na^+ and Ca^{2+} influx and currents at the AIS, we next measured somatic action potentials (APs) to extend our comparisons across *Scn2a*$^{+/-}$ and *Scn2a*$^{+/L1314P}$ genotypes. Somatic recordings, in contrast to high-speed imaging experiments described earlier, provide a more accessible approach for characterizing AP properties, and allow analysis from a much larger number of cells. Although the AIS is the region where AP initiation occurs, the soma also serves as the compartment where the integrated output of this process is read out. This perspective cannot be neglected when evaluating the consequences of *SCN2A* mutations, and could be of particular relevance for the KI animals, where previous tests failed to reveal a consistent pattern.

Whole-cell patch-clamp recordings were performed in brain slices prepared from 15 *Scn2a*$^{+/+}$ female mice, 12 *Scn2a*$^{+/-}$ female mice and 14 *Scn2a*$^{+/L1314P}$ female mice, at different postnatal days. In total, we collected data from 142 *Scn2a*$^{+/+}$ cells, 138 *Scn2a*$^{+/-}$ cells and 136 *Scn2a*$^{+/L1314P}$ cells, all included in the subsequent analysis (**Table 3.1**).

Age (days old)	**21**	**22**	**23**	**24**	**25**	**26**	**27**	**28**	**29**	**30**	**31**	**32**	**33**	**34**	**35**	**36**	**37**	**T**
***Scn2a*$^{+/+}$**	17	21	-	16	1	6	-	19	14	11	1	12	-	-	-	18	-	142
***Scn2a*$^{+/-}$**	23	7	11	12	-	12	30	3	-	20	-	-	17	-	-	3	-	138
***Scn2a*$^{+/L1314P}$**	-	20	22	11	4	10	10	22	2	-	21	4	-	-	11	-	5	136

Table 3.1 **Summary of number of cells at different postnatal days analyzed for somatic AP in 15 *Scn2a*$^{+/+}$ mice, 12 *Scn2a*$^{+/-}$ mice and 14 *Scn2a*$^{+/L1314P}$ mice.**

AP_{thr} (mV)	**P21-37**	**P21-24**	**P30-37**
***Scn2a*$^{+/+}$**	-58.2 ± 3.9 (N=142)	-57.7 ± 4.3 (N=54)	-58.6 ± 3.5 (N=42)
***Scn2a*$^{+/-}$**	-57.2 ± 4.1 (N=138)	-57.8 ± 3.9 (N=53)	-57.3 ± 3.9 (N=40)
***Scn2a*$^{+/L1314P}$**	-57.7 ± 4.4 (N=136)	-56.6 ± 4.4 (N=53)	-59.1 ± 5.1 (N=41)

AP_{amp} (mV)	**P21-37**	**P21-24**	**P30-37**
***Scn2a*$^{+/+}$**	81.4 ± 6.4 (N=142)	80.8 ± 6.4 (N=54)	80.2 ± 7.0 (N=42)
***Scn2a*$^{+/-}$**	79.4 ± 7.9** (N=138)	83.2 ± 8.3 (N=53)	75.5 ± 7.5* (N=40)
***Scn2a*$^{+/L1314P}$**	78.6 ± 7.4** (N=136)	76.9 ± 7.0** (N=53)	78.3 ± 6.7 (N=41)

AP_{wid} (ms)	**P21-37**	**P21-24**	**P30-37**
***Scn2a*$^{+/+}$**	1.32 ± 0.29 (N=142)	1.35 ± 0.25 (N=54)	1.17 ± 0.22 (N=42)
***Scn2a*$^{+/-}$**	1.36 ± 0.42 (N=138)	1.61 ± 0.45** (N=53)	1.19 ± 0.32 (N=40)
***Scn2a*$^{+/L1314P}$**	1.39 ± 0.41* (N=136)	1.40 ± 0.34 (N=53)	1.13 ± 0.35* (N=41)

Table 3.2 **Mean ± SD of AP_{thr}, AP_{amp}, and AP_{wid} in cells from 15 *Scn2a*$^{+/+}$ female mice, 12 *Scn2a*$^{+/-}$ female mice and 14 *Scn2a*$^{+/L1314P}$ female mice at three time windows (P21-37, P21-24 and P30-37).** The number of cells (N) for each population is indicated.

In these experiments, we elicited an AP by somatic injection of a current pulse of 50-300 pA amplitude and 150 ms durations in cells initially maintained at their resting membrane potential (V_{rest}), thereby minimizing the bridge potential, which was not corrected in this analysis. **Figure 3.7A** shows an example of a recording from a *Scn2a*$^{+/+}$ cell at P31 to illustrate the parameters that were analyzed.

Since the series resistance of the patch pipette in our experiments was typically in the 5-10 MΩ range, the resulting error caused by the bridge potential could introduce up to 3 mV in the estimate of the AP threshold (AP_{thr}). Thus, we focused the analysis on two parameters that are not affected by the bridge potential: the AP amplitude (AP_{amp}), defined as the difference between the AP peak (AP_{peak}) and AP_{thr}, and of the AP width (AP_{wid}), defined as the interval at which V_m is above the value corresponding to half of AP_{amp}. The scatter plots of the analyzed somatic AP parameters against age are reported in **Figure 3.6**.

As in the analysis of Na^+ and Ca^{2+} imaging experiments, cells were grouped into three age ranges (P21-37, P21-24 and P30-37). The averaged somatic APs for the three genotypes within these age groups are shown in **Figure 3.7B**. Although the overall traces appeared similar, the most evident differences were observed at P21-24: *Scn2a*$^{+/-}$ cells showed a wider AP, and the AP in *Scn2a*$^{+/L1314P}$ cells displayed a smaller amplitude. Quantitative statistics

(mean ± SD) for all parameters for the three strains and the three age groups are reported in **Figure 3.7C**.

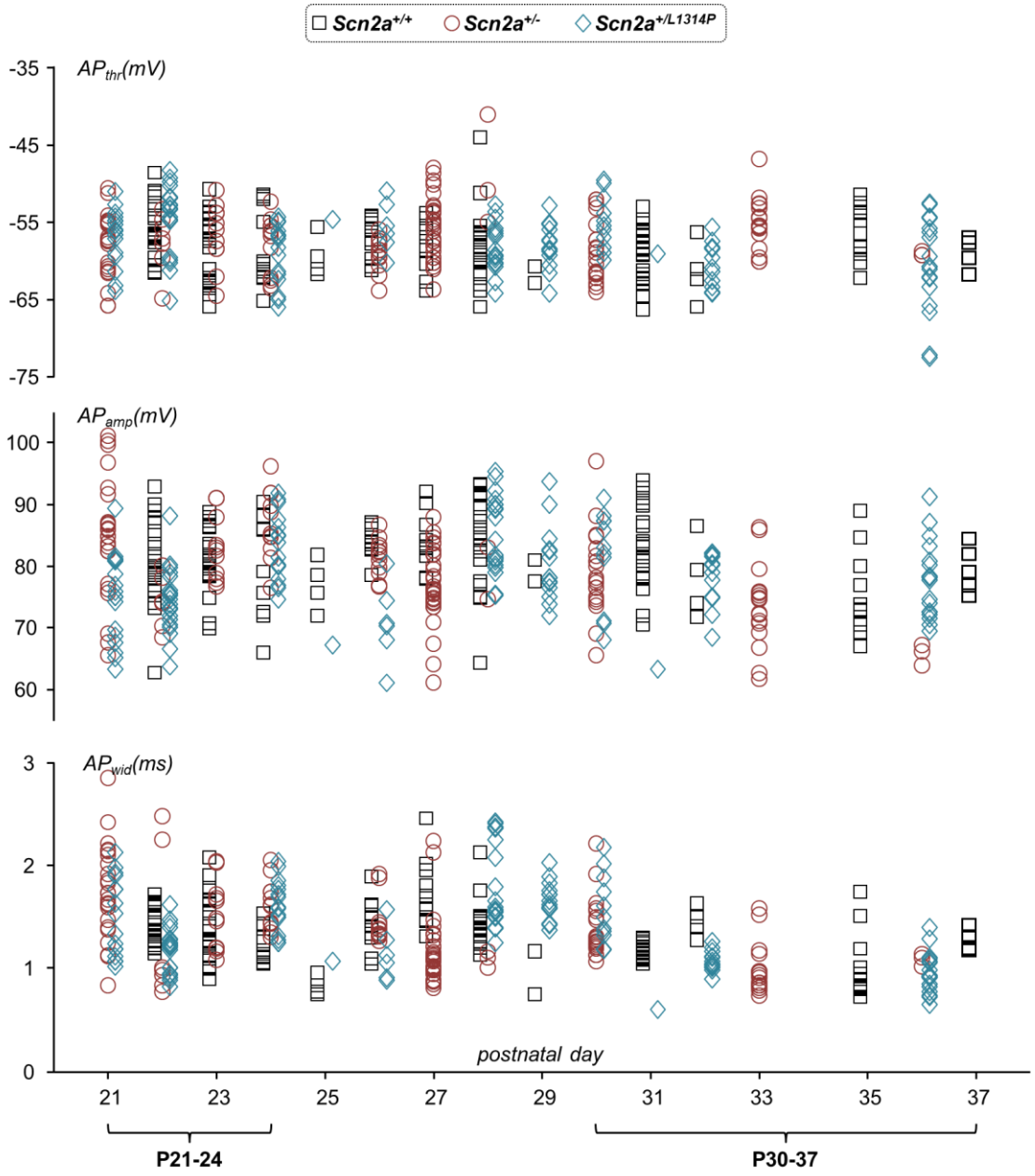

***Figure 3.6* Scatter plots of analyzed somatic action potential parameters against age.** Scatter plots of AP_{thr} (top), AP_{amp} (middle) and AP_{wid} (bottom) parameters in *142 Scn2a*$^{+/+}$ cells, in 138 *Scn2a*$^{+/-}$ and in 136 *Scn2a*$^{+/L1314P}$ cells. The two ranges (P21-24 and P30-37) are indicated

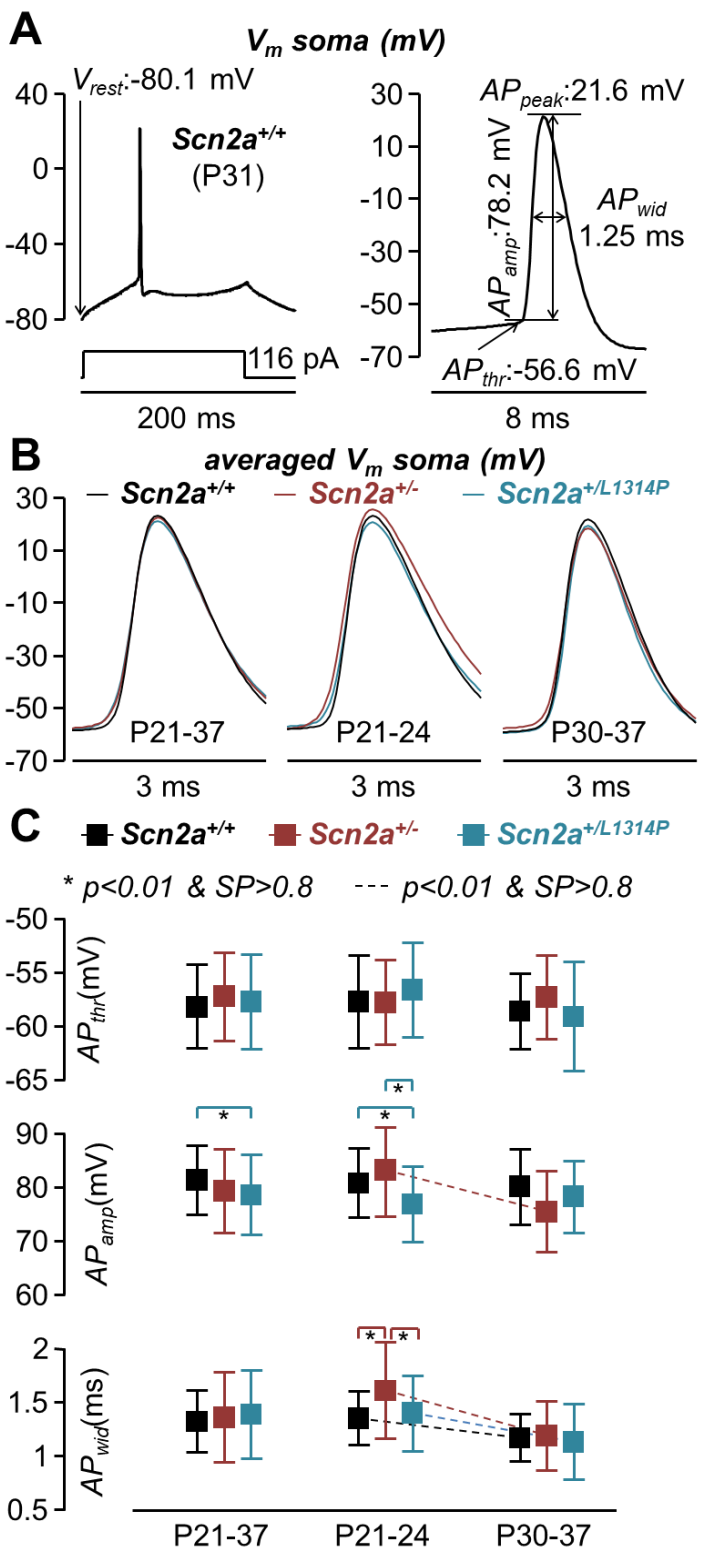

***Figure 3.7* Somatic AP of *Scn2a*$^{+/+}$, *Scn2a*$^{+/-}$ and *Scn2a*$^{+/L1314P}$ L5 pyramidal neurons.**

(A) On the left, somatic AP elicited by a 116 pA current pulse of 150 ms duration from a resting potential of -80.1 mV in a *Scn2a*$^{+/+}$ L5 pyramidal neuron at P31. On the right, illustration of the parameters used for the analysis: threshold (AP_{thr}, -56.6 mV), amplitude (AP_{amp}, 78.2 mV) calculated as difference from AP_{thr} and peak (AP_{peak}, 21.6 mV), and width (AP_{wid}, 1.25 ms) calculated as the interval at which V_m is above the value corresponding to half of AP_{amp}.

(B) Average of APs of all measured *Scn2a*$^{+/+}$ cells, *Scn2a*$^{+/-}$ cells, and *Scn2a*$^{+/L1314P}$ cells at P21-37, P21-24 and P30-37. Notice the greatest differences at P21-24.

(C) Mean ± SD of AP_{thr} (top), AP_{amp} (middle) and AP_{wid} (bottom) for *Scn2a*$^{+/+}$ cells, *Scn2a*$^{+/-}$ cells, and *Scn2a*$^{+/L1314P}$ cells at P21-37, P21-24 and P30-37. "*" indicates that the result of the two-sample KS-test between two groups of same age and different strain gave SP>0.8 and p<0.01. The dashed line indicates that the result of the two-sample KS-test between two age groups of the same strain gave SP>0.8 and p<0.01.

3.3.1 Somatic AP Amplitude in The Three Strains

As in the Na^+ imaging analysis of $R_{p/d}$ values, we assessed differences in AP parameters using the KS-test, considering that two groups are different when both SP is >0.8 and p-value is <0.01. Since AP_{thr} values were affected by errors in bridge potential, not surprisingly, no significant differences were detected for this parameter. In contrast, AP_{amp} values showed clear genotype and age-dependent effects. *Scn2a*$^{+/L1314P}$ cells exhibited reduced amplitudes compared to *Scn2a*$^{+/+}$ cells both across the full age range (P21-37; SP=0.929, p=0.001093) and in the youngest group (P21-24; SP=0.843, p=0.004413). Moreover, young *Scn2a*$^{+/-}$ cells displayed larger AP_{amp} values than *Scn2a*$^{+/L1314P}$ neurons (SP=0.989; $p=3.9\cdot10^{-5}$), but this parameter declined significantly in the older *Scn2a*$^{+/-}$ cells (SP=0.996; $p=7.1\cdot10^{-5}$).

3.3.2 Somatic AP Width in The Three Strains

AP_{wid} values also showed age dependence across all genotypes, being larger in younger than in older groups: in *Scn2a*$^{+/+}$ cells (SP=0.965; p=0.003498), in *Scn2a*$^{+/-}$ cells (SP=0.999; $p=0.7\cdot10^{-5}$), and in *Scn2a*$^{+/L1314P}$ cells (SP=0.962; $p=8.0\cdot10^{-5}$). In addition, within the youngest group, AP_{wid} values were larger in *Scn2a*$^{+/-}$ cells with respect to *Scn2a*$^{+/+}$ cells (SP=0.947; p=0.000693).

These results cannot be explained by changes in Na^+ current alone. The AP parameters analyzed here are tightly regulated by the interplay between Na^+ and K^+ currents, which shape the AP width and amplitude in opposite directions. An increase of Na^+ current generally leads to an increase of both AP_{amp} and AP_{wid}, whereas an increase of K^+ current produces the opposite effect, and reduces both parameters. In our dataset, if the reduction in the AP width with age were driven by Na^+, one would expect a corresponding decline in Na^+ influx with age. However, no such decrease was reported in our Na^+ imaging (**Figure 3.1D**), and in *Scn2a*$^{+/L1314P}$ cells Na^+ influx even increased, which excludes the sodium as the mechanism responsible for the AP sharpening. Instead, these changes can be explained only by an increase in K^+ current.

Likewise, in the young groups, the larger AP_{wid} observed in *Scn2a*$^{+/-}$ cells is consistent with reduced K^+ currents, and the smaller AP_{amp} observed in *Scn2a*$^{+/L1314P}$ cells can be best

attributed to relatively larger K^+ currents compared to *Scn2a*$^{+/+}$ cells. Notably, both voltage-gated K^+ channels (VGKCs) and Ca^{2+}-activated K^+ channels (CAKCs) are particularly enriched in the AIS compared to the soma, where they contribute to the largest changes in the shape of the generating AP.

Thus, although measured at the soma, the shifts in AP properties across genotypes and ages pointed toward mechanisms rooted at the AIS, which motivated us to directly examine the AP waveform at the site where these spikes are initiated.

3.4 Exceptionally Sharp Action Potentials Are Generated at The Distal AIS of *Scn2a*$^{+/L1314P}$ Cells

To test whether somatic differences in AP properties reflected changes in the shape of the generating spike at the AIS, we performed high-speed voltage imaging in L5PNs from the three strains. This approach complemented our prior Na^+ and Ca^{2+} imaging at the AIS, allowing us to directly address the AP waveform at the site of initiation and to construct a detailed profile of AP generation in the presence of *SCN2A* LoF mutations. We focused our analysis on the AP width (AP_{wid}), defined as the time interval during which the membrane potential (V_m) remains above half of the AP amplitude. **Figure 3.8A** shows an example from a *Scn2a*$^{+/+}$ cell at P26, where an AP evoked in the soma and the associated changes in membrane voltage were reported from three sites of 5 µm each along the AIS: distal (*d*, green traces), medial (*m*, red traces), and proximal (*p*, blue traces); AP_{wid} was then measured from each site as indicated (**Figure 3.8B**).

Figure 3.8C illustrates representative recordings from one L5PN per genotype, all obtained at postnatal day 23. In the *Scn2a*$^{+/+}$ cell (left), AP_{wid} values decreased progressively toward distal AIS regions: 0.95 ms at the proximal, 0.9 ms at the medial, and 0.7 ms at the distal site, consistent with the spatial sharpening of the AP along the AIS (Kole et al., 2007; Palmer & Stuart, 2006; Popovic et al., 2011). In the *Scn2a*$^{+/-}$ cell (middle), the AP was slightly wider at the proximal (1 ms) and the distal (0.75 ms) sites. In contrast, the *Scn2a*$^{+/L1314P}$ cell (right) showed a particularly sharper AP at the distal site (AP_{wid}=0.3 ms), with progressively larger AP_{wid} values at more proximal regions (0.50 ms at m, 0.80 ms at p).

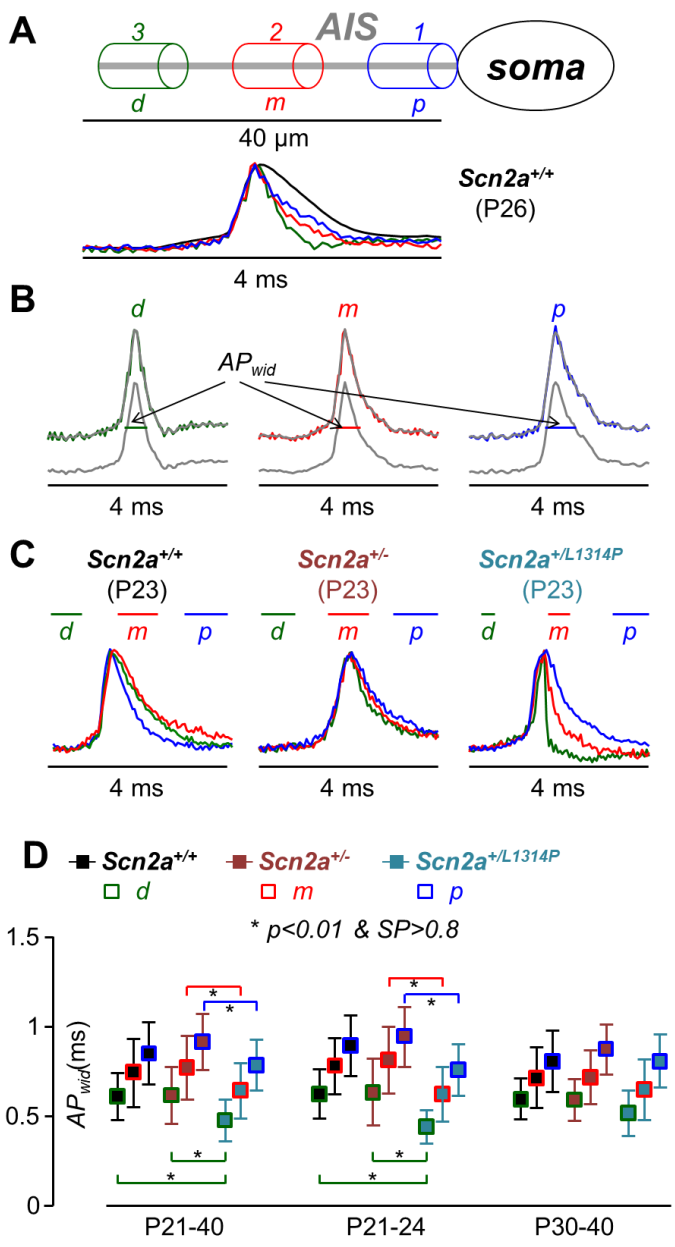

Figure 3.8 **Analysis of the action potential shape in the AIS of *Scn2a*$^{+/+}$, *Scn2a*$^{+/-}$ and *Scn2a*$^{+/L1314P}$ L5 pyramidal neurons.**

(A) Schematic representation of the imaging strategy showing the spatial profile of V_m transients in a representative *Scn2a*$^{+/+}$ neuron at P26 from three AIS regions (5 µm each): distal (d, green), medial (m, red), and proximal (p, blue), superimposed to the somatic AP (black trace).

(B) AP traces recorded from the three AIS sites of the same cell, indicating the AP_{wid} calculated as the time during which membrane potential remains above half-maximal amplitude.

(C) Same measurements and analysis for three representative L5 pyramidal neurons recorded at P23 from *Scn2a*$^{+/+}$ (left), *Scn2a*$^{+/-}$ (middle), and *Scn2a*$^{+/L1314P}$ (right). Notice the sharper AP waveform at the distal and medial sites in the *Scn2a*$^{+/L1314P}$ compared to the two other cells.

(D) Mean ± SD of AP_{wid} values for *Scn2a*$^{+/+}$ cells, *Scn2a*$^{+/-}$ cells, and *Scn2a*$^{+/L1314P}$ cells at P21-40, P21-24 and P30-40 at distal (d), medial (m), and proximal (p) AIS sites. "*" indicates that the result of the two-sample KS-test at one specific AIS site between two groups of same age and different strain gave SP>0.8 and p<0.01.

AP_{wid} (ms) **Scn2a$^{+/+}$**	**P21-40**	**P21-24**	**P30-40**
distal	0.611 ± 0.131 (N=47)	0.627 ± 0.136 (N=24)	0.595 ± 0.113 (N=20)
medial	0.744 ± 0.165 (N=47)	0.781 ± 0.158 (N=24)	0.71 ± 0.17 (N=20)
Proximal	0.847 ± 0.173 (N=47)	0.894 ± 0.17 (N=24)	0.802 ± 0.171 (N=20)

AP_{wid} (ms) **Scn2a$^{+/-}$**	**P21-40**	**P21-24**	**P30-40**
distal	0.612 ± 0.159 (N=47)	0.633 ± 0.187 (N=26)	0.586 ± 0.116 (N=21)
medial	0.77 ± 0.178 (N=47)	0.815 ± 0.188 (N=26)	0.714 ± 0.15 (N=21)
Proximal	0.91 ± 0.158 (N=47)	0.944 ± 0.168 (N=26)	0.867 ± 0.138 (N=21)

AP_{wid} (ms) **Scn2a$^{+/L1314P}$**	**P21-40**	**P21-24**	**P30-40**
distal	0.474 ± 0.117 (N=51)	0.435 ± 0.092 (N=23)	0.517 ± 0.127 (N=24)
medial	0.639 ± 0.155 (N=51)	0.622 ± 0.154 (N=23)	0.646 ± 0.169 (N=24)
Proximal	0.474 ± 0.117 (N=51)	0.759 ± 0.144 (N=23)	0.806 ± 0.148 (N=24)

Table 3.3 **Mean ± SD of AP_{wid} at proximal, medial, and distal AIS sites in cells from 26 *Scn2a$^{+/+}$* female mice, 23 *Scn2a$^{+/-}$* female mice and 29 *Scn2a$^{+/L1314P}$* female mice at three time windows (P21-37, P21-24 and P30-37).** The number of cells (N) for each population is indicated.

We quantified AP_{wid} in a total of 47 cells from 26 *Scn2a$^{+/+}$* females, 47 cells from 23 *Scn2a$^{+/-}$* females, and 51 cells from 29 *Scn2a$^{+/L1314P}$* females. Statistics (mean ± SD) values for the three strains and the three age groups at each AIS subregion are summarized in **Table 3.3** and **Figure 3.8D**. As expected from prior studies, APs were consistently wider at more proximal AIS sites in all genotypes. Two-sample Kolmogorov–Smirnov (KS) test was used to assess these differences at the three axonal site (distal, medial, proximal) and for each age window (P21-24, P30-40, and P21-40). Statistical significance was defined by $p < 0.01$ and SP > 0.8. No significant changes in AP_{wid} were detected between age groups in any genotype (P21-24 vs. P30-40), suggesting that AIS spike width remained relatively stable during the examined juvenile development.

Between the genotypes, however, clear differences were observed. In the youngest animals (P21-24), *Scn2a$^{+/L1314P}$* showed significantly smaller AP_{wid} at the distal AIS compared to both *Scn2a$^{+/+}$* (p=0.0003, SP=0.99) and to *Scn2a$^{+/-}$* (p=0.001, SP=0.98) cells. At the same age, a

similar pattern was evident at the medial and proximal sites, but only in comparison with *Scn2a*$^{+/-}$ cells (medial: p=0.003, SP=0.91; proximal: p=0.0018, SP=0.93).

When evaluating all ages together (P21-40), the same observations persisted. At the distal site, AP_{wid} remained significantly larger in *Scn2a*$^{+/+}$ (p=0.0002, SP=0.99) and *Scn2a*$^{+/-}$ (p=0.0001, SP=0.99) compared to *Scn2a*$^{+/L1314P}$, whereas at the medial and proximal AIS subregions, only *Scn2a*$^{+/-}$ cells showed increased AP_{wid} relative to *Scn2a*$^{+/L1314P}$ (medial: p=0.002, SP=0.92; proximal: p=0.002, SP=0.9). By contrast, in the older age group (P30-40), no differences were detected, suggesting that these alterations of the AP waveform are more relevant in the younger animals and tend to converge with age.

Overall, the direct assessment of the initiating AP aligns with the somatic analysis: in young *Scn2a*$^{+/L1314P}$ cells, APs were sharper distally than in both *Scn2a*$^{+/+}$ and *Scn2a*$^{+/-}$, and smaller widths at medial and proximal sites were also observed relative to *Scn2a*$^{+/-}$. Together with the reduced somatic AP amplitude observed earlier, these findings converge to a common scenario which is likely a contribution of the AIS expressed K^+ channels with a relatively increased K^+ conductance to the altered AP waveform in the KI model, an idea that we next approached using targeted pharmacological interventions aiming to dissect which of the K^+ conductances account for these outcomes.

3.5 The Effects of Blocking K_v1, K_v7, and BK Channels in The AIS

Finally, with K^+ role in the disrupted shape of the generating AP now evident from previous analyses, we asked which of the AIS predominantly expressed K^+ channel families mediate these effects. In a final set of experiments, we performed high speed voltage imaging combined with local pharmacological applications near the AIS in L5 pyramidal neurons from *Scn2a*$^{+/+}$, *Scn2a*$^{+/-}$, and *Scn2a*$^{+/L1314P}$ mice. We focused on well-established K^+ channels known to regulate the shape the AP at the AIS: namely the two VGKC subfamilies K_v1 and K_v7, and the Ca^{2+}-activated BK channels (Cooper, 2010; Filipis et al., 2023; Kole et al., 2007; Kuba et al., 2015).

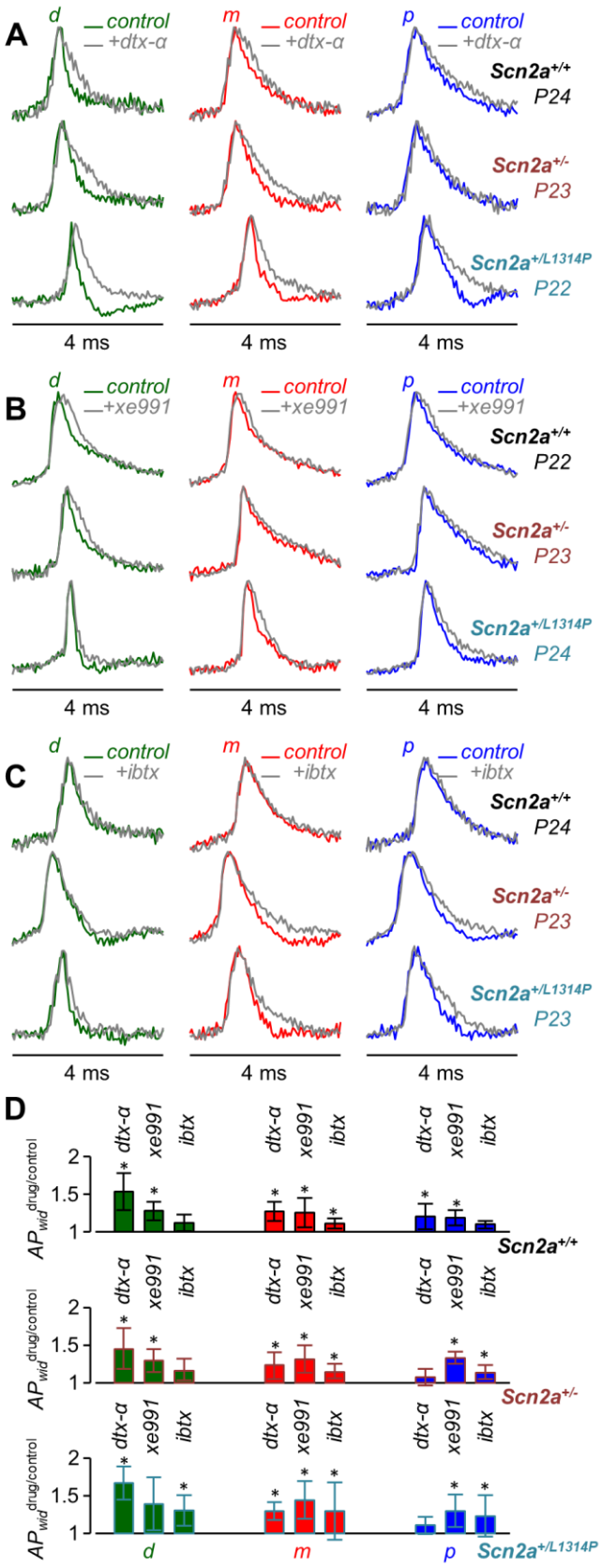

Figure 3.9 **Effects of local K_v1, K_v7, and BK channel blockers on AP waveform in the AIS of *Scn2a*$^{+/+}$, *Scn2a*$^{+/-}$, and *Scn2a*$^{+/L1314P}$ L5 pyramidal neurons.**

(A) Representative V_m transients from *Scn2a*$^{+/+}$ (P24), *Scn2a*$^{+/-}$ (P23), and *Scn2a*$^{+/L1314P}$ (P22) neurons before and after local application of dendrotoxin-α (DTX-α, 500 nM), across distal (d, green), medial (m, red), and proximal (p, blue) AIS sites. Notice the clear AP widening distally, with a maximal effect in the *Scn2a*$^{+/L1314P}$ cell.

(B) Same measurements in representative *Scn2a*$^{+/+}$ (P22), *Scn2a*$^{+/-}$ (P23), and *Scn2a*$^{+/L1314P}$ (P24) neurons after local application of XE991 (10 µM). Less widening is evident at the distal AIS of the *Scn2a*$^{+/L1314P}$ example compared to *Scn2a*$^{+/+}$ and *Scn2a*$^{+/-}$ cells; effects on medial and proximal sites appear comparable.

(C) Representative recordings from *Scn2a*$^{+/+}$ (P24), *Scn2a*$^{+/-}$ (P23), and *Scn2a*$^{+/L1314P}$ (P23) neurons after local application of iberiotoxin (Ibtx, 1 µM). Ibtx induced less visible effects in all sites in *Scn2a*$^{+/+}$ cell, relatively larger effects are shown mutant cells.

(D) Mean ± SD of AP_{wid} ratio (drug/control) for the three drugs across the three AIS sites in *Scn2a*$^{+/+}$, *Scn2a*$^{+/-}$, and *Scn2a*$^{+/L1314P}$ neurons. "*" indicates a significant change ($p<0.01$, paired t-test).

To isolate their contributions, we applied each blocker in independent experiments: dendrotoxin-α (DTX-α,), XE991, and iberiotoxin (IbTx), at 500 nM, 10 μM, and 1 μM respectively. To quantify the drug effects, we computed for each cell, at each AIS site (*d*: distal, *m*: medial, and *p*: proximal), the ratio of AP_{wid} after drug application relative to control condition ($AP_{wid\ drug}/AP_{wid\ control}$), allowing us to compare the AP widening driven by the blocking compounds across genotypes, since all three drugs act by slowing repolarization phase of generating APs. Of note, each drug was examined independently and no cell was exposed to more than one compound. These effects were evaluated using paired t-tests with α=0.01. Means ± SD for all drugs, genotypes, and AIS subregions are reported in **Figure 3.9D**.

3.5.1 K_v1 Channel Block Preferentially Widens Distal APs with The Strongest Effect in *Scn2a*$^{+/L1314P}$ Cells

DTX-α was tested in 9 *Scn2a*$^{+/+}$, 9 *Scn2a*$^{+/-}$, and 10 *Scn2a*$^{+/L1314P}$ cells. In the representative *Scn2a*$^{+/+}$example at P24 (**Figure 3.9A**), AP_{wid} increased from 0.5 ms to 0.7 ms at the distal site, from 0.85 to 1 ms at the medial site, and from 1.05 to 1.15 ms at the proximal site. A *Scn2a*$^{+/-}$ neuron at P23 displayed comparable effects, with widening from 0.65 to 0.90 ms distally, 0.70 to 0.95 ms medially, and 0.95 to 1.00 ms proximally. In contrast, the *Scn2a*$^{+/L1314P}$ example at P22 started from sharper APs (0.40, 0.50, 0.80 ms at d, m, p), yet still showed a larger widening after DTX-α (0.65, 0.75, 0.95 ms).

Statistical testing confirmed that local delivery of DTX-α widened the distal APs in all the three genotypes. The largest increase of 66%, interestingly, was observed in *Scn2a*$^{+/L1314P}$ cells ($p=1.0\cdot10^{-5}$), followed by 53% in WT (p=0.0001), and 42% in *Scn2a*$^{+/-}$ (p=0.00042). This effect remained significant in the three strains at the medial AIS site (+27%, +21%, +29% in WT, KO, KI; p =0.00016, 0.003, $1.6\cdot10^{-5}$, respectively). Whereas at proximal sites, a smaller but significant widening was evident only in WT cells (+19%, p=0.005).

3.5.2 Distal APs in *Scn2a*$^{+/L1314P}$ Cells Are Poorly Affected by K_v7 Channel Block

From the representative voltage transients from XE991 experiments shown in **Figure 3.9B**, the AP appeared clearly wider after adding the drug at all tested axonal sites in *Scn2a*$^{+/+}$ neuron at P22, and *Scn2a*$^{+/-}$ cell at P23. The *Scn2a*$^{+/L1314P}$ example at P24, however, showed no widening distally, while the effect was still apparent at medial and proximal sites.

Based on recordings from 8 WT, 9 KO, and 8 KI neurons, at distal AIS sites, XE991 application significantly increased the distal AP width in *Scn2a*$^{+/+}$ (+27%, p=9.1·10^{-5}) and *Scn2a*$^{+/-}$ (+29%, p=0.00066), but not in *Scn2a*$^{+/L1314P}$ cells. In contrast, XE991 produced a consistent widening in all three genotypes at the medial (WT +24.5%, p=0.005; KO +29%, p=0.0001; KI +40%, p=0.0002, respectively) and proximal (WT +19%, p=0.0015; KO +33%, p=8.49·10^{-6}; KI +27%, p=0.001, respectively) AIS subregions.

3.5.3 BK Channel Block Produces the Weakest Modulation of AP Shape

Representative Ibtx recordings are illustrated in **Figure 3.9C**. In the *Scn2a*$^{+/+}$ neuron at P24, only subtle changes were observed between the control traces and those following drug delivery. We noticed that Ibtx slightly widened the AP in the *Scn2a*$^{+/-}$ cell at P23 at medial and proximal sites, whereas a more pronounced widening was visible at the distal site in the *Scn2a*$^{+/L1314P}$ cell at P23.

Based on the analysis across 8 WT, 8 KO, and 9 KI neurons, Ibtx produced overall smaller effects compared to DTX-α and XE991 but nonetheless caused significant widening at selected AIS sites. At medial sites, Ibtx significantly increased AP_{wid} in the three animal groups (*Scn2a*$^{+/+}$ +8.5%, p=0.008; *Scn2a*$^{+/-}$ +14%, p=0.002; *Scn2a*$^{+/L1314P}$ +23%, p=0.00068). At proximal sites, significant widening was detected in both in *Scn2a*$^{+/-}$ (+13%, p=0.0031) and *Scn2a*$^{+/L1314P}$ (+19%, p=0.009), and at distal AIS sites selectively in *Scn2a*$^{+/L1314P}$ cells (+28%, p=0.0018).

In these pharmacological tests, we started with a prediction that if the sharper distal APs observed in *Scn2a*$^{+/L1314P}$ mice truly reflect an enhanced K^+ mediated repolarization, the local

block of the relevant K^+ channels should preferentially widen this AP in KI cells relative to WT and *Scn2a*$^{+/-}$. When applied, DTX-α produced the most robust AP widening at the distal region of the AIS in all genotypes, but its effect was interestingly largest in *Scn2a*$^{+/L1314P}$ with a 66% increase in distal AP width. BK block also caused increased width in the distal AP in *Scn2a*$^{+/L1314P}$ cells (+28%), but its effect was lower compared to DTX. XE991, however, widened the distal AP in the controls, but not in mutant mice, thus excluding any dominant role for K_v7 family (KCNQ/M) in shaping *Scn2a*$^{+/L1314P}$ AP distally.

Altogether, these results align with an increased K_v1 function in mediating the sharper spikes observed at the distal AIS in *Scn2a*$^{+/L1314P}$ mice. By contrast, the wider somatic APs observed in younger KO cells in previous somatic recordings were not reproduced in AIS voltage imaging, suggesting that the underlying mechanism is more complex than a simple deficit in K^+ repolarization at the AIS in these animals. It is worth noting that the interpretation of K^+ pharmacology differs fundamentally from Na^+ or Ca^{2+} manipulations, since blocking outward currents can affect the overall excitability. Accordingly, this analysis should be considered exploratory, and the mechanistic explanations of these heterogeneous findings require further investigation and will be addressed in the Discussion.

3.6 Summary and Insights

In this chapter, we characterized the physiological consequences of *SCN2A* loss-of-function mutations on the AP initiation in L5 pyramidal neurons. With sodium imaging we report that *Scn2a*$^{+/-}$ neurons displayed a marked reduction in proximal Na^+ influx, consistent with a persistent deficit in $Na_v1.2$-mediated currents, whereas *Scn2a*$^{+/L1314P}$ did not show any significant decline. We further confirmed the genotype-specific alterations of ionic mechanisms in the analysis of Ca^{2+} kinetics. The enhanced segregation in calcium currents component kinetics with age was absent in the two mutants. In addition, *Scn2a*$^{+/-}$ cells exhibited consistently reduced $Na_v1.2$- mediated Ca^{2+} influx, aligning with their $Na_v1.2$ deficits.

From whole-cell recordings, we tackled the somatic AP properties and we showed that AP amplitude was reduced in *Scn2a*$^{+/L1314P}$ cells, particularly at the early juvenile period, pointing to an increased K^+ current in these mice. However, a contrary scenario emerged

from AP width analysis, as this parameter was larger in young *Scn2a*$^{+/-}$ neurons, consistent with reduced K^+ conductance in this model. We next moved to voltage imaging at the AIS, which confirmed that these somatic changes reflected alterations at the site of AP initiation in *Scn2a*$^{+/L1314P}$ cells, where distal APs were sharper compared to both wild-type and *Scn2a*$^{+/-}$ cells, particularly in younger animals, which reinforced the hypothesis of an enhanced K^+ signal in the KI mice, and the view of divergent excitability profiles between the two *SCN2A* LoF models. Finally, we locally blocked AIS-enriched K^+ channels, and we identified the K_v1 as the main subfamily underlying currents that shape the differences observed primarily in the *Scn2a*$^{+/L1314P}$ model. In cells from *Scn2a*$^{+/-}$ animals, pharmacological effects were less straightforward, suggesting distinct alterations in the K^+ channel activities.

Overall, this chapter highlighted how the ionic mechanisms governing AP initiation at the AIS were reshaped in different manners in two heterozygous *SCN2A* LoF mouse models. Yet, the mechanistic basis of these changes remains unclear. In particular, the unanswered question whether the increased K^+ currents observed in *Scn2a*$^{+/L1314P}$ arise from an upregulation of K_v1 channel density, a spatial redistribution of ion channels, or a compensatory remodeling in the AIS. By the same token, *Scn2a*$^{+/-}$ cells also implied complex multiscale changes in both Na^+ and K^+ currents, which will be addressed in Chapter 6.

These findings established together a framework for the next Chapter. We will extend the analysis to somatic and dendritic compartments to investigate how the reported AIS-specific changes are translated at the level of back-propagating AP (bAP) events, and more broadly, how $Na_v1.2$ genetic disruptions affect the excitability and integrative properties of L5 pyramidal neurons.

4

Insights into Somatic and Dendritic Excitability in *Scn2a*$^{+/-}$ and *Scn2a*$^{+/L1314P}$ Mouse Models

4.1 SOMATIC ACTION POTENTIAL AMPLITUDE DURING SHORT-INTERVAL BURSTS……109
4.2 DESCRIPTIVE CHARACTERIZATION OF REGENERATIVE DENDRITIC CALCIUM RESPONSES IN *SCN2A* LOF MODELS……113
4.2.1 Dendritic Calcium Electrogenesis Increases with Age in Scn2a$^{+/-}$ but Declines in Scn2a$^{+/L1314P}$..... 115
4.2.2 Dendritic Ca^{2+} Electrogenesis Occurs at Comparable Frequencies Across Experimental Groups . 117
4.2.3 Dendritic Ca^{2+} Electrogenesis Amplitude Ratios in the Three Strains 120
4.3 SUMMARY AND INSIGHTS ……122

In the preceding chapter, we explored the *SCN2A* loss-of-function (LoF) effects on action potential (AP) initiation at the axon initial segment (AIS). Here, we extend this analysis to determine whether these mutations could alter neuronal excitability or disrupt related mechanisms in other neuronal compartments. Layer 5 pyramidal neurons (L5PNs) integrate inputs across different compartments with distinct biophysical properties: APs are initiated at the AIS, propagate along the axon, and backpropagate into somatic and dendritic domains (Stuart & Sakmann, 1994). In addition to its principal function in the AIS, $Na_v1.2$ is the

predominant sodium channel isoform in the dendrites of mature pyramidal cells, and is the only isoform supporting AP backpropagation and somatodendritic signal conduction (Hu et al., 2009). This may suggest that *SCN2A* haploinsufficiency could impair neuronal excitability beyond AP initiation and could have profound effects on modulating the mechanisms involved in dendritic AP backpropagation and synaptic integration. In line with this hypothesis, Spratt et al. (2019) reported that mature *SCN2A* haploinsufficiency neurons exhibit normal somatic firing, but their dendritic AP backpropagation and long-term potentiation were significantly reduced. Recent in vivo imaging also reported impaired dendritic integration in deep layer neurons (Wu et al., 2025). To investigate these outcomes, we implemented two approaches targeting the soma and distal apical dendrites. At the soma, firing fidelity depends on both the availability of sodium channels and the interplay between depolarizing and repolarizing ionic currents (Bean, 2007; Kole et al., 2008). We therefore asked whether $Na_v1.2$ LoF channelopathies might impair the neuron's ability to sustain somatic firing during rapid and repetitive activation. This question was addressed by evoking three consecutive somatic APs at 6 ms inter-pulse intervals. Repetitive firing at short intervals can cause a cumulative sodium channel inactivation, which leads to a progressive decay in spike amplitude due to reduced total sodium inward, a lower number of channels available for opening, and the altered biophysical properties of these already-inactivated and partially de-inactivated channels (Colbert et al., 1997). This resulting amplitude accommodation reflects the refractory state of the neuron and could serve as an indicator of intrinsic excitability.

In parallel, we assessed dendritic excitability in *SCN2A* LoF models narrowing our focus to a regenerative process critical for synaptic integration: the calcium electrogenesis. This mechanism, critically dependent on VGCCs, has been characterized in the rat neocortex (Larkum et al., 1999; Larkum & Zhu, 2002; Major et al., 2013; Schiller et al., 1997), and has been widely attributed to build-up of depolarization leading to Ca^{2+} spikes particularly in the distal apical trunk of thick-tufted L5PNs, with the largest Ca^{2+} transients about 400-700 µm from the soma, where high-frequency stimulations can recruit large, all-or-none, Ca^{2+} spikes (Larkum et al., 1999; Suzuki & Larkum, 2017; Waters et al., 2003). Different initiation mechanisms have been described, Larkum et al. (1999) demonstrated that this event can be

triggered by rapid temporal summation of bAPs, and referred to each neuron a critical frequency, defined as the lowest AP frequency at which bAPs summate sufficiently to initiate a Ca^{2+} spike (estimated ~60-100 Hz in rodent L5PNs). When reached, calcium influx increases in a non-linear manner, whereas only small graded bAP-evoked transients are observed below this critical value (Larkum et al., 1999; Waters et al., 2003). Further works confirmed that these Ca^{2+} spikes can serve as a functional readout of neuronal excitability (Antic, 2010; Major et al., 2013; Suzuki et al., 2017). Yet, no prior study has directly examined whether *SCN2A* LoF alters the generation of dendritic non-linear Ca^{2+} spikes in L5PNs.

In this chapter, we aimed to probe somatic and dendritic excitability in brain slices from wild-type, *Scn2a*$^{+/-}$ (KO), and *Scn2a*$^{+/L1314P}$ (KI) mice. Somatic spike amplitude stability was examined by eliciting three consecutive APs at a fixed short inter-pulse-interval (*IPI)* and computing the relative ratios of their amplitude. Second, in a separate set of experiments we paired the same stimulation protocol to high-speed calcium imaging to record distal calcium signals in the primary bifurcation of the apical dendrite. Our experimental design is adapted from the classical studies of bAP evoked dendritic electrogenesis: we used the inter-spike interval (*IPI*) as a tuning knob to elicit dendritic Ca^{2+} spikes where we progressively increased the *IPI* (6-14 ms) to determine the shortest interval capable of eliciting the non-linear Ca^{2+} response. Results are presented first for the somatic three APs analysis across age and strains, followed by dendritic calcium electrogenesis (prevalence, shortest-IPI distributions in responsive cells, and Ca^{2+} amplitude dynamics across genotypes).

4.1 Somatic Action Potential Amplitude During Short-Interval Bursts

We first tested whether repetitive firing at short inter-pulse intervals (*IPI*) alters the amplitude of consecutive somatic action potentials (APs). We performed whole-cell current-clamp recordings in cortical slices from 14 *Scn2a*$^{+/+}$ female mice, 13 *Scn2a*$^{+/-}$ female mice and 12 *Scn2a*$^{+/L1314P}$ female mice, spanning postnatal days from P21-36. Data were collected from 46 WT, 42 KO, and 48 KI L5 pyramidal neurons. In each cell, three consecutive APs were elicited from a holding potential of -70 mV by somatic injection of 2-3 nA, 3-4 ms current

pulses, spaced by a fixed *IPI* of 6 ms. We quantified the amplitude decay from a spike to another, and the cumulative amplitude changes over the spikes by calculating the three ratios: $R_1=AP_2/AP_1$ (second spike relative to the first), $R_2=AP_3/AP_2$ (third relative to the second), and $R_3=AP_3/AP_1$ (third relative to the first). **Figure 4.1A** shows an example recording from an *Scn2a*$^{+/-}$ cell at P30, illustrating the three parameters analyzed: R_1, R_2, and R_3. Analyses were performed across the entire juvenile age range (P21-36), in young (P21-24), and old (P30-36) subgroups to evaluate the genotype and age related effects. The averaged ratios (mean ± SD) for the three strains and age groups are reported in **Table 4.1**.

$R_1=AP_2/AP_1$	**P21-24**	**P30-36**	**P21-36**
***Scn2a*$^{+/+}$**	0.715 ± 0.107 (N=13)	0.710 ± 0.081 (N=13)	0.703 ± 0.118 (N=46)
***Scn2a*$^{+/-}$**	0.781 ± 0.053 (N=20)	0.771 ± 0.064 (N=12)	0.746 ± 0.097 (N=42)
***Scn2a*$^{+/L1314P}$**	0.778 ± 0.065 (N=17)	0.751 ± 0.085 (N=19)	0.756 ± 0.072 (N=48)

$R_2=AP_3/AP_2$	**P21-24**	**P30-36**	**P21-36**
***Scn2a*$^{+/+}$**	0.872 ± 0.112 (N=13)	0.836 ± 0.068 (N=13)	0.839 ± 0.135 (N=46)
***Scn2a*$^{+/-}$**	0.913 ± 0.063 (N=20)	0.941 ± 0.061 (N=12)	0.907 ± 0.086 (N=42)
***Scn2a*$^{+/L1314P}$**	0.946 ± 0.045 (N=17)	0.869 ± 0.073 (N=19)	0.890 ± 0.071 (N=48)

$R_3=AP_3/AP_1$	**P21-24**	**P30-36**	**P21-36**
***Scn2a*$^{+/+}$**	0.631 ± 0.161 (N=13)	0.597 ± 0.110 (N=13)	0.602 ± 0.174 (N=46)
***Scn2a*$^{+/-}$**	0.714 ± 0.083 (N=20)	0.726 ± 0.076 (N=12)	0.680 ± 0.122 (N=42)
***Scn2a*$^{+/L1314P}$**	0.738 ± 0.084 (N=17)	0.658 ± 0.124 (N=19)	0.677 ± 0.109 (N=48)

***Table 4.1* Mean ± SD of R_1 (AP_2/AP_1), R_2 (AP_3/AP_2), and R_3 (AP_3/AP_1) in cells from 14 *Scn2a*$^{+/+}$ female mice, 13 *Scn2a*$^{+/-}$ female mice, and 12 *Scn2a*$^{+/L1314P}$ female mice at three age windows (P21-24, P30-36, and P21-36).** The number of cells (N) for each population is indicated.

Differences in amplitude ratios were evaluated with the KS-test, considering two groups different when both SP > 0.80 and $p < 0.01$. Across the full juvenile range (P21-36), the ratios

between the first spike and the second spike ($R_1 = AP_2/AP_1$) were slightly higher in both mutant genotypes than *Scn2a*$^{+/+}$ cells (0.703 ± 0.118, N = 46), with mean values of 0.746 ± 0.097 in *Scn2a*$^{+/-}$ (N = 42) and 0.756 ± 0.072 in *Scn2a*$^{+/L1314P}$ (N = 48). These shifts, however, did not reach significance in any genotype or age comparison, and given that the analysis here involves three consecutive APs, the R_1 ratio alone is not sufficient under this complex scenario to capture all parameters involved during brief AP bursts.

In contrast, the second to third AP ratio ($R_2 = AP_3/AP_2$) revealed more selective effects. Within the pooled dataset (P21-36), mean values were 0.839 ± 0.135 in *Scn2a*$^{+/+}$, 0.907 ± 0.086 in *Scn2a*$^{+/-}$, and 0.890 ± 0.071 in *Scn2a*$^{+/L1314P}$ cells. In older animals (P30-36), R_2 values in *Scn2a*$^{+/-}$ were significantly higher than *Scn2a*$^{+/+}$ (0.941 ± 0.061 vs. 0.836 ± 0.068; KS-test, p = 0.0034, SP = 0.865), suggesting less attenuation from the second to third AP in old *Scn2a*$^{+/-}$ compared to WT cells. Additionally, a shift with age was detected only within *Scn2a*$^{+/L1314P}$ cells, where R_2 values decreased in the oldest group (P21-24: R_2 = 0.946 ± 0.045, N=17 to P30-36: R_2 = 0.869 ± 0.073, N=19; KS-test, p = 0.00144, SP=0.827), suggesting a greater decay in the amplitude of the third AP in older KI animals.

A similar pattern was observed for the cumulative ratio ($R_3 = AP_3/AP_1$), with full age range (P21-36) means of 0.602 ± 0.174 in *Scn2a*$^{+/+}$, 0.680 ± 0.122 in *Scn2a*$^{+/-}$, and 0.677 ± 0.109 in *Scn2a*$^{+/L1314P}$ cells. Only the older *Scn2a*$^{+/-}$ group (P30-36) differed significantly from WT (0.726 ± 0.076 vs. 0.597 ± 0.110; KS-test, p = 0.0063, SP = 0.821), consistent a with reduced amplitude decay in KO at this age across the three APs.

Altogether, under KS-test rule ($p < 0.01$ with PS > 0.80), significant differences were restricted to the third AP, and were more evident in older KO (*Scn2a*$^{+/-}$) neurons (P30-36), which showed a greater amplitude stability (less decay) over the three APs than WT (*Scn2a*$^{+/+}$) for both AP_3/AP_2 and AP_3/AP_1. Further, an age effect was detected only in *Scn2a*$^{+/L1314P}$ (KI) for AP_3/AP_2, which decreased from young (P21-24) to old (P30-36), indicating a greater decay in the third AP amplitude relative to the second, from early to late juvenile stages in KI mice.

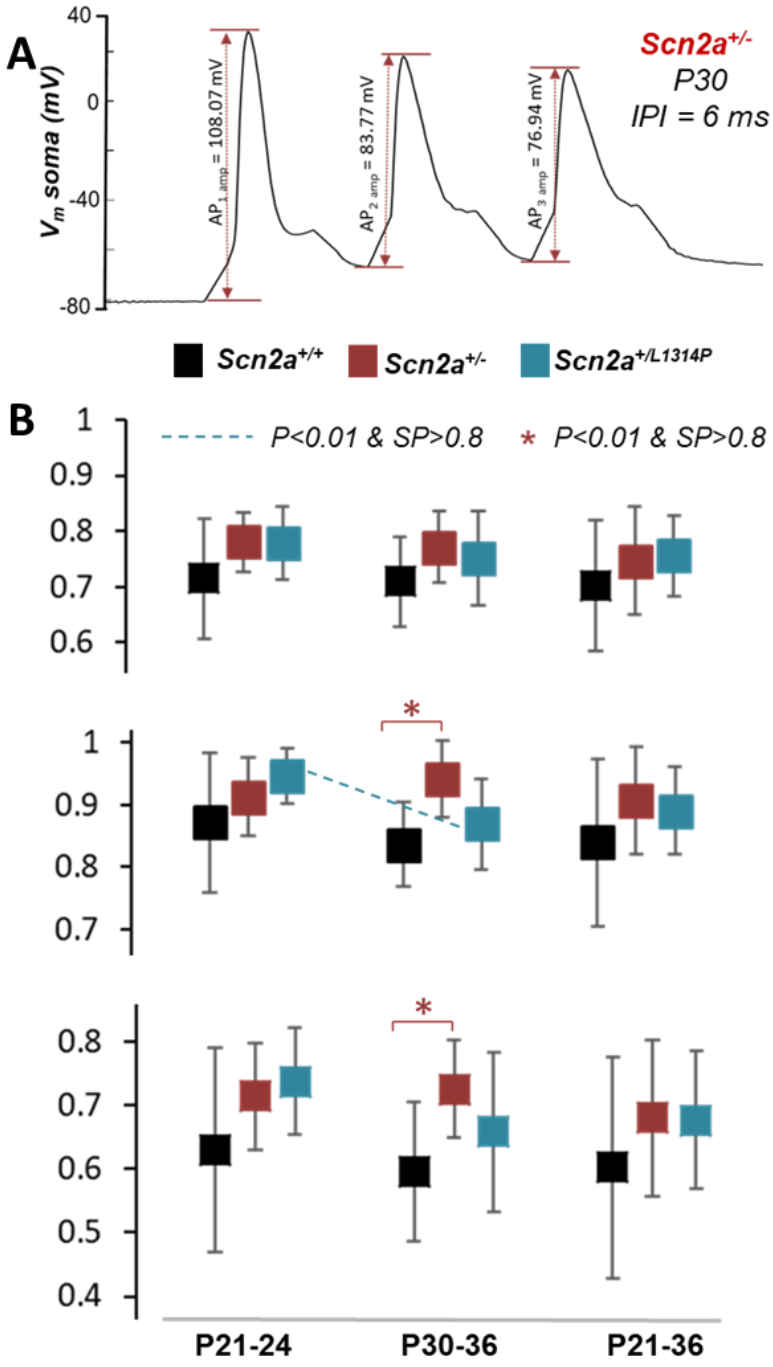

Figure 4.1 **Somatic AP amplitude ratios from three consecutive APs in *Scn2a*$^{+/+}$, *Scn2a*$^{+/-}$ and *Scn2a*$^{+/L1314P}$ L5 pyramidal neurons.**

(A) Example recording from a *Scn2a*$^{+/-}$ neuron at P30, showing three somatic APs evoked by three current pulses (3 nA, 3 ms each) at a fixed IPI of 6 ms. The amplitude ratios $R_1=AP_2/AP_1$, $R_2=AP_3/AP_2$, and $R_3=AP_3/AP_1$ were calculated to quantify the amplitude changes over the three AP spikes.

(B) Mean ± SD of R_1 (top), R_2 (middle), and R_3 (bottom) for *Scn2a*$^{+/+}$ cells (black; P21-24: N = 13; P30-36: N = 13; P21-36: N = 46), *Scn2a*$^{+/-}$ cells (red; P21-24: N = 20; P30-36: N = 12; P21-36: N = 42), and *Scn2a*$^{+/L1314P}$ cells (blue; P21-24: N = 17; P30-36: N = 19; P21-36: N = 48). "*" indicates that the result of the two-sample KS-test between two groups of the same age but different genotype gave SP > 0.80 and $p < 0.01$. Dashed line indicates significant KS-test differences between two age groups of the same genotype (SP > 0.80 and $p < 0.01$).

4.2 Descriptive Characterization of Regenerative Dendritic Calcium Responses in *SCN2A* LoF Models

We defined cells as Ca^{2+} electrogenesis-positive if they satisfied at least one of two criteria described in earlier research on dendritic Ca^{2+} regenerative events: nonlinear amplitude increases or sustained plateau responses.

The amplitude based supralinearity required that, within the three APs, the peak Ca^{2+} step evoked by the third AP (S_3) had to be at least ~two-fold larger than the second (S_2) (**see Figure 4.2B**). Based on previous investigations, no specific magnitude or numerical amount was implemented to define this nonlinearity. For instance, in vivo tuft recordings at 150 Hz showed an increase in the $\Delta F/F_0$ peak from 20% in two-AP burst to 58% in three-APs (Waters et al., 2003). On the other hand, Larkum et al. (1999) reported that in L5PNs, when reaching the critical frequency, a strong nonlinear response was produced, and the voltage integral almost doubled (1.9-fold). Similarly, supralinear burst-evoked Ca^{2+} rises were also estimated to double from 2 to 3 AP bursts in L5 distal dendrites (Kampa & Stuart, 2006, Fig1). Therefore, we chose a slightly more conservative threshold of $S_3/S_2 > 1.8$ for our ex-vivo recordings, in order to limit false negatives by missing slightly smaller cases, while remaining within the range of effects reported in the literature.

The second plateau-based criterion was established for cells with modest amplitude increase ($1.5 \leq S_3/S_2 \leq 1.8$), but prolonged Ca^{2+} signal elevation after the third AP. This can be defined as a sustained $\Delta F/F_0$ within ± 5% of its peak after the third AP toward the end of our 50 ms recording window (see **Figure 4.2C,D**). Such aspect of dendritic responses was also described in previous reports as a slow-rising plateau component in distal apical dendrites (Larkum et al., 2001), or plateau depolarizations lasting tens to hundreds milliseconds in prefrontal L5 neurons (Milojkovic et al., 2005), and is consistent with supralinear plateau Ca^{2+} responses reported by Kampa & Stuart (2006) during AP bursts.

This approach allowed capturing the two ways by which dendritic electrogenesis may manifest, either as sharp supralinear spikes, or longer lasting plateau-like transients. Cells not fulfilling either criterion were classified Ca^{2+} electrogenesis-negative (see **Figure 4.2A**). Example cells are illustrated in **Figure 4.2**.

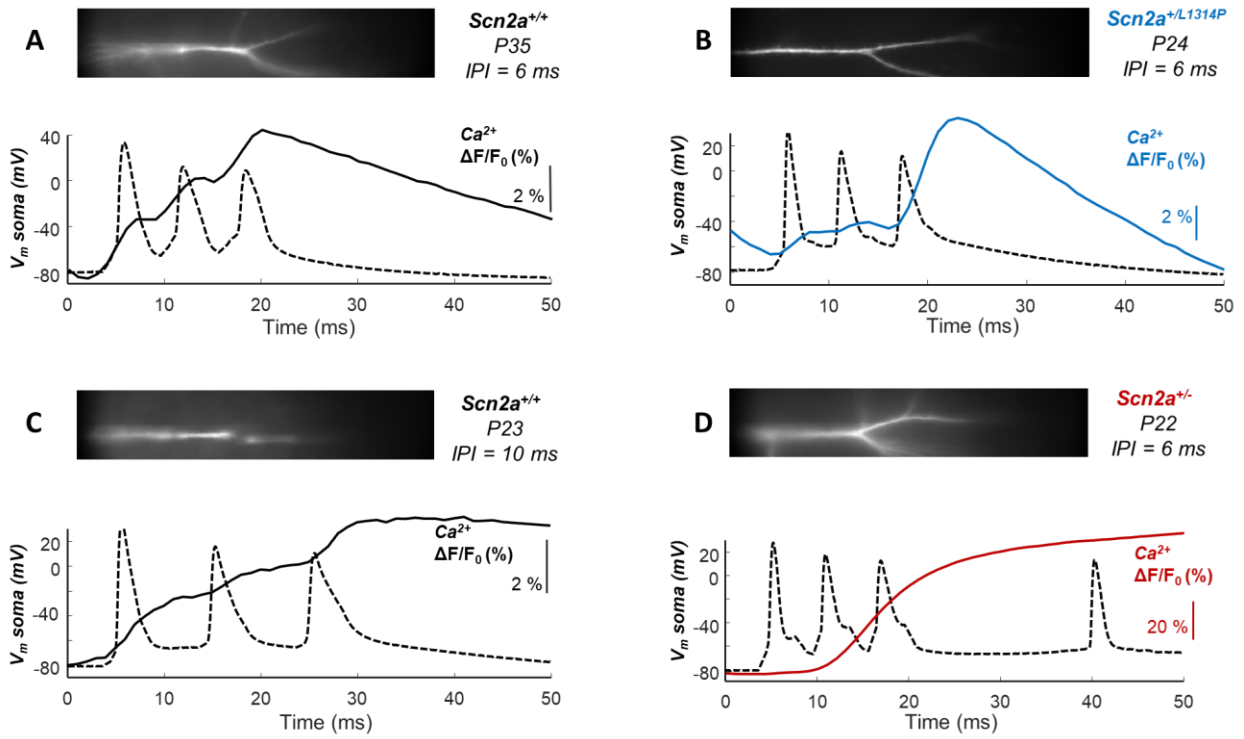

Figure 4.2 **Representative examples illustrating the classification criteria for dendritic** Ca^{2+} **electrogenesis.** Top: fluorescence images showing the main bifurcation of the apical dendrite in Layer 5 pyramidal neuron loaded with OGB-5N, with genotype and age indicated. Bottom: aligned traces of somatic membrane voltage (dashed black) and $\Delta F/F_0$ calcium transients (solid colored) during the firing of a three action potential burst at a specific inter-pulse interval (IPI) indicated. ***(A)*** Example of a cell classified as Ca^{2+} electrogenesis-negative with a linear Ca^{2+} response to different frequencies. ***(B)*** Amplitude-based Ca^{2+} electrogenesis-positive showing an afterdepolarization following the 3rd AP and a pronounced non-linear Ca^{2+} spike in the third step ($S_3/S_2 > 1.8$). ***(C)*** Plateau-based positive cell: a moderate amplitude increase ($1.5 \leq S_3/S_2 \leq 1.8$) followed by a sustained Ca^{2+} plateau (for ≥20 ms). (D) Ca^{2+} electrogenesis-positive cell fulfilling both criteria, showing a strong supralinear increase and prolonged plateau. These categories were used to classify dendritic Ca^{2+} electrogenesis across all recorded cells.

Subsequent quantitative analyses (such as prevalence, the threshold *IPI* for the first electrogenic event, S_3/S_2 ratios, etc.) were done only for Ca^{2+} electrogenesis-positive cells. This study has a qualitative and preliminary character, and statistical tests were applied only occasionally where the data justified it. Given the relatively small sample sizes, most of findings reported in the following section are descriptive, highlighting noticeable tendencies rather than statistical significance. Unless otherwise specified, comparisons were not statistically significant and need to be confirmed in larger datasets and are considered preliminary.

4.2.1 Dendritic Calcium Electrogenesis Increases with Age in *Scn2a*$^{+/-}$ but Declines in *Scn2a*$^{+/L1314P}$

Having defined the classification criteria, we next assessed the prevalence of dendritic Ca^{2+} electrogenesis across the KO and KI genotypes, and compared them to the WT. A total of 67 cells were analyzed, distributed as follows: 23 *Scn2a*$^{+/+}$, 23 *Scn2a*$^{+/-}$, and 21 *Scn2a*$^{+/L1314P}$ cells. **Table 4.2** summarizes the number and percentage of Ca^{2+} electrogenesis positive cells in each group. These proportions are presented descriptively, since no differences were observed in formal statistical comparisons.

Genotype	Total Cells	Ca^{2+} Electrogenesis-Positive Cells (N)	Ca^{2+} Electrogenesis Prevalence
***Scn2a*$^{+/+}$**	23	10	47.8%
***Scn2a*$^{+/-}$**	23	15	65.2%
***Scn2a*$^{+/L1314P}$**	21	13	61.9%

***Table 4.2* Summary of dendritic Ca^{2+} electrogenesis prevalence across genotypes.** For each genotype, the table reports the total number of L5PNs analyzed, the number of cells classified as Ca^{2+} electrogenesis-positive based on amplitude or plateau criteria, and the corresponding percentage of occurrence. Cells were classified as positive if they exhibited Ca^{2+} electrogenesis at any of the tested inter-pulse intervals (6, 8, 10, 12, or 14 ms). Data recorded from somatosensory cortical slices of juvenile female mice (P21-36), including 23 *Scn2a*$^{+/+}$ (WT), 23 *Scn2a*$^{+/-}$, (KO), and 21 *Scn2a*$^{+/L1314P}$ (KI) cells.

As shown in **Table 4.2**, dendritic Ca^{2+} electrogenesis was detected in approximately half of the wild-type (*Scn2a*$^{+/+}$) neurons (47.8%). In contrast, a higher proportion of *Scn2a*$^{+/-}$ (65.2%) and *Scn2a*$^{+/L1314P}$ (61.9%) cells were classified as Ca^{2+} electrogenesis-positive.

Surprisingly, both transgenic animal groups exhibited a higher occurrence of Ca^{2+} electrogenesis than controls under the same experimental conditions, with the KO group showing the highest overall prevalence of Ca^{2+} electrogenesis among the three genotypes. This hints at potential genotype-dependent modulation of regenerative dendritic responses. However, given that the dataset spans the juvenile window (P21-36), it was essential to evaluate whether the age influenced the likelihood of dendritic Ca^{2+} events. Therefore, we followed the same approach explained earlier in Chapter 3 to better examine the apical dendritic response across age groups within each genotype. Cells were grouped as follows: "young" (P21-24), "middle" (P25-29), and "old" (P30-36). **Table 4.3** summarizes the proportion of Ca^{2+} electrogenesis-positive cells within each age group and genotype; corresponding prevalence for the young and old age groups are also illustrated in **Figure 4.3** for easier comparison.

Age	***Scn2a*$^{+/+}$**	***Scn2a*$^{+/-}$**	***Scn2a*$^{+/L1314P}$**
Young *(P21-24)*	4/9 (44.4%)	4/8 (50.0%)	5/7 (71.4%)
Middle *(P25-29)*	2/3 (66.7%)	5/7 (71.4%)	3/4 (75.0%)
Old *(P30-36)*	4/11 (36.4%)	6/8 (75.0%)	5/10 (50.0%)

Table 4.3 **Prevalence of dendritic Ca^{2+} electrogenesis across genotypes and three age groups.**

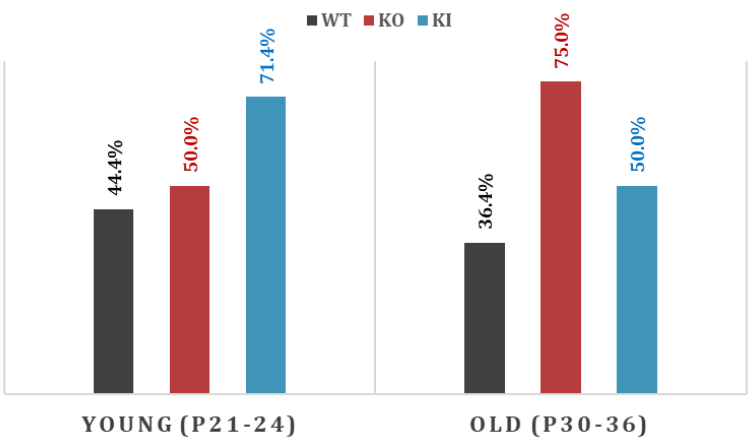

Figure 4.3 **Percentage of dendritic Ca^{2+} electrogenesis positive cells in *Scn2a*$^{+/+}$ (WT), *Scn2a*$^{+/-}$ (KO), and *Scn2a*$^{+/L1314P}$ (KI) mice across the two extremes age groups: young (P21-24) and old (P30-36).**

Both genotypes and age windows contributed to the heterogeneity of the rate of Ca^{2+} electrogenesis in the dendrites. The middle age group (P25-29) was not included in

subsequent comparisons because of its limited and uneven sample size. The young (P21-24) and old (P30-36) age groups displayed different patterns among genotypes. In *Scn2a*$^{+/+}$ cells, cells, the percentage of nonlinear calcium responses declined from 44.4% in the youngest to 36.4% in the oldest group, suggesting a reduced dendritic Ca^{2+} electrogenesis at the late juvenile period in controls. The two *SCN2A* LoF models, on the other hand, showed an opposite behavior. A notable increase with age was observed in *Scn2a*$^{+/-}$ cells, with 75% of them exhibiting non-linear Ca^{2+} responses in the old group, representing the highest prevalence at this age compared to WT and KO cells. Whereas *Scn2a*$^{+/L1314P}$ (KI) cells began with the highest rate in young cells (71.4%), but dropped to 50% in the old group, similar to the direction observed in wild-type.

Although the number of recorded cells per group limits statistical analysis, these findings suggest a distinct modulation of the refinement of dendritic regenerative capacity in the three genotypes. Notably, although both the *Scn2a*$^{+/-}$ and *Scn2a*$^{+/L1314P}$ model the LoF in *SCN2A* gene, they had different developmental patterns of dendritic excitability. While KI cells, showing an interestingly elevated calcium electrogenesis rate in the young age window, followed a direction similar to wild-type, KO neurons deviated from this pattern and reported increased regenerative potential with age.

4.2.2 Dendritic Ca^{2+} Electrogenesis Occurs at Comparable Frequencies Across Experimental Groups

To further characterize the properties of dendritic Ca^{2+} electrogenesis, we focused our analysis on the subset of cells classified as Ca^{2+} electrogenesis positive. Of these, we first examined the inter-pulse interval threshold (IPI_{thr}), defined as the shortest interval at which non-linear increase in $\Delta F/F_0$ was first detected. This measure, while it does not reflect the exact physiological "critical frequency" described in previous studies on dendritic Ca^{2+} spikes in pyramidal neurons, could serve as a standardized indicator of the frequency dependence and sensitivity of regenerative events, and the cell's overall excitability. Two example cells with representative Ca^{2+} traces at different *IPI*s and the corresponding threshold, where a supra-linear response first appeared, are shown in **Figure 4.4** Figure **4.5**.

Table 4.4 summarizes the distribution of *IPI* thresholds according to genotypes and age groups.

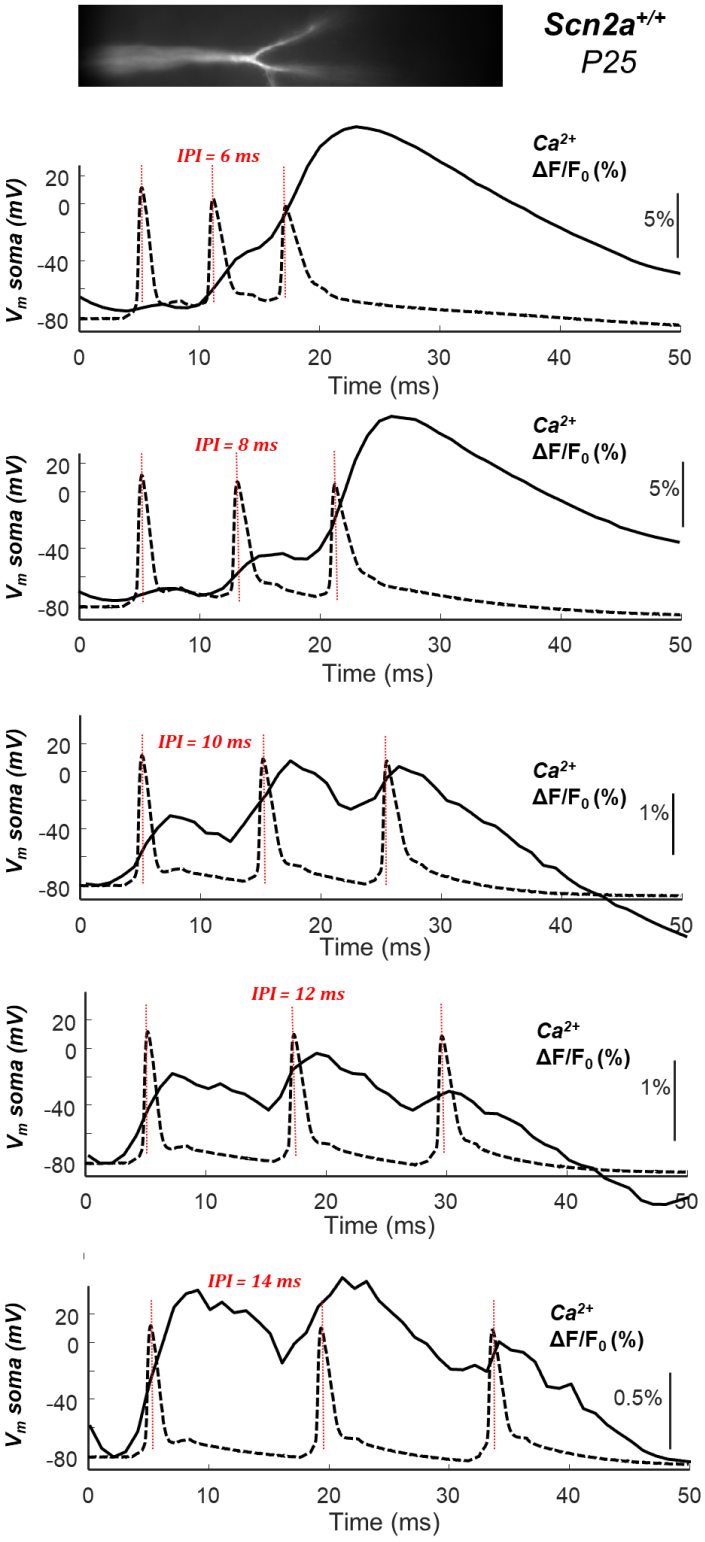

Figure 4.4 **Example of the determination of the interpulse interval threshold for dendritic Ca^{2+} electrogenesis.** *Top*, fluorescence image showing the primary bifurcation of a L5 pyramidal neuron loaded with OGB-5N from an *Scn2a*$^{+/+}$ at P25. *Below*, five panels showing each somatic membrane potential (V_m, dashed black) and the corresponding Ca^{2+} fluorescence ($\Delta F/F_0$, solid black) recorded simultaneously during the firing of three consecutive AP burst, evoked at increasing inter-pulse intervals (*IPI* = 6, 8, 10, 12, and 14 ms). IPIs are indicated in red in each panel, with red dashed lines. A large and supralinear increase in the Ca^{2+} signal is observed at *IPI* = 6 ms, and persisted slightly decreasing at 8 ms, marked by a nonlinear spike at the third step (S3. At longer *IPI*s (10–14 ms), corresponding to lower frequencies, the Ca^{2+} response decayed and failed to reach supralinear levels, consistent with frequency-dependent onset of all-or-none regenerative events in the apical dendrite. The interval threshold (IPI_{thr}) for this cell was determined to be 6 ms.

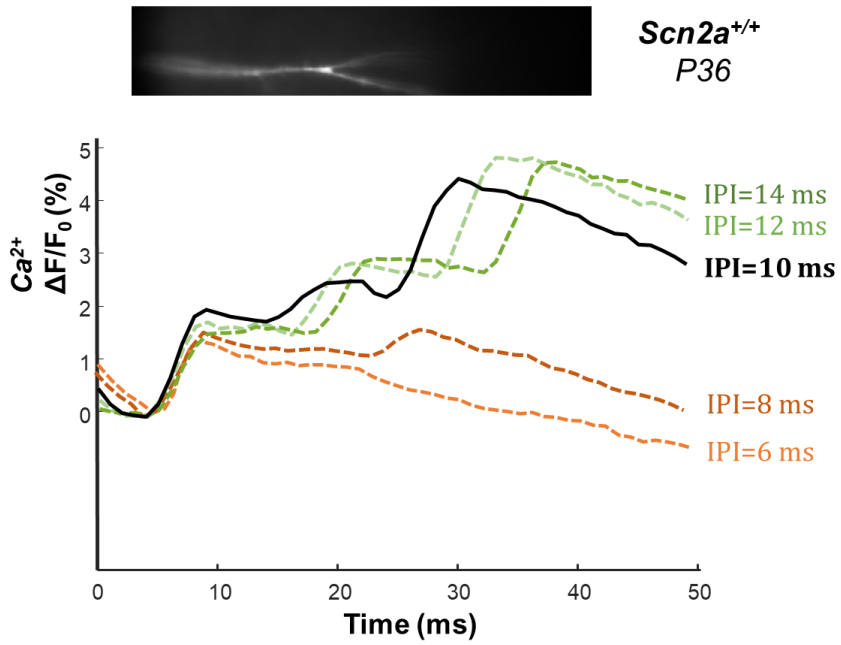

***Figure 4.5* Supralinear Ca^{2+} response evoked at intermediate *IPI*.** Top, the apical dendritic tuft of a *Scn2a*$^{+/+}$ L5PN at P36 loaded with OGB-5N, with the recording position centered around the main bifurcation. Bottom, $\Delta F/F_0$ traces overlaid during 3-AP burst elicited at different inter-pulse intervals (*IPI* = 6, 8, 10, 12, and 14 ms), with *IPI* values color-coded and indicated next to the traces. At *IPI* =10 ms (solid black), a supralinear increase was observed in the third step relative to the second (S_3/S_2 > 1.8), eliciting a regenerative spike of Ca^{2+}. At shorter IPIs (6 and 8 ms, orange traces), the Ca^{2+} response remained small. At longer intervals (12 and 14 ms, green), the Ca^{2+} response remained elevated but the steps approached linearity ($S_1 \simeq S_2 \simeq S_3$), and no sustained plateau was present. Based on the Ca^{2+} profile, this cell exhibits a frequency-selective window for Ca^{2+} electrogenesis, and the intermediate IPI=10 ms was therefore identified as the threshold.

IPI_{thr} (ms)	P21-24	P30-36	P21-36
***Scn2a*$^{+/+}$**	9.0 ± 3.46 (N=4)	8.0 ± 2.31 (N=4)	8.0 ± 2.67 (N=10)
***Scn2a*$^{+/-}$**	8.0 ± 1.63 (N=4)	7.0 ± 1.1 (N=6)	7.33 ± 1.8 (N=15)
***Scn2a*$^{+/L1314P}$**	6.8 ± 1.1 (N=5)	6.4 ± 0.89 (N=5)	7.5 ± 2.85 (N=13)

***Table 4.4.* Mean ± SD of IPI_{thr} in cells with nonlinear apical Ca^{2+} response from 10 *Scn2a*$^{+/+}$ female mice, 15 *Scn2a*$^{+/-}$ female mice and 13 *Scn2a*$^{+/L1314P}$ female mice at three time windows (P21-24, P30-36, and P21-36).** The number of cells (N) for each population is indicated.

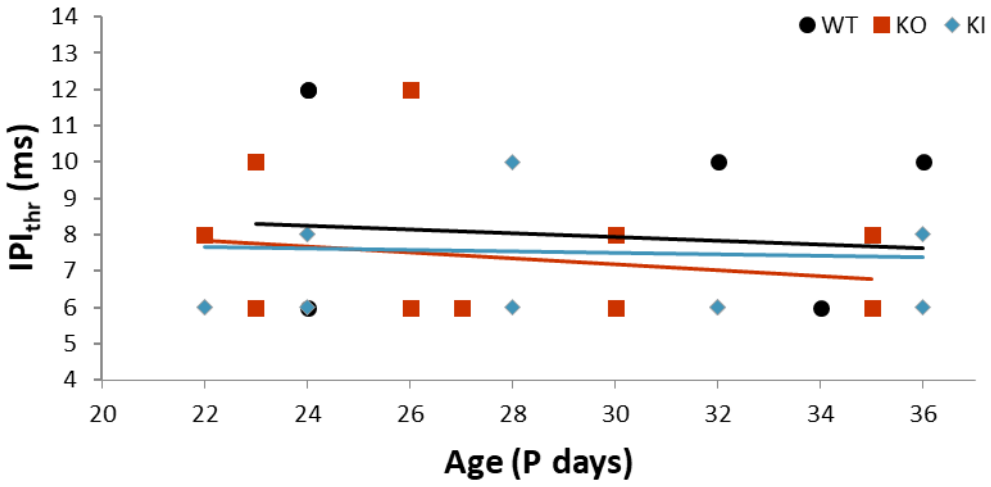

***Figure 4.6* Scatter plot showing individual *IPI* thresholds (ms) for supralinear calcium responses as a function of age for each genotype *Scn2a*$^{+/+}$ (black), *Scn2a*$^{+/-}$ (red), and *Scn2a*$^{+/L1314P}$ (blue).** Colored lines indicate linear fits for each group.

When pooling all ages, IPI_{thr} means were comparable between the three genotypes (*Scn2a*$^{+/+}$: 8.0 ± 2.67 ms, *Scn2a*$^{+/-}$: 7.33 ± 1.8 ms, *Scn2a*$^{+/L1314P}$: 7.54 ± 2.85 ms). Statistical comparisons using the two-sample WMW test did not identify significant differences between age groups within a genotype, or between genotypes at a specific age group due to the limited number of cells where we could capture the calcium spike in the apical dendritic tuft, and the overall similarity of thresholds between conditions. Descriptively, only minor shifts in the threshold profiles were noted: *Scn2a*$^{+/L1314P}$ cells showed lower IPI_{thr} across ages, suggesting that they required slightly higher stimulation frequencies for Ca^{2+} electrogenesis compared to WT; whereas *Scn2a*$^{+/-}$ cells exhibited a decline with age in their IPI_{thr}, indicating the need for higher frequencies to trigger regenerative dendritic responses in older KO mice.

4.2.3 Dendritic Ca^{2+} Electrogenesis Amplitude Ratios in the Three Strains

Lastly, in the final analysis across cells that exhibited nonlinear responses, we aimed to compare the relative increase in Ca^{2+} signals. We quantified the amplitude of the third step increase in dendritic Ca^{2+} (corresponding to the third evoked AP) relative to the preceding step by computing the ratio S_3/S_2. This analysis was restricted to amplitude-based Ca^{2+}

electrogenesis cells, with S_3/S_2 > 1.8, to ensure a homogeneous sample in which nonlinear responses were only driven by amplitude changes.

S_3/S_2	P21-24	P30-36	P21-36
***Scn2a*$^{+/+}$**	3.81 ± 1.82 (N=4)	2.45 ± 0.81 (N=3)	4.49 ± 4.02 (N=9)
***Scn2a*$^{+/-}$**	9.68 ± 7.51 (N=3)	16.36 ± 34.31 (N=6)	11.03 ± 22.26 (N=14)
***Scn2a*$^{+/L1314P}$**	19.04 ± 20.62 (N=5)	2.59 ± 0.48 (N=5)	8.91 ± 14.54 (N=13)

***Table 4.5* Mean ± SD of S_3/S_2 ratio in amplitude-based Ca^{2+} electrogenesis cells from 9 *Scn2a*$^{+/+}$ female mice, 14 *Scn2a*$^{+/-}$ female mice, and 13 Scn2a *Scn2a*$^{+/L1314P}$ female mice at three time windows (P21-24, P30-36, and P21-36).** *The number of cells (N) for each population is indicated.*

Across the whole examined age window (P21-36), S_3/S_2 ratios were quite variable between cells, with some outliers far exceeding the group means. This variability was more important in *Scn2a*$^{+/-}$ (11.03 ± 22.26, *N*=14) and *Scn2a*$^{+/L1314P}$ (8.91 ± 14.54, *N*=13), where some cells showed exceptionally large third-step spikes. In *Scn2a*$^{+/+}$, however, the magnitudes of supralinear responses were overall smaller and less spread (4.49 ± 4.02, *N*=9).

When further assessing the age effect within each strain, only *Scn2a*$^{+/L1314P}$ group had balanced sample sizes (young: *N*=5; old: *N*=5) that allowed comparison. Here, the ratio declined sharply from 19.04 ± 20.62 in young to 2.59 ± 0.48 in old group, and the supralinear increase was strong and variable at P21-24 and became more homogeneous with age approaching *Scn2a*$^{+/+}$ averages. However, this group had the largest third-step amplitude responses in old mice, exceeding both *Scn2a*$^{+/L1314P}$ and *Scn2a*$^{+/+}$ of the same age. Moreover, no statistical differences were found between the genotypes. Descriptively, KI and KO had opposing age-related patterns: in young, the highest ratio values were reported in KI, whereas in the old group, KO ranked highest.

Taken together, although the sample sizes are unavoidably too small to detect reliable differences among strains, these results confirm that dendritic Ca^{2+} electrogenesis is still present in both *SCN2A* LoF models.

4.3 Summary and Insights

In this chapter, we focused on the somatic and dendritic excitability of L5 pyramidal neurons in *SCN2A* loss-of-function models using whole-cell recordings and high-speed calcium imaging during brief bursts of 3 APs. We reported first that old *Scn2a*$^{+/-}$ cells retained more amplitude at the soma, with significantly higher AP_3/AP_2 and AP_3/AP_1 ratios than wild types, while old *Scn2a*$^{+/L1314P}$ neurons had an increasing somatic decay rates leading to a progressive reduction in the third AP amplitude, consistent with opposing developmental profiles of somatic spike stability between the two models.

In the distal dendrites, both KI and KO cells showed a higher overall prevalence of calcium electrogenesis than controls, but *Scn2a*$^{+/-}$ neurons reported an increase with age while *Scn2a*$^{+/L1314P}$ neurons showed a decline after an early peak. Further characterization of the frequency dependence of these nonlinear calcium responses across genotypes revealed comparable frequency sensitivities for all ages combined, yet subtle changes were detected between age groups in KO and WT mice. Finally, third-step Ca^{2+} increase (S_3/S_2) was largest in young *Scn2a*$^{+/L1314P}$ but fell toward wild-type levels with age, in contrary this calcium response magnitude increased with age in old *Scn2a*$^{+/-}$ neurons.

Collectively, these results suggest that loss-of-function of *SCN2A* alters mechanisms of AP backpropagation at both the soma and dendrite, but with divergent age-dependent trajectories for *Scn2a*$^{+/-}$ and *Scn2a*$^{+/L1314P}$ mice models. The KO model acquired dendritic regenerative capability and somatic firing stability during juvenile development, whereas, the KI model showed a progressive decline in both compartments. Interestingly, the presence of backpropagating AP-evoked regenerative responses in both mutants indicates that $Na_v1.2$ loss-of-function does not abolish these processes, but instead reshapes them through a genotype and age-dependent manner. Again, these observations emphasize the complex and dynamic nature of excitability regulation in *SCN2A*-related disorders and calls for a mechanistic interpretation that will be developed in the discussion.

5

Analysis of The Effect of the Scorpion Toxin AaH-II On Action Potential Generation in The Axon Initial Segment

5.1 AAH-II PROLONGS INACTIVATION OF $NA_V1.2$ AND $NA_V1.6$ WITH LIMITED ISOFORM SELECTIVITY 126

5.1.1 AUTOMATED PATCH-CLAMP IN HEK293 CELLS EXPRESSING EITHER $NA_V1.2$ OR $NA_V1.6$ **126**

5.1.2 ASSESSMENT OF AAH-II SELECTIVITY BETWEEN $NA_V1.2$ AND $NAV1.6$ **127**

5.2 LOCAL AAH-II DELIVERY IN L5 PYRAMIDAL NEURONS ALTERS SOMATIC AP SHAPE IN A CONCENTRATION-DEPENDENT MANNER 129

5.3 AAH-II ALTERS THE ACTION POTENTIAL PREFERENTIALLY IN THE AIS 131

5.4 AAH-II ENHANCES SODIUM AND CALCIUM INFLUX IN THE AIS 132

5.5 AAH-II SELECTIVELY ENHANCES $NA_V1.2$-MEDIATED CA^{2+} INFLUX IN THE DISTAL AIS 134

5.6 SUMMARY AND INSIGHTS 136

Previous chapters of this dissertation explored the physiological consequences of loss-of-function of *SCN2A* in genetically modified mouse models, a secondary goal of the grant that funded this thesis was to test the effect $Na_V1.2$ enhancers and their potential ability to rescue physiological functions. In line with this goal this chapter presents a pilot study performed only in wild-type mice to evaluate the effects of a VGNC activator, the AaH-II. This study, published in February 2024, was aimed at assessing the hypothesis that selective activation

of $Na_v1.2$ by a strong VGNC modulator at low concentrations may potentially compensate for impaired channel function or rescue excitability in *SCN2A*-related LoF disorders.

Of the known VGNSC modulators, the α-scorpion toxin AaH-II, isolated from *Androctonus australis hector* venom, binds to mammalian sodium channels with nanomolar affinity and slows down the onset of their inactivation, thus prolonging the channel open time and enhancing sodium current (Alami et al., 2003; Billen et al., 2008; Duval et al., 1989). While the systemic toxicity of this peptide has been well established, including effects such as paralysis and cardiac arrhythmia (Bosmans & Tytgat, 2006; Sami-Merah et al., 2008), AaH-II has also drawn attention as a potential pharmacological probe. As for other peptides targeting VGNCs, it may be used to offer insights into ion channel behavior within their native environment, under physiologically relevant conditions, or to serve as a building block in the design for new drugs. For example, Amm VIII, a similar scorpion toxin, was reported to induce hyperalgesic effects through the gain-of-function of VGNCs (Abbas et al., 2013). Whereas Hm1a, a selective activator of Nav1.1 known as the principal VGNC expressed in GABAergic interneurons, had the potential to rescue seizures and prevent premature mortality in mouse models of Dravet syndrome (Richards et al., 2018). However, such effects are highly dose-dependent, and low levels are often required to minimize off-target toxicity. Detailed characterizations of VGNC modulators at sub-saturating concentrations are therefore crucial, in particular when considering these peptides for CNS applications. However, it is worth mentioning that peptide toxins like AaH-II have a poor penetration across the blood-brain barrier and therefore its systemic application as such would not be suitable. From this perspective, our study presents a proof-of-principle where advanced optical techniques were used for the first time to investigate their subcellular effects on neuronal excitability.

As we have extensively stated in previous sections the viable role of the AIS in neocortical pyramidal neurons for the initiation of APs, we now turn to a pharmacological perspective. The AIS, with its high VGNC density, particularly the main co-expressed isoforms $Na_v1.2$ and $Na_v1.6$, is considered a key candidate for pharmacological interventions aimed at modulating the excitability (Huang & Rasband, 2018; Kole & Stuart, 2008; Leterrier, 2016). Yet the

subcellular actions of VGNC-targeting compounds in this compartment remain insufficiently explored. Moreover, drug sensitivities toward one of these isoforms of another remains highly challenging.

To address these questions, we performed a characterization of the mutated toxin AaH-IIR^{62}K (referred after as AaH-II) using a combination of automated patch-clamp recordings in heterologous systems and high-resolution electrophysiological and optical approaches in acute neocortical slices, with a special focus on the AIS. The AaH-IIR^{62}K variant was previously described by Montnach et al. (2022) in the context of developing photoactivatable peptide toxins for targeted spatiotemporal control of VGICs. In their study, the mutated form of AaH-II was obtained by replacing arginine at position 62 with lysine (R62K), to allow its chemical caging with a photoactivable Nvoc group. After light-induced uncaging, the modified toxin replicated classical AaH-II effects, such as slowing the inactivation kinetics in hNa$_v$1.2-expressing HEK293 cells and a strong paralytic effect was reported in zebrafish larvae; thus confirming the retained functional activity of the mutated toxin.

In the present study, we employed the active form of AaH-IIR^{62}K (non-photoactivable) to examine its direct action on neuronal VGNCs in acute mouse neocortical slices. We provide evidence that despite minimal effects on somatic AP at 7 nM local delivery of AaH-II, AIS recordings revealed pronounced broadening of the AP spike, accompanied with increased late-phase Na^+ and Ca^{2+} influx.

This work was conducted in collaboration with Michel De Waard's team (Nantes), who carried out HEK293 cell assays to determine AaH-II's activity profile on Na$_v$1.2 and Na$_v$1.6. The ex-vivo electrophysiology and imaging experiments were performed jointly with Laila Blömer, a PhD student and later postdoctoral fellow, who performed the voltage imaging experiments. I was responsible for all sodium and calcium imaging experiments reported in this chapter.

5.1 AaH-II Prolongs Inactivation of $Na_v1.2$ and $Na_v1.6$ with Limited Isoform Selectivity

5.1.1 Automated Patch-Clamp in HEK293 Cells Expressing Either $Na_v1.2$ or $Na_v1.6$

In order to assess the isoform selectivity of AaH-II, automated whole-cell voltage-clamp recordings were performed in HEK293 cells stably expressing either human $Na_v1.2$ or $Na_v1.6$ channels. The experimental procedure was almost the same as previously reported in the work of Montnach et al. (2022). Cells were cultured in Dulbecco's Modified Eagle's Medium (DMEM) supplemented with 10% fetal bovine serum, 1 mM pyruvic acid, 4.5 g/L glucose, 4 mM glutamine, 800 µg/mL G418, 10 U/mL penicillin, and 10 µg/mL streptomycin, and incubated at 37 °C in a 5% CO_2 environment. For electrophysiological recordings, cells were detached using trypsin and were diluted to about 300,000 cells/mL.

Recordings were carried out using a SyncroPatch 384PE system (Nanion, München, Germany), according to the manufacturer's recommended protocols. Medium-resistance single holes' chips were used (4.52 ± 0.08 MΩ). All recording steps, from cell trapping, seal generation, whole-cell access, to data acquisition were achieved automatically with the PatchControl384 v1.5.2 and Biomek v1.0 software. Experiments were performed at room temperature (18–22 °C), cells were held at −100 mV and currents were sampled at 20 kHz.

The intracellular solution was (in mM): 10 CsCl, 110 CsF, 10 NaCl, 10 EGTA, and 10 HEPES (pH 7.2, 280 mOsm); and the extracellular solution contained (in mM): 140 NaCl, 4 KCl, 2 $CaCl_2$, 1 $MgCl_2$, 5 glucose, and 10 HEPES (pH 7.4, 298 mOsm). After 2 minutes of control, AaH-IIR^{62}K, a mutated form of AaH-II, was added through bath perfusion and diluted in the extracellular solution containing 0.3% BSA.

Toxin effect was quantitatively evaluated by determination of T_{50} parameter, defined as the time point at which the sodium current decayed to 50% of the difference between its peak amplitude and the residual current at the end of the depolarization. T_{50} values were

measured before and after 15 min incubation in the presence of AaH-IIR62K, and the effect of the toxin was expressed as the change in T_{50} relative to the baseline value.

5.1.2 Assessment of AaH-II Selectivity Between $Na_v1.2$ and $Na_v1.6$

To characterize the selectivity of AaH-II, we first conducted a dose-response analysis of the peptide action in HEK293 cells stably expressing either human $Na_v1.2$ or $Na_v1.6$ channels, with automated whole-cell patch-clamp recordings. This analysis was necessary to establish the efficacy of the toxin on the two VGNC isoforms expressed in L5PNs. Na^+ currents were induced by 50-ms depolarizing pulses from -100 mV to 0 mV, and the inactivation kinetics were assessed by calculating the half-inactivation time (T_{50}) defined as the time at which the Na^+ current reached 50% of its current peak (red arrows in **Figure 5.1A**). For each condition, T_{50} was then measured before and after 15 minutes of toxin incubation.

Representative example traces (**Figure 5.1A**) show that bath perfusion of AaH-II at 0.3 nM or 10 nM prolonged the inactivation time course for both $Na_v1.2$ and $Na_v1.6$ mediated Na^+ currents. This effect manifested as a visibly slower decay of the current over the 50-ms step with higher toxin concentration producing longer inactivation times. The test was conducted in distinct groups of cells that were exposed to concentrations ranging from 0.01 nM to 10 nM. The effects of the toxin at different concentrations on current amplitudes are summarized in **Table 5.1**. T_{50} values were normalized to baseline values obtained from each cell before the application of the toxin; and the concentration-response curves based on normalized T_{50} values (plotted in **Figure 5.1B**), revealed a sigmoidal profile for both isoforms. The effect already reached a plateau at 3 nM, and no additional increase in Na^+ current was observed even at higher concentrations.

Notably, the responses of $Na_v1.2$ and $Na_v1.6$ were similar across the entire concentration range, suggesting that AaH-II has a poor discrimination between the two isoforms and exerts a comparable modulatory activity on their inactivation kinetics.

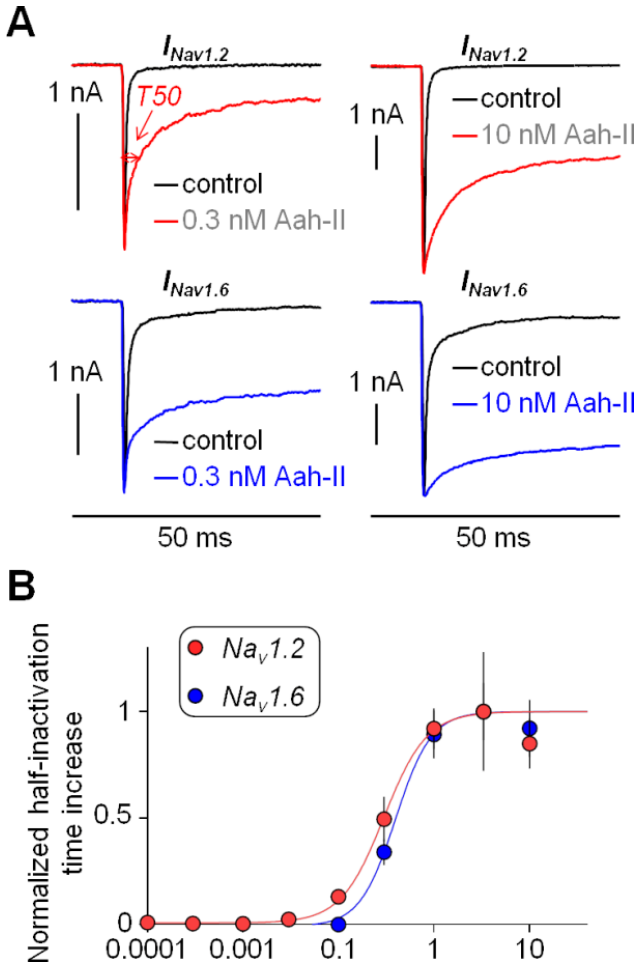

Figure 5.1 **Concentration-response analysis of the effect of AaH-II on $Na_v1.2$ and $Na_v1.6$ currents in HEK293 cells.** ***(A)*** Sodium currents recorded in HEK293 cells expressing either human $Na_v1.2$ or $Na_v1.6$ under control conditions and after addition of 0.3 nM or 10 nM of AaH-II. Red and blue traces correspond to $Na_v1.2$ and $Na_v1.6$ currents, respectively, in the presence of the toxin; the half-inactivation time (T_{50}) measured at 0.3 nM AaH-II is indicated by red arrows in the top-left panel ***(B)*** Mean ± SEM of the normalized increase in T_{50} following AaH-II addition at different concentrations for $Na_v1.2$ and for $Na_v1.6$ currents. Values reported in the plot were as follows. For $Na_v1.2$ (red lines and symbols): 0.01 nM – 0.004 ± 0.006 (N=7); 0.03 nM – 0.02 ± 0.01 (N=6); 0.1 nM 0.13 ± 0.04 (N=4); 0.3 nM 0.49 ± 0,11 (N=5); 1 nM – 0.92 ± 0.09 (N=9); 3 nM – 1 ± 0.28 (N=4); 10 nM – 0.85 ± 0.12 (N=6). For $Na_v1.6$ (blue lines and symbols): 0.01 nM – 0.01 ± 0.005 (N=7); 0.03 nM – 0.007 ± 0.005 (N=9); 0.1 nM - 0.0009 ± 0.006 (N=2); 0.3 nM – 0.34 ± 0.06 (N=20); 1 nM – 0.89 ± 0.11 (N=16); 3 nM – 1 ± 0.13 (N=20); 10 nM – 0.92 ± 0.13 (N=17). AaH-II prolonged inactivation in both isoforms with comparable dose-dependent effects, implying a poor discrimination between $Na_v1.2$ and $Na_v1.6$.

Concentration (nm)	**0.01**	**0.03**	**0.1**	**0.3**	**1**	**3.3**	**10**
$Na_v1.2$	8.2 ± 9.7 (N=7)	14.4 ± 3.2 (N=6)	6.9 ± 11.7 (N=4)	30.2 ± 5.7 (N=5)	31.8 ± 9.9 (N=9)	30.4 ± 9.4 (N=4)	56.5 ± 11.4 (N=6)
$Na_v1.6$	8.3 ± 2.4 (N=7)	−1.8 ± 4.2 (N=9)	−0.0 ± 3.3 (N=2)	4.5 ± 3.4 (N=20)	9.8 ± 3.3 (N=16)	20.7 ± 6.7 (N=20)	13.6 ± 5.0 (N=17)

Table 5.1 **Mean ± SEM of the percentage change in current amplitude induced by AaH-II in HEK293 cells expressing either $Na_v1.2$ or $Na_v1.6$ channels.** Values are reported for each concentration tested, from 0.01 nM to 10 nM. *"N" indicates the number of cells recorded per condition.*

5.2 Local AaH-II Delivery in L5 Pyramidal Neurons Alters Somatic AP Shape in a Concentration-Dependent Manner

Building on the insights gained from our heterologous-expression results, the goal of the next experiment was to establish at which concentration the toxin effectively reshapes action potentials (APs) in L5PNs within their native cellular environment. We performed whole-cell current-clamp recordings from L5PNs in cortical brain slices, following the procedure outlined in the Methods chapter, with a local application of AaH-II. Specifically, APs were elicited from a holding potential of -80 mV using 2-3 nA current pulses of 3-4 ms duration. Since Montnach et al. (2022) reported in an analogous study that the equivalent concentration producing an effect in brain slices was approximately 40-fold larger with respect to the experiments in HEK293 cells, we first tested the effect of local delivery of 40 nM AaH-II, anticipating a maximal effect at this concentration. As shown in **Figure 5.2A**, this concentration consistently and dramatically distorted the AP kinetics in all five tested cells, with an increase in the AP amplitude and a broadening of its waveform. The quantification of the change in AP width, defined as the time at which V_m > -30 mV during the AP, revealed a statistically significant increase of 60.19 ± 28.82% (p < 0.01, paired t-test).

To determine the minimal effective concentration required to produce for an effect, we tested AaH-II at three lower concentrations: 5 nM, 10 nM, and 20 nM, as shown in the example of **Figure 5.2B**. These concentrations induced progressively larger effects evaluated in terms of the changes in AP amplitude and width. As presented in **Figure 5.2C**, across eight cells, the width increased significantly at 10 nM (12.83 ± 7.77%, p = 0.0094) and 20 nM (25.41 ± 12.75%, p = 0.0034), whereas 5 nM produced a detectable change in only 50% of the cells. Amplitude changes remained consistently less than 3% and were not statistically significant at any concentration. Altogether, these results indicate that 10-20 nM is the effective concentration range for AaH-II–induced AP widening in L5PNs. Given that 5 nM was insufficient to induce a consistent effect on AP width, whereas 10 nM resulted in a substantial and significant change, an intermediate concentration of 7 nM was selected for subsequent experiments. This concentration produced a minimal yet consistently detectable

effect on the somatic AP, suggesting that it can be used in further experiments aimed at subcellular regions.

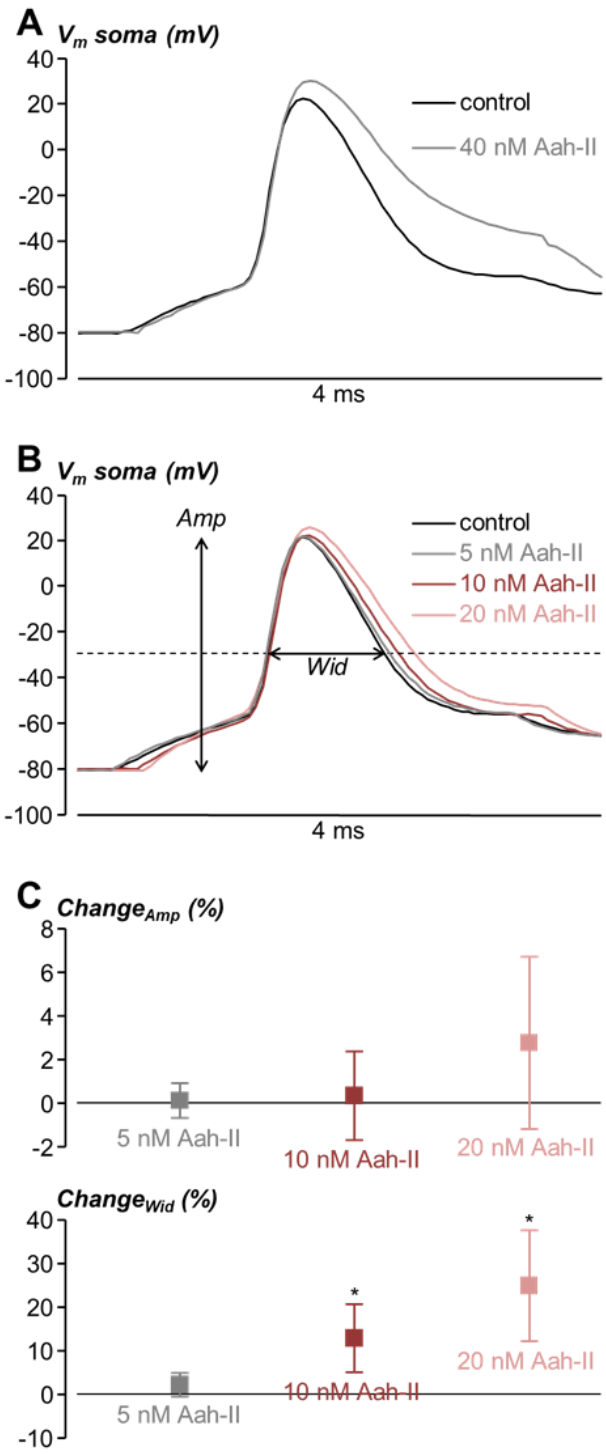

Figure 5.2* Concentration-dependent effect of AaH-II on the somatic action potential (AP) of layer 5 pyramidal neurons in brain slices.** ***(A) Representative somatic AP elicited by brief current pulse injection in control condition (black trace) and after local application of 40 nM AaH-II (grey trace), showing AP widening. ***(B)*** Somatic APs recorded in a different L5 pyramidal neuron under control conditions (black trace) and after local delivery of 5 nM (grey), 10 nM (red) and 20 nM (pink) AaH-II. The amplitude (Amp) and width (Wid), used for the analysis, are indicated for the control trace. ***(C)*** Quantification of the relative change (Mean ± SD, N=8 cells) in AP Amp (top) and Wid (bottom) following AaH-II application at 5 nM (grey lines and symbols), 10 nM (red lines and symbols) and 20 nM (pink lines and symbols). At 10 nM and 20 nM, AaH-II significantly increased AP width (*p = 0.0094 and *p = 0.0034, respectively; paired t-test). No significant change was observed in AP amplitude. Individual values (mean ± SD) reported in the plot were the followings. For the Amp parameter: 5 nM - 0.13±0.81%; 10 nM - 0.33±2.02%; 20 nM 2.80±3.94%. For the Wid parameter: 5 nM - 2.34±2.65%; 10 nM - 12.83±7.77%; 20 nM 25.41±12.75%. "*" indicates that the change in the parameter was significant.

5.3 AaH-II alters the Action Potential Preferentially in the AIS

Having established 7 nM as an intermediate concentration expected to produce a consistent somatic effect, in the following experiment we investigated the effect of AaH-II on the generating APs at the level of the AIS. Given the high density of VGNCs expressed at this site, the toxin was expected to elicit an enhanced effect compared to the soma. To this end, L5PNS were filled with the voltage-sensitive dye JPW1114, allowing simultaneous somatic patch-clamp recordings and optical voltage imaging at the AIS in order to compare the somatic to the AIS action potentials. To standardize the analysis and reduce the variability along the AIS, we averaged fluorescence over a 20 µm segment located ~10-30 µm from the soma.

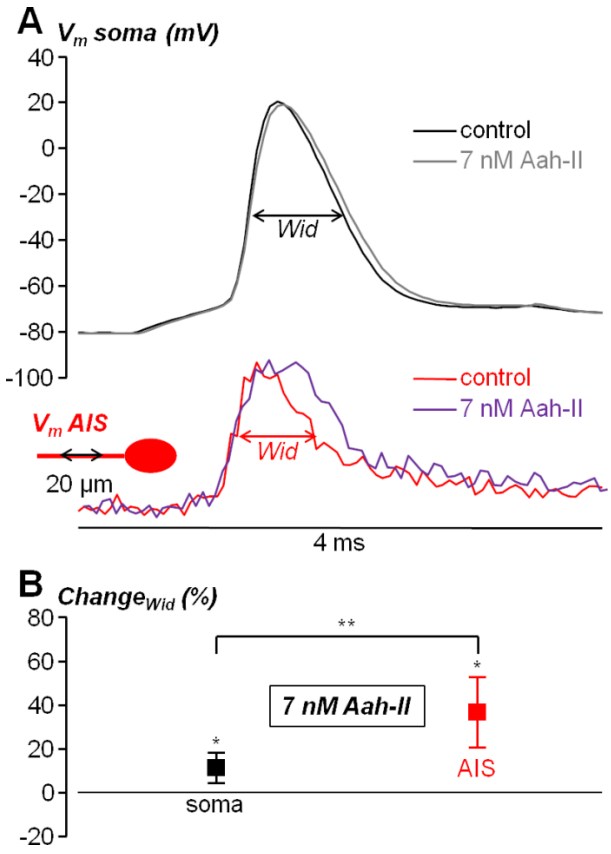

Figure 5.3* Effect of local delivery of 7 nM AaH-II on the action potential (AP) waveform at the soma and axon initial segment (AIS) of layer 5 pyramidal neurons.** ***(A) Top: somatic AP elicited by current pulse injection in a L5 pyramidal neuron in control condition (black trace) and after local delivery of 7 nM AaH-II (grey trace). Bottom: Corresponding AIS AP (recorded ~10-30 µm from the soma) in the same cell in control condition (red trace) and after AaH-II delivery (purple trace). The width parameter (*Wid)* used for the analysis is indicated for both compartment, soma and AIS, in the control condition. ***(B)*** Quantification of AP width changes (mean ± SD, N=9 cells) following AaH-II addition at the *soma* (black lines and symbols) and AIS (red lines and symbols). Values reported in the plot were 11.50±6.81 for the soma and 37.24±16.13 for the AIS. "*" indicates that AaH-II significantly widened APs at both compartments (*p = 0.0095 for soma; *p = 0.0034 for AIS; paired t-tests). "**" indicates that the change was significantly larger in the AIS ($p = 3.4 \cdot 10^{-4}$, paired t-test).

Figure 5.3A shows an example where the local delivery of 7 nM AaH-II resulted in a moderate increase in somatic AP width of ~7%, but a substantially greater widening of the AP waveform at the AIS ~40% in the same cell. This compartment-specific difference in the drug effect was consistent across N = 8 cells. In the soma, the average increase in AP width was significant (11.50 ± 6.81%), confirming the reliability of 7 nM as a minimally effective concentration. In the AIS, however, the AP was more affected, and the change in its width reached 37.24 ± 16.13%, significantly exceeding the somatic response ($p < 0.01$, paired *t*-test; **Figure 5.3B**). These results, besides validating the use of 7 nM for probing the AaH-II effects, demonstrate that under identical conditions of local toxin delivery, the AIS displays greater susceptibility to AaH-II, suggesting a regionally amplified pharmacological sensitivity that reflects the differences in channel distribution and density at the subcellular level, and calls for a closer look at the ionic dynamics shaping the AIS excitability.

5.4 AaH-II Enhances Sodium and Calcium Influx in the AIS

To probe the ionic mechanisms underlying the accentuated spike widening that we reported at the AIS, we next turned to high-speed optical imaging of Na^+ and Ca^{2+} dynamics during AP generation, thinking that studying the action of the toxin in a region enriched in its molecular targets, the VGNCs, would offer a more sensitive and physiologically relevant readout compared to somatic waveform analysis alone. Furthermore, the alterations in AP waveform offer important information regarding channel kinetics, but do not directly relate to the subthreshold or late-phase ionic fluxes that shape excitability at the subcellular level. In particular, both persistent sodium currents and activity-dependent calcium entry may contribute to compartment-specific responses that remain masked in somatic recordings.

To explore this, we performed targeted recordings of Na^+ and Ca^{2+} transients in the AIS of L5PNs, following the identical protocol of local application of 7 nM AaH-II. Neurons were loaded through the patch pipette with either the Na^+ indicator ING-2 or the Ca^{2+} indicator Oregon Green BAPTA-5N (OG5N), and fluorescence signals from the same AIS region (~10-30 μm from the soma) were recorded using high-speed imaging at 10k frames/s.

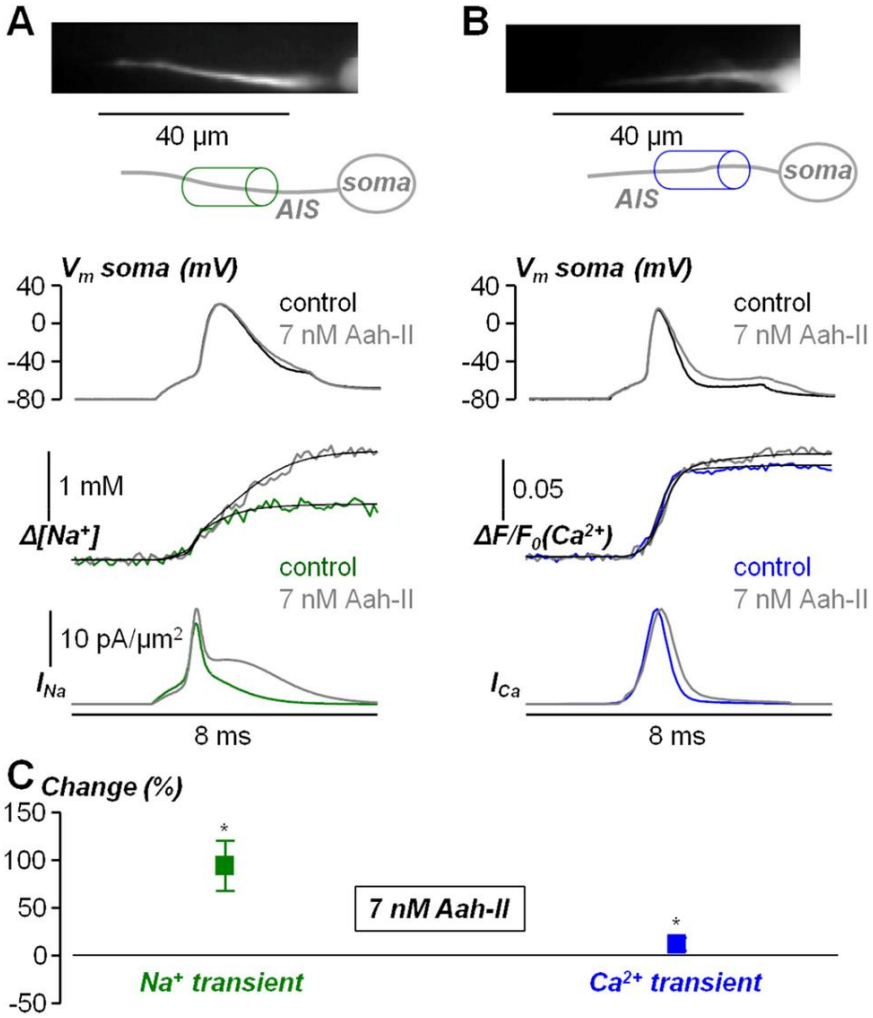

Figure 5.4 **Effect of local delivery of 7 nM AaH-II on the Na^+ and Ca^{2+} influx during the AP generation in the AIS of L5 pyramidal neurons.** ***(A)*** Top, fluorescence image of the AIS region filled with the Na^+ indicator ING-2 with a corresponding schematic indicating the region of interest (green). Middle, somatic AP in control solution (black trace) and after local delivery of 7 nM AaH-II (grey trace). Bottom, associated Na^+ transients fitted with a model function to calculate the Na^+ current (I_{Na}) in control (green trace) and AaH-II (grey trace) condiitons. ***(B)*** Top, fluorescence image of the AIS filled with the Ca^{2+} indicator OGB-5N with a schematic indicating the region of interest (blue). Middle, somatic AP in control (black trace) and after AaH-II delivery (grey trace). Bottom, associated Ca^{2+} transients fitted with a model function to estimate the Ca^{2+} current (I_{Ca}) in control (blue trace) and AaH-II (grey trace) conditions. ***(C)*** Mean ± SD (N=9 cells) of the relative changes in Na^+ (green lines and symbols) and Ca^{2+} (blue lines and symbols) following AaH-II application. Na^+ and Ca^{2+} signals increased by 85.2 ± 25.9%for Na^+ and 11.1 ± 5.3% Ca^{2+} respectively. "*" indicates statistically significant changes for Na^+ ($p = 1.07 \cdot 10^{-6}$, paired t-test) and Ca^{2+} ($p = 1.58 \cdot 10^{-5}$, paired t-test).

As illustrated in the representative traces of **Figure 5.4A**, AaH-II delivery induced a large increase in the late Na^+ influx, suggesting an impaired inactivation of VGNCs and thus an increase in the non-inactivating persistent Na^+ current. This effect was observed in all 9 cells tested, with the average increase in Na^+ fluorescence being 85.2 ± 25.9% ($p < 0.01$, paired t-test) (**Figure 5.4C**). In a complementary set of experiments, AaH-II application produced, however, a small but steady enhancement of the Ca^{2+} influx during the AP, corresponding to a widening of the Ca^{2+} current (**Figure 5.4B**), with an average increase of 11.1 ± 5.3% across 9 cells ($p < 0.01$, paired t-test). Collectively, these findings indicate that even minimal local exposure to AaH-II was capable of altering Na^+ and Ca^{2+} currents at the AIS, mostly through the substantial amplification of Na^+ inward and by the increase of Ca^{2+} influx.

5.5 AaH-II Selectively Enhances Nav1.2-Mediated Ca^{2+} Influx in the Distal AIS

It is not surprising that in the previous experiment, the Na^+ influx was more strongly affected than Ca^{2+}, given that Ca^{2+} entry in the AIS is predominantly mediated by VGCCs, which are less sensitive to alterations in Na_v channels (Lipkin et al., 2021). However, the smaller yet consistent increase in Ca^{2+} signals following the AaH-II application required further investigation into its origin. As previously discussed in Chapter 3, we considered the spatial heterogeneity of calcium entry mechanisms along the AIS. In earlier research from our group, we demonstrated that in the distal AIS, the predominant source of Ca^{2+} influx is not VGCCs, but rather $Na_v1.2$ channels themselves, owing to their physiological Ca^{2+} permeability.

Therefore, we hypothesized that: if AaH-II prolongs $Na_v1.2$ inactivation, Ca^{2+} entry through these channels should be enhanced specifically in the distal AIS, where $Na_v1.2$-mediated Ca^{2+} conductance is abundantly relevant. In contrast, the change in the AP waveform induced by the toxin would be expected to have negligible effects on the VGCC component of Ca^{2+} influx. To assess this hypothesis, we reanalyzed the Ca^{2+} imaging dataset by distinguishing between distal (30-40 μm from the soma) and proximal (5-15 μm) regions of the AIS.

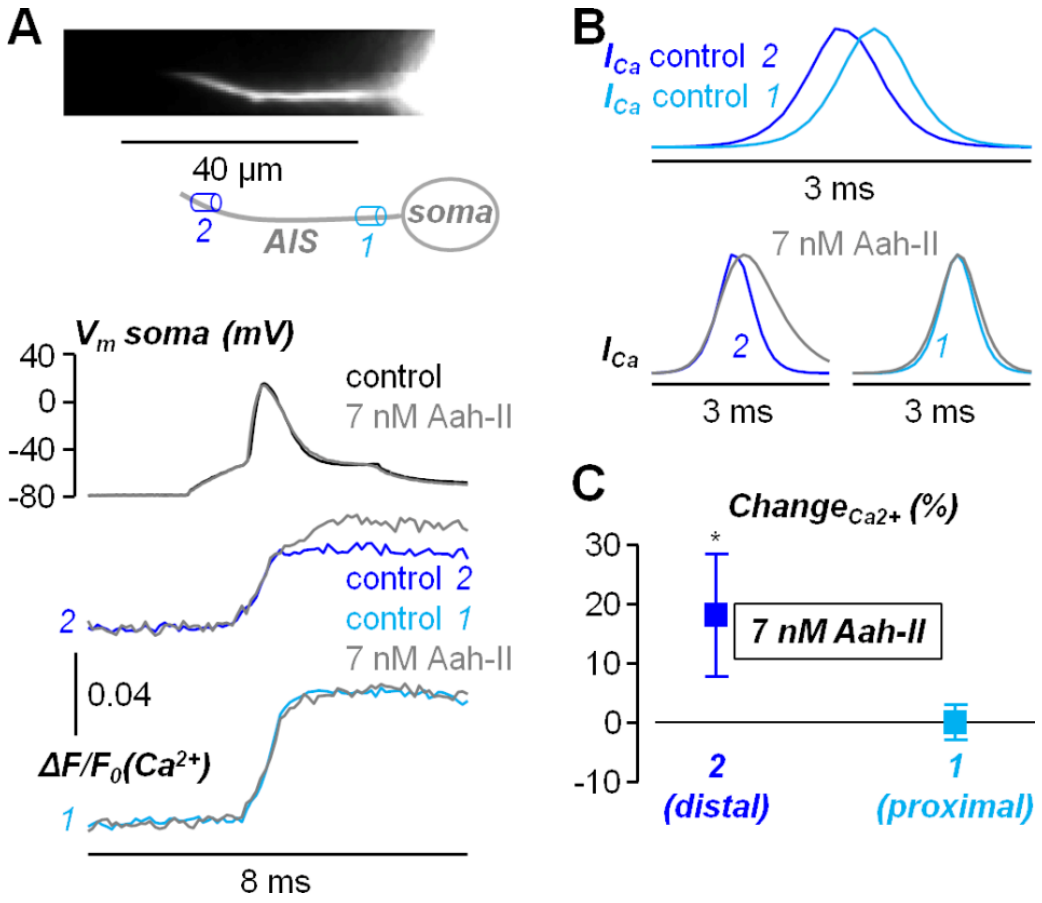

Figure 5.5 **AaH-II delivery increase Ca^{2+} influx associated with the AP only in the distal AIS.** ***(A)*** Top, fluorescence image of the AIS loaded with Ca^{2+} indicator (OGB-5N), with schematic reconstruction indicating two regions of interest: proximal (1) and distal (2). Middle, somatic AP in control (black trace) and after AaH-II delivery (grey trace). Bottom, corresponding Ca^{2+} transients in regions 1 and 2 in control (dark blue and light blue traces respectively) and after delivering 7 nM of AaH-II (grey traces). ***(B)*** Top, superimposed Ca^{2+} currents (I_{Ca}) in distal (2) and proximal (1) regions under control conditions showing the different kinetics. Bottom, ICa in each region before (blue traces) and after AaH-II delivery (grey traces), showing current widening only in the (2) distal AIS. ***(C)*** Mean ± SD (N=9 cells) of AaH-II-induced changes in Ca^{2+} in distal AIS regions (30-40 µm from the soma, dark blue lines and symbols) and in proximal AIS regions (5-15 µm from the soma, light blue lines and symbols). Values reported in the plot were 18.7 ± 10.3% in the distal AIS and 0.0 ± 3.0% in the proximal AIS. "*" indicates that the change was significant only in the distal AIS (p = 0.0011, paired t-test).

In the representative example of **Figure 5.5A**, local delivery of AaH-II caused an increase in Ca^{2+} influx in the distal AIS, while the proximal AIS was unaffected. In **Figure 5.5B**, the estimated Ca^{2+} traces show that under control conditions, the peak of the distal Ca^{2+} current occurred before the peak of the proximal Ca^{2+} current. Following toxin application, only the

distal Ca^{2+} current exhibited a widening of its shape, suggesting a selective effect of the drug on this compartment's Ca^{2+} component. Across 9 cells tested, the mean ± SD change in the maximum Ca^{2+} transients were 18.7 ± 10.3% in the distal AIS and 0.0 ± 3.0% in the proximal AIS (**Figure 5.5C**), with significance observed exclusively in the distal domain ($p < 0.01$, paired t-test). More specifically, the additional Ca^{2+} signal evoked by delayed $Na_v1.2$ inactivation was found to exhibit slower kinetics relative to control, indicating a spurious component likely arising from the toxin-induced prolongation of channel opening at the distal part of the AIS.

These results reveal that, beyond the expected effects on Na^+ conductance, AaH-II also amplifies a Ca^{2+} signal component attributable to $Na_v1.2$ activity in the distal AIS: an additional, often overlooked, target of its action. Although this reinforces the effect of AaH-II on Nav1.2 and modulation of its kinetics, it does not exclude the possibility that the drug also acts on other VGNC subtypes, such as $Na_v1.6$, co-expressed in the AIS.

5.6 Summary and Insights

In this chapter, the effects of the VGNC modulator AaH-II were analyzed at a physiologically relevant concentration in wild type L5PNs using subcellular targeted delivery and high-resolution optical imaging. With the broader goal of evaluating pharmacological strategies relevant to $Na_v1.2$ loss-of-function, this work evaluated the effect of AaH-II under conditions where somatic effects were minimal yet potentially informative. While cell-based assays in HEK-293 cells initially confirmed that AaH-II shifts inactivation of both $Na_v1.2$ and $Na_v1.6$, distinct and compartment-specific ionic consequences were observed in ex-vivo analysis.

At 7 nM, AaH-II induced a small but significant increase in the width of the somatic AP, and voltage imaging experiments revealed that the toxin had a stronger impact on the AP waveform at the AIS, under identical stimulation and delivery conditions, pointing to the increased sensitivity of this area to sodium channel alterations. Sodium imaging in this same region showed a prominent increase in late-phase Na^+ influx corresponding to the non-inactivating, slow component of the current caused by the prolonged Na_v channel

inactivation. Another small but significant increase was observed in the Ca^{2+} entry in complementary calcium imaging experiments, and further analysis confirmed that this change was restricted to the distal end of the AIS. Based on earlier evidence for $Na_V1.2$-elicited Ca^{2+} permeability in this compartment, these results suggested that prolonged inactivation affects not only the sodium inward, but also the time and magnitude of calcium entry. Interestingly, the distal Ca^{2+} current moved to a slower, delayed mechanism which may indicate a novel consequence of sustained opening of VGNC on intracellular pathways.

In summary, these findings highlight how low-concentration AaH-II, despite a lack of isoform selectivity, when tested at highly sensitive subcellular regions, induces specific alterations in ionic conductance. Although AaH-II meets neither the selectivity nor gating-modulation criteria for therapeutic rescue in *SCN2A* LoF disorders, its activity at the AIS reveals a spatially structured sensitivity toward inactivation kinetics and underscore the importance of high-resolution pharmacological approaches to characterize the VGNC modulators at their sites of subcellular enrichment, a methodological direction pursued further in the general discussion.

"If the human brain were so simple
that we could understand it,
we would be so simple that we couldn't."
- Emerson M. Pugh, *The Biological Origin of Human Values* (1977)

6

DISCUSSION

6.1 KEY STRENGTHS OF THE PRESENT WORK……139
6.1.1 Leveraging Sample Size Magnitude for Juvenile Characterization…… 139
6.1.2 Strengthening Reliability with Rigorous Statistics…… 140
6.1.3 A Dual-Model Approach to SCN2A LoF…… 140
6.1.4 Synergistic Multi-Compartment Analysis to Understand $Na_V1.2$ Channelopathies Pathophysiology……141
6.2 AIS IONIC MECHANISMS IN *SCN2A* LOF MODELS……142
6.2.1 Canonical AIS Ionic Refinement in WT L5PNs…… 142
6.2.2 Disrupted Ionic Refinement in SCN2A Mutant Models…… 144
6.2.2.1 Reduced $Na_V1.2$ Mediated Influx in Haploinsufficiency……144
6.2.2.2 Subtle Perturbations of AIS influxes Currents in *Scn2a*$^{+/L1314P}$……145
6.2.3 Methodological Constraints…… 146
6.3 ACTION POTENTIAL WAVEFORM ALONG THE SOMA-AIS AXIS……147
6.3.1 Baseline Waveform Refinement in WT Somatosensory L5PNs…… 147
6.3.2 Transient Perturbations in SCN2A LoF Models…… 150
6.3.2.1 Somatic and Proximal Impairments in Haploinsufficient neurons……150
6.3.2.2 Early Juvenile Initiation-Site Dysregulation in KI Neurons……151
6.4 REMODELING OF POTASSIUM CURRENTS IN *SCN2A* PATHOPHYSIOLOGY……152
6.4.1 Distal AIS Kv1-Dominated Phenotype in L1314P Mutants…… 153
6.4.2 Somatic-Proximal Potassium Current Deficits in Haploinsufficient Neurons…… 154
6.4.3 How local is a "local" potassium block when interpreted with AP waveform?…… 155
6.5 AIS PLASTICITY AND MECHANISTIC COMPLEXITY IN *SCN2A* LOF PHENOTYPES……156
6.5.1 From Channel Dysfunction to Structural-Functional Remodeling at the AIS…… 157
6.5.2 Plasticity, Channel Remodeling, and Alternative Mechanisms in SCN2A LoF models…… 159
6.6 SOMATODENDRITIC EXCITABILITY IN *SCN2A* LOF……161
6.7 AAH-II CHARACTERIZATION AND $NA_V1.2$ MODULATION FOR *SCN2A* LOF RESCUE……164
6.8 CHALLENGES OF MODELING DISEASE WITH HAPLOINSUFFICIENT ANIMALS……166
6.9 TOWARD A BETTER UNDERSTANDING OF *SCN2A*-RELATED DISORDERS BEYOND GAIN AND LOSS-OF-FUNCTION……168

Despite the increasing number of defined *SCN2A* variants, the cellular phenotypes by which these mutations shape neuronal excitability across development remain poorly understood. Human neurodevelopmental disorders, including ASD, often unfold over extended timescales and exhibit age-specific phenotypes not observed in a simplified model. Thus, untangling their physiological basis requires an integrative framework that links cellular mechanisms over developmental windows, brain compartments, and experimental modalities. An ideal body of research would encompass in vivo recordings, structural microscopy, human-derived systems, behavioral analysis, proteomics, and network-level analyses. However, unfortunately, each of these modalities has its own limitations, and ironically, as one narrows the scope to attain greater precision, it is often at the cost of fogging the broader physiological phenotype. In practice, most studies, including ours, have to navigate within these narrower methodological constraints. In this project, we tackled this complexity by focusing on a defined postnatal window (P21-40) and using ex vivo electrophysiology and optical imaging. Through the following discussion, I will provide an interpretation of our findings across neuronal compartments, starting from the ionic basis of spike generation at the AIS, progressing through somatic excitability, and culminating in dendritic calcium electrogenesis. Our wild-type controls, in conjunction with the existing rich literature, will serve as the baseline for establishing normal developmental trajectories, which will then anchor our comparative analyses of the KO and KI models of *SCN2A* LoF. Further, by age-stratifying the analysis, we will report transient phenotypes not revealed by pooled comparisons, which will help to interpret the signature of each mutation in light of basic physiological ion channels mechanisms.

6.1 Key Strengths of the Present Work

6.1.1 Leveraging Sample Size Magnitude for Juvenile Characterization

Before delving into a detailed interpretation of our findings, it is worth emphasizing that this work offers a novel and in-depth physiological characterization of *SCN2A* LoF related disorders. Being grounded on a large sample size, rarely attained in comparable electrophysiology and optical imaging studies, the findings presented in preceding chapters

are built on datasets collected from over a 1000 cells from layer 5 somatosensory cortex, obtained from more than 260 mice of three different genotypes. For comparison, high quality studies on Nav1.2 mutations, such as Spratt et al. (2019) and Ogiwara et al. (2018) typically analyzed between 20 to 50 cells per genotype, and even the more detailed report by Spratt et al. (2021) reached samples sizes of ~60-77 neurons in their largest groups, making the present study, to our knowledge, the largest ex vivo dataset reported for *SCN2A* LoF models. Moreover, by recording from mice between the third and fifth postnatal weeks, we were able to provide a mapping of excitability changes across the juvenile period. This developmental window has only been the subject of limited high-resolution characterization to date, despite its importance for late refinement and fine tuning of cortical circuits, and potential critical periods for therapeutic interventions.

6.1.2 Strengthening Reliability with Rigorous Statistics

Furthermore, throughout the analysis presented in chapter 3 and 4, we adopted a highly rigorous statistical power to list any finding as significant. We combined the strict 0.01 p-value threshold with only large effect sizes, and we required a power exceeding 80% to accept the observed effect in most analyses. With this approach, we complemented earlier work where results were generally reported without explicit power considerations by providing additional statistical stringency, which is particularly important within the context of neurodevelopmental disorders, and neuroscience research in general, where low sample sizes and statistical power have been a concern that casts the field findings into doubt by challenging reproducibility and interpretation (Nord et al., 2017).

6.1.3 A Dual-Model Approach to *SCN2A* LoF

Another noteworthy strength of this study is the direct comparison of two distinct LoF models of the same gene: a heterozygous knock-out *Scn2a*$^{+/-}$ in parallel with a patient-derived heterozygous knock-in (*Scn2a*$^{+/L1314P}$). Considerable advances have been made to previous work examining either KO models (as in Spratt et al., 2019; Nelson et al., 2024), or KI variants alone such as the *Scn2a*$^{+/K1422E}$ mouse model (Echevarria-Cooper et al., 2022).

And though Ogiwara et al. (2018) did include both a KO and a KI, their approach focused on seizures characterization using in vivo EEG with behavioral and histological assays, they did not address ionic mechanisms at the cellular or subcellular level. Our work, however, stands out for reporting a comparative analysis of two model types both of ASD, under the same experimental framework, using multi-compartment recordings which affords unprecedented insights into subtle divergences in ionic mechanisms, AIS physiology, excitability profiles, and developmental trajectories, which would remain otherwise obscured. By virtue of this design, this study builds a strong translational bridge connecting the preclinical "theoretical" perspective offered by KO models with existing clinical phenotypes recapitulated in knock-ins.

6.1.4 Synergistic Multi-Compartment Analysis to Understand $Na_v1.2$ Channelopathies Pathophysiology

A major analytical contribution of this thesis is its methodological scope. We interrogated different aspects of action potential physiology and analyzed VGIC kinetics at sub-millisecond scale using a synergistic approach, which includes three major ingredients: whole-cell electrophysiology, ultrafast imaging of the V_m as well as Ca^{2+} and Na^+ transients, and targeted pharmacological manipulation. In addition, we systematically addressed the excitability at different compartments: the soma, the AIS, and the distal apical dendrites, while earlier studies mostly used specialized approaches to focus on isolated compartments. By building upon earlier findings that have greatly advanced our *SCN2A* channelopathy knowledge, and extending them with a higher degree of spatial and functional precision, this study presents novel mechanistic insights into the compartment-specific roles of $Na_v1.2$ during AP initiation, dynamics of backpropagation, and its interplay with other channels, providing thus a physiological model of how *SCN2A* loss remodels excitability across neuronal domains, and particularly the AIS.

6.2 AIS Ionic Mechanisms in *SCN2A* LoF Models

6.2.1 Canonical AIS Ionic Refinement in WT L5PNs

Immunolabeling and electrophysiological studies in rodent cortex have shown $Na_v1.2$-enriched proximal AIS regions and $Na_v1.6$-enriched distal AIS regions, with distinct gating properties that endow distal AIS with a lower threshold for action potential (AP) initiation and proximal AIS with higher threshold channels (Hu et al., 2009; Lorincz & Nusser, 2008). Previous high-resolution work from our group confirmed this aforementioned subdomain specialization using isoform-selective manipulations toward $Na_v1.2$ and $Na_v1.6$, which altered AIS signals in distinct ways that matched the expected proximal $Na_v1.2$ and distal $Na_v1.6$ distributions (Filipis et al., 2023). These findings laid a foundation for the present investigation of AIS ionic mechanisms across development.

Our optical Na^+ measurements in WT neurons align with this compartmental arrangement. With maturation (P21-24 to P30-40), the proximal-to-distal sodium fluorescence ratio ($R_{p/d}$) showed a trend toward ~1, indicating a gradual refinement and strengthening of $Na_v1.2$ contribution at the proximal AIS. This result suggests that with progressive $Na_v1.6$ predominance distally, Nav1.2 remains an important proximal contributor to Na^+ influx into late juvenile stages, consistent with prior reports indicating that the developmental shift from $Na_v1.2$ to $Na_v1.6$ does not extinguish proximal $Na_v1.2$ (Lorincz & Nusser, 2008).

A second layer of analysis was achieved by evaluating the $Na_v1.2$-mediated Ca^{2+} permeability. Hanemaaijer et al. (2020) previously estimated that $Na_v1.2$ conducts ~0.4% Ca^{2+} relative to Na^+, relying on TTX sensitivity and kinetics of this Ca^{2+} component matching Na_v activation. Building on this, our group recently demonstrated that Ca^{2+} signals at the distal AIS are mediated by $Na_v1.2$ rather than $Na_v1.6$, and that this Ca^{2+} component can activate BK channels to shape early AP repolarization (Filipis et al., 2023). In light of these findings, we hypothesized that developmental changes in $Na_v1.2$ expression or kinetics should be reflected in calcium readouts, particularly in the spatiotemporal profile of calcium currents.

To assess the Na_v-dependent Ca^{2+} contribution in the AIS calcium signal, we quantified the distal-to-proximal I_{Ca} peak delay. We report that in wild-type pyramidal neurons, the delay increased across the third to fifth postnatal weeks, revealing a progressive temporal separation between the fast distal $Na_v1.2$-mediated Ca^{2+} influx and the slower proximal VGCC-mediated component. This pattern confirms the distal prominence of $Na_v1.2$-mediated entry, in line with our previous work (Filipis et al., 2023). Importantly, the present study adds that this $Na_v1.2$-Ca^{2+} component undergoes refinement during the juvenile window: the distal Ca^{2+} rise becomes increasingly early relative to the proximal AIS, highlighting a previously underappreciated pattern in the maturation of AIS Ca^{2+} signaling in WT neurons.

A potential question that might surface here is how do these two forms of $Na_v1.2$ refinement, proximal localization of its sodium influx and distal enhancement of associated calcium signals, coexist during development? The short answer would be that these mechanisms are complementary, not contradictory. As $Na_v1.6$ accumulates distally and mediates earlier AP initiation at more hyperpolarized potentials, the resulting faster and steeper AP onset in distal AIS regions overlaps more effectively with the brief $Na_v1.2$ conductive windows, thereby increasing their driving force and open time, and boosting the Ca^{2+} entry through the residual distal $Na_v1.2$ pool even if the overall $Na_v1.2$ expression shifts proximally (Hu 2009, Leterrier 2018, Li et al., 2023; Osorio 2009; Yang et al., 2019). Meanwhile, the proximal AIS remains more facilitative to VGCCs activation. In the mouse cortical L5PNs, AIS expresses a combination of Ca_v3 (T-type) channel hotspots and more diffused Ca_v2 channels (Lipkin et al., 2021). The relatively slower proximal spikes create a larger temporal window for these Cav channels to activate, leading to a delayed and likely Ca_v-dominated calcium signals, diluting the relative contribution of $Na_v1.2$ (Bender et al., 2010; Bender & Trussell, 2009).

Taken together, these results indicate that wild-type neurons undergo coordinated maturation of the AIS ionic mechanisms during juvenile period, characterized by a reinforcement of proximal $Na_v1.2$-mediated sodium influx, paralleled by an increasing earlier shift of the distal $Na_v1.2$-dependent calcium signal relative to proximal VGCC-mediated entry. This structured maturation provides a framework through which the alterations in *SCN2A* mutant models can now be interpreted.

6.2.2 Disrupted Ionic Refinement in *SCN2A* Mutant Models

6.2.2.1 Reduced $Na_v1.2$ Mediated Influx in Haploinsufficiency

Scn2a$^{+/-}$ neurons failed to undergo the normal refinement of AIS sodium and calcium dynamics observed in WT animals. From both Na^+ and Ca^{2+} analyses we observed two main characteristics. First, these cells are characterized by a persistent reduction in the proximal AIS sodium influx, and the developmental increase in this component was absent. Our second main observation was the Ca^{2+} signal failure to display the age-dependent temporal shift seen in controls and, and more severely, the consistently shorter distal-proximal Ca^{2+} delays in *Scn2a*$^{+/-}$ compared to wild-type, indicating that the developmental progression of distal $Na_v1.2$ activity was disrupted. Despite these impairments, distal Na^+ influx remained preserved, consistent with $Na_v1.6$ dominant roles in mediating Na^+ influx and spike initiation at the distal AIS. Together, these findings point to a compartment-specific vulnerability: the proximal roles of $Na_v1.2$ are selectively reduced, while distal Na^+ currents remain largely intact. This aligns with well-established polarized distributions of VGNC isoforms at the AIS (Hu et al., 2009; Lorincz & Nusser, 2010; Tian et al., 2014), and extends them by showing that the distal $Na_v1.6$ cannot fully compensate for altered $Na_v1.2$ function in the proximal axon, at least not by P40.

The selective deficits that we report in this model are not surprising, both consistent with an underlying loss of functional $Na_v1.2$ channels at the AIS, which further disrupts the maturation of associated conductance kinetics. Previous studies converge with this interpretation: slowed AP upstrokes and altered excitability were reported in *Scn2a*$^{+/-}$ L5PNs by Spratt et al. (2019), and impaired spike initiation with higher thresholds was described in conditional knockouts by Ogiwara et al. (2018). While those studies primarily interpreted deficits in terms of somatodendritic integration, the reduced number of $Na_v1.2$ channels at the AIS in *Scn2a*$^{+/-}$ that we present may constitute itself a primary determinant of these broader excitability impairments. This possibility was addressed and will be examined in a later section of this Chapter.

6.2.2.2 Subtle Perturbations of AIS influxes Currents in *Scn2a*$^{+/L1314P}$

If we consider how a missense LoF mutation might subtly alter the ionic mechanisms that shape the AP generation, the *Scn2a*$^{+/L1314P}$ model offers a compelling example. In contrast to the partial loss of functional $Na_v1.2$ channels inferred from the sodium and calcium imaging in the haploinsufficient mouse model, we observed that Na^+ amplitude in KI cells was nearly indistinguishable from WT. However, when we turned to Ca^{2+} kinetics, slight but consistent perturbations appeared. Our analysis showed, a dissociation between fine-tuning of Na^+ and Ca^{2+} influx at the AIS. On one hand, age-dependent increases in proximal Na^+ influx were preserved, suggesting that the sodium conductance was maintained. On the other hand, while baseline distal-proximal Ca^{2+} delays were comparable to controls, the expected age-dependent increase in temporal separation was not achieved, indicating that the $Na_v1.2$- Ca^{2+} signal failed to undergo the temporal refinement seen in WT cells. Together these results argue against a simple quantitative reduction in $Na_v1.2$ function and instead suggest that the L1314P mutation disrupts the functional dynamics of $Na_v1.2$ at the AIS.

When comparing these findings to the KO model, it becomes evident that the ionic pathophysiology differs between the two genotypes. Haploinsufficiency leads to a clear quantitative deficit in $Na_v1.2$ activity. In contrast, the L1314P mutations outcomes, to this point, remain inconclusive with no overt reduction in Na^+ amplitude, and only subtle disruptions in Ca^{2+} kinetics, despite the presence of a pathogenic *SCN2A* variant.

In the broader context of *SCN2A* mutations, this divergence illustrates how even two "loss-of-function" genotypes can differentially shape the AIS ion channel functions. Prior studies have addressed the heterogeneity of *SCN2A* variants indicating that different missense mutations can produce mixed and sometimes "opposing" biophysical effects, including altered gating and sometimes a combination of GoF/LoF features (Ben-Shalom et al., 2017; Echevarria-Cooper et al., 2022). Thus, the assumption that all LoF mutations converge on a common pathophysiology is overly simplistic. Our data support the interpretation that the KI and KO models represent mechanistically distinct forms of AIS disruption. This distinction, first revealed by sodium and calcium measurements, will take on further

relevance as we turn to action potential waveform analysis and somatodendritic excitability, where the consequences of these alterations were expected to manifest more profoundly.

6.2.3 Methodological Constraints

The use of high-speed fluorescence imaging allows subcellular resolution of Na^+ dynamics along the AIS; an approach that extends beyond conventional electrophysiological methods. However, the conversion of fluorescence signals into estimates of ionic current requires several modeling steps, including kinetic fitting of transients and estimation of AIS morphology. Small errors in these procedures can affect the precision of absolute current values. In addition, the temporal resolution of our recordings (100 µs per frame) under-samples and smooths the sub-millisecond kinetics of VGNCs, which include both a fast inactivation component and a slower or persistent component (Kay et al., 1998; Raman & Bean, 2001). We mitigated this by focusing our analysis on the amplitude of fitted Na^+ transients, which is not subject to these errors, and calculated the proximal-to-distal ratio (Rp/d), which relatively overcomes the variability between cells. As a result, our measurements reflect integrated charge entry across frames rather than the instantaneous peak of the fast current. In addition, the attribution of proximal influx to $Na_v1.2$ and distal influx to $Na_v1.6$ remains indirect, being inferred from prior knowledge of channel localization and toxin sensitivity, rather than from isoform-specific measurements. A similar limitation applies to our interpretation of Ca^{2+} signals. The separation of Ca^{2+} currents mediated by $Na_v1.2$ from those mediated by VGCCs rests on kinetics and spatial assumptions from prior work, based on which we interpreted fast distal Ca^{2+} signals as a proxy for $Na_v1.2$-mediated entry. This approach, however, remains an indirect measure; for instance, developmental or genotype-dependent changes in AP waveform or in the density and distribution of VGCCs at the AIS, could influence distal and proximal Ca^{2+} peaks independently of $Na_v1.2$. Thus, one should be careful not to over-interpret the evident contribution of $Na_v1.2$ to AIS Ca^{2+} influx. What we propose is that the difference in I_{Ca} temporal kinetics resonates with $Na_v1.2$ function, without directly quantifying its specific Ca^{2+} component.

6.3 Action Potential Waveform Along the Soma-AIS Axis

With sodium and calcium imaging, we revealed specific perturbations of AIS influx, and obtained high-resolution insights into ionic signatures sculpted by $Na_v1.2$ dysfunctions in KO and KI mouse models, however these mechanisms only comprise one dimensional projection of a broader excitability landscape, and do not fully capture the integrative effects on neuronal output. The action potential waveform, in contrast, arises from the coordinated interplay of multiple conductance, including potassium, and provides an integrative readout of underlying ion channel dynamics. In this context, $Na_v1.2$ plays a dual role. Although AP initiation is primarily driven by $Na_v1.6$ at the distal AIS, $Na_v1.2$ contributes critically with its Ca^{2+} permeability that activates CAKCs, particularly BK channels, which despite their lower density compared to K_v1 subtypes, considerably influence the repolarization and spike width of generating APs (Echevarria-Cooper et al., 2022; Filipis et al., 2023; Hu et al., 2009; Trimmer, 2015). The impaired maturation of calcium signals observed in both *SCN2A* mutant models is therefore expected to impact this $Na_v1.2$-BK coupling axis. Moreover, because the initiating spike at the AIS determines the waveform as it backpropagates to the soma, even distal alterations are expected to influence somatic AP parameters. In *Scn2a*$^{+/-}$ neurons, reduced proximal Na^+ influx also suggests an impaired backpropagation, a process that has been shown to be particularly dependent on $Na_v1.2$ function. For both models, we speculated that reported influx and currents disruptions will translate into quantifiable alterations of AP waveform, which we tested by examining AP shape in two compartments: the soma through whole-cell patch clamp recordings, and the AIS using ultrafast voltage imaging.

6.3.1 Baseline Waveform Refinement in WT Somatosensory L5PNs

To establish a baseline for later comparisons of AP waveforms in KO and KI mouse models, it was necessary to first analyze the refinement of somatic L5PN action potential properties in wild-type mice during the juvenile window.

Most prior work assumes that intrinsic spike maturation is essentially complete by the end of the third postnatal week in rodents; as a consequence, the juvenile (P21-40) and adult (P>42) periods have received far less attention when characterizing postnatal development of AP active and passive properties. For instance, Zhang (2004) recorded L5PNs in the rat medial prefrontal cortex from P1 to P36 and concluded that P21 marks the achievement of adult-like properties. He showed that over the first three weeks, the AP threshold shifted about 13 mV more negatively, the spike amplitude increased by 30 mV in the first two weeks and then plateaued, and the half-width fell by 75% reaching near-mature values by P21. Another study by Etherington and Williams (2011) examined rat primary visual cortex, layer-5 thick-tufted pyramidal neurons from P11 to P29, and reported similar developmental trajectories: a more negative threshold from ~P11 to P15 that stabilized by P25–P29, an amplitude rising early then plateauing by late juvenile, and an almost 50% drop in the half-width between P11 and P15 with further narrowing to a stable value by P25-P29. Pérez-García and colleagues (2021) extended the picture in rat primary motor cortex L5PNs, from P2 to P44. This study, though carried out on the motor cortex, is one of the few that explicitly covered our juvenile period, which they named “early adulthood”. They found no age effect on threshold and described it as established at birth, with amplitude increasing over the first month, and AP duration decreasing with age, reaching mature values by the end of P30.

Across these and other reports from different cortical regions, pyramidal neurons showed a common refinement of their APs: an early increase in AP amplitude and a decay in AP duration as they approach maturity. These changes were attributed to tuning the balance between sodium influx and potassium efflux, considered the primary determinant of how AP amplitude and width evolve with age. Consistently, an up-regulation or maturation of voltage-dependent Na^+ and K^+ conductance underlies the AP shape refinement observed through the first postnatal month (Bahrey & Moody, 2003; Zhang, 2004; Etherington and Williams, 2011; Kroon et al 2019).

Our somatosensory cortex WT analysis across P21-36 shows a pattern that is both consistent and informative relative to the abovementioned studies. For the AP threshold, we refrain from making claims due to bias introduced by bridge error in our recordings; also, the major shift reported in medial prefrontal and visual cortex reports was expected to largely precede

our recording window. The somatic AP amplitude however, stayed mostly the same between P21 and P36, which matches the mature plateaus reported in all three studies. Most critically, the somatic AP half-width continued to narrow in late juveniles, about 13% from P21-24 to P30-37, indicating a less pronounced sharpening than in early development, yet an ongoing fine-tuning of repolarization during this period, a window often presumed by many studies to be already mature by P21. Considering the Na^+-K^+ interplay, our sodium imaging results showed no decline in Na^+ levels with age over this period, making thus a continued strengthening of K^+-mediated repolarization in somatosensory L5PNs the most reasonable explanation for the progressive reduction in AP width observed as animals transition through the late-juvenile period.

As for the AP shape at its site of generation in wild-types, our voltage imaging recordings showed a consistent proximal to distal narrowing ($AP_{wid\ \text{proximal}} > AP_{wid\ \text{medial}} > AP_{wid\ \text{distal}}$). This spatial profile aligns with the segregation of Na_v isoforms and AIS K^+ channel organization in L5PNs described earlier in the Introduction of this thesis. In mature neurons, the enrichment of the lower-threshold $Na_v1.6$ isoforms in the distal AIS establishes a trigger zone about ~30-40 μm from the soma with accelerated onsets (Palmer & Stuart, 2006; Popovic et al., 2011). In parallel, low-threshold K_v1 conductance concentrated along the initial ~50 μm of the axon provides a rapid outward current during the early repolarization (Kole et al., 2007), in addition to $Na_v1.2$-BK coupling, which adds a fast repolarizing drive during AP initiation at the distal AIS (Filipis et al.,2023). Altogether these intrinsic AIS mechanisms support the generation of APs at the distal AIS with lower thresholds and sharper waveforms than those arising in proximal and somatic regions, closely matching our V_m data in WT cells. During the examined age period, this spatial profile of AIS AP waveform was maintained, suggesting that the AIS compartmentalization was already established by P21. Nevertheless, distal APs appeared slightly sharper in the old group, suggesting subtle refinements of underlying ionic mechanisms, particularly the K^+ mediated repolarization, which mirrors the somatic AP sharpening reported in whole-cell recordings, implying that the AP waveform maturation, while largely achieved by the third postnatal week, is not entirely static thereafter and remains sensitive to developmental regulations.

6.3.2 Transient Perturbations in *SCN2A* Lof Models

6.3.2.1 Somatic and Proximal Impairments in Haploinsufficient Neurons

We built on the conserved WT patterns, and by examining the AP waveform we saw that both *SCN2A* models followed the expected trajectory of somatic AP sharpening with age and the proximal to distal narrowing of AIS spikes. This suggests that the $Na_v1.2$ impairments did not derail the maturation trajectory of AP properties, however, clear differences emerged in each model particularly during early juvenile ages (P21-24). In haploinsufficient (*Scn2a*$^{+/-}$) neurons, the soma was the main site of disruption: spikes were wider in young animals, pointing to a transient prolonged repolarization. Since Na^+ influx was clearly not elevated relative to WT, this phenotype is more reasonably explained by a delay in K^+ current maturation or incomplete recruitment of K^+ channel, leaving lower outward current to repolarize the spike; alternatively, it may reflect a direct downregulation of K^+ channels themselves. By P30-37, haploinsufficient cells did sharpen their somatic spikes, suggesting that K^+ currents eventually strengthened over development, but at this stage the loss of proximal $Na_v1.2$ Na^+ influx became the limiting factor: somatic AP amplitude, which remained stable throughout the juvenile window in WT animals and in previous reports, fell below the baseline in KO neurons. This decrease aligns with our Na^+ analysis, which revealed attenuated proximal influx at the same age. Given that the proximal AIS supports AP backpropagation, its impaired Na^+ conductance likely reduces the somatic spike amplitude, illustrating how KO neurons transition from a K^+ dominated early phenotype (wide APs) to a Na^+ dominated late phenotype (reduced amplitude). Importantly, AIS voltage imaging demonstrated that the waveform at the initiation site was conserved across the examined period in KO neurons, with no significant deviations from WT despite the somatic perturbations. And although our Ca^{2+} imaging indicated that the $Na_v1.2$-BK coupling was impaired in old KO, this did not translate into a marked widening of the AIS AP itself, suggesting that while $Na_v1.2$ mediated Ca^{2+} entry is necessary for the modulation of distal repolarization, BK channels role is not the primary determinant of the generating AP width at the AIS, and the missing BK repolarization could have been compensated by other K^+

outward pathways. And it appears that the major consequence of $Na_v1.2$ haploinsufficiency was to reduce the proximal support for AP backpropagation.

6.3.2.2 Early Juvenile Initiation-Site Dysregulation in KI Neurons

The AP shape analysis in the knock-in model was particularly informative, as neither Na^+ nor Ca^{2+} imaging alone revealed strong abnormalities. It presented almost an opposite phenotype to the KO model, with alterations emerging at both the soma and AIS, particularly in younger juveniles. At P21-24, *Scn2a*$^{+/L1314P}$ fired somatic APs of reduced amplitudes. Their Na^+ influx found comparable to WT cells rules out any Na^+ deficit and points instead to an imbalance in favor of K^+ currents. This effect was consistent across the AIS domain where a stronger K^+ conductance was also evident: distal APs were sharper than in both WT and KO, indicating that the site of initiation itself was skewed toward excessive repolarization. Thus, in contrast to the *Scn2a*$^{+/-}$ model, the KI phenotype appears to reside at the initiation zone, with soma and AIS both reflecting a K^+ dominated imbalance at early juvenile stages. By P30-37, these disruptions largely converged to the WT profile: somatic AP widths narrowed following the normal trajectory, and amplitudes were no longer reduced, and the exceptionally sharp distal APs were restricted to the young group.

These findings suggest that the increase in Na^+ influx during maturation had possibly restored the Na^+/K^+ balance, and that the KI phenotype was transient and most prominent at early juvenile ages.

Taken together, these patterns further reinforced the distinct and compartment-specific perturbations across our two LoF models. Importantly, if ages were pooled, the differences that we report would have been masked, as overall averages look quite similar between the three strains. One intriguing aspect is that the main Na^+ and Ca^{2+} impairments in KO neurons emerged in older juveniles, consistent with a loss of functional $Na_v1.2$, whereas the AP shape analysis revealed an additional phenotype, involving a modulation of K^+ currents which was confined to the younger age group. This underlines that even within the juvenile window, AP fine-tuning mechanisms remain age-sensitive and undergo specific layers of refinement, such that only by comparing the third to fifth postnatal weeks do divergent electrophysiological outcomes become evident.

The conclusion of particular interest was that K^+ conductance primarily underlies the observed AP waveform changes, whether through insufficient recruitment in *Scn2a*$^{+/-}$ or excessive repolarization in *Scn2a*$^{+/L1314P}$. But at the same time, explaining these phenotypes is far from straightforward. While the KI model perturbations could in theory be explained by compensatory upregulation of K_v1 repolarization at the distal AIS, either through elevated trafficking-targeting of K_v1 subunits or shifts in their gating to faster kinetics, the nearly preserved Na^+ influx and the transient nature of this phenotype also make the AIS plasticity an alternative plausible interpretation. Specifically, a shrinking and a distal relocation of the AIS domain, with a possible redistribution of ion channels could reproduce a comparable phenotype without requiring a local increase in K^+ current. In the following sections, we address these two hypotheses separately, beginning with pharmacological manipulations of potassium channels.

6.4 Remodeling of Potassium Currents in *SCN2A* Pathophysiology

In line with the first hypothesis, by far, dysregulated potassium conductance emerged as a major modulator of changes in AP shape across both *SCN2A* models. This link is not unprecedented, as prior *SCN2A* LoF work demonstrated that reduced $Na_v1.2$ activity reshapes potassium channel-dependent repolarization. In conditional cortical *SCN2A* KO neurons, Spratt et al. (2021) described a remarkable paradox: a major Na^+ current loss was associated to intrinsic hyperexcitablity characterized by smaller AP amplitudes with slower repolarization and reduced AHPs. In computational and dynamic clamp methods this phenotype was rescued by injecting a transient K^+ conductance, thus confirming an alteration in K^+ outward current. Zhang et al. (2021) reported complementary evidence in a gene-trap model with 68% $Na_v1.2$ deficiency, which reported an excessive firing with broader spikes and depolarized resting potentials. Remarkably, normal excitability in these models could be restored with a broad K^+ channel opener. Potassium current remodeling in the presence of $Na_v1.2$ dysfunctions extends to GoF conditions: in Kearney et al. (2006) transgenic *Scn2a(Q54)* model, *KCNQ2* deletion has dramatically worsened seizures. Conversely, in a $K_v1.1$-null epilepsy model, *SCN2A* haploinsufficiency prolonged survival and

reduced seizure duration (Mishra et al., 2017), demonstrating the reciprocal leverage that exists between Na^+ and K^+ currents across disease. A recent work using early *SCN2A*-LoF induced pluripotent stem cell (iPSC) cortical neurons also adds a developmental angle suggesting that K^+ conductance remodeling may be a late maturing feature in these conditions rather than immediate (Asadollahi et al., 2023).

Together, the cited studies provide an overview of established alterations in K^+ currents within the context of *SCN2A* pathophysiology. In our young $Scn2a^{+/-}$ data, the widening of somatic spikes is most consistent with slowed repolarization, aligning with LoF work evidence implicating less K^+ channel recruitment. Whereas, the KI model reveals a distinct pattern with an elevated K^+ current leading to sharper AIS spikes, an age dependent phenotype that was not previously reported. Accordingly, a plausible test of these mechanisms was to evaluate the effects of local pharmacological manipulations at the AIS, targeting main potassium channel families K_v1, K_v7, and BK.

6.4.1 Distal AIS Kv1-Dominated Phenotype in L1314P Mutants

K_v1 block preferentially widened the distal AIS spikes, and DTX's effect was maximal in $Scn2a^{+/L1314P}$ cells (+66%). This suggests that the KI sharpened waveform might reflect an enhanced low-threshold Kv1 current at the site of AP initiation. As demonstrated by Kole et al. (2007), $K_v1.1/1.2$ enrichment over the first ~50 μm of the unmyelinated axon supports early repolarization and spike narrowing, and blocking these channels causes a distance-dependent increase in AP half-width. In contrast, the XE-991 (K_v7 inhibition) widened distal APs in controls but not in KI. This comparatively weaker effect does not exclude Kv7's broader roles in regulating thresholds and excitability, but rather implicates that the KI phenotype is not predominantly K_v7-driven. This result fits with reported functions of $K_v7.2/7.3$: though predominantly expressed toward distal regions of the AIS, they primarily stabilize the resting membrane potential, increase the Na_v availability, and control the AP thresholds, with minimal direct recruitment for early repolarization of single APs (Battefeld et al., 2014; Shah et al., 2008). On the other hand, BK block increased distal width in KI (+28%) but considerably less than DTX-α; and in WT cells, distal effects were smaller than

with other compounds. This observation further reinforces our earlier conclusion from Ca^{2+} and V_m imaging that, although BK activation through $Na_v1.2$-mediated Ca^{2+} accelerates early repolarization distally, it does not provide the primary determinant of generating AP widths in this juvenile window. Altogether, these points support a dominant K_v1 mechanism underlying the *Scn2a*$^{+/L1314P}$ sharp waveform at the AIS, with BK channels providing a contributory role.

6.4.2 Somatic-Proximal Potassium Current Deficits in Haploinsufficient Neurons

The same pharmacology assays in *Scn2a*$^{+/-}$ cells did not produce larger or selective widening at distal AIS sites compared to WT, which was expected from V_m findings showing no significant AIS waveform deviations in the KO model, thus implying that early K^+ current insufficiency is not centered at the initiation distal site. Since the main waveform disruption in KO manifests as widened somatic APs, the pharmacology analysis in this case should focus on proximal to somatic effects. K_v7 and BK manipulations did not distinguish KO cells from WT, however, α-DTX widened WT APs proximally but showed attenuated impact in KO, consistent with the scenario of reduced K_v1 conductance at baseline. In other words, these findings indicate that KO K^+ current perturbations, in contrast to KI, do not arise from distal AIS, which explains why AIS K^+ channel pharmacology could not explain the KO's somatic phenotype.

In conclusion, the early somatic widening most likely reflects K^+ conductance deficit outside the initiation zone, with reduced proximal Kv1 influence relative to WT. This pattern aligns with Zhang et al. (2021) work, where severe $Na_v1.2$ loss hyperexcitability was attributed to somatic downregulation of multiple K^+ channels, including $K_v1.1/1.2$, and where applying α-DTX blocked ~30% of total K^+ current in WT versus only ~10% in $Na_v1.2$-deficient neurons. Overall, the pharmacology refined our descriptive framework, and suggested a candidate altered potassium conductance and highlighted possible sites of dysregulation. Most importantly, all what precedes confirmed further different K^+ current remodeling mechanisms in two LoF models: KO shows K^+ conductance deficit in the young group, with a possible K_v1 insufficiency, and a reduced $Na_v1.2$ activity later; AIS targeted K^+ pharmacology

had limited explanatory power for KO somatic AP alterations, whereas the same tests in KI suggests an excessive early K_v1 conductance at the distal AIS.

6.4.3 How Local Is A "Local" Potassium Block When Interpreted with AP Waveform?

Of note, it is crucial to emphasize in our pharmacological interpretations dominant rather than exclusive roles for a certain K^+ conductance. K^+ channel pharmacology constraints are numerous, and interpreting AP shape changes after blocking one conductance is fundamentally different from testing Na^+ or Ca^{2+} channel drugs on ion influx. Blocking Na^+ or Ca^{2+} channels locally reduce the local inward current, which we could characterize with our optical recordings at the same site. Whereas blocking K^+ current at one site, for instance at the distal AIS, alters the waveform which then propagates bidirectionally, thus any AIS perturbation can impact the AP throughout the entire neuron. Consequently, K^+ blocker effects are non-local, and AP shape readouts are not strictly specific to one compartment or another.

Beyond this conceptual constraint, several methodological limitations justify considering this analysis as investigatory. First is the question of K_v modulators selectivity, potentially targeting the desired families at our chosen doses, though indirect effects must be considered. In addition, effective concentrations and spread magnitude in local application are not standardized, and largely depend on pipette position, amount of pressure, and tissue geometry, which all make strict quantitative comparisons across sites or drugs not guaranteed. Accordingly, our K^+ channel targeted AIS pharmacology should be read as identifying which conductance exerts a dominant influence under our conditions, without definitely excluding contributions from other isoforms. Deeper mechanistic interpretations can be made through a L5PN computational model that captures AIS initiation dynamics, ideally fit and validated to our geometry, channel densities and kinetics from electrophysiology and imaging data.

6.5 AIS Plasticity and Mechanistic Complexity in *SCN2A* LoF Phenotypes

In the following section, we consider the second explanatory route anticipated earlier: AIS plasticity. Tracking the juvenile period (P21-37), we were able to map age and compartment specific AIS phenotypes. In *Scn2a*$^{+/-}$, we observed wider somatic spikes in the young group (P21-24) whereas the AP waveform at the site of initiation remained near WT, pointing to a slow repolarization at the soma-proximal AIS domains rather than an increased sodium influx. By late juvenile (P30-37), we reported a reduction in proximal Na^+ influx and distal $Na_v1.2$-mediated Ca^{2+} component, with a disruption of both signals refinement. Despite these impairments, we confirmed that distal Na^+ influx remained preserved and that the waveform at distal AIS was also maintained. At the soma level, AP half-widths recovered, however somatic AP amplitudes declined, consistent with attenuated proximal Na^+ support for backpropagation. We tested the K^+ current remodeling reported in the young group with local pharmacology, which showed no selective distal impairments, and suggested a pattern that was compatible with a weaker somatic-proximal K_v1 recruitment.

In *Scn2a*$^{+/L1314P}$, we report a transient and distinct phenotype. In early juvenile mice, we observed reduced somatic AP amplitude together with sharpened distal AIS spikes, despite almost normal AIS Na^+ currents, indicating an excessive early repolarization at the initiation zone. Across P21-37, we found a preserved AIS Na^+ influx, while similarly to KO, $Na_v1.2$-mediated Ca^{2+} signals showed a disrupted refinement. In the old group (P30-37), alterations in AP shape at both the soma and distal AIS largely converged toward WT profiles, consistent with maturation possibly restoring the Na^+/K^+ balance. To identify which K^+ pathway was altered earlier, we also applied targeted K^+ pharmacology which suggested a distally dominant K_v1 conductance with smaller BK and Kv7 contributions.

Overall, KO and KI diverge in their AIS alterations: haploinsufficiency selectively alters proximal integrative functions without destabilizing distal initiation, characterized with a proximal K^+ conductance insufficiency in early juveniles that evolves into a clearly reduced

$Na_V1.2$ activity at later stages. The L1314P missense, in contrast, produces a transient phenotype centered at the AP generation site characterized by an increased K_V1 activity in early juveniles that normalizes with development.

6.5.1 From Channel Dysfunction to Structural-Functional Remodeling at The AIS

While our analysis allowed us to reveal some levels of perturbations, explaining these phenotypes is far from straightforward. Neurodevelopmental disorder phenotypes are often the convergence of a pathophysiology that unfolds across multiple scales, from ion channel dysfunction at the subcellular level, to altered intrinsic excitability, and changes in circuit activity and behavior; and the picture is rarely linear. Particularly, neurons and networks also engage powerful homeostatic plasticity that stabilizes firing, and that reshapes excitability by masking primary defects or sometimes inverting the apparent sites or directions of dysfunction, rendering simple interpretations of physiological outcomes inherently limited. Added to this, distinct conductance profiles can produce similar spike phenotypes, while the same mutation can manifest differently across developmental stages, cell types, and brain regions due to the onset of different compensatory adjustments among ionic currents, breaking down simple narratives of one cause-one effect (Turrigiano, 2011). Moreover, the developmental context is also critical in shaping outcomes: the direction and magnitude of perturbations, as well as associated compensatory homeostasis depend largely on when and where such phenotype is expressed (Nelson & Valakh, 2015). Critically, this plasticity is not restricted to synapses, structural remodeling is also established at the level of neuronal compartments. In such a dynamic system, clinical outcomes and phenotypes that we observe may not reflect a single pathogenic mechanism, but a layered phenotype shaped by both disruptions and adaptations. What if this complexity actually resides, or even originates, in one of the most finely tuned and highly regulated domains of the neuron?

The axon initial segment (AIS) is not defined merely by its ion channel composition, it is considered among the most molecularly specialized neuronal compartments. In short, without revisiting the detailed AIS architecture described earlier in the Introduction of this thesis, the AIS has a distinguished intricate cytoskeletal architecture and scaffolded nano-

domains ensuring specific trafficking, targeting, clustering, stoichiometry, retention of membrane proteins, and ultimately its role as the site of AP initiation. This assembly is primarily maintained by actin rings and βIV-spectrin that form a membrane-associated periodic skeleton organizing and stabilizing membrane proteins. Ankyrin-G (AnkG) bridges this lattice to VGCs and cell-adhesion molecules (CAMs), and its loss disperses AIS identity and axonal-somatodendritic polarity (Hedstrom et al., 2008). Na_v channels targeting, in particular, is highly mediated by AnkG and depends on a conserved binding motif whose phosphorylation by CK2 strengthens the immobilization of channels (BréChet et al., 2008). Stoichiometry adds another dimension of regulation as Na_v channels auxiliary subunits and AIS CAM can modulate trafficking, gating or AIS stability without altering α-subunit levels (Hull & Isom, 2017). Further, AIS identity and neuronal polarity are maintained by active endocytic clearance pathways that selectively eliminate mislocalized AIS membrane components (Van Beuningen et al., 2015). This scaffold underlies as well compartmentalized enrichment of $Na_v1.2$ proximally and $Na_v1.6$ distally, together with a defined potassium channel expression, adapted to their roles in AP initiation, propagation, backpropagation, and waveform shaping. Importantly these molecular patterns are developmentally specified, with transitional expressions, $Na_v1.2$ to $Na_v1.6$ for instance, which emerge during postnatal development and maturation of excitability reference. Therefore, AIS pathophysiology in *SCN2A* disorders carries a concrete regulation, and must be interpreted as the result of coordinated disruptions at different levels instead of an altered Na^+ conductance alone.

What further distinguishes the AIS is its homeostatic plasticity, this highly maintained structure is in fact not static: modifications in its length, position or molecular composition can be triggered by physiological changes or pathological alterations, allowing neurons to recalibrate their intrinsic excitability (Grubb & Burrone, 2010; Jamann et al., 2018; Yamada and Kuba, 2016; Yoshimura and Rasband, 2014). Emerging evidence indicates that AIS structural remodeling and adaptive mechanisms are relevant in various neurological disorders. In epilepsy models for example, chronic seizures induce functionally significant AIS relocation and length changes in pyramidal and granule neurons, with major shifts in excitability (Harty et al., 2013). In Alzheimer's disease (AD) tissue and models, AIS scaffold disruptions have been also reported. Postmortem AD cortex showed abnormal AIS length.

In addition, transgenic mice showed an AnkG depletion and significantly shortened AIS, with a corresponding impaired synaptic plasticity as neurons fail to exhibit the normal LTP-associated AIS elongation seen in WT cells (Li et al., 2024). Similar alterations have been also reported in Human iPSC models of Amyotrophic lateral sclerosis (ALS), where AIS length dynamically changes from elongation and hyerexcitability at early disease stages to shortening and hypoexcitability later, this remodeling was also paralleled with changes in AnkG and Na_v channels (Harley et al., 2023).

The functional outcome, whether an increase or a decrease in excitability, depends on the route of remodeling: shortening or distal relocation of the AIS, as shown in dentate granule cells, hippocampal cultures, and sensory cortex in vivo, increase spike threshold and limit repetitive firing, thereby more commonly linked to hypoexcitability (Evans et al., 2015; Grubb & Burrone, 2010; Jamann et al., 2021). While theory and computational models show that distal shifts can sometimes increase excitability depending on axial coupling and local hyperpolarizing currents (Goethals & Brette, 2020). In contrast, AIS elongation, observed after sensory deprivation or afferent loss, tends to increase excitability (Kuba et al., 2010). Another report by Kuba et. al (2015) showed that this hyperexcitability is often associated to redistribution of ion channels, such as decreased K_v1 and increased K_v7, to reduce early repolarization and facilitate spike initiation (Kuba et al., 2015). Overall, these examples illustrate how neurons engage AIS structural plasticity, either by changing length or location of this domain, as a common mechanism to offset alterations in excitability across different pathological conditions (Hsu et al., 2014).

6.5.2 Plasticity, Channel Remodeling, And Alternative Mechanisms in *SCN2A* LoF Models

In light of this complexity, our early juvenile KI phenotype: sharp distal AIS spikes with reduced somatic amplitudes, may reflect a structural remodeling of the AIS rather than compensatory K_v1 upregulation. Mechanistically, a shorter AIS squeezes the initiation site, increasing the effective leverage of existing distal K_v1 pool without any increase of their expression levels, which might result in an apparent upregulation of these channels as DTX pharmacology suggests. In parallel, a distal shift for the AIS moves the spike onset to a region

that is relatively enriched with $Na_v1.6$ and K_v1 channels at the same time, leading to faster and sharper distal spikes, in line with *Scn2a*$^{+/L1314P}$ distal AIS signature reported with our V_m imaging. Such relocation, as reported, can weaken soma-AIS coupling because of the increased electronic distance between the soma and the initiation zone, which perhaps leads to a drop in somatic AP amplitudes even if local AIS Na^+ influx remains indistinguishable from WT levels (Goethals & Brette, 2020; Gulledge & Bravo, 2016). These geometry effects have been associated in earlier studies to decreased excitability, and adhere to biologically plausible mechanisms: activity dependent changes in AIS location have been correlated with an increase in current thresholds (Evans et al., 2013), AIS shortening in parallel can occur within hours and drive a clear functional impact on repetitive firing. Moreover, clathrin-mediated endocytosis of sodium channels, especially at the distal AIS, provides a mechanistic bridge between activity and geometry changes without a concomitant increase in local Na^+ current density (Fréal et al.,2023). Finally, this structural plasticity is reversible on the developmental timescale: AIS position and length recalibrate with changing activity, and channel clustering balance readjusts, which offer an explanation for the late-juvenile convergence of KI AIS phenotypes towards WT profiles (Grubb & Burrone, 2010).

To test the AIS plasticity in this case, compartmental AIS NEURON model that systematically varies the start and the length of AIS, with fixed ion channel density, would be insightful to predict the distal spike sharpening and reduced somatic amplitude against an alternative K_v1 upregulation, in order to distinguish underlying mechanisms for these features. Experimentally, AIS geometry and ion channel expression could be assessed with immunolabeling to map the AIS position and length compared to WT. These methods were described by Fréal et al. (2023) and provide a template for submicron AIS geometry and channel clustering measurements, which could potentially inform our model.

Beyond geometry-based mechanisms, other molecular explanations have been proposed for the KI model. Our collaborators Massimo Mantegazza and Sandrine Cestèle report that ASD-linked *SCN2A* variants, including L1314P, induce negative dominance in vitro, which leads to a bigger decrease in functional $Na_v1.2$ channels than what is caused by pure LoF mutations. Their molecular analysis also revealed that *Scn2a*$^{+/L1314P}$ mice have reduced membrane expression of $Na_v1.2$ channels but normal mRNA levels, suggesting that the molecular

mechanism may involve protein folding or trafficking impairments (personal communications, unpublished). In principle, such negative dominance would titrate shared trafficking and targeting capacity at the AIS, thereby limiting WT-$Na_v1.2$ recruitments. The outcome of such overall loss in WT channels would in theory cause a reduction of proximal AIS Na^+ current. However, our recordings did not show any Na^+ influx decrease in the juvenile KI somatosensory cortex. Thus, while negative dominance remains mechanistically plausible, it is not directly supported by our Na^+ imaging data. Of note, their assays targeted younger mice and prefrontal cortex, whereas our dataset covers older juveniles and somatosensory cortex. The developmental and regional mismatch could perhaps explain this non-alignment, highlighting again that *SCN2A* pathophysiology and AIS channel expression are highly sensitive to when and where experiments are performed (Turrigiano, 2012).

In contrast, our data could not provide solid evidence that a similar plasticity or geometry remodeling underlie the KO phenotype. The maintained AIS waveform and distal Na^+ influx, together with no pharmacological evidence of dominant distal K^+ conductance, argue instead for a proximal deficit, developmentally altering ion channels outside the site of AP initiation. In early juveniles: a deficit in somatic and proximal AIS K^+ conductance produces wider somatic spikes, while in later juveniles the phenotype shifts to a proximal Na^+ partial loss, mirroring a reduced expression of $Na_v1.2$ channels and leading to attenuated backpropagation support and reduced somatic AP amplitudes. This interpretation is in line with previous *SCN2A* haploinsufficiency studies, where combined deficits in Na^+ current and K^+ conductance remodeling were documented and generally linked to paradoxical hyperexcitability (Spratt et al., 2021; Zhang et al., 2021). While we cannot exclude subtle AIS reconfiguration, our findings do not strongly suggest such a mechanism in haploinsufficiency conditions, or not in an apparent way at least.

6.6 Somatodendritic Excitability in *SCN2A* LoF

In the previous part of the Discussion we have seen how *SCN2A* mutations reshape AIS excitability through different ionic mechanisms. However, although the AIS represents a hub for $Na_v1.2$ enrichment, and is the site of AP generation, this only tells one part of the story. In the following section, we see how these perturbations may extend into other neuronal

compartments, specifically along the somatodendritic axis. Dendrites have emerged as a likely locus of pathology in *SCN2A* conditions, with deficits in dendritic signaling, integration, and LTP reported both in cortical slices and in vivo imaging (Spratt et al., 2019; Wu et al.,2025). Such clinical outcomes are not surprising, considering that $Na_v1.2$ is the predominant sodium channel isoform expressed in dendrites where it supports AP backpropagation and serves as critical link between initiation, calcium electrogenesis, and synaptic plasticity (Hu et al., 2009; Spratt et al., 2019; Wu et al.,2025). To address this issue, we examined first AP amplitude accommodation in the soma during a burst of three APs at 6 ms inter-pulse intervals, as measurement of cumulative Na_v channel inactivation and intrinsic firing capability (Colbert et al., 1997; Bean, 2007). In parallel, we addressed the question of whether *SCN2A* LoF alters dendritic Ca^{2+} electrogenesis, a regenerative event that arises when high-frequency backpropagating APs occur and that may provide instructive signals for dendritic integration and synaptic plasticity, by recruiting VGCCs and NMDA receptors in the distal apical trunk, producing all-or-none Ca^{2+} spikes, and serving as an integrative readout for dendritic excitability (Larkum et al., 1999a; Waters et al., 2003; Suzuki & Larkum, 2017). Physiologically, these mechanisms are far more complex than single APs since they unfold over tens of milliseconds and engage further processes, including different conductance. Moreover, since Ca^{2+} supralinear spikes occur only above a critical frequency of bAPs that Larkum et al. (1999a) described as "threshold", even minor shifts in backpropagation efficacy or dendritic membrane state in the presence of $Na_v1.2$ dysfunctions can determine whether a burst crosses this non-linear threshold or not (Larkum et al; 1999a). In turn, this may critically change dendritic integration in this cell type. To this end, our comparisons were based on simple parameters such as R_1, R_2, R_3 for somatic amplitude decay in bursts; prevalence, *IPI* threshold, and S_3/S_2 for dendritic Ca^{2+} spikes, since we cannot quantitatively describe the complexity implicated. This investigation therefore holds a qualitative and preliminary aspect, reflecting both the increased dimensionality of somatodendritic excitability and the novelty of this approach. Indeed, unlike AIS analysis, which relied on established protocols and nearly a decade of work in our laboratory, these experiments opened a new line of measurements in *SCN2A*-related disorders, but remain nonetheless limited to establish firm mechanistic conclusions.

In WT neurons, somatic excitability during short bursts was largely stable across age, in line with conserved single AP amplitudes observed earlier. We detected Ca^{2+} electrogenesis in about half of the cells, with a slight age-dependent decline (young ~44% to old ~36%) and an overall prevalence lower than for both transgenic mice models. Earlier work established a sharp increase in dendritic non-linear events during the first postnatal month, which corresponds to our young (P21-24) to mid (P25-30) juvenile groups, which our dataset could not fully capture (P25-30; N=3). Thereby, we suggest that the apparent lack of this refinement between young and old WTs may reflect sampling limitations rather than a true absence of developmental modulation (Atkinson & Williams, 2009; Grewe, 2010).

In *Scn2a*$^{+/-}$ neurons, despite single APs being wider at the soma, suggesting an insufficient proximal K^+ channel recruitment, burst fidelity (R1-R3) and dendritic Ca^{2+} prevalence were indistinguishable from WT. By late juvenile ages, however, the phenotype became more complex and turned into an apparent paradox. AIS Na^+ influx was reduced proximally and single somatic AP amplitudes declined. Interestingly, during 3 AP bursts, KO neurons showed less decay than WT, and dendritic Ca^{2+} electrogenesis prevalence reached the highest levels among the three strains (~75%), with some cells exhibiting strong S3/S2 amplification. Theoretically, reduced proximal Na^+ should weaken backpropagation, in line with what Spratt et al. (2019) reported by examining mature *Scn2a*$^{+/-}$ pyramidal cells in prefrontal cortex. Using trains of high-frequency bursts (2APs at > 100Hz), they imaged Ca^{2+} transients and found a rapid attenuation with increasing distance from the soma, culminating in an absence of transients in most distal dendritic tufts. They further linked this deficit to a reduced synaptic strength and impaired burst-dependent LTP. In contrast, our somatosensory cortex data showed that Ca^{2+} electrogenesis was not suppressed, and by late juvenile, it was paradoxically enhanced. These results do not undermine $Na_v1.2$ contributions to dendritic excitability or bAP associated plasticity, but instead underscore the non-uniformity in phenotypes across compartments, cortical regions, and developmental stages, where distinct compensatory mechanisms may take place.

Moving to the KI phenotype, the previous analysis showed a clear developmental transition. In young animals, the AIS revealed sharper distal APs and preserved Na^+ amplitude, consistent with enhanced distal K_v1 repolarization or AIS remodeling. At the soma, bursts

showed minimal decay, and dendritic Ca^{2+} electrogenesis prevalence was high (~71%) with large S_3/S_2 ratios, pointing to another apparently contradictory outcome relative to the hypoexcitability expected from AIS findings. In the old group, however, both soma and dendrite measurements converged toward WT levels: burst decay increased and dendritic Ca^{2+} prevalence dropped to ~50%. These traits suggest an early transient state of enhanced dendritic responsiveness. The developmental shifts mirror our age dependent phenotype from AIS observations, where the initially sharp distal signature progressively turned into more balanced AP waveforms by P30-37.

With these soma-dendrite observations, nothing but another layer of complexity is added to the landscape. In both KO and KI mice models, *SCN2A* LoF did not abolish somatic stability of AP in bursts and bAP-evoked Ca^{2+} electrogenesis. These processes were instead reshaped with divergent age-dependent trajectories, highlighting the distinct remodeling of excitability in *SCN2A*-related disorders. It is worth, once more, stressing out the fact that dendritic Ca^{2+} electrogenesis itself is a heterogeneous mechanism that depends on multiple levels of regulation: it can be driven by VGCCs and exhibits a strict critical-frequency dependence for bAP trains, with sensitivity to VGCC block and local inhibition (Larkum et al., 1999b); it can be also amplified by NMDA receptor recruitment during coincident bAPs and synaptic activity (Suzuki & Larkum, 2017); and it is strongly gated by inhibition, including GABA-B receptor mediated suppression of distal Ca^{2+} spikes in L5PNs (Larkum et al., 2007; Pérez-Garci et al., 2012). Under such a complex framework, our descriptive analysis can be informative but not sufficient for any conclusion. And the key message would be essentially that *SCN2A* LoF phenotypes cannot be narrowed to simple compartmental deficits.

6.7 AaH-II Characterization and $Na_v1.2$ Modulation for *SCN2A* LoF Rescue

As part of the broader objective of this project to explore potential pharmacological strategies for $Na_v1.2$ dysfunction, a portion of this thesis was dedicated to examining the effects of the scorpion toxin AaH-II (in WT cells only). Previous studies have analyzed the effects of AaH-II using patch-clamp recordings from sites that do not necessarily correspond

to regions of highest VGNC density. The rationale of our work was instead to probe the effect of the toxin at subcellular domains with enriched Na^+ channel expression, under conditions where somatic effects were just detectable. We first reported that local application of AaH-II produced a significant increase in the width of the somatic AP at a low 7 nM concentration, ~ 10 times less with respect to the VGNC inhibitor G1G4-huwentoxin-IV used in a previous study (Filipis et al., 2023). When we analyzed the corresponding AP in the AIS, using a V_m indicator, the widening was significantly larger. Consistent with this result, local delivery of AaH-II in the same region showed a significant increase in Na^+ influx associated with firing activity (Baranauskas et al., 2013; Fleidervish et al., 2010). Not surprisingly, since the primary effect of AaH-II was to slow down VGNC inactivation, the larger influx could be attributed to the slow (or persistent) component of the Na^+ current, which is normally larger for $Na_v1.6$ in control condition (Astman et al., 2006; Katz et al., 2018). When analyzing Ca^{2+} influx associated with the AP, we found a significant increase after local delivery of AaH-II, that was however substantially smaller with respect to the increase in Na^+ influx, and further analysis confirmed that this change was restricted to the distal part of the AIS, in line with previous demonstration that the $Na_v1.2$-mediated Ca^{2+} current is dominant in the distal AIS regions where VGCC-mediated Ca^{2+} current is relatively weaker (Filipis et al., 2023). Notably, Ca^{2+} transients in the presence of AaH-II were wider and displayed delayed kinetics, suggesting that prolonged inactivation introduces abnormal ionic dynamics at the AIS that could perturb axonal homeostasis.

From a methodological perspective, by combining targeted pharmacological delivery with subcellular optical recordings from the AIS, AaH-II revealed a spatially structured sensitivity. These results highlight the importance of high-resolution pharmacological approaches for characterizing VGNC modulators at their specific sites of enrichment (AIS, nodes of Ranvier), since whole-cell approaches may underestimate critical physiological alterations.

From a therapeutic standpoint, AaH-II does not meet the criteria for a potential rescue in *SCN2A* LoF conditions. First, heterologous expression experiments confirmed that the toxin lacks isoform selectivity, shifting the kinetics of both $Na_v1.2$ and $Na_v1.6$. Second, its primary action was slowing down the inactivation of Na_v isoforms and increasing the Ca^{2+} influx, an effect that could be deleterious if chronically increased. Moreover, in both KO and KI genotypes, our analysis showed that *SCN2A* LoF induces complex remodeling of AIS, soma,

and dendrite compartments, specific to each mutation and age window. Therefore, pharmacological tuning of $Na_v1.2$ activity alone is unlikely to restore the network function.

Overall, the development of $Na_v1.2$-targeted therapies remains highly challenging. On one hand, the high structural homology across Na_v isoforms makes true $Na_v1.2$ selectivity difficult, and raises the risk of undesired effects (Wisedchaisri & El-Din, 2022). In addition, as we have discussed through our analyses, *SCN2A* variants display a great heterogeneity, with transient and sometimes paradoxical alterations, which complicate the linearity of pharmacological interventions. Besides, these mutations are often accompanied with homeostatic regulation that could counteract perturbations in excitability (O'Leary et al., 2014; Turrigiano, 2012). Altogether, these are some of the considerations that make the rescue of *SCN2A* LoF far from being achievable by simple channel enhancers. Effective strategies instead, require highly selective compounds that reestablish physiological gating properties of $Na_v1.2$, with complementary approaches that also target compensatory conductance and mechanisms during critical developmental windows, to align with the subcellular physiology of *SCN2A*-related channelopathies and guide the design of potential therapeutic agents.

6.8 Challenges of Modeling Disease with Haploinsufficient Animals

A critical observation is that *in* $Scn2a^{+/-}$ neurons, despite carrying a theoretical 50% reduction in *SCN2A*, the proximal sodium influx deficit was not proportionally larger than that observed under partial pharmacological block. In our data, the mean proximal-to-distal sodium influx ratio ($R_{p/d}$) decreased from 0.92 ± 0.40 in WT neurons to 0.64 ± 0.17 in $Scn2a^{+/-}$ neurons (P21-P40), indicating an approximate 30% relative reduction in proximal sodium influx. This effect was remarkably similar to that reported following local pharmacological block of $Na_v1.2$, using the huwentoxin-IV, which also reduced proximal Na^+ transients by ~30% (Filipis et al., 2023). Overall, this suggests that the KO AIS exhibited regulatory mechanisms, and that ion channel expression and function are subject to homeostatic control (Turrigiano, 2012; O'Leary et al., 2013). In short, these data challenge the assumption of a linear genotype-phenotype coupling in monogenic channelopathies, and

instead points to a model where the regulatory feedback is relevant during juvenile cortical development. Such nonlinearity is widely observed in heterozygous models, consistent with the Gene Balance Hypothesis, where single-allele loss systems reveal degenerate regulatory networks and produce mild phenotypes instead of direct gene-dose effect (Birchler & Veitia, 2012; O'Leary et al., 2013; O'Leary et al., 2014).

Heterozygous KO models nonetheless remain useful, since they recapitulate the genetic state of many human patients. Numerous dominant neurological disorders from Dravet syndrome (*SCN1A*) to *KCNQ2*-related epilepsies are caused by LoF in a single allele, making heterozygous models essential for studying disease mechanisms in a patient-relevant context (Anderson et al., 2017). These models often manifest core features of the human condition (e.g. seizures, cognitive deficits), providing solid platforms to test interventions. Their limitation, however, is that phenotypic outcomes are not easily predictable or linearly scaled to gene dose. Homeostatic regulatory feedback can obscure the direct effects of the gene loss, meaning phenotypes may be milder or differ substantially from what a simple "50% loss" expectation would suggest. For instance, the severity of epilepsy in haploinsufficient channel models can vary dramatically with genetic background or age as other modifiers kick in (see the website aesnet.org). Since this complexity makes interpretation challenging, one should ideally discern which changes are primary consequences of the gene reduction and which arise from the organism's regulatory response. In short, heterozygous models add interpretative complexity even if they are preclinically relevant.

Thus, rather than considering heterozygous KO models as static reflections of gene levels, it is more accurate to treat them as dynamic systems shaped by adaptive and regulatory adjustments. Importantly, the partial "phenotypic rescue" seen in haploinsufficient models to counteract the imposed deficit, offers itself a powerful dynamic perspective: it means these models not only inform us about the gene's role, but also uncover some of homeostatic and network-level adaptations engaged to preserve function. Notably, those adaptations can become targets for therapy. For example, in epileptic mice with *SCN1A* or *KCNQ2* haploinsufficiency, researchers found that tweaking a compensating channel, reducing Nav1.6 (*SCN8A*) activity, could ameliorate seizures and prolong survival (see aesnet.org).

Such findings illustrate that the "buffering" partners in these networks, whether manifested by other ion channel remodeling, signaling pathways, or transcriptional regulators, might be leveraged therapeutically. In summary, haploinsufficient models could reveal complex multi-layered phenotypes and homeostatic processes, shaped by both deficits and adaptations, which, if understood, could offer new avenues for targeted therapies to stabilize network function in disease (Shabani et al., 2024).

6.9 Toward A Better Understanding of *SCN2A*-Related Disorders Beyond Gain and Loss-Of-Function

In the end, between the joy of discovery and the despair of uncertainty, Science remains both exhilarating and humbling, and every discovery deepens our sense of how much lies beyond our grasp. Yet, our only solace remains in dogged curiosity and determination that are incessantly reborn with every new encounter with the unknown. Biological systems, in fact, seldom behave according to simple rules and the brain is no exception. We explored in this thesis how excitability was altered in juvenile L5PNs by *SCN2A* dysfunction using two LoF models. We detected an early deficiency of potassium channel recruitment in the proximal AIS compartment in haploinsufficient cells, which evolved into reduced $Na_v1.2$ activity at later stages. Paradoxically, at this age, we found that somatodendritic regenerative activities were not suppressed, but rather increased. In contrast, we observed a transient phenotype at the AIS for the L1314P missense mutation, in which young neurons exhibited sharpened distal waveforms, preserved sodium current amplitude, and smaller somatic APs, likely due to upregulated K_v1 function or AIS remodeling. These hypoexcitable somato-axonal features were intriguingly associated with enhanced dendritic electrogenesis. As the animals matured, these alterations shifted toward the WT profile. Finally, by applying the scorpion toxin AaH-II at the AIS, we were able to provide partial, yet not selective, slowing down of $Na_v1.2$ inactivation, which spatially modulated associated currents of Na^+ and Ca^{2+}, emphasizing the relevance of localized subcellular pharmacological intervention.

In summary, neither model truly behaved as a loss-of-function, and both exhibited distinct mixed phenotypes based on compensatory remodeling and developmental context. Our results, along with recent literature, converge on a consistent message: *SCN2A*-related disease does not abide by the traditional gain vs loss-of-function dichotomy. Pathogenic variants implicate developmental and homeostatic mechanisms in ways that obfuscate categorical boundaries.

Beyond channel physiology, this work highlights both the promise and the limitations of animal models for dissecting *SCN2A*-associated diseases in autistic conditions. The two transgenic lines studied here have been behaviorally characterized as exhibiting autism-like phenotypes. Within this framework, our findings provide a cellular perspective on how intrinsic excitability remodeling during juvenile cortical maturation could influence activity-dependent circuit refinement, a process strongly implicated in autism spectrum disorders. *SCN2A* dysfunction did not just cause uniform hypoexcitability; instead, it led to temporally evolving and compartment-specific shifts in excitability, which could affect how cortical neurons integrate and propagate information.

More generally, the potential translation of ion channel physiology from rodents to humans is constrained by the human-specific nature of these disorders. Features such as language impairment, cognitive delays, and complex social reciprocity develop within prolonged human developmental courses that no mouse assay can replicate. Models can mimic genetic and molecular signatures, but they cannot recapitulate the human experience that starts already in the embryonic stage.

For these reasons, naive interventions to address GoF/LoF would be misguided. Both experimental and clinical findings demonstrate that strict labels are oversimplified and may mislead genotype-phenotype correlations and treatment. A more nuanced framework will need to incorporate biophysical and network-level analyses, age-dependent factors, and homeostatic plasticity to better understand *SCN2A* disorders and guide therapeutic applications.

Bibliography

Abbas, F., Blömer, L.A., Millet, H. *et al.* Analysis of the effect of the scorpion toxin AaH-II on action potential generation in the axon initial segment. *Scientific Reports, 14,* 4967 (2024). https://doi.org/10.1038/s41598-024-55315-y

Abbas, F., İpek, Ö. Y., Moreau, P., & Canepari, M. (2025). Neuronal Imaging at 8-Bit Depth to Combine High Spatial and High Temporal Resolution with Acquisition Rates Up to 40 kHz. *Journal of Biophotonics, 18*(3), e202400513. https://doi.org/10.1002/jbio.202400513

Abbas, N., Gaudioso-Tyzra, C., Bonnet, C., Gabriac, M., Amsalem, M., Lonigro, A., Padilla, F., Crest, M., Martin-Eauclaire, M., & Delmas, P. (2013). The scorpion toxin Amm VIII induces pain hypersensitivity through gain-of-function of TTX-sensitive Na+ channels. Pain, 154(8), 1204–1215. https://doi.org/10.1016/j.pain.2013.03.037

Abbott, M., Bender, K. J., Brunklaus, A., Demarest, S., Egan, S., Haviland, I., Kearney, J. A., Myers, L. S., Olson, H. E., Sanders, S. J., SanInocencio, C., Symonds, J., & Thompson, C. H. (2024). SCN2A-Related Disorders. In Cambridge University Press eBooks. https://doi.org/10.1017/9781009530361

Abdelsayed, M., Sokolov, S., & Ruben, P. C. (2013). A thermosensitive mutation alters the effects of lacosamide on slow inactivation in neuronal voltage-gated sodium channels, NaV1.2. Frontiers in Pharmacology, 4. https://doi.org/10.3389/fphar.2013.00121

Adelman, J. P. (2016). SK channels and calmodulin. Channels, 10(1), 1–6. https://doi.org/10.1080/19336950.2015.1029688

AES | Home. (n.d.). Default. https://aesnet.org/

Ahern, C. A., Payandeh, J., Bosmans, F., & Chanda, B. (2015). The hitchhiker's guide to the voltage-gated sodium channel galaxy. The Journal of General Physiology, 147(1), 1–24. https://doi.org/10.1085/jgp.201511492

Ahn, M., Beacham, D., Westenbroek, R. E., Scheuer, T., & Catterall, W. A. (2007). Regulation of NAV1.2 channels by Brain-Derived Neurotrophic Factor, TRKB, and Associated FYN Kinase. Journal of Neuroscience, 27(43), 11533–11542. https://doi.org/10.1523/jneurosci.5005-06.2007

Akaike, N., & Takahashi, K. (1992). Tetrodotoxin-sensitive calcium-conducting channels in the rat hippocampal CA1 region. The Journal of Physiology, 450(1), 529–546. https://doi.org/10.1113/jphysiol.1992.sp019141

Alami, M., Vacher, H., Bosmans, F., Devaux, C., Rosso, J., Bougis, P. E., Tytgat, J., Darbon, H., & Martin-Eauclaire, M. (2003). Characterization of Amm VIII from Androctonus mauretanicus mauretanicus: a new scorpion toxin that discriminates between neuronal and skeletal sodium channels. Biochemical Journal, 375(3), 551–560. https://doi.org/10.1042/bj20030688

Alexander, S., Mathie, A., & Peters, J. (2011). ION CHANNELS. British Journal of Pharmacology, 164(s1). https://doi.org/10.1111/j.1476-5381.2011.01649_5.x

Alvarez, O., & Latorre, R. (2017). The enduring legacy of the "constant-field equation" in membrane ion transport. The Journal of General Physiology, 149(10), 911–920. https://doi.org/10.1085/jgp.201711839

Aman, T. K., Grieco-Calub, T. M., Chen, C., Rusconi, R., Slat, E. A., Isom, L. L., & Raman, I. M. (2009). Regulation of Persistent Na Current by Interactions between β Subunits of

Voltage-Gated Na Channels. Journal of Neuroscience, 29(7), 2027–2042. https://doi.org/10.1523/jneurosci.4531-08.2009

Anderson, L. L., Hawkins, N. A., Thompson, C. H., Kearney, J. A., & George, A. L. (2017). Unexpected efficacy of a novel sodium channel modulator in Dravet syndrome. Scientific Reports, 7(1). https://doi.org/10.1038/s41598-017-01851-9

Angelides, K. J., Elmer, L. W., Loftus, D., & Elson, E. (1988). Distribution and lateral mobility of voltage-dependent sodium channels in neurons [published erratum appears in J Cell Biol 1989 May;108(5):preceding 2001]. The Journal of Cell Biology, 106(6), 1911–1925. https://doi.org/10.1083/jcb.106.6.1911

Antic, S. D., Zhou, W., Moore, A. R., Short, S. M., & Ikonomu, K. D. (2010). The decade of the dendritic NMDA spike. Journal of Neuroscience Research, 88(14), 2991–3001. https://doi.org/10.1002/jnr.22444

Asadollahi, R., Delvendahl, I., Muff, R., Tan, G., Rodríguez, D. G., Turan, S., Russo, M., Oneda, B., Joset, P., Boonsawat, P., Masood, R., Mocera, M., Ivanovski, I., Baumer, A., Bachmann-Gagescu, R., Schlapbach, R., Rehrauer, H., Steindl, K., Begemann, A., . . . Rauch, A. (2023). Pathogenic SCN2A variants cause early-stage dysfunction in patient-derived neurons. Human Molecular Genetics, 32(13), 2192–2204. https://doi.org/10.1093/hmg/ddad048

Astman, N., Gutnick, M. J., & Fleidervish, I. A. (2006). Persistent sodium current in layer 5 neocortical neurons is primarily generated in the proximal axon. Journal of Neuroscience, 26(13), 3465–3473. https://doi.org/10.1523/jneurosci.4907-05.2006

Atkinson, S. E., & Williams, S. R. (2009). Postnatal development of dendritic synaptic integration in rat neocortical pyramidal neurons. Journal of Neurophysiology, 102(2), 735–751. https://doi.org/10.1152/jn.00083.2009

Augustine, G. J., & Kasai, H. (2006). Bernard Katz, quantal transmitter release and the foundations of presynaptic physiology. The Journal of Physiology, 578(3), 623–625. https://doi.org/10.1113/jphysiol.2006.123224

Baek, J., Rubinstein, M., Scheuer, T., & Trimmer, J. S. (2014). Reciprocal changes in phosphorylation and methylation of mammalian brain sodium channels in response to seizures. Journal of Biological Chemistry, 289(22), 15363–15373. https://doi.org/10.1074/jbc.m114.562785

Bagnéris, C., Naylor, C. E., McCusker, E. C., & Wallace, B. (2014). Structural model of the open–closed–inactivated cycle of prokaryotic voltage-gated sodium channels. The Journal of General Physiology, 145(1), 5–16. https://doi.org/10.1085/jgp.201411242

Bahrey, H. L. P., & Moody, W. J. (2003). Early development of Voltage-Gated ion currents and firing properties in neurons of the mouse cerebral cortex. Journal of Neurophysiology, 89(4), 1761–1773. https://doi.org/10.1152/jn.00972.2002

Baker, A., Kalmbach, B., Morishima, M., Kim, J., Juavinett, A., Li, N., & Dembrow, N. (2018). Specialized subpopulations of Deep-Layer pyramidal neurons in the neocortex: bridging cellular properties to functional consequences. Journal of Neuroscience, 38(24), 5441–5455. https://doi.org/10.1523/jneurosci.0150-18.2018

Baker, P. F., Hodgkin, A. L., & Ridgway, E. B. (1971). Depolarization and calcium entry in squid giant axons. The Journal of Physiology, 218(3), 709–755. https://doi.org/10.1113/jphysiol.1971.sp009641

Baranauskas, G., David, Y., & Fleidervish, I. A. (2013). Spatial mismatch between the Na + flux and spike initiation in axon initial segment. Proceedings of the National Academy of Sciences, 110(10), 4051–4056. https://doi.org/10.1073/pnas.1215125110

Barker, B., Young, G., Soubrane, C., Stephens, G., Stevens, E., & Patel, M. (2016). Ion channels. In Elsevier eBooks (pp. 11–43). https://doi.org/10.1016/b978-0-12-802381-5.00002-6

Barnett, M. W., & Larkman, P. M. (2007, June 1). The action potential. Practical Neurology. https://pn.bmj.com/content/7/3/192.long

Battaglioli, E., Andrés, M. E., Rose, D. W., Chenoweth, J. G., Rosenfeld, M. G., Anderson, M. E., & Mandel, G. (2002). REST repression of neuronal genes requires components of the HSWI·SNF complex. Journal of Biological Chemistry, 277(43), 41038–41045. https://doi.org/10.1074/jbc.m205691200

Battefeld, A., Tran, B. T., Gavrilis, J., Cooper, E. C., & Kole, M. H. P. (2014). Heteromeric KV7.2/7.3 channels differentially regulate action potential initiation and conduction in neocortical myelinated axons. Journal of Neuroscience, 34(10), 3719–3732. https://doi.org/10.1523/jneurosci.4206-13.2014

Beacham, D., Ahn, M., Catterall, W. A., & Scheuer, T. (2007). Sites and molecular mechanisms of modulation of NAV1.2 channels by FyN tyrosine kinase. Journal of Neuroscience, 27(43), 11543–11551. https://doi.org/10.1523/jneurosci.1743-07.2007

Beckh, S., Noda, M., Lübbert, H., & Numa, S. (1989). Differential regulation of three sodium channel messenger RNAs in the rat central nervous system during development. EMBO Journal, 8(12), 3611–3616. https://doi.org/10.1002/j.1460-2075.1989.tb08534.x

Bean, B. (2009). Neuronal pacemaking. In Elsevier eBooks (pp. 717–726). https://doi.org/10.1016/b978-008045046-9.01653-3

Bean, B. P. (2007). The action potential in mammalian central neurons. Nature Reviews. Neuroscience, 8(6), 451–465. https://doi.org/10.1038/nrn2148

Bell, D. C., Leanza, L., Gentile, S., & Sauter, D. R. (2023). News and views on ion channels in cancer: is cancer a channelopathy? Frontiers in Pharmacology, 14. https://doi.org/10.3389/fphar.2023.1258933

Belyaev, N. D., Wood, I. C., Bruce, A. W., Street, M., Trinh, J., & Buckley, N. J. (2004). Distinct RE-1 Silencing Transcription Factor-containing Complexes Interact with Different Target Genes. Journal of Biological Chemistry, 279(1), 556–561. https://doi.org/10.1074/jbc.m310353200

Bender, K. J., Ford, C. P., & Trussell, L. O. (2010). Dopaminergic modulation of axon initial segment calcium channels regulates action potential initiation. Neuron, 68(3), 500–511. https://doi.org/10.1016/j.neuron.2010.09.026

Bender, K. J., & Trussell, L. O. (2009). ANK CA2+ Channels influence action potential generation and timing. Neuron, 61(2), 259–271. https://doi.org/10.1016/j.neuron.2008.12.004

Bender, K. J., & Trussell, L. O. (2012). The physiology of the Axon initial segment. Annual Review of Neuroscience, 35(1), 249–265. https://doi.org/10.1146/annurev-neuro-062111-150339

Beneski, D. A., & Catterall, W. A. (1980). Covalent labeling of protein components of the sodium channel with a photoactivable derivative of scorpion toxin. Proceedings of the

National Academy of Sciences, 77(1), 639–643. https://doi.org/10.1073/pnas.77.1.639

Bennett, V., & Lorenzo, D. N. (2013). Spectrin- and Ankyrin-Based membrane domains and the evolution of vertebrates. Current Topics in Membranes, 1–37. https://doi.org/10.1016/b978-0-12-417027-8.00001-5

Benoit, E., & Dubois, J. M. (1987). Properties of maintained sodium current induced by a toxin from Androctonus scorpion in frog node of Ranvier. The Journal of Physiology, 383(1), 93–114. https://doi.org/10.1113/jphysiol.1987.sp016398

Ben-Shalom, R., Keeshen, C. M., Berrios, K. N., An, J. Y., Sanders, S. J., & Bender, K. J. (2017). Opposing effects on NA V 1.2 function underlie differences between SCN2A variants observed in individuals with autism spectrum disorder or infantile seizures. Biological Psychiatry, 82(3), 224–232. https://doi.org/10.1016/j.biopsych.2017.01.009

Berecki, G., Howell, K. B., Heighway, J., Olivier, N., Rodda, J., Overmars, I., Vlaskamp, D. R. M., Ware, T. L., Ardern-Holmes, S., Lesca, G., Alber, M., Veggiotti, P., Scheffer, I. E., Berkovic, S. F., Wolff, M., & Petrou, S. (2022). Functional correlates of clinical phenotype and severity in recurrent SCN2A variants. Communications Biology, 5(1). https://doi.org/10.1038/s42003-022-03454-1

Bernèche, S., & Roux, B. (2005). A Gate in the Selectivity Filter of Potassium Channels. Structure, 13(4), 591–600. https://doi.org/10.1016/j.str.2004.12.019

Bernstein, J. (1902). Untersuchungen zur Thermodynamik der bioelektrischen Ströme. Pflügers Archiv - European Journal of Physiology, 92(10–12), 521–562. https://doi.org/10.1007/bf01790181

Bi, G., & Poo, M. (2001). Synaptic Modification by correlated Activity: HEBB's postulate revisited. Annual Review of Neuroscience, 24(1), 139–166. https://doi.org/10.1146/annurev.neuro.24.1.139

Billen, B., Bosmans, F., & Tytgat, J. (2008). Animal peptides targeting Voltage-Activated sodium channels. Current Pharmaceutical Design, 14(24), 2492–2502. https://doi.org/10.2174/138161208785777423

Birchler, J. A., & Veitia, R. A. (2012). Gene balance hypothesis: Connecting issues of dosage sensitivity across biological disciplines. *Proceedings of the National Academy of Sciences of the United States of America, 109*(37), 14746–14753. https://doi.org/10.1073/pnas.1207726109

Blömer, L. A., Canepari, M., & Filipis, L. (2021). Ultrafast sodium imaging of the axon initial segment of neurons in mouse brain slices. Current Protocols, 1(3). https://doi.org/10.1002/cpz1.64

Blömer, L. A., Giacalone, E., Abbas, F., Filipis, L., Tegolo, D., Migliore, M., & Canepari, M. (2024). Kinetics and functional consequences of BK channels activation by N-type Ca2+ channels in the dendrite of mouse neocortical layer-5 pyramidal neurons. Frontiers in Cellular Neuroscience, 18. https://doi.org/10.3389/fncel.2024.1353895

Bock, O. (2013). Cajal, Golgi, Nansen, Schäfer and the neuron Doctrine. Endeavour, 37(4), 228–234. https://doi.org/10.1016/j.endeavour.2013.06.006

Boda, N., Leaf, N., Fonseca, N., & Eisenberg, N. (2015). Energetics of ion competition in the DEKA selectivity filter of neuronal sodium channels. Condensed Matter Physics, 18(1), 13601. https://doi.org/10.5488/cmp.18.13601

Boiko, T., Rasband, M. N., Levinson, S., Caldwell, J. H., Mandel, G., Trimmer, J. S., & Matthews, G. (2001). Compact myelin dictates the differential targeting of two sodium channel isoforms in the same axon. Neuron, 30(1), 91–104. https://doi.org/10.1016/s0896-6273(01)00265-3

Bosmans, F., & Tytgat, J. (2006). Voltage-gated sodium channel modulation by scorpion α-toxins. Toxicon, 49(2), 142–158. https://doi.org/10.1016/j.toxicon.2006.09.023

Brachet, A., Leterrier, C., Irondelle, M., Fache, M., Racine, V., Sibarita, J., Choquet, D., & Dargent, B. (2010). Ankyrin G restricts ion channel diffusion at the axonal initial segment before the establishment of the diffusion barrier. The Journal of Cell Biology, 191(2), 383–395. https://doi.org/10.1083/jcb.201003042

Brackenbury, W. J., & Isom, L. L. (2011). NA+ Channel ? Subunits: Overachievers of the Ion Channel family. Frontiers in Pharmacology, 2. https://doi.org/10.3389/fphar.2011.00053

BréChet, A., Fache, M., Brachet, A., Ferracci, G., Baude, A., Irondelle, M., Pereira, S., Leterrier, C., & Dargent, B. (2008). Protein kinase CK2 contributes to the organization of sodium channels in axonal membranes by regulating their interactions with ankyrin G. The Journal of Cell Biology, 183(6), 1101–1114. https://doi.org/10.1083/jcb.200805169

Bricelj, V. M., Connell, L., Konoki, K., MacQuarrie, S. P., Scheuer, T., Catterall, W. A., & Trainer, V. L. (2005). Sodium channel mutation leading to saxitoxin resistance in clams increases risk of PSP. Nature, 434(7034), 763–767. https://doi.org/10.1038/nature03415

Brown, D. A., & Passmore, G. M. (2009). Neural KCNQ (Kv7) channels. British Journal of Pharmacology, 156(8), 1185–1195. https://doi.org/10.1111/j.1476-5381.2009.00111.x

Button, K. S., Ioannidis, J. P. A., Mokrysz, C., Nosek, B. A., Flint, J., Robinson, E. S. J., & Munafò, M. R. (2013). Power failure: why small sample size undermines the reliability of neuroscience. Nature Reviews. Neuroscience, 14(5), 365–376. https://doi.org/10.1038/nrn3475

Calin-Jageman, R. J. (2018, June 15). The New Statistics for Neuroscience Majors: Thinking in Effect Sizes. https://pmc.ncbi.nlm.nih.gov/articles/PMC6057753/

Candenas, L., Seda, M., Noheda, P., Buschmann, H., Cintado, C. G., Martin, J. D., & Pinto, F. M. (2006). Molecular diversity of voltage-gated sodium channel α and β subunit mRNAs in human tissues. European Journal of Pharmacology, 541(1–2), 9–16. https://doi.org/10.1016/j.ejphar.2006.04.025

Canepari, M., Djurisic, M., & Zecevic, D. (2007). Dendritic signals from rat hippocampal CA1 pyramidal neurons during coincident pre- and post-synaptic activity: a combined voltage- and calcium-imaging study. The Journal of Physiology, 580(2), 463–484. https://doi.org/10.1113/jphysiol.2006.125005

Catterall, W. A. (2000). From ionic currents to molecular mechanisms. Neuron, 26(1), 13–25. https://doi.org/10.1016/s0896-6273(00)81133-2

Catterall, W. A. (2010). Ion Channel Voltage Sensors: Structure, Function, and Pathophysiology. Neuron, 67(6), 915–928. https://doi.org/10.1016/j.neuron.2010.08.021

Catterall, W. A. (2012). Voltage-gated sodium channels at 60: structure, function and pathophysiology. The Journal of Physiology, 590(11), 2577–2589. https://doi.org/10.1113/jphysiol.2011.224204

Catterall, W. A. (2013). Structure and function of voltage-gated sodium channels at atomic resolution. Experimental Physiology, 99(1), 35–51. https://doi.org/10.1113/expphysiol.2013.071969

Catterall, W. A., Goldin, A. L., & Waxman, S. G. (2005). International Union of Pharmacology. XLVII. Nomenclature and Structure-Function Relationships of Voltage-Gated Sodium Channels. Pharmacological Reviews, 57(4), 397–409. https://doi.org/10.1124/pr.57.4.4

Catterall, W. A., Perez-Reyes, E., Snutch, T. P., & Striessnig, J. (2005). International Union of Pharmacology. XLVIII. Nomenclature and Structure-Function Relationships of Voltage-Gated Calcium Channels. Pharmacological Reviews, 57(4), 411–425. https://doi.org/10.1124/pr.57.4.5

Catterall, W. A., Wisedchaisri, G., & Zheng, N. (2017). The chemical basis for electrical signaling. Nature Chemical Biology, 13(5), 455–463. https://doi.org/10.1038/nchembio.2353

Catterall, W. A., Wisedchaisri, G., & Zheng, N. (2020). The conformational cycle of a prototypical voltage-gated sodium channel. Nature Chemical Biology, 16(12), 1314–1320. https://doi.org/10.1038/s41589-020-0644-4

Cestèle, S., Qu, Y., Rogers, J. C., Rochat, H., Scheuer, T., & Catterall, W. A. (1998). Voltage Sensor–Trapping. Neuron, 21(4), 919–931. https://doi.org/10.1016/s0896-6273(00)80606-6

Chahine, M. (2011). Regulatory role of voltage-gated Na+ channel β subunits in sensory neurons. Frontiers in Pharmacology, 2. https://doi.org/10.3389/fphar.2011.00070

Channelpedia - Search results. (n.d.). Retrieved June 29, 2025, from https://channelpedia.epfl.ch/wikis/search?utf8=%E2%9C%93&keyword=nav1.2

Chen, C., & Cannon, S. C. (1995). Modulation of Na+channel inactivation by the ?1 subunit: A deletion analysis. Pflügers Archiv - European Journal of Physiology, 431(2), 186–195. https://doi.org/10.1007/bf00410190

Chen, I., & Lui, F. (2023, August 14). Neuroanatomy, Neuron Action Potential. StatPearls - NCBI Bookshelf. Retrieved June 13, 2025, from https://www.ncbi.nlm.nih.gov/books/NBK546639/

Chen, Y., Yu, F. H., Surmeier, D. J., Scheuer, T., & Catterall, W. A. (2006). Neuromodulation of NA+ channel slow inactivation via CAMP-Dependent protein kinase and protein kinase C. Neuron, 49(3), 409–420. https://doi.org/10.1016/j.neuron.2006.01.009

Chong, J. A., Tapia-Ramirez, J., Kim, S., Toledo-Aral, J. J., Zheng, Y., Boutros, M. C., Altshuller, Y. M., Frohman, M. A., Kraner, S. D., & Mandel, G. (1995). REST: A mammalian silencer protein that restricts sodium channel gene expression to neurons. Cell, 80(6), 949–957. https://doi.org/10.1016/0092-8674(95)90298-8

Chow, L. W. C., & Leung, Y. M. (2020). The versatile Kv channels in the nervous system: actions beyond action potentials. Cellular and Molecular Life Sciences, 77(13), 2473–2482. https://doi.org/10.1007/s00018-019-03415-8

Chrysafides, S. M., Bordes, S. J., & Sharma, S. (2023, April 10). Physiology, resting potential. StatPearls - NCBI Bookshelf. Retrieved June 30, 2025, from https://www.ncbi.nlm.nih.gov/books/NBK538338

Clare, J. J., Tate, S. N., Nobbs, M., & Romanos, M. A. (2000). Voltage-gated sodium channels as therapeutic targets. Drug Discovery Today, 5(11), 506–520. https://doi.org/10.1016/s1359-6446(00)01570-1

Clark, B. D., Goldberg, E. M., & Rudy, B. (2009). Electrogenic tuning of the Axon initial segment. The Neuroscientist, 15(6), 651–668. https://doi.org/10.1177/1073858409341973

Cohen, J. (1988). Statistical Power Analysis for the Behavioral Sciences. https://doi.org/10.4324/9780203771587

Colbert, C. M., Magee, J. C., Hoffman, D. A., & Johnston, D. (1997). Slow Recovery from Inactivation of Na+Channels Underlies the Activity-Dependent Attenuation of Dendritic Action Potentials in Hippocampal CA1 Pyramidal Neurons. Journal of Neuroscience, 17(17), 6512–6521. https://doi.org/10.1523/jneurosci.17-17-06512.1997

Colbert, C. M., & Pan, E. (2002). Ion channel properties underlying axonal action potential initiation in pyramidal neurons. Nature Neuroscience, 5(6), 533–538. https://doi.org/10.1038/nn0602-857

Cooper, E. C. (2010). Made for "anchorin": Kv7.2/7.3 (KCNQ2/KCNQ3) channels and the modulation of neuronal excitability in vertebrate axons. Seminars in Cell and Developmental Biology, 22(2), 185–192. https://doi.org/10.1016/j.semcdb.2010.10.001

Cotman, C. W., & McGaugh, J. L. (1980). Basic Principles of Neuronal Signaling. In Elsevier eBooks (pp. 111–150). https://doi.org/10.1016/b978-0-12-191650-3.50009-x

Cueni, L., Canepari, M., Luján, R., Emmenegger, Y., Watanabe, M., Bond, C. T., Franken, P., Adelman, J. P., & Lüthi, A. (2008). T-type Ca2+ channels, SK2 channels and SERCAs gate sleep-related oscillations in thalamic dendrites. Nature Neuroscience, 11(6), 683–692. https://doi.org/10.1038/nn.2124

Curtis, H. J., & Cole, K. S. (1942). Membrane resting and action potentials from the squid giant axon. Journal of Cellular and Comparative Physiology, 19(2), 135–144. https://doi.org/10.1002/jcp.1030190202

Davis, J. Q., Lambert, S., & Bennett, V. (1996). Molecular composition of the node of Ranvier: identification of ankyrin-binding cell adhesion molecules neurofascin (mucin+/third FNIII domain-) and NrCAM at nodal axon segments. The Journal of Cell Biology, 135(5), 1355–1367. https://doi.org/10.1083/jcb.135.5.1355

De Kovel, C. G. F., Syrbe, S., Brilstra, E. H., Verbeek, N., Kerr, B., Dubbs, H., Bayat, A., Desai, S., Naidu, S., Srivastava, S., Cagaylan, H., Yis, U., Saunders, C., Rook, M., Plugge, S., Muhle, H., Afawi, Z., Klein, K., Jayaraman, V., . . . Koeleman, B. P. C. (2017). Neurodevelopmental disorders caused by de novo variants in KCNB1 genotypes and phenotypes. JAMA Neurology, 74(10), 1228. https://doi.org/10.1001/jamaneurol.2017.1714

De Lera Ruiz, M., & Kraus, R. L. (2015). Voltage-Gated Sodium Channels: structure, function, pharmacology, and clinical indications. Journal of Medicinal Chemistry, 58(18), 7093–7118. https://doi.org/10.1021/jm501981g

Debanne, D., & Garrido, J. J. (2018). Axon Initial Segment. Encyclopedia of Life Sciences, 1–7. https://doi.org/10.1002/9780470015902.a0000004

Del Castillo, J., & Katz, B. (1954). Quantal components of the end-plate potential. The Journal of Physiology, 124(3), 560–573. https://doi.org/10.1113/jphysiol.1954.sp005129

Delvendahl, I., Jablonski, L., Baade, C., Matveev, V., Neher, E., & Hallermann, S. (2015). Reduced endogenous Ca 2+ buffering speeds active zone Ca 2+ signaling. Proceedings

of the National Academy of Sciences, 112(23). https://doi.org/10.1073/pnas.1508419112

DiStefano, N., Cooper, J. N., Elisha, D. H., Zalta, M., Mittal, J., Cohen, D., Monterrubio, A., Hossain, R., Sangadi, A., Mittal, R., & Eshraghi, A. A. (2025). Decoding SCN2A variants: bridging genetics and phenotypes in autism Spectrum Disorder. Journal of Clinical Medicine, 14(11), 3790. https://doi.org/10.3390/jcm14113790

Dodson, P. D., Barker, M. C., & Forsythe, I. D. (2002). Two heteromeric KV1 potassium channels differentially regulate action potential firing. Journal of Neuroscience, 22(16), 6953–6961. https://doi.org/10.1523/jneurosci.22-16-06953.2002

Drukarch, B., & Wilhelmus, M. M. M. (2023). Thinking about the action potential: the nerve signal as a window to the physical principles guiding neuronal excitability. Frontiers in Cellular Neuroscience, 17. https://doi.org/10.3389/fncel.2023.1232020

Duval, A., MalCot, C. O., Pelhate, M., & Rochat, H. (1989). Changes in Na channel properties of frog and rat skeletal muscles induced by the AaH II toxin from the scorpion Androctonus australis. Pflügers Archiv - European Journal of Physiology, 415(3), 361–371. https://doi.org/10.1007/bf00370889

Dzhashiashvili, Y., Zhang, Y., Galinska, J., Lam, I., Grumet, M., & Salzer, J. L. (2007). Nodes of Ranvier and axon initial segments are ankyrin G–dependent domains that assemble by distinct mechanisms. The Journal of Cell Biology, 177(5), 857–870. https://doi.org/10.1083/jcb.200612012

Echevarria-Cooper, D. M., Hawkins, N. A., Misra, S. N., Huffman, A. M., Thaxton, T., Thompson, C. H., Ben-Shalom, R., Nelson, A. D., Lipkin, A. M., George, A. L., Jr, Bender, K. J., & Kearney, J. A. (2022). Cellular and behavioral effects of altered NaV1.2 sodium channel ion permeability in Scn2a K1422E mice. Human Molecular Genetics, 31(17), 2964–2988. https://doi.org/10.1093/hmg/ddac087

Elston, G. N. (2003). Cortex, Cognition and the Cell: New Insights into the Pyramidal Neuron and Prefrontal Function. Cerebral Cortex, 13(11), 1124–1138. https://doi.org/10.1093/cercor/bhg093

Enderle, J. (2005). BIOELECTRIC PHENOMENA. In Elsevier eBooks (pp. 627–691). https://doi.org/10.1016/b978-0-12-238662-6.50013-6

England, S., & De Groot, M. J. (2009). Subtype-selective targeting of voltage-gated sodium channels. British Journal of Pharmacology, 158(6), 1413–1425. https://doi.org/10.1111/j.1476-5381.2009.00437.x

Etherington, S. J., & Williams, S. R. (2011). Postnatal development of intrinsic and synaptic properties transforms signaling in the layer 5 excitatory neural network of the visual cortex. Journal of Neuroscience, 31(26), 9526–9537. https://doi.org/10.1523/jneurosci.0458-11.2011

Evans, M. D., Dumitrescu, A. S., Kruijssen, D. L., Taylor, S. E., & Grubb, M. S. (2015). Rapid Modulation of Axon Initial Segment Length Influences Repetitive Spike Firing. Cell Reports, 13(6), 1233–1245. https://doi.org/10.1016/j.celrep.2015.09.066

Evans, M. D., Sammons, R. P., Lebron, S., Dumitrescu, A. S., Watkins, T. B. K., Uebele, V. N., Renger, J. J., & Grubb, M. S. (2013). Calcineurin signaling mediates Activity-Dependent relocation of the axon initial segment. Journal of Neuroscience, 33(16), 6950–6963. https://doi.org/10.1523/jneurosci.0277-13.2013

Fanger, C. M., Ghanshani, S., Logsdon, N. J., Rauer, H., Kalman, K., Zhou, J., Beckingham, K., Chandy, K. G., Cahalan, M. D., & Aiyar, J. (1999). Calmodulin mediates calcium-

dependent activation of the intermediate conductance KCA Channel,IKCA1. Journal of Biological Chemistry, 274(9), 5746–5754. https://doi.org/10.1074/jbc.274.9.5746

Fatt, P., & Katz, B. (1952, May 28). Spontaneous subthreshold activity at motor nerve endings. https://pmc.ncbi.nlm.nih.gov/articles/PMC1392564

Feliciangeli, S., Chatelain, F. C., Bichet, D., & Lesage, F. (2015). The family of K2P channels: Salient structural and functional properties. *The Journal of Physiology, 593*(12), 2587–2603. https://doi.org/10.1113/jphysiol.2014.287268

Filipis, L., Blömer, L. A., Montnach, J., Loussouarn, G., De Waard, M., & Canepari, M. (2023). Nav1.2 and BK channel interaction shapes the action potential in the axon initial segment. The Journal of Physiology, 601(10), 1957–1979. https://doi.org/10.1113/jp283801

Filipis, L., & Canepari, M. (2020). Optical measurement of physiological sodium currents in the axon initial segment. The Journal of Physiology, 599(1), 49–66. https://doi.org/10.1113/jp280554

Fleidervish, I. A., Lasser-Ross, N., Gutnick, M. J., & Ross, W. N. (2010). Na+ imaging reveals little difference in action potential–evoked Na+ influx between axon and soma. Nature Neuroscience, 13(7), 852–860. https://doi.org/10.1038/nn.2574

Fletcher, A. (2011). Action potential: generation and propagation. Anaesthesia & Intensive Care Medicine, 12(6), 258–262. https://doi.org/10.1016/j.mpaic.2011.03.010

Focken, T., Chowdhury, S., Zenova, A., Grimwood, M. E., Chabot, C., Sheng, T., Hemeon, I., Decker, S. M., Wilson, M., Bichler, P., Jia, Q., Sun, S., Young, C., Lin, S., Goodchild, S. J., Shuart, N. G., Chang, E., Xie, Z., Li, B., . . . Safina, B. S. (2018). Design of Conformationally Constrained Acyl Sulfonamide Isosteres: Identification of N-([1,2,4]Triazolo[4,3-a]pyridin-3-yl)methane-sulfonamides as Potent and Selective hNaV1.7 Inhibitors for the Treatment of Pain. Journal of Medicinal Chemistry, 61(11), 4810–4831. https://doi.org/10.1021/acs.jmedchem.7b01826

Fotia, A. B., Ekberg, J., Adams, D. J., Cook, D. I., Poronnik, P., & Kumar, S. (2004). Regulation of neuronal voltage-gated sodium channels by the Ubiquitin-Protein ligases NEDD4 and NEDD4-2. Journal of Biological Chemistry, 279(28), 28930–28935. https://doi.org/10.1074/jbc.m402820200

Fréal, A., Jamann, N., Bos, J. T., Jansen, J., Petersen, N., Ligthart, T., Hoogenraad, C. C., & Kole, M. H. P. (2023). Sodium channel endocytosis drives axon initial segment plasticity. Science Advances, 9(37). https://doi.org/10.1126/sciadv.adf3885

Freeman, S. A., Desmazières, A., Fricker, D., Lubetzki, C., & Sol-Foulon, N. (2015). Mechanisms of sodium channel clustering and its influence on axonal impulse conduction. Cellular and Molecular Life Sciences, 73(4), 723–735. https://doi.org/10.1007/s00018-015-2081-1

Fritz, C. O., Morris, P. E., & Richler, J. J. (2011). Effect size estimates: Current use, calculations, and interpretation. Journal of Experimental Psychology General, 141(1), 2–18. https://doi.org/10.1037/a0024338

Fu, J. M., Satterstrom, F. K., Peng, M., Brand, H., Collins, R. L., Dong, S., Wamsley, B., Klei, L., Wang, L., Hao, S. P., Stevens, C. R., Cusick, C., Babadi, M., Banks, E., Collins, B., Dodge, S., Gabriel, S. B., Gauthier, L., Lee, S. K., . . . Talkowski, M. E. (2022). Rare coding variation provides insight into the genetic architecture and phenotypic context of autism. Nature Genetics, 54(9), 1320–1331. https://doi.org/10.1038/s41588-022-01104-0

Fukuoka, T., & Noguchi, K. (2011). Comparative study of voltage-gated sodium channel α-subunits in non-overlapping four neuronal populations in the rat dorsal root ganglion. Neuroscience Research, 70(2), 164–171. https://doi.org/10.1016/j.neures.2011.01.020

Gargus, J. J. (2003). Unraveling monogenic channelopathies and their implications for complex polygenic disease. The American Journal of Human Genetics, 72(4), 785–803. https://doi.org/10.1086/374317

Garrido, J. J. (2023). Contribution of Axon initial segment structure and channels to brain pathology. Cells, 12(8), 1210. https://doi.org/10.3390/cells12081210

Garrido, J. J., Giraud, P., Carlier, E., Fernandes, F., Moussif, A., Fache, M., Debanne, D., & Dargent, B. (2003). A targeting motif involved in sodium channel clustering at the axonal initial segment. Science, 300(5628), 2091–2094. https://doi.org/10.1126/science.1085167

Gasser, A., Ho, T. S., Cheng, X., Chang, K., Waxman, S. G., Rasband, M. N., & Dib-Hajj, S. D. (2012). An AnkyrinG-Binding motif is necessary and sufficient for targeting NAV1.6 sodium channels to axon initial segments and nodes of Ranvier. Journal of Neuroscience, 32(21), 7232–7243. https://doi.org/10.1523/jneurosci.5434-11.2012

Gazina, E. V., Leaw, B. T., Richards, K. L., Wimmer, V. C., Kim, T. H., Aumann, T. D., Featherby, T. J., Churilov, L., Hammond, V. E., Reid, C. A., & Petrou, S. (2015). 'Neonatal' Nav1.2 reduces neuronal excitability and affects seizure susceptibility and behaviour. Human Molecular Genetics, 24(5), 1457–1468. https://doi.org/10.1093/hmg/ddu562

Gazina, E. V., Richards, K., Mokhtar, M., Thomas, E., Reid, C., & Petrou, S. (2010). Differential expression of exon 5 splice variants of sodium channel α subunit mRNAs in the developing mouse brain. Neuroscience, 166(1), 195–200. https://doi.org/10.1016/j.neuroscience.2009.12.011

Gentet, L. J., Stuart, G. J., & Clements, J. D. (2000). Direct measurement of specific membrane capacitance in neurons. Biophysical Journal, 79(1), 314–320. https://doi.org/10.1016/s0006-3495(00)76293-x

Ghovanloo, M., Peters, C. H., & Ruben, P. C. (2018). Effects of acidosis on neuronal voltage-gated sodium channels: Nav1.1 and Nav1.3. Channels, 12(1), 367–377. https://doi.org/10.1080/19336950.2018.1539611

Gillentine, M. A., Wang, T., & Eichler, E. E. (2022). Estimating the Prevalence of De Novo Monogenic Neurodevelopmental Disorders from Large Cohort Studies. Biomedicines, 10(11), 2865. https://doi.org/10.3390/biomedicines10112865

Goethals, S., & Brette, R. (2020). Theoretical relation between axon initial segment geometry and excitability. eLife, 9. https://doi.org/10.7554/elife.53432

Goldberg, E. M., Clark, B. D., Zagha, E., Nahmani, M., Erisir, A., & Rudy, B. (2008). K+ channels at the axon initial segment dampen Near-Threshold excitability of neocortical Fast-Spiking GABAergic interneurons. Neuron, 58(3), 387–400. https://doi.org/10.1016/j.neuron.2008.03.003

Goldin, A. L. (1999). Diversity of mammalian Voltage-Gated sodium channels. Annals of the New York Academy of Sciences, 868(1), 38–50. https://doi.org/10.1111/j.1749-6632.1999.tb11272.x

Goldin, A. L. (2001). Resurgence of sodium channel research. Annual Review of Physiology, 63(1), 871–894. https://doi.org/10.1146/annurev.physiol.63.1.871

Goldin, A. L., Barchi, R. L., Caldwell, J. H., Hofmann, F., Howe, J. R., Hunter, J. C., Kallen, R. G., Mandel, G., Meisler, M. H., Netter, Y. B., Noda, M., Tamkun, M. M., Waxman, S. G., Wood, J. N., & Catterall, W. A. (2001). Nomenclature of Voltage-Gated Sodium Channels. Neuron, 28(2), 365–368. https://doi.org/10.1016/s0896-6273(00)00116-1

Goodchild, S. J., Shuart, N. G., Williams, A. D., Ye, W., Parrish, R. R., Soriano, M., Thouta, S., Mezeyova, J., Waldbrook, M., Dean, R., Focken, T., Ghovanloo, M., Ruben, P. C., Scott, F., Cohen, C. J., Empfield, J., & Johnson, J. (2024). Molecular Pharmacology of Selective NaV1.6 and Dual NaV1.6/NaV1.2 Channel Inhibitors that Suppress Excitatory Neuronal Activity Ex Vivo. ACS Chemical Neuroscience, 15(6), 1169–1184. https://doi.org/10.1021/acschemneuro.3c00757

Grewe, N. (2010). Back-propagation of physiological action potential output in dendrites of slender-tufted L5A pyramidal neurons. Frontiers in Cellular Neuroscience. https://doi.org/10.3389/fncel.2010.00013

Grider, M. H., Jessu, R., & Kabir, R. (2023, May 8). Physiology, Action Potential. StatPearls - NCBI Bookshelf. Retrieved June 15, 2025, from https://www.ncbi.nlm.nih.gov/books/NBK538143

Grubb, M. S., & Burrone, J. (2010). Activity-dependent relocation of the axon initial segment fine-tunes neuronal excitability. Nature, 465(7301), 1070–1074. https://doi.org/10.1038/nature09160

Grubb, M. S., Shu, Y., Kuba, H., Rasband, M. N., Wimmer, V. C., & Bender, K. J. (2011). Short- and Long-Term plasticity at the Axon initial segment. Journal of Neuroscience, 31(45), 16049–16055. https://doi.org/10.1523/jneurosci.4064-11.2011

Guan, D., Horton, L. R., Armstrong, W. E., & Foehring, R. C. (2011). Postnatal development of A-type and Kv1- and Kv2-mediated potassium channel currents in neocortical pyramidal neurons. Journal of Neurophysiology, 105(6), 2976–2988. https://doi.org/10.1152/jn.00758.2010

Gulledge, A. T., & Bravo, J. J. (2016). Neuron morphology influences axon initial segment plasticity. eNeuro, 3(1), ENEURO.0085-15.2016. https://doi.org/10.1523/eneuro.0085-15.2016

Guo, Q., Wang, D., He, X., Feng, Q., Lin, R., Xu, F., Fu, L., & Luo, M. (2015). Whole-Brain mapping of inputs to projection neurons and cholinergic interneurons in the dorsal striatum. PLoS ONE, 10(4), e0123381. https://doi.org/10.1371/journal.pone.0123381

Gutman, G. A., Chandy, K. G., Grissmer, S., Lazdunski, M., Mckinnon, D., Pardo, L. A., Robertson, G. A., Rudy, B., Sanguinetti, M. C., Stühmer, W., & Wang, X. (2005). International Union of Pharmacology. LIII. Nomenclature and Molecular Relationships of Voltage-Gated Potassium Channels. Pharmacological Reviews, 57(4), 473–508. https://doi.org/10.1124/pr.57.4.10

Hamill, O. P., Marty, A., Neher, E., Sakmann, B., & Sigworth, F. J. (1981). Improved patch-clamp techniques for high-resolution current recording from cells and cell-free membrane patches. Pflügers Archiv - European Journal of Physiology, 391(2), 85–100. https://doi.org/10.1007/bf00656997

Hammond, C. (2024). *Cellular and molecular neurophysiology* (5th ed.). Elsevier. https://doi.org/10.1016/C2020-0-03928-9

Hanemaaijer, N. A., Popovic, M. A., Wilders, X., Grasman, S., Arocas, O. P., & Kole, M. H. (2020). Ca2+ entry through NaV channels generates submillisecond axonal Ca2+ signaling. eLife, 9. https://doi.org/10.7554/elife.54566

Harley, P., Kerins, C., Gatt, A., Neves, G., Riccio, F., Machado, C. B., Cheesbrough, A., R'Bibo, L., Burrone, J., & Lieberam, I. (2023). Aberrant axon initial segment plasticity and intrinsic excitability of ALS hiPSC motor neurons. Cell Reports, 42(12), 113509. https://doi.org/10.1016/j.celrep.2023.113509

Harraz, O. F., & Delpire, E. (2023). Recent insights into channelopathies. Physiological Reviews, 104(1), 23–31. https://doi.org/10.1152/physrev.00022.2023

Hartshorne, R. P., & Catterall, W. A. (1981). Purification of the saxitoxin receptor of the sodium channel from rat brain. Proceedings of the National Academy of Sciences, 78(7), 4620–4624. https://doi.org/10.1073/pnas.78.7.4620

Hartshorne, R. P., & Catterall, W. A. (1984). The sodium channel from rat brain. Purification and subunit composition. Journal of Biological Chemistry, 259(3), 1667–1675. https://doi.org/10.1016/s0021-9258(17)43460-0

Hartshorne, R. P., Messner, D. J., Coppersmith, J. C., & Catterall, W. A. (1982). The saxitoxin receptor of the sodium channel from rat brain. Evidence for two nonidentical beta subunits. Journal of Biological Chemistry, 257(23), 13888–13891. https://doi.org/10.1016/s0021-9258(19)45312-x

Harty, R. C., Kim, T. H., Thomas, E. A., Cardamone, L., Jones, N. C., Petrou, S., & Wimmer, V. C. (2013). Axon initial segment structural plasticity in animal models of genetic and acquired epilepsy. Epilepsy Research, 105(3), 272–279. https://doi.org/10.1016/j.eplepsyres.2013.03.004

Hedstrom, K. L., Ogawa, Y., & Rasband, M. N. (2008). AnkyrinG is required for maintenance of the axon initial segment and neuronal polarity. The Journal of Cell Biology, 183(4), 635–640. https://doi.org/10.1083/jcb.200806112

Hedstrom, K. L., Xu, X., Ogawa, Y., Frischknecht, R., Seidenbecher, C. I., Shrager, P., & Rasband, M. N. (2007). Neurofascin assembles a specialized extracellular matrix at the axon initial segment. The Journal of Cell Biology, 178(5), 875–886. https://doi.org/10.1083/jcb.200705119

Heinemann, S. H., Terlau, H., Stühmer, W., Imoto, K., & Numa, S. (1992). Calcium channel characteristics conferred on the sodium channel by single mutations. Nature, 356(6368), 441–443. https://doi.org/10.1038/356441a0

Hendriks, K., Öster, C., & Lange, A. (2021). Structural plasticity of the selectivity filter in cation channels. Frontiers in Physiology, 12. https://doi.org/10.3389/fphys.2021.792958

Heron, S. E., Crossland, K. M., Andermann, E., Phillips, H. A., Hall, A. J., Bleasel, A., Shevell, M., Mercho, S., Seni, M., Guiot, M., Mulley, J. C., Berkovic, S. F., & Scheffer, I. E. (2002). Sodium-channel defects in benign familial neonatal-infantile seizures. The Lancet, 360(9336), 851–852. https://doi.org/10.1016/s0140-6736(02)09968-3

Hille, B. (1971). The permeability of the sodium channel to organic cations in myelinated nerve. The Journal of General Physiology, 58(6), 599–619. https://doi.org/10.1085/jgp.58.6.599

Höber, R. (1905). Über den Einfluss der Salze auf den Ruhestrom des Froschmuskels. Pflügers Archiv - European Journal of Physiology, 106–106(10–12), 599–635. https://doi.org/10.1007/bf01679564

Hodgkin, A. L., & Huxley, A. F. (1939). Action Potentials Recorded from Inside a Nerve Fibre. Nature, 144(3651), 710–711. https://doi.org/10.1038/144710a0

Hodgkin, A. L., & Huxley, A. F. (1952). A quantitative description of membrane current and its application to conduction and excitation in nerve. The Journal of Physiology, 117(4), 500–544. https://doi.org/10.1113/jphysiol.1952.sp004764

Hodgkin, A. L., & Katz, B. (1949). The effect of sodium ions on the electrical activity of the giant axon of the squid. The Journal of Physiology, 108(1), 37–77. https://doi.org/10.1113/jphysiol.1949.sp004310

Holz, R. W., & Fisher, S. K. (2012). Synaptic Transmission and Cellular Signaling. In Elsevier eBooks (pp. 235–257). https://doi.org/10.1016/b978-0-12-374947-5.00012-2

Horrigan, F. T., & Aldrich, R. W. (2002). Coupling between Voltage Sensor Activation, Ca2+ Binding and Channel Opening in Large Conductance (BK) Potassium Channels. The Journal of General Physiology, 120(3), 267–305. https://doi.org/10.1085/jgp.20028605

Hougaard, C., Eriksen, B. L., Jørgensen, S., Johansen, T. H., Dyhring, T., Madsen, L. S., Strøbæk, D., & Christophersen, P. (2007). Selective positive modulation of the SK3 and SK2 subtypes of small conductance Ca2+-activated K+ channels. British Journal of Pharmacology, 151(5), 655–665. https://doi.org/10.1038/sj.bjp.0707281

Hsu, W. J., Nilsson, C. L., & Laezza, F. (2014). Role of the axonal initial segment in psychiatric disorders: function, dysfunction, and Intervention. Frontiers in Psychiatry, 5. https://doi.org/10.3389/fpsyt.2014.00109

Hu, W., Tian, C., Li, T., Yang, M., Hou, H., & Shu, Y. (2009). Distinct contributions of Nav1.6 and Nav1.2 in action potential initiation and backpropagation. Nature Neuroscience, 12(8), 996–1002. https://doi.org/10.1038/nn.2359

Huang, C. Y., & Rasband, M. N. (2018). Axon initial segments: structure, function, and disease. Annals of the New York Academy of Sciences, 1420(1), 46–61. https://doi.org/10.1111/nyas.13718

Huang, J., Fan, X., Jin, X., Lyu, C., Guo, Q., Liu, T., Chen, J., Davakan, A., Lory, P., & Yan, N. (2024). Structural basis for human Cav3.2 inhibition by selective antagonists. Cell Research, 34(6), 440–450. https://doi.org/10.1038/s41422-024-00959-8

Hull, J. M., & Isom, L. L. (2017). Voltage-gated sodium channel β subunits: The power outside the pore in brain development and disease. Neuropharmacology, 132, 43–57. https://doi.org/10.1016/j.neuropharm.2017.09.018

Imbrici, P., Liantonio, A., Camerino, G. M., De Bellis, M., Camerino, C., Mele, A., Giustino, A., Pierno, S., De Luca, A., Tricarico, D., Desaphy, J., & Conte, D. (2016). Therapeutic Approaches to Genetic Ion Channelopathies and Perspectives in Drug Discovery. Frontiers in Pharmacology, 7. https://doi.org/10.3389/fphar.2016.00121

Inda, M. C., DeFelipe, J., & Muñoz, A. (2006). Voltage-gated ion channels in the axon initial segment of human cortical pyramidal cells and their relationship with chandelier cells. Proceedings of the National Academy of Sciences, 103(8), 2920–2925. https://doi.org/10.1073/pnas.0511197103

Jaafari, N., & Canepari, M. (2015). Functional coupling of diverse voltage-gated Ca2+ channels underlies high fidelity of fast dendritic Ca2+ signals during burst firing. The Journal of Physiology, 594(4), 967–983. https://doi.org/10.1113/jp271830

Jack, J. J. B., Noble, D., & Tsien, R. W. (1976). Electric current flow in excitable cells. American Heart Journal, 91(6), 828. https://doi.org/10.1016/s0002-8703(76)80560-1

Jamann, N., Dannehl, D., Lehmann, N. *et al.* Sensory input drives rapid homeostatic scaling of the axon initial segment in mouse barrel cortex. *Nat Commun* 12, 23 (2021). https://doi.org/10.1038/s41467-020-20232-x

Jarnot, M., & Corbett, A. M. (2006). Immunolocalization of NaV1.2 channel subtypes in rat and cat brain and spinal cord with high affinity antibodies. Brain Research, 1107(1), 1–12. https://doi.org/10.1016/j.brainres.2006.05.090

Jenkins, P. M., & Bender, K. J. (2025). Axon Initial Segment Structure and function in Health and disease. Physiological Reviews. https://doi.org/10.1152/physrev.00030.2024

Jenkins, S. M., & Bennett, V. (2001). Ankyrin-G coordinates assembly of the spectrin-based membrane skeleton, voltage-gated sodium channels, and L1 CAMs at Purkinje neuron initial segments. The Journal of Cell Biology, 155(5), 739–746. https://doi.org/10.1083/jcb.200109026

Jensen, B., Strobaek, D., Olesen, S., & Christophersen, P. (2001). The Ca2+-Activated K+ Channel of Intermediate Conductance:A Molecular Target for Novel Treatments? Current Drug Targets, 2(4), 401–422. https://doi.org/10.2174/1389450013348173

Jiang, S., Guan, Y., Chen, S., Jia, X., Ni, H., Zhang, Y., Han, Y., Peng, X., Zhou, C., Li, A., Luo, Q., & Gong, H. (2020). Anatomically revealed morphological patterns of pyramidal neurons in layer 5 of the motor cortex. Scientific Reports, 10(1). https://doi.org/10.1038/s41598-020-64665-2

Jones, K. M. (2022). "You've got to work on this Axon": J. Z. Young and Squid Giant Axon Preparations in 20th-Century Neurobiology**. Berichte Zur Wissenschaftsgeschichte, 45(3), 317–331. https://doi.org/10.1002/bewi.202200021

Jurkat-Rott, K., Lerche, H., Weber, Y., & Lehmann-Horn, F. (2010). Hereditary channelopathies in neurology. Advances in Experimental Medicine and Biology, 305–334. https://doi.org/10.1007/978-90-481-9485-8_18

Kadir, L. A., Stacey, M., & Barrett-Jolley, R. (2018). Emerging roles of the membrane potential: action beyond the action potential. Frontiers in Physiology, 9. https://doi.org/10.3389/fphys.2018.01661

Kampa, B. M., & Stuart, G. J. (2006). Calcium Spikes in Basal Dendrites of Layer 5 Pyramidal Neurons during Action Potential Bursts. Journal of Neuroscience, 26(28), 7424–7432. https://doi.org/10.1523/jneurosci.3062-05.2006

Kandel, E. R., Schwartz, J. H., Jessell, T. M., Siegelbaum, S. A., & Hudspeth, A. J. (2013). Principles of neural science (5th ed.). McGraw-Hill.

Karimi, A., Odenthal, J., Drawitsch, F., Boergens, K. M., & Helmstaedter, M. (2020). Cell-type specific innervation of cortical pyramidal cells at their apical dendrites. eLife, 9. https://doi.org/10.7554/elife.46876

Kass, R. S. (2005). The channelopathies: novel insights into molecular and genetic mechanisms of human disease. Journal of Clinical Investigation, 115(8), 1986–1989. https://doi.org/10.1172/jci26011

Katz, B., & Miledi, R. (1967). A study of synaptic transmission in the absence of nerve impulses. The Journal of Physiology, 192(2), 407–436. https://doi.org/10.1113/jphysiol.1967.sp008307

Katz, E., Stoler, O., Scheller, A., Khrapunsky, Y., Goebbels, S., Kirchhoff, F., Gutnick, M. J., Wolf, F., & Fleidervish, I. A. (2018). Role of sodium channel subtype in action potential generation by neocortical pyramidal neurons. Proceedings of the National Academy of Sciences, 115(30). https://doi.org/10.1073/pnas.1720493115

Kaupp, U. B., & Seifert, R. (2002). Cyclic Nucleotide-Gated ion channels. Physiological Reviews, 82(3), 769–824. https://doi.org/10.1152/physrev.00008.2002

Kay, A. R., Sugimori, M., & Llinás, R. (1998). Kinetic and stochastic properties of a persistent sodium current in mature guinea pig cerebellar purkinje cells. Journal of Neurophysiology, 80(3), 1167–1179. https://doi.org/10.1152/jn.1998.80.3.1167

Kearney, J. A., Yang, Y., Beyer, B., Bergren, S. K., Claes, L., DeJonghe, P., & Frankel, W. N. (2006). Severe epilepsy resulting from genetic interaction between Scn2a and Kcnq2. Human Molecular Genetics, 15(6), 1043–1048. https://doi.org/10.1093/hmg/ddl019

Kerr, N. C., Gao, Z., Holmes, F. E., Hobson, S., Hancox, J. C., Wynick, D., & James, A. F. (2007). The sodium channel Nav1.5a is the predominant isoform expressed in adult mouse dorsal root ganglia and exhibits distinct inactivation properties from the full-length Nav1.5 channel. Molecular and Cellular Neuroscience, 35(2), 283–291. https://doi.org/10.1016/j.mcn.2007.03.002

Kim, D. M., & Nimigean, C. M. (2016). Voltage-Gated Potassium Channels: A Structural Examination of Selectivity and Gating. Cold Spring Harbor Perspectives in Biology, 8(5), a029231. https://doi.org/10.1101/cshperspect.a029231

King, A. N., Manning, C. F., & Trimmer, J. S. (2014). A unique ion channel clustering domain on the axon initial segment of mammalian neurons. The Journal of Comparative Neurology, 522(11), 2594–2608. https://doi.org/10.1002/cne.23551

Kita, T., & Kita, H. (2012). The subthalamic nucleus is one of multiple innervation sites for Long-Range corticofugal axons: a Single-Axon tracing study in the RAT. Journal of Neuroscience, 32(17), 5990–5999. https://doi.org/10.1523/jneurosci.5717-11.2012

Kloth, K., Denecke, J., Hempel, M., Johannsen, J., Strom, T. M., Kubisch, C., & Lessel, D. (2017). First de novo ANK3 nonsense mutation in a boy with intellectual disability, speech impairment and autistic features. European Journal of Medical Genetics, 60(9), 494–498. https://doi.org/10.1016/j.ejmg.2017.07.001

Köhler, M., Hirschberg, B., Bond, C. T., Kinzie, J. M., Marrion, N. V., Maylie, J., & Adelman, J. P. (1996). Small-Conductance, Calcium-Activated Potassium Channels from Mammalian Brain. Science, 273(5282), 1709–1714. https://doi.org/10.1126/science.273.5282.1709

Kole, M. H., Letzkus, J. J., & Stuart, G. J. (2007). Axon Initial segment KV1 channels control axonal action potential waveform and synaptic efficacy. Neuron, 55(4), 633–647. https://doi.org/10.1016/j.neuron.2007.07.031

Kole, M. H. P., & Stuart, G. J. (2008). Is action potential threshold lowest in the axon? Nature Neuroscience, 11(11), 1253–1255. https://doi.org/10.1038/nn.2203

Kolmogorov, A. L. (1933). Sulla determinazione empirica di una legge di distribuzione. Giornale Dell'Istituto Italiano Degli Attuari, 4, 83–91. https://ci.nii.ac.jp/naid/10030673552

Kotler, O., Khrapunsky, Y., Shvartsman, A., Dai, H., Plant, L. D., Goldstein, S. A., & Fleidervish, I. (2022). SUMOylation of NaV1.2 channels regulates the velocity of backpropagating action potentials in cortical pyramidal neurons. bioRxiv (Cold Spring Harbor Laboratory). https://doi.org/10.1101/2022.08.02.502500

Kraner, S. D., Tanaka, J. C., & Barchi, R. L. (1985). Purification and functional reconstitution of the voltage-sensitive sodium channel from rabbit T-tubular membranes. Journal of

Biological Chemistry, 260(10), 6341–6347. https://doi.org/10.1016/s0021-9258(18)88977-3

Kroon, T., Van Hugte, E., Van Linge, L., Mansvelder, H. D., & Meredith, R. M. (2019). Early postnatal development of pyramidal neurons across layers of the mouse medial prefrontal cortex. Scientific Reports, 9(1). https://doi.org/10.1038/s41598-019-41661-9

Kruth, K. A., Grisolano, T. M., Ahern, C. A., & Williams, A. J. (2020). SCN2A channelopathies in the autism spectrum of neuropsychiatric disorders: a role for pluripotent stem cells? Molecular Autism, 11(1). https://doi.org/10.1186/s13229-020-00330-9

Krzywinski, M., & Altman, N. (2013). Power and sample size. Nature Methods, 10(12), 1139–1140. https://doi.org/10.1038/nmeth.2738

Kshatri, A. S., Gonzalez-Hernandez, A., & Giraldez, T. (2018). Physiological Roles and Therapeutic Potential of Ca2+ Activated Potassium Channels in the Nervous System. Frontiers in Molecular Neuroscience, 11. https://doi.org/10.3389/fnmol.2018.00258

Kuang, Q., Purhonen, P., & Hebert, H. (2015). Structure of potassium channels. Cellular and Molecular Life Sciences, 72(19), 3677–3693. https://doi.org/10.1007/s00018-015-1948-5

Kuba, H., Oichi, Y., & Ohmori, H. (2010). Presynaptic activity regulates Na+ channel distribution at the axon initial segment. Nature, 465(7301), 1075–1078. https://doi.org/10.1038/nature09087

Kuba, H., Yamada, R., Ishiguro, G., & Adachi, R. (2015). Redistribution of Kv1 and Kv7 enhances neuronal excitability during structural axon initial segment plasticity. Nature Communications, 6(1). https://doi.org/10.1038/ncomms9815

Kullmann, D. M. (2002). The neuronal channelopathies. Brain, 125(6), 1177–1195. https://doi.org/10.1093/brain/awf130

Kullmann, D. M. (2010). Neurological channelopathies. Annual Review of Neuroscience, 33(1), 151–172. https://doi.org/10.1146/annurev-neuro-060909-153122

Kullmann, D. M., & Waxman, S. G. (2010). Neurological channelopathies: new insights into disease mechanisms and ion channel function. The Journal of Physiology, 588(11), 1823–1827. https://doi.org/10.1113/jphysiol.2010.190652

Larkum, M. E., Kaiser, K. M. M., & Sakmann, B. (1999). Calcium electrogenesis in distal apical dendrites of layer 5 pyramidal cells at a critical frequency of back-propagating action potentials. Proceedings of the National Academy of Sciences, 96(25), 14600–14604. https://doi.org/10.1073/pnas.96.25.14600

Larkum, M. E., Waters, J., Sakmann, B., & Helmchen, F. (2007). Dendritic spikes in apical dendrites of neocortical layer 2/3 pyramidal neurons. Journal of Neuroscience, 27(34), 8999–9008. https://doi.org/10.1523/jneurosci.1717-07.2007

Larkum, M. E., & Zhu, J. J. (2002). Signaling of Layer 1 and Whisker-Evoked CA2+and NA+Action potentials in distal and terminal dendrites of Rat neocortical pyramidal NeuronsIn VitroandIn Vivo. Journal of Neuroscience, 22(16), 6991–7005. https://doi.org/10.1523/jneurosci.22-16-06991.2002

Larkum, M. E., Zhu, J. J., & Sakmann, B. (1999). A new cellular mechanism for coupling inputs arriving at different cortical layers. Nature, 398(6725), 338–341. https://doi.org/10.1038/18686

Larkum, M. E., Zhu, J. J., & Sakmann, B. (2001). Dendritic mechanisms underlying the coupling of the dendritic with the axonal action potential initiation zone of adult rat layer 5 pyramidal neurons. The Journal of Physiology, 533(2), 447–466. https://doi.org/10.1111/j.1469-7793.2001.0447a.x

Léna, I., & Mantegazza, M. (2019). NaV1.2 haploinsufficiency in Scn2a knock-out mice causes an autistic-like phenotype attenuated with age. Scientific Reports, 9(1). https://doi.org/10.1038/s41598-019-49392-7

Lesage, F. (2003). Pharmacology of neuronal background potassium channels. Neuropharmacology, 44(1), 1–7. https://doi.org/10.1016/S0028-3908(02)00339-8

Leterrier, C. (2016). The Axon initial segment, 50Years later. Current Topics in Membranes, 185–233. https://doi.org/10.1016/bs.ctm.2015.10.005

Leterrier, C., Brachet, A., Dargent, B., & Vacher, H. (2010). Determinants of voltage-gated sodium channel clustering in neurons. Seminars in Cell and Developmental Biology, 22(2), 171–177. https://doi.org/10.1016/j.semcdb.2010.09.014

Leterrier, C., Potier, J., Caillol, G., Debarnot, C., Boroni, F. R., & Dargent, B. (2015). Nanoscale architecture of the Axon initial segment reveals an organized and robust scaffold. Cell Reports, 13(12), 2781–2793. https://doi.org/10.1016/j.celrep.2015.11.051

Lezmy, J., Lipinsky, M., Khrapunsky, Y., Patrich, E., Shalom, L., Peretz, A., Fleidervish, I. A., & Attali, B. (2017). M-current inhibition rapidly induces a unique CK2-dependent plasticity of the axon initial segment. Proceedings of the National Academy of Sciences, 114(47). https://doi.org/10.1073/pnas.1708700114

Li, M., West, J. W., Lai, Y., Scheuer, T., & Catterall, W. A. (1992). Functional modulation of brain sodium channels by cAMP-dependent phosphorylation. Neuron, 8(6), 1151–1159. https://doi.org/10.1016/0896-6273(92)90135-z

Li, T., Tian, C., Scalmani, P., Frassoni, C., Mantegazza, M., Wang, Y., Yang, M., Wu, S., & Shu, Y. (2014). Action potential initiation in neocortical inhibitory interneurons. PLoS Biology, 12(9), e1001944. https://doi.org/10.1371/journal.pbio.1001944

Li, Y., Liu, H., Xia, M., & Gong, H. (2016). Lysine and the NA+/K+ selectivity in mammalian Voltage-Gated sodium channels. PLoS ONE, 11(9), e0162413. https://doi.org/10.1371/journal.pone.0162413

Li, Y., Wang, H., Wang, Y., Chen, Z., Liu, Y., Tian, W., Kang, X., Pashang, A., Kulasiri, D., Yang, X., Li, H. W., & Zhang, Y. (2024). Alterations in the axon initial segment plasticity is involved in early pathogenesis in Alzheimer's disease. MedComm, 5(11). https://doi.org/10.1002/mco2.768

Li, Y., Yuan, T., Huang, B., Zhou, F., Peng, C., Li, X., Qiu, Y., Yang, B., Zhao, Y., Huang, Z., & Jiang, D. (2023). Structure of human NaV1.6 channel reveals Na+ selectivity and pore blockade by 4,9-anhydro-tetrodotoxin. Nature Communications, 14(1). https://doi.org/10.1038/s41467-023-36766-9

Liang, L., Darbandi, S. F., Pochareddy, S., Gulden, F. O., Gilson, M. C., Sheppard, B. K., Sahagun, A., An, J., Werling, D. M., Rubenstein, J. L. R., Sestan, N., Bender, K. J., & Sanders, S. J. (2021). Developmental dynamics of voltage-gated sodium channel isoform expression in the human and mouse brain. Genome Medicine, 13(1). https://doi.org/10.1186/s13073-021-00949-0

Linford, N. J., Cantrell, A. R., Qu, Y., Scheuer, T., & Catterall, W. A. (1998). Interaction of batrachotoxin with the local anesthetic receptor site in transmembrane segment IVS6

of the voltage-gated sodium channel. Proceedings of the National Academy of Sciences, 95(23), 13947–13952. https://doi.org/10.1073/pnas.95.23.13947

Lipkin, A. M., Cunniff, M. M., Spratt, P. W. E., Lemke, S. M., & Bender, K. J. (2021). Functional microstructure of CAV-Mediated calcium signaling in the axon initial segment. Journal of Neuroscience, 41(17), 3764–3776. https://doi.org/10.1523/jneurosci.2843-20.2021

Lipscombe, D., Allen, S. E., & Toro, C. P. (2013). Control of neuronal voltage-gated calcium ion channels from RNA to protein. Trends in Neurosciences, 36(10), 598–609. https://doi.org/10.1016/j.tins.2013.06.008

Litt, M. (1989). Localization of a human brain sodium channel gene (SCN2A) to chromosome 2. Genomics, 5(2), 204–208. https://doi.org/10.1016/0888-7543(89)90047-5

Liu, Y., Bassetto, C. A. Z., Pinto, B. I., Iyer, A., Lueck, J. D., & Bezanilla, F. (2023). A mechanistic reinterpretation of fast inactivation in voltage-gated Na^+ channels. Nature Communications, 14, 5072. https://doi.org/10.1038/s41467-023-40514-4

Liu, Y., & Bezanilla, F. (2025). A sodium channel mutant removes fast inactivation with the inactivation particle bound. Journal of General Physiology, 157(1), e202413667. https://doi.org/10.1085/jgp.202413667

López-Muñoz, F., Boya, J., & Alamo, C. (2006). Neuron theory, the cornerstone of neuroscience, on the centenary of the Nobel Prize award to Santiago Ramón y Cajal. Brain Research Bulletin, 70(4–6), 391–405. https://doi.org/10.1016/j.brainresbull.2006.07.010

Lorincz, A., & Nusser, Z. (2008). Cell-Type-Dependent molecular composition of the axon initial segment. Journal of Neuroscience, 28(53), 14329–14340. https://doi.org/10.1523/jneurosci.4833-08.2008

Lorincz, A., & Nusser, Z. (2010). Molecular Identity of Dendritic Voltage-Gated Sodium channels. Science, 328(5980), 906–909. https://doi.org/10.1126/science.1187958

Love, R. J., & Webb, W. G. (1992). Neuronal function in the nervous system. In Elsevier eBooks (pp. 46–58). https://doi.org/10.1016/b978-0-7506-9076-8.50010-1

Madden, J. A., & Rusch, N. J. (2001). Electrophysiology of Vascular Smooth Muscle. In Elsevier eBooks (pp. 213–227). https://doi.org/10.1016/b978-012656975-9/50013-4

Major, G., Larkum, M. E., & Schiller, J. (2013). Active properties of neocortical pyramidal neuron dendrites. Annual Review of Neuroscience, 36(1), 1–24. https://doi.org/10.1146/annurev-neuro-062111-150343

Mantegazza, M., Cestèle, S., & Catterall, W. A. (2021). Sodium channelopathies of skeletal muscle and brain. Physiological Reviews, 101(4), 1633–1689. https://doi.org/10.1152/physrev.00025.2020

Marek, G. J., & Schoepp, D. D. (2021). Cortical influences of serotonin and glutamate on layer V pyramidal neurons. Progress in Brain Research, 341–378. https://doi.org/10.1016/bs.pbr.2020.11.002

Mason, E. R., Wu, F., Patel, R. R., Xiao, Y., Cannon, S. C., & Cummins, T. R. (2019). Resurgent and gating pore currents induced byDe novo SCN2AEpilepsy mutations. eNeuro, 6(5), ENEURO.0141-19.2019. https://doi.org/10.1523/eneuro.0141-19.2019

Massey, F. J. (1951). The Kolmogorov-Smirnov test for goodness of fit. Journal of the American Statistical Association, 46(253), 68–78. https://doi.org/10.1080/01621459.1951.10500769

Mathie, A., & Veale, E. L. (2008). Neuronal potassium channels. In Springer eBooks (pp. 2792–2797). https://doi.org/10.1007/978-3-540-29678-2_3922

McCormick, D. A., & Bal, T. (1997). Sleep and arousal: Thalamocortical mechanisms. Annual Review of Neuroscience, 20, 185–215. https://doi.org/10.1146/annurev.neuro.20.1.185

Meriney, S. D., & Fanselow, E. E. (2019a). Basics of Cellular Neurophysiology. In Elsevier eBooks (pp. 19–34). https://doi.org/10.1016/b978-0-12-815320-8.00003-x

Meriney, S. D., & Fanselow, E. E. (2019b). The Formation and Structure of Synapses. In Elsevier eBooks (pp. 7–18). https://doi.org/10.1016/b978-0-12-815320-8.00002-8

Meves, H., & Vogel, W. (1973). Calcium inward currents in internally perfused giant axons. The Journal of Physiology, 235(1), 225–265. https://doi.org/10.1113/jphysiol.1973.sp010386

Miceli, F., Striano, P., Soldovieri, M. V., Fontana, A., Nardello, R., Robbiano, A., Bellini, G., Elia, M., Zara, F., Taglialatela, M., & Mangano, S. (2015). A novel KCNQ3 mutation in familial epilepsy with focal seizures and intellectual disability. Epilepsia, 56(2). https://doi.org/10.1111/epi.12887

Millichap, J. J., Park, K. L., Tsuchida, T., Ben-Zeev, B., Carmant, L., Flamini, R., Joshi, N., Levisohn, P. M., Marsh, E., Nangia, S., Narayanan, V., Ortiz-Gonzalez, X. R., Patterson, M. C., Pearl, P. L., Porter, B., Ramsey, K., McGinnis, E. L., Taglialatela, M., Tracy, M., . . . Cooper, E. C. (2016). KCNQ2 encephalopathy. Neurology Genetics, 2(5). https://doi.org/10.1212/nxg.0000000000000096

Milojkovic, B. A., Radojicic, M. S., & Antic, S. D. (2005). A Strict Correlation between Dendritic and Somatic Plateau Depolarizations in the Rat Prefrontal Cortex Pyramidal Neurons. Journal of Neuroscience, 25(15), 3940–3951. https://doi.org/10.1523/jneurosci.5314-04.2005

Minassian, N. A., Gibbs, A., Shih, A. Y., Liu, Y., Neff, R. A., Sutton, S. W., Mirzadegan, T., Connor, J., Fellows, R., Husovsky, M., Nelson, S., Hunter, M. J., Flinspach, M., & Wickenden, A. D. (2013). Analysis of the structural and molecular basis of voltage-sensitive sodium channel inhibition by the spider toxin HuWentoxin-IV (M-TRTX-HH2A). Journal of Biological Chemistry, 288(31), 22707–22720. https://doi.org/10.1074/jbc.m113.461392

Mishra, V., Karumuri, B. K., Gautier, N. M., Liu, R., Hutson, T. N., Vanhoof-Villalba, S. L., Vlachos, I., Iasemidis, L., & Glasscock, E. (2017). Scn2a deletion improves survival and brain–heart dynamics in the Kcna1-null mouse model of sudden unexpected death in epilepsy (SUDEP). Human Molecular Genetics, 26(11), 2091–2103. https://doi.org/10.1093/hmg/ddx104

Miyashita, Y. (2022). Operating principles of the cerebral cortex as a six-layered network in primates: beyond the classic canonical circuit model. Proceedings of the Japan Academy Series B, 98(3), 93–111. https://doi.org/10.2183/pjab.98.007

Moberg, S., & Takahashi, N. (2022). Neocortical layer 5 subclasses: From cellular properties to roles in behavior. Frontiers in Synaptic Neuroscience, 14. https://doi.org/10.3389/fnsyn.2022.1006773

Mondal, A. K., Carrillo, E., Jayaraman, V., & Twomey, E. C. (2025). Glutamate gating of AMPA-subtype iGluRs at physiological temperatures. Nature. https://doi.org/10.1038/s41586-025-08770-0

Montnach, J., Blömer, L. A., Lopez, L., Filipis, L., Meudal, H., Lafoux, A., Nicolas, S., Chu, D., Caumes, C., Béroud, R., Jopling, C., Bosmans, F., Huchet, C., Landon, C., Canepari, M., & De Waard, M. (2022). In vivo spatiotemporal control of voltage-gated ion channels by using photoactivatable peptidic toxins. Nature Communications, 13(1). https://doi.org/10.1038/s41467-022-27974-w

Männikkö, R., & Kullmann, D. M. (2024). Structure–function and pharmacologic aspects of ion channels relevant to neurologic channelopathies. Handbook of Clinical Neurology, 1–23. https://doi.org/10.1016/b978-0-323-90820-7.00009-4

Nadella, N., Ghosh, A., & Chu, X. (2022, February 15). Hyperexcitability in adult mice with severe deficiency in NaV1.2 channels. https://pmc.ncbi.nlm.nih.gov/articles/PMC8918607

Nahm, F. S. (2016). Nonparametric statistical tests for the continuous data: the basic concept and the practical use. Korean Journal of Anesthesiology, 69(1), 8. https://doi.org/10.4097/kjae.2016.69.1.8

Namadurai, S., Yereddi, N. R., Cusdin, F. S., Huang, C. L., Chirgadze, D. Y., & Jackson, A. P. (2015). A new look at sodium channel β subunits. Open Biology, 5(1), 140192. https://doi.org/10.1098/rsob.140192

Nanou, E., & Catterall, W. A. (2018). Calcium channels, synaptic plasticity, and neuropsychiatric disease. Neuron, 98(3), 466–481. https://doi.org/10.1016/j.neuron.2018.03.017

Nau, C., & Leipold, E. (2017). Voltage-gated sodium channels and pain. e-Neuroforum, 23(3), 123–130. https://doi.org/10.1515/nf-2017-a017

Neher, E., & Sakmann, B. (1976). Single-channel currents recorded from membrane of denervated frog muscle fibres. Nature, 260(5554), 799–802. https://doi.org/10.1038/260799a0

Nelson, A. D., Catalfio, A. M., Gupta, J. P., Min, L., Caballero-Florán, R. N., Dean, K. P., Elvira, C. C., Derderian, K. D., Kyoung, H., Sahagun, A., Sanders, S. J., Bender, K. J., & Jenkins, P. M. (2024). Physical and functional convergence of the autism risk genes Scn2a and Ank2 in neocortical pyramidal cell dendrites. Neuron, 112(7), 1133-1149.e6. https://doi.org/10.1016/j.neuron.2024.01.003

Nelson, S. B., & Valakh, V. (2015). Excitatory/Inhibitory balance and circuit homeostasis in autism spectrum disorders. Neuron, 87(4), 684–698. https://doi.org/10.1016/j.neuron.2015.07.033

Nevin, S. T., Lawrence, N., Nicke, A., Lewis, R. J., & Adams, D. J. (2020). Functional modulation of the human voltage-gated sodium channel NaV1.8 by auxiliary β subunits. Channels, 15(1), 79–93. https://doi.org/10.1080/19336950.2020.1860399

N'Gouemo, P. (2011). Targeting BK (big potassium) channels in epilepsy. Expert Opinion on Therapeutic Targets, 15(11), 1283–1295. https://doi.org/10.1517/14728222.2011.620607

Noda, M., Ikeda, T., Kayano, T., Suzuki, H., Takeshima, H., Kurasaki, M., Takahashi, H., & Numa, S. (1986). Existence of distinct sodium channel messenger RNAs in rat brain. Nature, 320(6058), 188–192. https://doi.org/10.1038/320188a0

Noda, M., Ikeda, T., Suzuki, H., Takeshima, H., Takahashi, T., Kuno, M., & Numa, S. (1986). Expression of functional sodium channels from cloned cDNA. Nature, 322(6082), 826–828. https://doi.org/10.1038/322826a0

Noda, M., Shimizu, S., Tanabe, T., Takai, T., Kayano, T., Ikeda, T., Takahashi, H., Nakayama, H., Kanaoka, Y., Minamino, N., Kangawa, K., Matsuo, H., Raftery, M. A., Hirose, T., Inayama, S., Hayashida, H., Miyata, T., & Numa, S. (1984). Primary structure of Electrophorus electricus sodium channel deduced from cDNA sequence. Nature, 312(5990), 121–127. https://doi.org/10.1038/312121a0

Nord, C. L., Valton, V., Wood, J., & Roiser, J. P. (2017). Power-Up: A reanalysis of "Power failure" in Neuroscience using mixture modeling. Journal of Neuroscience, 37(34), 8051–8061. https://doi.org/10.1523/jneurosci.3592-16.2017

Numa, S., & Noda, M. (1986). Molecular structure of sodium channels. Annals of the New York Academy of Sciences, 479(1), 338–355. https://doi.org/10.1111/j.1749-6632.1986.tb15580.x

O'Connell, A. D., Morton, M. J., & Hunter, M. (2002). Two-pore domain K+ channels—molecular sensors. Biochimica Et Biophysica Acta (BBA) - Biomembranes, 1566(1–2), 152–161. https://doi.org/10.1016/s0005-2736(02)00597-7

Ogiwara, I., Miyamoto, H., Tatsukawa, T., Yamagata, T., Nakayama, T., Atapour, N., Miura, E., Mazaki, E., Ernst, S. J., Cao, D., Ohtani, H., Itohara, S., Yanagawa, Y., Montal, M., Yuzaki, M., Inoue, Y., Hensch, T. K., Noebels, J. L., & Yamakawa, K. (2018). Nav1.2 haplodeficiency in excitatory neurons causes absence-like seizures in mice. Communications Biology, 1(1). https://doi.org/10.1038/s42003-018-0099-2

O'Leary, T., Williams, A. H., Caplan, J. S., & Marder, E. (2013). Correlations in ion channel expression emerge from homeostatic tuning rules. *Proceedings of the National Academy of Sciences of the United States of America, 110*(28), E2645–E2654. https://doi.org/10.1073/pnas.1309966110

O'Leary, T., Williams, A. H., Franci, A., & Marder, E. (2014). Cell Types, Network Homeostasis, and Pathological Compensation from a Biologically Plausible Ion Channel Expression Model. Neuron, 82(4), 809–821. https://doi.org/10.1016/j.neuron.2014.04.002

Oliveira, J. S., Redaelli, E., Zaharenko, A. J., Cassulini, R. R., Konno, K., Pimenta, D. C., Freitas, J. C., Clare, J. J., & Wanke, E. (2004). Binding specificity of sea anemone toxins to NAV 1.1-1.6 sodium channels. Journal of Biological Chemistry, 279(32), 33323–33335. https://doi.org/10.1074/jbc.m404344200

Onwuli, D. O., & Beltran-Alvarez, P. (2015). An update on transcriptional and post-translational regulation of brain voltage-gated sodium channels. Amino Acids, 48(3), 641–651. https://doi.org/10.1007/s00726-015-2122-y

Palay, S. L., Sotelo, C., Peters, A., & Orkand, P. M. (1968). THE AXON HILLOCK AND THE INITIAL SEGMENT. The Journal of Cell Biology, 38(1), 193–201. https://doi.org/10.1083/jcb.38.1.193

Palmer, L. M., & Stuart, G. J. (2006). Site of Action potential initiation in Layer 5 pyramidal neurons. Journal of Neuroscience, 26(6), 1854–1863. https://doi.org/10.1523/jneurosci.4812-05.2006

Pan, X., Li, Z., Huang, X., Huang, G., Gao, S., Shen, H., Liu, L., Lei, J., & Yan, N. (2019). Molecular basis for pore blockade of human Na + channel Na v 1.2 by the μ-conotoxin KIIIA. Science, 363(6433), 1309–1313. https://doi.org/10.1126/science.aaw2999

Pan, Z., Kao, T., Horvath, Z., Lemos, J., Sul, J., Cranstoun, S. D., Bennett, V., Scherer, S. S., & Cooper, E. C. (2006). A common Ankyrin-G-Based mechanism retains KCNQ and

NAVChannels at electrically active domains of the axon. Journal of Neuroscience, 26(10), 2599–2613. https://doi.org/10.1523/jneurosci.4314-05.2006

Papazian, D. M., Schwarz, T. L., Tempel, B. L., Jan, Y. N., & Jan, L. Y. (1987). Cloning of Genomic and Complementary DNA from Shaker , a Putative Potassium Channel Gene from Drosophila. Science, 237(4816), 749–753. https://doi.org/10.1126/science.2441470

Patino, G. A., & Isom, L. L. (2010). Electrophysiology and beyond: Multiple roles of Na+ channel β subunits in development and disease. Neuroscience Letters, 486(2), 53–59. https://doi.org/10.1016/j.neulet.2010.06.050

Payandeh, J., El-Din, T. M. G., Scheuer, T., Zheng, N., & Catterall, W. A. (2012). Crystal structure of a voltage-gated sodium channel in two potentially inactivated states. Nature, 486(7401), 135–139. https://doi.org/10.1038/nature11077

Payandeh, J., Scheuer, T., Zheng, N., & Catterall, W. A. (2011). The crystal structure of a voltage-gated sodium channel. Nature, 475(7356), 353–358. https://doi.org/10.1038/nature10238

Pearce, J. M. S. (2004). Sir Charles Scott Sherrington (1857–1952) and the synapse. Journal of Neurology Neurosurgery & Psychiatry, 75(4), 544. https://doi.org/10.1136/jnnp.2003.017921

Pedarzani, P., McCutcheon, J. E., Rogge, G., Jensen, B. S., Christophersen, P., Hougaard, C., Strøbæk, D., & Stocker, M. (2005). Specific enhancement of SK channel activity selectively potentiates the afterhyperpolarizing current IAHP and modulates the firing properties of hippocampal pyramidal neurons. Journal of Biological Chemistry, 280(50), 41404–41411. https://doi.org/10.1074/jbc.m509610200

Pedarzani, P., Mosbacher, J., Rivard, A., Cingolani, L. A., Oliver, D., Stocker, M., Adelman, J. P., & Fakler, B. (2001). Control of electrical activity in central neurons by modulating the gating of small conductance CA2+-activated K+ channels. Journal of Biological Chemistry, 276(13), 9762–9769. https://doi.org/10.1074/jbc.m010001200

Pedarzani, P., & Stocker, M. (2008). Molecular and cellular basis of small- and intermediate-conductance, calcium-activated potassium channel function in the brain. Cellular and Molecular Life Sciences, 65(20), 3196–3217. https://doi.org/10.1007/s00018-008-8216-x

Pérez-Garci, E., Larkum, M. E., & Nevian, T. (2012). Inhibition of dendritic Ca2+ spikes by GABAB receptors in cortical pyramidal neurons is mediated by a direct Gi/o-βγ-subunit interaction with Cav1 channels. The Journal of Physiology, 591(7), 1599–1612. https://doi.org/10.1113/jphysiol.2012.245464

Perez-García, P., Pardillo-Díaz, R., Geribaldi-Doldán, N., Gómez-Oliva, R., Domínguez-García, S., Castro, C., Nunez-Abades, P., & Carrascal, L. (2021). Refinement of active and passive membrane properties of layer V pyramidal neurons in rat primary motor cortex during postnatal development. Frontiers in Molecular Neuroscience, 14. https://doi.org/10.3389/fnmol.2021.754393

Petersen, A. V., Cotel, F., & Perrier, J. (2016). Plasticity of the Axon Initial Segment: Fast and Slow Processes with Multiple Functional Roles. The Neuroscientist, 23(4), 364–373. https://doi.org/10.1177/1073858416648311

Planells-Cases, R., Caprini, M., Zhang, J., Rockenstein, E., Rivera, R., Murre, C., Masliah, E., & Montal, M. (2000). Neuronal death and perinatal lethality in Voltage-Gated sodium

channel AII-Deficient mice. Biophysical Journal, 78(6), 2878–2891. https://doi.org/10.1016/s0006-3495(00)76829-9

Popovic, M. A., Foust, A. J., McCormick, D. A., & Zecevic, D. (2011). The spatio-temporal characteristics of action potential initiation in layer 5 pyramidal neurons: a voltage imaging study. The Journal of Physiology, 589(17), 4167–4187. https://doi.org/10.1113/jphysiol.2011.209015

Principles of Neural Science, Fifth Edition | AccessBiomedical Science | McGraw Hill Medical. (n.d.). https://accessbiomedicalscience.mhmedical.com/book.aspx?bookid=1049

Qin, N., D'Andrea, M. R., Lubin, M., Shafaee, N., Codd, E. E., & Correa, A. M. (2003). Molecular cloning and functional expression of the human sodium channel β1B subunit, a novel splicing variant of the β1 subunit. European Journal of Biochemistry, 270(23), 4762–4770. https://doi.org/10.1046/j.1432-1033.2003.03878.x

Qiu, Q., Yang, M., Gong, D., Liang, H., & Chen, T. (2025). Potassium and calcium channels in different nerve cells act as therapeutic targets in neurological disorders. Neural Regeneration Research, 20(5), 1258–1276. https://doi.org/10.4103/nrr.nrr-d-23-01766

Qu, Y., Curtis, R., Lawson, D., Gilbride, K., Ge, P., DiStefano, P., Silos-Santiago, I., Catterall, W., & Scheuer, T. (2001). Differential Modulation of Sodium Channel Gating and Persistent Sodium Currents by the β1, β2, and β3 Subunits. Molecular and Cellular Neuroscience, 18(5), 570–580. https://doi.org/10.1006/mcne.2001.1039

Ragsdale, D. S., McPhee, J. C., Scheuer, T., & Catterall, W. A. (1994). Molecular determinants of State-Dependent block of NA + channels by local anesthetics. Science, 265(5179), 1724–1728. https://doi.org/10.1126/science.8085162

Rajakulendran, S., & Kullmann, D. (2013). Inherited Ion channel disorders of the brain. Advances in Clinical Neuroscience & Rehabilitation. https://doi.org/10.47795/qojv5711

Raman, I. M., & Bean, B. P. (2001). Inactivation and recovery of sodium currents in cerebellar purkinje neurons: evidence for two mechanisms. Biophysical Journal, 80(2), 729–737. https://doi.org/10.1016/s0006-3495(01)76052-3

Ramaswamy, S., & Markram, H. (2015). Anatomy and physiology of the thick-tufted layer 5 pyramidal neuron. Frontiers in Cellular Neuroscience, 9. https://doi.org/10.3389/fncel.2015.00233

Rasband, M. N. (2010). The axon initial segment and the maintenance of neuronal polarity. Nature Reviews. Neuroscience, 11(8), 552–562. https://doi.org/10.1038/nrn2852

Raymond, C. K., Castle, J., Garrett-Engele, P., Armour, C. D., Kan, Z., Tsinoremas, N., & Johnson, J. M. (2004). Expression of alternatively spliced sodium channel A-Subunit genes. Journal of Biological Chemistry, 279(44), 46234–46241. https://doi.org/10.1074/jbc.m406387200

Raz, A., & Perouansky, M. (2018). Central Nervous System Physiology. In Elsevier eBooks (pp. 145–173). https://doi.org/10.1016/b978-0-323-48110-6.00008-9

Reiner, A., Jiao, Y., Del Mar, N., Laverghetta, A. V., & Lei, W. L. (2003). Differential morphology of pyramidal tract-type and intratelencephalically projecting-type corticostriatal neurons and their intrastriatal terminals in rats. The Journal of Comparative Neurology, 457(4), 420–440. https://doi.org/10.1002/cne.10541

Richards, K. L., Milligan, C. J., Richardson, R. J., Jancovski, N., Grunnet, M., Jacobson, L. H., Undheim, E. a. B., Mobli, M., Chow, C. Y., Herzig, V., Csoti, A., Panyi, G., Reid, C. A., King,

G. F., & Petrou, S. (2018). Selective Na V 1.1 activation rescues Dravet syndrome mice from seizures and premature death. Proceedings of the National Academy of Sciences, 115(34). https://doi.org/10.1073/pnas.1804764115

Riordan, J. R., Rommens, J. M., Kerem, B., Alon, N., Rozmahel, R., Grzelczak, Z., Zielenski, J., Lok, S., Plavsic, N., Chou, J., Drumm, M. L., Iannuzzi, M. C., Collins, F. S., & Tsui, L. (1989). Identification of the cystic fibrosis gene: cloning and characterization of complementary DNA. Science, 245(4922), 1066–1073. https://doi.org/10.1126/science.2475911

Rojas-Piloni, G., Guest, J. M., Egger, R., Johnson, A. S., Sakmann, B., & Oberlaender, M. (2017). Relationships between structure, in vivo function and long-range axonal target of cortical pyramidal tract neurons. Nature Communications, 8(1). https://doi.org/10.1038/s41467-017-00971-0

Romand, S., Wang, Y., Toledo-Rodriguez, M., & Markram, H. (2011). Morphological development of Thick-Tufted layer V pyramidal cells in the rat somatosensory cortex. Frontiers in Neuroanatomy, 5. https://doi.org/10.3389/fnana.2011.00005

Rozo, J. A., Martínez-Gallego, I., & Rodríguez-Moreno, A. (2024). Cajal, the neuronal theory and the idea of brain plasticity. Frontiers in Neuroanatomy, 18. https://doi.org/10.3389/fnana.2024.1331666

Rubinstein, M., Han, S., Tai, C., Westenbroek, R. E., Hunker, A., Scheuer, T., & Catterall, W. A. (2015). Dissecting the phenotypes of Dravet syndrome by gene deletion. Brain, 138(8), 2219–2233. https://doi.org/10.1093/brain/awv142

Rush, A. M., Dib-Hajj, S. D., & Waxman, S. G. (2005). Electrophysiological properties of two axonal sodium channels, Nav1.2 and Nav1.6, expressed in mouse spinal sensory neurones. The Journal of Physiology, 564(3), 803–815. https://doi.org/10.1113/jphysiol.2005.083089

Sailer, C. A., Hu, H., Kaufmann, W. A., Trieb, M., Schwarzer, C., Storm, J. F., & Knaus, H. (2002). Regional Differences in Distribution and Functional Expression of Small-Conductance Ca2+-Activated K+Channels in Rat Brain. Journal of Neuroscience, 22(22), 9698–9707. https://doi.org/10.1523/jneurosci.22-22-09698.2002

Sami-Merah, S., Hammoudi-Triki, D., Martin-Eauclaire, M., & Laraba-Djebari, F. (2008). Combination of two antibody fragments F(ab′)2/Fab: An alternative for scorpion envenoming treatment. International Immunopharmacology, 8(10), 1386–1394. https://doi.org/10.1016/j.intimp.2008.05.011

Sánchez-Ponce, D., DeFelipe, J., Garrido, J. J., & Muñoz, A. (2012). Developmental expression of KV potassium channels at the axon initial segment of cultured hippocampal neurons. PLoS ONE, 7(10), e48557. https://doi.org/10.1371/journal.pone.0048557

Sanders, S. J., Campbell, A. J., Cottrell, J. R., Moller, R. S., Wagner, F. F., Auldridge, A. L., Bernier, R. A., Catterall, W. A., Chung, W. K., Empfield, J. R., George, A. L., Hipp, J. F., Khwaja, O., Kiskinis, E., Lal, D., Malhotra, D., Millichap, J. J., Otis, T. S., Petrou, S., . . . Bender, K. J. (2018). Progress in understanding and Treating SCN2A-Mediated Disorders. Trends in Neurosciences, 41(7), 442–456. https://doi.org/10.1016/j.tins.2018.03.011

Sanders, S. J., Murtha, M. T., Gupta, A. R., Murdoch, J. D., Raubeson, M. J., Willsey, A. J., Ercan-Sencicek, A. G., DiLullo, N. M., Parikshak, N. N., Stein, J. L., Walker, M. F., Ober, G. T., Teran, N. A., Song, Y., El-Fishawy, P., Murtha, R. C., Choi, M., Overton, J. D., Bjornson, R. D., . . . State, M. W. (2012). De novo mutations revealed by whole-exome sequencing

are strongly associated with autism. Nature, 485(7397), 237–241. https://doi.org/10.1038/nature10945

Santana, L. F., GóMez, A. M., & Lederer, W. J. (1998). Ca 2+ flux through promiscuous cardiac NA + channels: Slip-Mode conductance. Science, 279(5353), 1027–1033. https://doi.org/10.1126/science.279.5353.1027

Sarao, R., Gupta, S. K., Auld, V. J., & Dunn, R. J. (1991). Developmentaly regulated alternative RNA splicing of rat brain sodium channel mRNAs. Nucleic Acids Research, 19(20), 5673–5679. https://doi.org/10.1093/nar/19.20.5673

Satterstrom, F. K., Kosmicki, J. A., Wang, J., Breen, M. S., De Rubeis, S., An, J., Peng, M., Collins, R., Grove, J., Klei, L., Stevens, C., Reichert, J., Mulhern, M. S., Artomov, M., Gerges, S., Sheppard, B., Xu, X., Bhaduri, A., Norman, U., . . . Walters, R. K. (2020). Large-Scale Exome sequencing study implicates both developmental and functional changes in the neurobiology of autism. Cell, 180(3), 568-584.e23. https://doi.org/10.1016/j.cell.2019.12.036

Schade, S. D., & Brown, G. B. (2000). Identifying the promoter region of the human brain sodium channel subtype II gene (SCN2A). Molecular Brain Research, 81(1–2), 187–190. https://doi.org/10.1016/s0169-328x(00)00145-5

Schafer, D. P., Custer, A. W., Shrager, P., & Rasband, M. N. (2006). Early events in node of Ranvier formation during myelination and remyelination in the PNS. Neuron Glia Biology, 2(2), 69–79. https://doi.org/10.1017/s1740925x06000093

Schampel, A., & Kuerten, S. (2017). Danger: High Voltage—The role of Voltage-Gated calcium channels in central nervous system pathology. Cells, 6(4), 43. https://doi.org/10.3390/cells6040043

Schiller, J., Schiller, Y., Stuart, G., & Sakmann, B. (1997). Calcium action potentials restricted to distal apical dendrites of rat neocortical pyramidal neurons. The Journal of Physiology, 505(3), 605–616. https://doi.org/10.1111/j.1469-7793.1997.605ba.x

Schmalhofer, W. A., Calhoun, J., Burrows, R., Bailey, T., Kohler, M. G., Weinglass, A. B., Kaczorowski, G. J., Garcia, M. L., Koltzenburg, M., & Priest, B. T. (2008). ProTX-II, a selective inhibitor of NAV1.7 sodium channels, blocks action potential propagation in nociceptors. Molecular Pharmacology, 74(5), 1476–1484. https://doi.org/10.1124/mol.108.047670

Schumacher, M. A., Rivard, A. F., Bächinger, H. P., & Adelman, J. P. (2001). Structure of the gating domain of a Ca2+-activated K+ channel complexed with Ca2+/calmodulin. Nature, 410(6832), 1120–1124. https://doi.org/10.1038/35074145

Schwiening, C. J. (2012). A brief historical perspective: Hodgkin and Huxley. The Journal of Physiology, 590(11), 2571–2575. https://doi.org/10.1113/jphysiol.2012.230458

Seiffert, S., Pendziwiat, M., Bierhals, T., Goel, H., Schwarz, N., Van Der Ven, A., Boßelmann, C. M., Lemke, J., Syrbe, S., Willemsen, M. H., Hedrich, U. B. S., Helbig, I., & Weber, Y. (2022). Modulating effects of FGF12 variants on NaV1.2 and NaV1.6 being associated with developmental and epileptic encephalopathy and Autism spectrum disorder: A case series. EBioMedicine, 83, 104234. https://doi.org/10.1016/j.ebiom.2022.104234

Sempere-Ferràndez, A., Martínez, S., & Geijo-Barrientos, E. (2019). Synaptic mechanisms underlying the intense firing of neocortical layer 5B pyramidal neurons in response to cortico-cortical inputs. Brain Structure and Function, 224(4), 1403–1416. https://doi.org/10.1007/s00429-019-01842-8

Seyfarth, E. (2005). Julius Bernstein (1839–1917): pioneer neurobiologist and biophysicist. Biological Cybernetics, 94(1), 2–8. https://doi.org/10.1007/s00422-005-0031-y

SFARI Gene - Welcome. (n.d.). SFARI Gene. Retrieved June 28, 2025, from https://gene.sfari.org/

Shabani, K., Krupp, J., Lemesre, E., Lévy, N., & Tran, H. (2024). Voltage-Gated Ion Channel Compensatory Effect in DEE: Implications for future therapies. Cells, 13(21), 1763. https://doi.org/10.3390/cells13211763

Shah, M. M., Migliore, M., Valencia, I., Cooper, E. C., & Brown, D. A. (2008). Functional significance of axonal Kv7 channels in hippocampal pyramidal neurons. Proceedings of the National Academy of Sciences, 105(22), 7869–7874. https://doi.org/10.1073/pnas.0802805105

Shah, N. H., & Aizenman, E. (2013). Voltage-Gated Potassium Channels at the Crossroads of Neuronal Function, Ischemic Tolerance, and Neurodegeneration. Translational Stroke Research, 5(1), 38–58. https://doi.org/10.1007/s12975-013-0297-7

Shai, A. S., Anastassiou, C. A., Larkum, M. E., & Koch, C. (2015). Physiology of Layer 5 Pyramidal Neurons in Mouse Primary Visual Cortex: Coincidence Detection through Bursting. PLoS Computational Biology, 11(3), e1004090. https://doi.org/10.1371/journal.pcbi.1004090

Shaw, K. A., Williams, S., Patrick, M. E., Valencia-Prado, M., Durkin, M. S., Howerton, E. M., Ladd-Acosta, C. M., Pas, E. T., Bakian, A. V., Bartholomew, P., Nieves-Muñoz, N., Sidwell, K., Alford, A., Bilder, D. A., DiRienzo, M., Fitzgerald, R. T., Furnier, S. M., Hudson, A. E., Pokoski, O. M., . . . Maenner, M. J. (2025). Prevalence and early identification of autism spectrum disorder among children aged 4 and 8 years — Autism and Developmental Disabilities Monitoring Network, 16 sites, United States, 2022. MMWR Surveillance Summaries, 74(2), 1–22. https://doi.org/10.15585/mmwr.ss7402a1

Shaya, D., Kreir, M., Robbins, R. A., Wong, S., Hammon, J., Brüggemann, A., & Minor, D. L. (2011). Voltage-gated sodium channel (NaV) protein dissection creates a set of functional pore-only proteins. Proceedings of the National Academy of Sciences, 108(30), 12313–12318. https://doi.org/10.1073/pnas.1106811108

Shen, H., Zhou, Q., Pan, X., Li, Z., Wu, J., & Yan, N. (2017). Structure of a eukaryotic voltage-gated sodium channel at near-atomic resolution. Science, 355(6328). https://doi.org/10.1126/science.aal4326

Shin, W., Kweon, H., Kang, R., Kim, D., Kim, K., Kang, M., Kim, S. Y., Hwang, S. N., Kim, J. Y., Yang, E., Kim, H., & Kim, E. (2019). SCN2A haploinsufficiency in mice suppresses hippocampal neuronal excitability, excitatory synaptic drive, and Long-Term potentiation, and spatial learning and memory. Frontiers in Molecular Neuroscience, 12. https://doi.org/10.3389/fnmol.2019.00145

Shu, Y., Duque, A., Yu, Y., Haider, B., & McCormick, D. A. (2007). Properties of Action-Potential initiation in neocortical pyramidal cells: evidence from whole cell axon recordings. Journal of Neurophysiology, 97(1), 746–760. https://doi.org/10.1152/jn.00922.2006

Simonti, M. (2025a). A new mouse model of non-syndromic autism spectrum disorder carrying the human negative-dominant mutation L1314P of the SCN2A/Nav1.2 sodium channel. Abstract PS3.033 presented at NeuroFrance 2025, Montpellier, France. Available at https://efaidnbmnnnibpcajpcglclefindmkaj/https://pdf-program.abstractserver.com/?congress=nf2025

Simonti, M. (2025b). Phénotype autistique et mécanismes physiopathologiques chez des souris modélisant des mutations humaines du gène SCN2A. Doctoral dissertation, Université Côte d'Azur. Available at https://theses.fr/2025COAZ6011

Smirnov, N. (1948). Table for estimating the goodness of fit of empirical distributions. The Annals of Mathematical Statistics, 19(2), 279–281. https://doi.org/10.1214/aoms/1177730256

Sokolova, O., Kolmakova-Partensky, L., & Grigorieff, N. (2001). Three-Dimensional Structure of a Voltage-Gated Potassium Channel at 2.5 nm Resolution. Structure, 9(3), 215–220. https://doi.org/10.1016/s0969-2126(01)00578-0

Sotelo, C. (2020). The history of the Synapse. The Anatomical Record, 303(5), 1252–1279. https://doi.org/10.1002/ar.24392

Spillane, J., Kullmann, D. M., & Hanna, M. G. (2015). Genetic neurological channelopathies: molecular genetics and clinical phenotypes. Journal of Neurology Neurosurgery & Psychiatry, jnnp-311233. https://doi.org/10.1136/jnnp-2015-311233

Spratt, P. W., Alexander, R. P., Ben-Shalom, R., Sahagun, A., Kyoung, H., Keeshen, C. M., Sanders, S. J., & Bender, K. J. (2021). Paradoxical hyperexcitability from NaV1.2 sodium channel loss in neocortical pyramidal cells. Cell Reports, 36(5), 109483. https://doi.org/10.1016/j.celrep.2021.109483

Spratt, P. W., Ben-Shalom, R., Keeshen, C. M., Burke, K. J., Clarkson, R. L., Sanders, S. J., & Bender, K. J. (2019). The Autism-Associated gene SCN2A contributes to dendritic excitability and synaptic function in the prefrontal cortex. Neuron, 103(4), 673-685.e5. https://doi.org/10.1016/j.neuron.2019.05.037

Spruston, N. (2008). Pyramidal neurons: dendritic structure and synaptic integration. Nature Reviews. Neuroscience, 9(3), 206–221. https://doi.org/10.1038/nrn2286

Srinivasan, Y., Elmer, L., Davis, J., Bennett, V., & Angelides, K. (1988). Ankyrin and spectrin associate with voltage-dependent sodium channels in brain. Nature, 333(6169), 177–180. https://doi.org/10.1038/333177a0

Stuart, G. J., & Sakmann, B. (1994). Active propagation of somatic action potentials into neocortical pyramidal cell dendrites. Nature, 367(6458), 69–72. https://doi.org/10.1038/367069a0

Stuart, G., Schiller, J., & Sakmann, B. (1997). Action potential initiation and propagation in rat neocortical pyramidal neurons. The Journal of Physiology, 505(3), 617–632. https://doi.org/10.1111/j.1469-7793.1997.617ba.x

Sun, J., Liu, Y., Baudry, M., & Bi, X. (2020). SK2 channel regulation of neuronal excitability, synaptic transmission, and brain rhythmic activity in health and diseases. Biochimica Et Biophysica Acta (BBA) - Molecular Cell Research, 1867(12), 118834. https://doi.org/10.1016/j.bbamcr.2020.118834

Suzuki, M., & Larkum, M. E. (2017). Dendritic calcium spikes are clearly detectable at the cortical surface. Nature Communications, 8(1). https://doi.org/10.1038/s41467-017-00282-4

Syrbe, S., Zhorov, B. S., Bertsche, A., Bernhard, M. K., Hornemann, F., Mütze, U., Hoffmann, J., Hörtnagel, K., Kiess, W., Hirsch, F. W., Lemke, J. R., & Merkenschlager, A. (2016). Phenotypic Variability from Benign Infantile Epilepsy to Ohtahara Syndrome Associated with a Novel Mutation in SCN2A. Molecular Syndromology, 7(4), 182–188. https://doi.org/10.1159/000447526

Tian, C., Zhu, R., Zhu, L., Qiu, T., Cao, Z., & Kang, T. (2014). Potassium Channels: Structures, Diseases, and Modulators. Chemical Biology & Drug Design, 83(1), 1–26. https://doi.org/10.1111/cbdd.12237

Tikhonov, D. B., & Zhorov, B. S. (2004). Modeling P-Loops Domain of Sodium Channel: Homology with Potassium Channels and Interaction with Ligands. Biophysical Journal, 88(1), 184–197. https://doi.org/10.1529/biophysj.104.048173

Trimmer, J. S. (2015). Subcellular localization of K+ channels in mammalian brain neurons: remarkable precision in the midst of extraordinary complexity. Neuron, 85(2), 238–256. https://doi.org/10.1016/j.neuron.2014.12.042

Tsukamoto, T., Chiba, Y., Wakamori, M., Yamada, T., Tsunogae, S., Cho, Y., Sakakibara, R., Imazu, T., Tokoro, S., Satake, Y., Adachi, M., Nishikawa, T., Yotsu-Yamashita, M., & Konoki, K. (2017). Differential binding of tetrodotoxin and its derivatives to voltage-sensitive sodium channel subtypes (Na v 1.1 to Na v 1.7). British Journal of Pharmacology, 174(21), 3881–3892. https://doi.org/10.1111/bph.13985

Turrigiano, G. (2012). Homeostatic Synaptic Plasticity: local and global mechanisms for stabilizing neuronal function. Cold Spring Harbor Perspectives in Biology, 4(1), a005736. https://doi.org/10.1101/cshperspect.a005736

Vacher, H., Mohapatra, D. P., & Trimmer, J. S. (2008). Localization and targeting of Voltage-Dependent ion channels in mammalian central neurons. Physiological Reviews, 88(4), 1407–1447. https://doi.org/10.1152/physrev.00002.2008

Van Beuningen, S. F., Will, L., Harterink, M., Chazeau, A., Van Battum, E. Y., Frias, C. P., Franker, M. A., Katrukha, E. A., Stucchi, R., Vocking, K., Antunes, A. T., Slenders, L., Doulkeridou, S., Smitt, P. S., Altelaar, A. M., Post, J. A., Akhmanova, A., Pasterkamp, R. J., Kapitein, L. C., . . . Hoogenraad, C. C. (2015). TRIM46 controls neuronal polarity and axon specification by driving the formation of parallel microtubule arrays. Neuron, 88(6), 1208–1226. https://doi.org/10.1016/j.neuron.2015.11.012

Van Loo, K. M. J., & Becker, A. J. (2020). Transcriptional regulation of channelopathies in genetic and acquired epilepsies. Frontiers in Cellular Neuroscience, 13. https://doi.org/10.3389/fncel.2019.00587

Vaughn, M. J., & Haas, J. S. (2022). On the Diverse Functions of Electrical Synapses. Frontiers in Cellular Neuroscience, 16. https://doi.org/10.3389/fncel.2022.910015

Veech, R. L., Kashiwaya, Y., & King, M. T. (1995). The resting membrane potential of cells are measures of electrical work, not of ionic currents. Integrative Physiological and Behavioral Science, 30(4), 283–307. https://doi.org/10.1007/bf02691602

Verriello, L., Belluzzo, M., Pauletto, G., Torre, C. D., D'Esposito, F., Gagliano, C., Musa, M., Bertolotti, C., & Zeppieri, M. (2025). Channels out of Order: A Review of Central and Peripheral Nervous System Channelopathies. Discovery Medicine, 37(193), 244. https://doi.org/10.24976/discov.med.202537193.20

Villa, C., & Combi, R. (2016). Potassium Channels and Human Epileptic Phenotypes: An Updated Overview. Frontiers in Cellular Neuroscience, 10. https://doi.org/10.3389/fncel.2016.00081

Von Reyn, C. R., Spaethling, J. M., Mesfin, M. N., Ma, M., Neumar, R. W., Smith, D. H., Siman, R., & Meaney, D. F. (2009). Calpain mediates proteolysis of the Voltage-Gated sodium channel A-Subunit. Journal of Neuroscience, 29(33), 10350–10356. https://doi.org/10.1523/jneurosci.2339-09.2009

Wang, C., Wei, Z., Chen, K., Ye, F., Yu, C., Bennett, V., & Zhang, M. (2014). Structural basis of diverse membrane target recognitions by ankyrins. eLife, 3. https://doi.org/10.7554/elife.04353

Wang, J., Ou, S., & Wang, Y. (2017). Distribution and function of voltage-gated sodium channels in the nervous system. Channels, 11(6), 534–554. https://doi.org/10.1080/19336950.2017.1380758

Wanner, S. G., Koch, R. O., Koschak, A., Trieb, M., Garcia, M. L., Kaczorowski, G. J., & Knaus, H. (1999). High-Conductance Calcium-Activated Potassium Channels in Rat Brain: Pharmacology, Distribution, and Subunit Composition. Biochemistry, 38(17), 5392–5400. https://doi.org/10.1021/bi983040c

Waters, J., Larkum, M., Sakmann, B., & Helmchen, F. (2003). Supralinear Ca2+Influx into Dendritic Tufts of Layer 2/3 Neocortical Pyramidal NeuronsIn VitroandIn Vivo. Journal of Neuroscience, 23(24), 8558–8567. https://doi.org/10.1523/jneurosci.23-24-08558.2003

Wei, A. D., Gutman, G. A., Aldrich, R., Chandy, K. G., Grissmer, S., & Wulff, H. (2005). International Union of Pharmacology. LII. Nomenclature and Molecular Relationships of Calcium-Activated Potassium Channels. Pharmacological Reviews, 57(4), 463–472. https://doi.org/10.1124/pr.57.4.9

Westenbroek, R. E., Merrick, D. K., & Catterall, W. A. (1989). Differential subcellular localization of the RI and RII Na+ channel subtypes in central neurons. Neuron, 3(6), 695–704. https://doi.org/10.1016/0896-6273(89)90238-9

Westenbroek, R., Noebels, J., & Catterall, W. (1992). Elevated expression of type II Na+ channels in hypomyelinated axons of shiverer mouse brain. Journal of Neuroscience, 12(6), 2259–2267. https://doi.org/10.1523/jneurosci.12-06-02259.1992

Whitaker, W. R., Faull, R. L., Waldvogel, H. J., Plumpton, C. J., Emson, P. C., & Clare, J. J. (2001). Comparative distribution of voltage-gated sodium channel proteins in human brain. Molecular Brain Research, 88(1–2), 37–53. https://doi.org/10.1016/s0169-328x(00)00289-8

Wilson, M. J., Yoshikami, D., Azam, L., Gajewiak, J., Olivera, B. M., Bulaj, G., & Zhang, M. (2011). μ-Conotoxins that differentially block sodium channels NaV1.1 through 1.8 identify those responsible for action potentials in sciatic nerve. Proceedings of the National Academy of Sciences, 108(25), 10302–10307. https://doi.org/10.1073/pnas.1107027108

Wisedchaisri, G., & El-Din, T. M. G. (2022). Druggability of Voltage-Gated sodium Channels—Exploring old and new drug receptor sites. Frontiers in Pharmacology, 13. https://doi.org/10.3389/fphar.2022.858348

Wolff, M., Johannesen, K. M., Hedrich, U. B. S., Masnada, S., Rubboli, G., Gardella, E., Lesca, G., Ville, D., Milh, M., Villard, L., Afenjar, A., Chantot-Bastaraud, S., Mignot, C., Lardennois, C., Nava, C., Schwarz, N., Gérard, M., Perrin, L., Doummar, D., . . . Møller, R. S. (2017). Genetic and phenotypic heterogeneity suggest therapeutic implications in SCN2A-related disorders. Brain, 140(5), 1316–1336. https://doi.org/10.1093/brain/awx054

Wollner, D. A., & Catterall, W. A. (1986). Localization of sodium channels in axon hillocks and initial segments of retinal ganglion cells. Proceedings of the National Academy of Sciences, 83(21), 8424–8428. https://doi.org/10.1073/pnas.83.21.8424

Workman, A. D., Charvet, C. J., Clancy, B., Darlington, R. B., & Finlay, B. L. (2013). Modeling Transformations of Neurodevelopmental Sequences across Mammalian Species. Journal of Neuroscience, 33(17), 7368–7383. https://doi.org/10.1523/jneurosci.5746-12.2013

Wright, S. H. (2004). Generation of resting membrane potential. AJP Advances in Physiology Education, 28(4), 139–142. https://doi.org/10.1152/advan.00029.2004

Wu, H., Shen, L., Indajang, J., Savalia, N. K., Johnson, T. G., Qu, J., Bender, K. J., & Kwan, A. C. (2025). Autism-associated Scn2a haploinsufficiency disrupts in vivo dendritic signaling and impairs flexible decision-making. bioRxiv (Cold Spring Harbor Laboratory). https://doi.org/10.1101/2025.04.08.647866

Xu, X., & Shrager, P. (2005). Dependence of axon initial segment formation on Na+ channel expression. Journal of Neuroscience Research, 79(4), 428–441. https://doi.org/10.1002/jnr.20378

Yamada, R., & Kuba, H. (2016). Structural and functional plasticity at the Axon initial segment. Frontiers in Cellular Neuroscience, 10. https://doi.org/10.3389/fncel.2016.00250

Yamagata, T., Ogiwara, I., Mazaki, E., Yanagawa, Y., & Yamakawa, K. (2017). Nav1.2 is expressed in caudal ganglionic eminence-derived disinhibitory interneurons: Mutually exclusive distributions of Nav1.1 and Nav1.2. Biochemical and Biophysical Research Communications, 491(4), 1070–1076. https://doi.org/10.1016/j.bbrc.2017.08.013

Yamaji, N., Little, M. J., Nishio, H., Billen, B., Villegas, E., Nishiuchi, Y., Tytgat, J., Nicholson, G. M., & Corzo, G. (2009). Synthesis, solution structure, and phylum selectivity of a spider Δ-Toxin that slows inactivation of specific voltage-gated sodium channel subtypes. Journal of Biological Chemistry, 284(36), 24568–24582. https://doi.org/10.1074/jbc.m109.030841

Yamano, R., Miyazaki, H., & Nukina, N. (2022). The diffuse distribution of Nav1.2 on mid-axonal regions is a marker for unmyelinated fibers in the central nervous system. Neuroscience Research, 177, 145–150. https://doi.org/10.1016/j.neures.2021.11.005

Yang, J., Xiao, Y., Li, L., He, Q., Li, M., & Shu, Y. (2019). Biophysical properties of somatic and axonal Voltage-Gated sodium channels in midbrain dopaminergic neurons. Frontiers in Cellular Neuroscience, 13. https://doi.org/10.3389/fncel.2019.00317

Ye, M., Yang, J., Tian, C., Zhu, Q., Yin, L., Jiang, S., Yang, M., & Shu, Y. (2018). Differential roles of NaV1.2 and NaV1.6 in regulating neuronal excitability at febrile temperature and distinct contributions to febrile seizures. Scientific Reports, 8(1). https://doi.org/10.1038/s41598-017-17344-8

Yoon, S., Piguel, N. H., & Penzes, P. (2022). Roles and mechanisms of ankyrin-G in neuropsychiatric disorders. Experimental & Molecular Medicine, 54(7), 867–877. https://doi.org/10.1038/s12276-022-00798-w

Yoshimura, T., & Rasband, M. N. (2014). Axon initial segments: diverse and dynamic neuronal compartments. Current Opinion in Neurobiology, 27, 96–102. https://doi.org/10.1016/j.conb.2014.03.004

Yu, E. J., Ko, S., Lenkowski, P. W., Pance, A., Patel, M. K., & Jackson, A. P. (2005). Distinct domains of the sodium channel β3-subunit modulate channel-gating kinetics and

subcellular location. Biochemical Journal, 392(3), 519–526. https://doi.org/10.1042/bj20050518

Yu, F. H., & Catterall, W. A. (2003). Overview of the voltage-gated sodium channel family. Genome Biology, 4(3), 207. https://doi.org/10.1186/gb-2003-4-3-207

Yu, F. H., & Catterall, W. A. (2004). The VGL-Chanome: a protein superfamily specialized for electrical signaling and ionic homeostasis. Science S STKE, 2004(253). https://doi.org/10.1126/stke.2532004re15

Yu, F. H., Mantegazza, M., Westenbroek, R. E., Robbins, C. A., Kalume, F., Burton, K. A., Spain, W. J., McKnight, G. S., Scheuer, T., & Catterall, W. A. (2006). Reduced sodium current in GABAergic interneurons in a mouse model of severe myoclonic epilepsy in infancy. Nature Neuroscience, 9(9), 1142–1149. https://doi.org/10.1038/nn1754

Yu, Y., Maureira, C., Liu, X., & McCormick, D. (2010). P/Q and N Channels Control Baseline and Spike-Triggered Calcium Levels in Neocortical Axons and Synaptic Boutons. Journal of Neuroscience, 30(35), 11858–11869. https://doi.org/10.1523/jneurosci.2651-10.2010

Yusifov, T., Savalli, N., Gandhi, C. S., Ottolia, M., & Olcese, R. (2008). The RCK2 domain of the human BK Ca channel is a calcium sensor. Proceedings of the National Academy of Sciences, 105(1), 376–381. https://doi.org/10.1073/pnas.0705261105

Zeidan, J., Fombonne, E., Scorah, J., Ibrahim, A., Durkin, M. S., Saxena, S., Yusuf, A., Shih, A., & Elsabbagh, M. (2022). Global prevalence of autism: A systematic review update. Autism Research, 15(5), 778–790. https://doi.org/10.1002/aur.2696

Zeng, Q., Yang, Y., Duan, J., Niu, X., Chen, Y., Wang, D., Zhang, J., Chen, J., Yang, X., Li, J., Yang, Z., Jiang, Y., Liao, J., & Zhang, Y. (2022). SCN2A-Related Epilepsy: the phenotypic spectrum, treatment and Prognosis. Frontiers in Molecular Neuroscience, 15. https://doi.org/10.3389/fnmol.2022.809951

Zhang, J., Chen, X., Eaton, M., Wu, J., Ma, Z., Lai, S., Park, A., Ahmad, T. S., Que, Z., Lee, J. H., Xiao, T., Li, Y., Wang, Y., Olivero-Acosta, M. I., Schaber, J. A., Jayant, K., Yuan, C., Huang, Z., Lanman, N. A., . . . Yang, Y. (2021). Severe deficiency of the voltage-gated sodium channel NaV1.2 elevates neuronal excitability in adult mice. Cell Reports, 36(5), 109495. https://doi.org/10.1016/j.celrep.2021.109495

Zhang, Z. (2004). Maturation of layer V pyramidal neurons in the rat prefrontal cortex: intrinsic properties and synaptic function. Journal of Neurophysiology, 91(3), 1171–1182. https://doi.org/10.1152/jn.00855.2003

Zhao, P., Waxman, S. G., & Hains, B. C. (2006). Sodium Channel Expression in the Ventral Posterolateral Nucleus of the Thalamus after Peripheral Nerve Injury. Molecular Pain, 2. https://doi.org/10.1186/1744-8069-2-27

Zhu, X., Yu, Y., Jiang, Z., Otani, Y., & Fujitani, M. (2025). Ankyrin-G and its binding partners in neurons: orchestrating the molecular structure of the axon initial segment. Biomolecules, 15(6), 901. https://doi.org/10.3390/biom15060901

Zonta, B., Desmazieres, A., Rinaldi, A., Tait, S., Sherman, D. L., Nolan, M. F., & Brophy, P. J. (2011). A Critical Role for Neurofascin in Regulating Action Potential Initiation through Maintenance of the Axon Initial Segment. Neuron, 69(5), 945–956. https://doi.org/10.1016/j.neuron.2011.02.021